



HAL
open science

Energy relaxation mechanisms in plasmonic nanocomposite materials under femtosecond laser excitation

Balint Eles

► **To cite this version:**

Balint Eles. Energy relaxation mechanisms in plasmonic nanocomposite materials under femtosecond laser excitation. Optics / Photonics. Université de Lyon, 2022. English. NNT : 2022LYSES027 . tel-04023476

HAL Id: tel-04023476

<https://theses.hal.science/tel-04023476>

Submitted on 10 Mar 2023

HAL is a multi-disciplinary open access archive for the deposit and dissemination of scientific research documents, whether they are published or not. The documents may come from teaching and research institutions in France or abroad, or from public or private research centers.

L'archive ouverte pluridisciplinaire **HAL**, est destinée au dépôt et à la diffusion de documents scientifiques de niveau recherche, publiés ou non, émanant des établissements d'enseignement et de recherche français ou étrangers, des laboratoires publics ou privés.



Order number NNT: 2022LYSES027

PhD Thesis in Optics, Photonics, Laser

Completed at
University of Lyon

**Doctoral School N° 488
Sciences, Ingénierie, Santé**

Publicly defended on 18/07/2022, by:
Balint Eles

Energy relaxation mechanisms in plasmonic nanocomposite materials under femtosecond laser excitation

In front of the jury composed of

BONSE, Jörn	Principal researcher, Bundesanstalt für Materialforschung und-prüfung (BAM), Berlin, Germany	Reviewer
GROJO, David	Research director, Aix-Marseille Université, Marseille, France	Reviewer
SIEGEL, Jan	Researcher, Instituto de Óptica IO-CSIC, Madrid, Spain	Examiner
STOIAN, Razvan	Research director, Laboratoire Hubert Curien, UJM/CNRS UMR5516, Saint-Étienne, France	Examiner
CRUT, Aurélien	Professor assistant, Université de Lyon, CNRS, Université Claude Bernard Lyon 1, Institut Lumière Matière, Villeurbanne, France	Examiner
DESTOUCHES, Nathalie	Professor, Laboratoire Hubert Curien, UJM/CNRS UMR5516, Saint-Étienne, France	Director
HUBERT, Christophe	Professor assistant, Laboratoire Hubert Curien, UJM/CNRS UMR5516, Saint-Étienne, France	Co-Director

Acknowledgement

Hereby I would like to express my sincere gratitude to my thesis supervisor, Professor Nathalie Destouches for providing me guidance throughout the long process of learning the methodology of research. I greatly appreciate her profound involvement in my work, and I am going to keep the good memories of our interactions during the long years of the thesis work. Furthermore, I would also like to thank my co-supervisor Dr. Christophe Hubert for the daily casual discussions on my projects that helped me to keep my enthusiasm.

My thanks and appreciations go to all my colleagues who have personally accompanied me throughout years, and with whom I could share all my thoughts concerning not exclusively research topics.

Beside the people from my laboratory, enormous contribution was made by all my relatives thousands of kilometers away who always listened to me and provided precious advice. Their support truly helped me to keep on working. Special thanks to you: my beloved parents, siblings and Andika.

Contents

Introduction	1
1 Laser-matter interactions of metallic NPs	4
1.1 Electronic properties of noble metals	4
1.2 Optical response of noble metals	6
1.3 Ultrafast energy relaxation mechanisms below reshaping fluence threshold.....	10
1.4 NP shape transformations under intense laser excitation	16
1.4.1 Photo-oxidation	16
1.4.2 Heat-assisted NP growth mechanisms.....	17
1.4.3 Competition between growth and shrinkage	19
1.4.4 Timescales of the different processes	20
1.4.5 NP reshaping involving melting	21
1.4.6 Laser-induced anisotropic NP reshaping.....	23
1.5 Laser-driven material organizations	25
1.5.1 Laser-induced periodic surface structures	25
1.5.1.1 Electromagnetic approaches	25
1.5.1.2 Matter reorganization theories	27
1.5.2 Self-organization of metallic NPs	28
2 Time-resolved techniques for characterizing laser-matter interactions	31
2.1 Ultrafast pump-probe spectroscopy of plasmonic nano-objects.....	31
2.2 Ultrafast pump-probe microscopy	36
2.2.1 Spatially-overlapped pump and probe beams.....	37
2.2.2 Raster scanning.....	38
2.2.3 Optical microscopy approach	39

2.3	Quadriwave lateral shearing interferometry	40
2.3.1	Measurement principles.....	40
2.3.2	Example applications.....	43
3	Mechanisms driving the self-organized reshaping of plasmonic metasurfaces	45
3.1	Introduction.....	45
3.2	Experimental methods	46
3.2.1	Preparation of Ag/TiO ₂ multilayer nanocomposite by physical vapor deposition	46
3.2.2	High-repetition-rate pump-probe microscopy setup	48
3.3	Numerical approaches	54
3.3.1	Modeling the laser-induced temperature profile	54
3.3.2	Electromagnetic calculations.....	56
3.4	Experimental results	58
3.4.1	Laser fluence-dependent spectral kinetics.....	59
3.4.2	Multipulse evolution of the optical anisotropy.....	60
3.4.3	Effect of the heat accumulation.....	61
3.4.4	Time-resolved experiments on short timescale	64
3.4.5	<i>Ex situ</i> electron microscopy of structural changes	65
3.4.6	Comparison of <i>in situ</i> thermal annealing to laser-induced heating	70
3.5	Discussion.....	73
3.5.1	Morphological transformations	73
3.5.2	Optical origin of self-organized reshaping	79
3.6	Conclusion	83
4	Ultrafast dynamics of plasmonic NP shape transformations	84
4.1	Introduction.....	84
4.2	Experimental methods	86
4.2.1	Transient absorption spectroscopy for reversible excitation	86

4.2.2	Pump-probe microscopy for irreversible excitation	88
4.3	Results and discussions.....	91
4.3.1	Reversible energy relaxation	92
4.3.2	Discussion on transient absorption spectra.....	96
4.3.3	Ultrafast dynamics of irreversible transformations below the single-pulse ablation threshold	97
4.3.4	Local laser fluence-dependent dynamics.....	99
4.3.5	Temporal dynamics of NP reshaping in the multipulse regime	100
4.3.6	Ultrafast response below reshaping threshold.....	103
4.3.7	Discussion on irreversible sample transformations	104
4.3.7.1	Electron microscopy revealing NP shape transformations	104
4.3.7.2	Mechanisms driving the NP reshaping	108
4.3.8	Dynamics above single-pulse ablation threshold	110
4.3.9	Local fluence-dependent dynamics above the ablation threshold.....	114
4.3.10	Discussion on ablation phenomena	116
4.4	Conclusion	118

5 Investigation of coherent acoustic pulse emission by plasmonic NP ensembles..... 120

5.1	Introduction.....	120
5.2	Principles of coherent acoustic pulse excitation and detection	121
5.2.1	Opto-acoustic conversion	121
5.2.2	Principles of detecting the acoustic pulse propagation.....	123
5.3	Multilayer samples with different Ag thicknesses.....	126
5.4	Results and discussion	127
5.4.1	Detection of acoustic pulse propagation.....	127
5.4.2	Acoustic frequency-dependent attenuation in disordered materials.....	133
5.4.3	Numerical investigation of acoustic wavefront distortions	135
5.5	Conclusion	139

General conclusions and perspectives	140
Appendix	143
Bibliography.....	144

Abstract

The present thesis is devoted to analyze the multitime scale response of plasmonic nanocomposite materials submitted to femtosecond laser irradiation. Understanding the energy relaxation pathways following the laser excitation in such materials paves the way for well-controlled laser processing that is particularly important for the laser-based micro- and nanostructuring of metasurfaces. The material studied throughout the work is a composite of silver nanoislands encapsulated between two titania layers, deposited on glass substrate. The system exhibits rich dynamics under reversible and irreversible relaxation conditions that serve as the main focus of the present work.

The thesis relies on three main pillars. The first part describes the complex interplay of the mechanisms leading to laser-induced anisotropic shape transformation and formation of self-organized nanopatterns. The irreversible material shape transformation is demonstrated to origin from the accumulative effect of tens of thousands of laser pulses with distinctive intermediate states of matter. These states are characterized via a broad range of experimental techniques revealing the structural transformations and corresponding optical response of the system. The decisive role of laser-induced temperature rise is deeply analyzed in this multipulse phenomenon using numerical methods. Additionally, the quantitative investigation of characteristic self-organized nanogratings with drastically varying spatial profiles is discussed by means of combining the structural observations with rigorous electromagnetic calculations. The provided general description of the course of fundamental physico-chemical mechanisms contributes to the development of plasmonic metasurface applications in domains requiring anisotropic optical response and organized nanoparticle arrangement on the nanometer scale.

The subsequent experiments aim at characterizing the ultrafast dynamics of the shape transformations using pump-probe microscopy experiments. The ultrafast phenomena reflect the pulse-by-pulse transformation of the optical response in the accumulative regime, and the observed dynamics is interpreted based on the literature of photoexcited plasmonic systems, as well as *ex situ* structural characterizations. The latter clearly reveal traces of ultrafast phenomena driving the shape transformations. The results demonstrate the variation of the ultrafast electron dynamics due to pulse-by-pulse system transformations. Additionally, the ultrafast dynamics of ablation processes of plasmonic nanocomposites is discussed with combined quantitative phase-sensitive measurements.

The material response in the weak excitation regime below reshaping energy threshold is investigated using transient spectroscopic methods. The experiments reveal the ability of a single layer of silver nanoislands with broad shape dispersion and characteristic size variations to excite coherent acoustic pulses. Various samples with drastically different nanoisland morphologies are tested, and the propagation of acoustic pulses in glass substrate is monitored. Quantitative analysis of the acoustic wave features is conducted using a simplified theoretical model revealing the key parameters affecting the acoustic pulse emission properties of such inhomogeneous nanoparticle ensembles.

Introduction

Controlling the properties of metallic nanoparticles (NPs) ensembles in a host matrix plays important role in fabricating plasmonic nanocomposite materials. The optical response of such materials is dominated by one or several resonances in their absorption and scattering spectra, called localized surface plasmon resonances (LSPR). The emergence of such resonances is a direct consequence of the size reduction in the nanoscale. LSPR is a collective oscillation of conduction electrons, which is excited by the incoming electric field of the incident light. The enhanced light absorption and scattering close to the resonance frequencies possess high potential for tailoring the optical response of materials. This collective property is highly sensitive to the shape and size distribution of the plasmonic ensemble, material properties, as well as the inter-particle distance and the dielectric permittivity of the host environment.

There were several approaches aiming to tailor the optical response of plasmonic nanocomposite materials in scalable performance. Among those, lasers have been used to alter the optical response of nanocomposites by tuning the ensemble characteristics of the NPs by inducing organization on the nanometer-micrometer scale [1]. In other works, metallic NPs were shaped into anisotropic shapes along the laser polarization to tailor dichroic optical properties which is highly required, *e.g.* in applications related to visual appearance [2], [3]. Furthermore, the laser-induced structural reorganization of various nanocomposites, metals and dielectrics emerged as fruitful nanostructuring technique. The applications of laser-controlled nanostructures were widely examined by both scientific and engineering communities. One of the main directions is the controlled formation of organized nanostructures served as diffractive optical elements manipulating the optical spectra. The properties of such nano-gratings were demonstrated to be controllable by irradiation parameters such as laser polarization, wavelength, fluence, and scan speed, which was useful for color marking, encryption, and optical data storage [4], [5]. Additionally, plasmonic NPs and nanostructures were demonstrated to have great potential in nano-imaging [6] and light engineering metamaterials [7]. The number of possible applications of the latter consisting of artificially designed structures are rapidly growing, including *e.g.* metasurface-based holography [8]. In other fields, the idea of applying plasmonic nanocomposites in photocatalysis resulted in the birth of rapidly flourishing research domain, which encapsulated noble NPs such as Au and Ag into various host media, *e.g.* semiconductors [9]. The photocatalytic effect resulted from the light absorption in the visible and near-infrared wavelength range and the nearfield enhancement effect due to the LSPR. The plasmonic absorption by the metallic NPs injected free electrons into the nearby semiconductors of suitable band gaps. Contacting noble metal with a semiconductor forms a so-called Schottky junction that

efficiently separates the electrons and holes to avoid the recombination due to the buildup of an internal electric field.

In parallel to the rapidly growing number of applications, several characterization techniques for small nano-objects were developed, *e.g.* high-resolution transmission electron microscopy, scanning tunneling microscopy and atomic force microscopy. Additionally, the development of femtosecond (fs) laser sources enabled the realization of time-resolved studies of the ultrafast material response to photoexcitation. These techniques are based on optical monitoring the relaxation mechanisms on various timescales, achieved by measuring the transient changes induced in the transmission/reflection/scattering of the sample. Contributions permitted to determine the size-dependent timescales of the internal energy redistribution mechanisms via the electron and lattice interactions [10], enabled to study acoustic vibrations of nano-objects [11], their cooling and shape transformations [12]. Additionally, the recent development of single-particle time-resolved optical spectroscopy has allowed to explore the more precise correlation between the measured dynamics and the morphology of the nano-object [13]. Exploiting the development of this concept, investigations of vibrational properties of single nanometric size objects have raised a large technological and fundamental interest during the last decade. They have been motivated by the need for the deeper understanding of the fundamental acoustic energy transfer at the nanoscale, or investigation of the vibrational response of nm-sized objects in comparison to bulk partners [14]. In the case of metallic NPs, such studies mostly focused on nano-objects formed by a single material component, with various shapes and sizes [15]. In case of metallic thin films, time-resolved ultrafast techniques were applied to study acoustic wave generation, propagation and attenuation in various materials [16], [17]. As the wavelength of such acoustic waves are in the order of magnitude of tens of nanometers, monitoring the wave propagation was proved to be versatile for non-invasive spatial profiling of the material [18]. Furthermore, ultrafast single-particle techniques enabled to investigate spatial variations in photoexcited phenomena triggered in nano-objects, providing information on the spatial distribution of energy relaxation related to structural properties [19]. The need for the more precise understanding of the fundamental background of all previously mentioned applications and principles seeded the work described in the present dissertation. The scope of the thesis covers the investigations of laser-matter interactions in nanocomposite materials containing of noble metal NPs by means of a combination of time-resolved *in situ* pump-probe techniques and various *ex situ* investigations.

The thesis is organized into five chapters. In the first chapter, the physical properties of bulk and nanoscale noble metals are described from theoretical point of view. The electronic properties of bulk metals are first reviewed, followed by their optical response. The decisive effect of nanoscale confinement is then discussed. Subsequently, the ultrafast relaxation mechanisms

triggered by the impulsive excitation of a metallic NP is discussed in details. In regard of the results presented later, the relaxation mechanisms is divided into two groups, discussing the relevant scenarios of reversible and irreversible material relaxation pathways separately. The latter involve complete shape transformation and material reorganization. In the subsequent chapter, the relevant time-resolved experimental techniques are reviewed that are widely used by the research community for characterizing the time-dependent material relaxation with high temporal and spatial resolutions. The subsequent three chapters contain the description of the results obtained throughout the preparation of the present work.

The third chapter describes a study aiming to characterize the mechanisms of material relaxation in plasmonic nanocomposites leading to laser-induced anisotropic NP shape transformation and organized arrangement of NP ensembles under fs pulse excitation. The study explores the intermediate states of the material when submitted to thousands of intense fs laser pulses, using numerous experimental characterizations and modeling the laser-induced temperature profile in the system. The laser-induced nanoscale organization is analyzed using quantitative electromagnetic calculations.

In the fourth chapter, the ultrafast dynamics of the photo-excited plasmonic nanocomposites is investigated using pump-probe techniques. The aim of that chapter is to understand how the electron and lattice dynamics, and the slower cooling dynamics of the heated system evolve in case of pulse-by-pulse irreversible transformations under multiple fs laser excitation. Additionally, experiments explore the ultrafast dynamics of nanocomposite ablation.

In the last chapter, the excitation and propagation of coherent acoustic pulses emitted by random plasmonic NPs are investigated. Several nanocomposites containing different NP morphologies are tested in order to understand the mechanisms of coherent pulse excitation by random arrangement of acoustic sources. The energy dissipation during the acoustic pulse propagation in glass medium is monitored in details using pump-probe technique.

The thesis is finished by a general conclusion of the main results and perspectives of the future works.

1 Laser-matter interactions of metallic NPs

The ultrafast excitation of plasmonic NP ensembles leads to a time-dependent modification of the electronic, thermal and structural properties. Additionally, if the excitation is sufficiently strong, irreversible modifications of these parameters can be provoked. Following the instantaneous photon absorption, the material relaxation spans over multiple timescales with a broad variety of physico-chemical phenomena involved. The aim of this chapter is to provide a detailed description of the course of mechanisms triggered by photoexcitation in plasmonic systems. In the first part, the electronic and optical properties of bulk noble metals are discussed, that are widely used for plasmonics applications. Afterwards, the optical response of metallic nano-objects with simple geometries is described, with particular regard for their LSPR. Subsequently, the description of the relaxation pathways on different timescales for reversible and irreversible excitations are discussed. In the latter case, the description focuses on relevant laser-induced NP shape transformations and the formation of self-organized nanostructures.

1.1 Electronic properties of noble metals

The optical response of metals (absorption and scattering) reflects the interaction of light with its electrons, and is therefore closely linked to its electronic band structure. Ag belongs to the family of noble metals. The Ag atoms are organized in a face-centered cubic (fcc) crystalline lattice. The interactions between atoms induce a broadening of the discrete energy levels of atoms leading to a continuum of electronic states, called electronic bands. In noble metals, the atomic d orbitals contribute to completely filled and weakly dispersed d bands (valence band) whereas the hybridized s - p atomic orbitals form the partially filled s - p band (conduction band). The valence band is the highest energy band completely filled with electrons, and the conduction band is the lowest energy band partially filled. At $T = 0$ K, the energy bands are filled until the Fermi energy E_F . Electrons in the conduction band are delocalized being thus responsible for most electrical and thermal transport properties, while the valence bands electrons contribute only little to these features [20]. Figure 1.1 shows a schematic view of the band structure of noble metals. There are two distinct light absorption mechanisms demonstrated in this figure. First, photon-excited transitions between quasi-free electronic states within the conduction band (intraband transitions). In this case, transition to a higher-energy state of this band implies a momentum increase. The momentum of the absorbed photon being negligible, interaction with a third body (another electron, phonon or lattice defect) is necessary to respect momentum conservation [21]. The second type of transition is photon-excited transitions of valence electrons

to the conduction band (interband transitions). These transitions may occur only for high enough photon energies, in order to allow for the direct (vertical) transition of electron from the valence band to a free state of the conduction band. The associated threshold, corresponding to the energy difference between the top of the valence band and E_F is about 4 eV for Ag [22].

The electrons in the conduction band can be described as quasi-free electrons with a dispersion relation, *i.e.*, energy E vs. wave vector \mathbf{k} of the states [23]:

$$E(\mathbf{k}) = \frac{\hbar^2 k^2}{2m^*}, \quad (1.1)$$

where m^* is the electron effective mass, which includes the effects of the interactions of the electron with the ionic lattice and \hbar is the reduced Planck constant. m^* is linked to the Fermi energy as

$$E_F = \frac{\hbar^2}{2m^*} (3\pi n_e)^{2/3}, \quad (1.2)$$

where n_e describes the conduction electron density of the metal. In connection with E_F , one can define several important physical quantities such as Fermi temperature $T_F = E_F/k_B$ with k_B being the Boltzmann constant and the Fermi velocity $V_F = \sqrt{\frac{2E_F}{m^*}}$ [20].

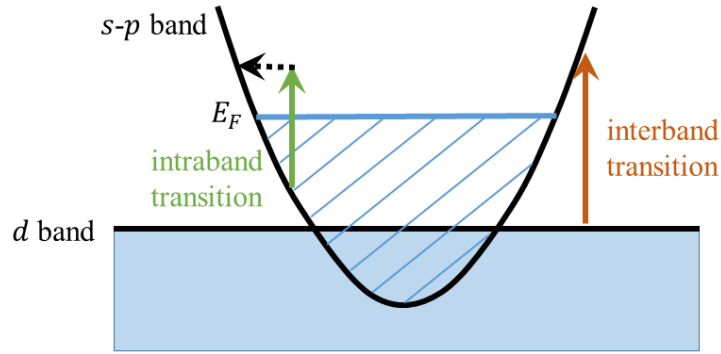


Figure 1.1 – Demonstration of the band structure of noble metals showing a low-dispersed valence band (filled d band) and a partially filled conduction band ($s-p$ band). Photon absorption by a valence band electron can result in the transition towards conduction band (interband transition). The intraband transitions are accompanied by the assistance of another quantity indicated by dashed line (phonon, another electron or lattice defect). Figure is adapted from [21].

1.2 Optical response of noble metals

In metals, the optical properties are ruled by the response of electrons to external electromagnetic field. Considering a monochromatic electromagnetic field with wave vector \mathbf{k} and angular frequency ω

$$\mathbf{E}(\mathbf{r}, t) = \Re(\mathbf{E}_0 e^{i(\mathbf{k}\mathbf{r} - \omega t)}) \quad (1.3)$$

interacting with a material, a polarization density \mathbf{P} is induced due to the displacement of the bound positive and negative charges. In the case of a homogeneous, linear and isotropic material, the polarization is expressed simply as $\mathbf{P} = \varepsilon_0 \chi \mathbf{E}$, where the electric susceptibility $\chi(\omega)$ is a scalar function of ω , and ε_0 is the vacuum permittivity. The electric displacement can be expressed as

$$\mathbf{D} = \varepsilon_0 \mathbf{E} + \mathbf{P} = \varepsilon_0 \varepsilon \mathbf{E}, \quad (1.4)$$

where $\varepsilon = 1 + \chi$ represents the dielectric function (or relative permittivity) of the material. ε may be written as $\varepsilon(\omega) = \varepsilon_1(\omega) + i\varepsilon_2(\omega)$, with ε_1 and ε_2 related through the Kramers-Kronig relation. Alternatively, the optical properties can be described using the complex optical index $\tilde{n} = n + i\kappa$, related to ε via

$$\varepsilon_1 + i\varepsilon_2 = (n + i\kappa)^2. \quad (1.5)$$

Its real part n is the refraction index, related to the phase velocity of light in the material, while the extinction coefficient κ specifies the absorption of electromagnetic energy by the solid. In the case of noble metals, the real and imaginary dielectric functions can be separated in two contributions, corresponding to interaction of the field with electrons in the conduction band (intraband contribution) and to photoexcited transitions (interband contribution). Classically, intraband transitions are described by the Drude model, based on the quantities ε^D and χ_D , while interband transitions are governed by ε^{ib} and χ^{ib} , related to ε via

$$\varepsilon = 1 + \chi_D + \chi^{ib} = \varepsilon^D + \varepsilon^{ib} - 1. \quad (1.6)$$

The Drude part of the dielectric function ε^D is associated to the absorption of light by electrons in the conduction band. In this picture, they are considered as a free gas, being described by the classical kinetic gas theory [24]. An isolated atom represents a positively charged nucleus, surrounded by bound electrons, and one or several conduction electrons. Their conduction electrons are delocalized and free to move in the lattice. These electrons create a gas of floating negatively charged electrons. The atoms' nuclei surrounded by the bound electrons become a

positively charged lattice. The electron scattering processes are introduced in a phenomenological way as a friction with characteristic time τ [20]. Indeed, τ is the electron optical relaxation time, which is determined by electron-electron (e-e) and electron-phonon (e-ph) scattering (neglecting electron-defect scattering) with simultaneous exchange of the energy of a photon. The probability of photon scattering is proportional to $1/\tau$ since it has to be assisted by a third quasi-particle (phonon or electron) to satisfy energy and momentum conservations [25]. Assuming the contributions to be uncorrelated, one can write

$$\frac{1}{\tau} = \frac{1}{\tau_{e-e}} + \frac{1}{\tau_{e-ph}}. \quad (1.7)$$

At room temperature, the dominant contribution to τ in bulk metals originates from the e-ph scattering term. To account for the fact that the electrons are weakly bound instead of completely free, the electron mass m_e appearing in the original Drude model must be replaced by the effective mass m^* , as described in the previous section. In the presence of an oscillating electric field $\mathbf{E}(t) = \mathbf{E}_0 \cos(\omega t)$, position \mathbf{r} of an electron follows the equation of motion [21]:

$$m^* \frac{d^2 \mathbf{r}}{dt^2} = -m^* \gamma \frac{d\mathbf{r}}{dt} - e\mathbf{E}, \quad (1.8)$$

where $-e$ is the electron charge and $\gamma = 1/\tau$. From the solution $\mathbf{r}(t)$ of equation 1.8 in the stationary regime, the polarization of the metal is obtained through $\mathbf{P} = -n_e e \mathbf{r}$. As previously described, \mathbf{P} is defined as $\mathbf{P} = \epsilon_0 \chi \mathbf{E}$, therefore the Drude permittivity is provided as:

$$\epsilon^D(\omega) = 1 + \chi^D = 1 - \frac{\omega_p^2}{\omega(\omega + i\gamma)}, \quad (1.9)$$

where $\omega_p = \sqrt{\frac{n_e e^2}{m_e \epsilon_0}}$ is the plasma frequency. By expressing the real and imaginary parts of ϵ , assuming that $\omega \gg \gamma$, one finds:

$$\begin{aligned} \epsilon_1^D(\omega) &= 1 - \frac{\omega_p^2}{\omega^2 + \gamma^2} \approx -\frac{\omega_p^2}{\omega^2} \\ \epsilon_2^D(\omega) &= \frac{\omega_p^2 \gamma}{\omega(\omega^2 + \gamma^2)} \approx \frac{\omega_p^2 \gamma}{\omega^3}. \end{aligned} \quad (1.10)$$

The low-energy part of $\varepsilon(\omega)$ can be well-reproduced within this framework, due to the interband transitions being resonant only for higher energies. The fit in the infrared part of the spectrum allows thus to extract the values of the plasma frequency and damping rate, yielding $\omega_p = 8.98$ eV and $\gamma = 0.020$ eV for Ag [20].

The term ε^{ib} in Eq. (1.6) is associated to interband transitions of electrons from low energy bands (*e.g.* localized d-band) to bands of higher energy induced by absorption of an incoming photon [26]. The interband transition contribution to the stationary absorption spectrum of Ag can be computed through models developed to interpret thermomodulation experiments on bulk noble metals investigating the temperature-dependent optical response of a thin metallic film in equilibrium conditions. Rosei *et al.* developed a model for computing the interband component of the imaginary dielectric function ε_2^{ib} for incident photon energies close to the interband transition threshold for noble metals like Ag [27]. After calculating ε_2^{ib} , the real part ε_1^{ib} of ε^{ib} is deduced using the Kramers–Kronig relation [28].

The optical response of a metallic nano-object in a dielectric environment strongly differs from that of the bulk. Dielectric confinement induces resonances in the absorption and scattering spectra of metallic nano-objects, known as LSPR. These resonances allow the sensitive probing of the relaxation phenomena determining the ultrafast dynamics of a nano-object after its sudden excitation. These resonances, associated to a collective electron motion induced by light, result in a strong enhancement of the electromagnetic field in and around the nano-objects. Their amplitudes, spectral positions and widths are strongly dependent on the geometry, size and composition of the nano-objects, as well as on their local environment. When an electromagnetic wave illuminates the nano-object, the electrons oscillate along the light polarization. This electronic periodic movement induces electric fields inside the NP and scattered one, propagating through the external matrix (from the NPs towards every direction). Considering a transparent environment, the incident power loss (extinction) W_{ext} in the propagation direction is caused by the sum of the absorbed power W_{abs} and scattered power W_{scat} by the nano-object. Therefore, if one defines the extinction cross-sections σ as the ratio of the powers over the average incident light intensity, then [21]

$$\sigma_{ext} = \sigma_{abs} + \sigma_{scat}. \quad (1.11)$$

Providing analytic expressions for the total cross-sections is possible in simple cases. It should be noted that the extinction cross-section is proportional to the particle volume while the scattering cross-section is linear to its square [20]. For small nano-objects (NP diameter $\ll \lambda$), the scattering cross-section becomes negligible yielding to an extinction cross-section which is dominated by absorption.

The metal properties related to the quasi-free electrons are modified in a nano-object due to their interaction with the interface [25]. Consequently, the intraband contribution to the dielectric constant of the metallic NP preserves its Drude form with the scattering time τ' expressed as

$$\frac{1}{\tau'} = \frac{1}{\tau} + \frac{V_F}{R} g_S. \quad (1.12)$$

The first term $1/\tau$ reflects bulk-like electron scattering in the particle. The second term is proportional to the Fermi velocity V_F divided by the radius R of the assumed spherical NP, with a frequency and electron distribution - dependent proportionality factor g_S of the order of 1 [25]. It is a direct consequence of the limitation of the electron motion. Classically, it can be interpreted as being due to electron scattering off the surface whose probability becomes comparable to the other scattering processes in sufficiently small NPs.

In most experiments, ensembles of NPs dispersed in a liquid or solid matrix or deposited on a substrate are investigated. In such cases, effective medium approximations could be used, which allow to model the macroscopic properties of composite materials based on the properties and the relative fractions of its components. There are many different effective medium approximations that are valid in peculiar cases. A well-known formula is provided by Maxwell Garnett. It states that the effective permittivity ε_{eff} of a composite containing of a host material with ε_h permittivity including small spherical particles with ε_i permittivity distributed randomly but uniformly on average is provided as [29]

$$\varepsilon_{eff} = \varepsilon_h \frac{\varepsilon_h + \frac{1+2f}{3}(\varepsilon_i - \varepsilon_h)}{\varepsilon_h + \frac{1-f}{3}(\varepsilon_i - \varepsilon_h)}, \quad (1.13)$$

where f is the volume fraction of the inclusion.

1.3 Ultrafast energy relaxation mechanisms below reshaping fluence threshold

In this section, the reversible temporal-dependent response of plasmonic NPs following ultrafast laser excitation is detailed. The energy deposition into the electrons is realized by absorption of the pump beam creating electrons that are spread over different levels in the conduction band. In metallic nanostructures, light absorption is enhanced by exciting the LSPR. Figure 1.2A demonstrates the course of the subsequent energy relaxation pathways on various time-scales after the photoexcitation.

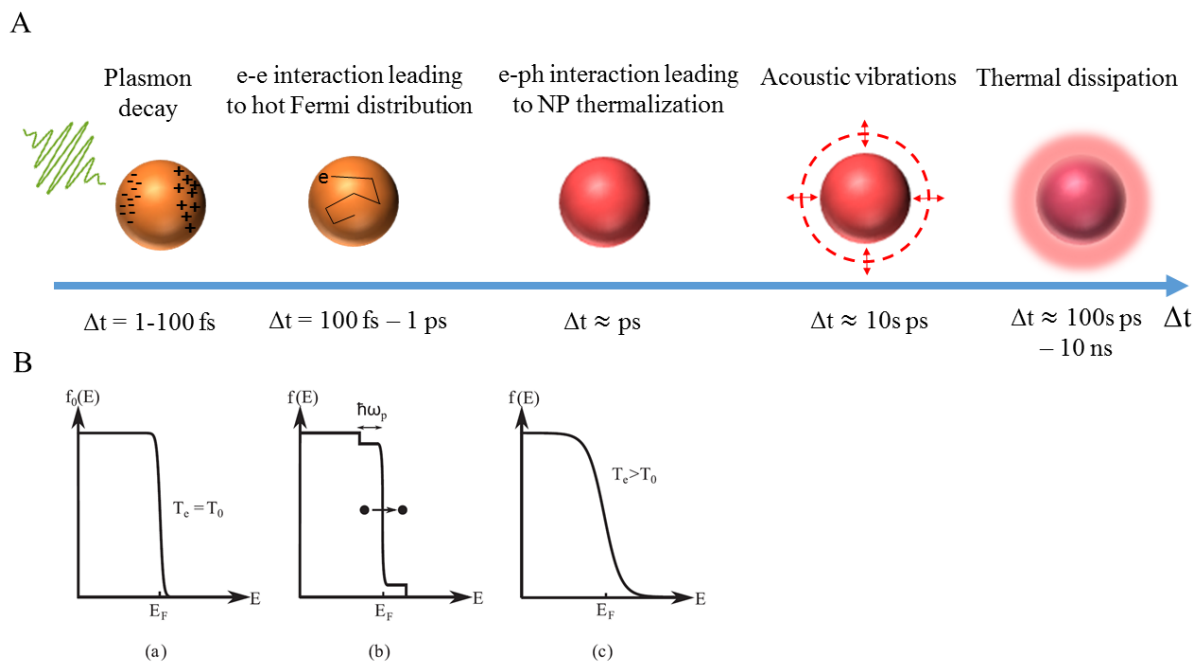


Figure 1.2 – Photoexcitation of a metallic NP. A: Sketch of events and approximate timescales following photon absorption. B: Evolution of the electron distribution function $f(E)$. (a) An equilibrium function f_0 before excitation, (b) athermal distribution following instantaneous excitation with pump photon energy of $\hbar\omega_p$, and (c) a hot Fermi distribution, after e-e interaction. Image B is taken from [20].

Following the instantaneous light absorption, the collective motion of the conduction electrons can be damped radiatively by re-emission of a photon or non-radiatively through the creation of hot electrons via Landau damping on a timescale ranging from 1 to 100 fs [30]. The electrons will quickly redistribute their energy among many lower-energy electrons via e-e scattering processes. Time-resolved studies evidenced that the characteristic timescale for this process is in the range of 100 fs to 1 ps resulting in a formation of hot Fermi–Dirac energy distribution characterized by a large electron temperatures [22], [25]. A demonstration of the variation of the electron energy distribution $f(E)$ following the photoexcitation is demonstrated in Figure

1.2B. Experiments conducted in the low perturbation regime, where the electron distribution is only slightly disturbed, revealed size-dependent rate of e-e interaction, *i.e.*, the magnitude of the e-e relaxation decreases by roughly a factor of 2 as the size of the particles decreases from 26 nm diameter to 3 nm diameter [31].

At this stage of the relaxation, interactions with phonons increase. The subsequent thermal equilibration of electrons with the lattice occurs over a longer timescale of several ps. The coupling between the hot electrons and the phonon modes of the particle can be described by the two-temperature model (TTM) [32]. In this model, the rate of energy exchange between the electrons and phonons is given by coupled differential equations

$$C_e(T_e) \frac{dT_e}{dt} = -g(T_e - T_l) \quad (1.14a)$$

$$C_l \frac{dT_l}{dt} = g(T_e - T_l), \quad (1.14b)$$

where T_e and T_l are the electronic and lattice temperatures, C_l is the lattice heat capacity, $C_e(T_e)$ is the temperature-dependent electronic heat capacity [24], and g is the e-ph coupling constant [10]. The room temperature electronic heat capacity is much smaller than the lattice heat capacity [24]. This has a consequence that the initial electronic temperature after laser excitation is much higher than the temperature of the equilibrated electron-phonon system. Additionally, relaxation time of this process exhibits strong pump laser intensity-dependence. The increase in lattice temperature from optical excitation is typically a few K to tens of K in the low perturbation regime, although it is possible to trigger reversible shape transformation upon strong heating, *e.g.* melting, fragmentation or ablation. These mechanisms are further detailed in the following section. Transient absorption experiments on different kinds of NPs showed a strong dependence of the electron-phonon coupling time on the particle size, *i.e.*, faster relaxation times towards smaller NP sizes [33], [34]. This was explained in terms of coupling to surface phonon modes, which causes an increase in the value of the e-ph coupling constant [35]. However, for noble NPs, some results reported almost no size dependence [36].

Raising the lattice temperature results in a small amount of expansion of the lattice. This expansion can excite coherent vibrational normal modes of the nano-object volume [15], [37], [38]. The vibrational properties of nanometric size objects have raised a large technological and fundamental interest during the last decade. Coherently excited vibrational modes have been detected for a wide range of different size and shape particles in time-resolved experiments. These vibrational modes have size-dependent periods of typically ~ 1 to few tens of ps, and are damped in a few hundred ps. The excited modes give rise to modulations in the optical response

of the material. The acoustic vibrations of a nano-object modify the interatomic distances due to dynamical volume changes resulting in a modulation of its dielectric function, which is reflected as oscillations in time-resolved signals. Their period directly reflects the dominantly excited vibrational modes, while their damping contains information on the mode damping rates [11].

A demonstration can be seen in Figure 1.3 where Ag nanospheres in glass medium (a) and Au nanorods in aqueous solution (b) were investigated using pump-probe technique [11].

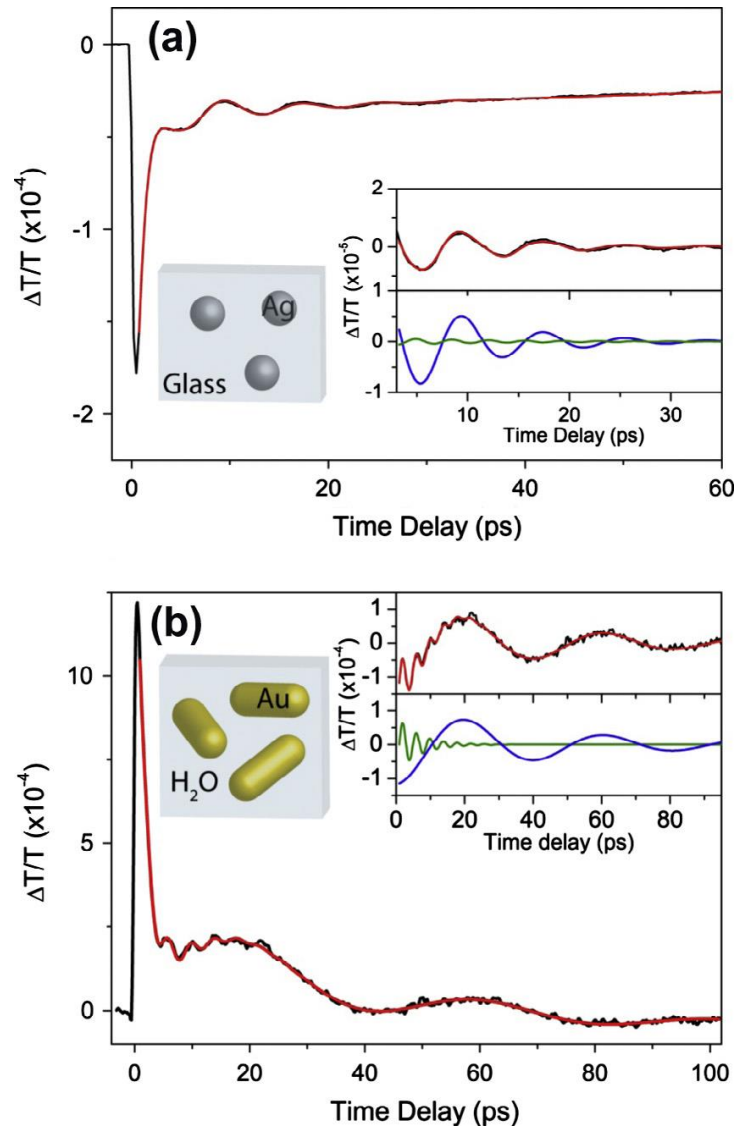


Figure 1.3 – Time-resolved detection of acoustic vibrations in different NPs. (a) Ag nanospheres embedded in glass (mean diameter $D = 26$ nm). The bare experimental signal and its fit with sum of two exponentials and two damped sinusoids are shown in black and red, respectively. Inset: (top) experiment (black) and fit (red) oscillating parts; (bottom) the two damped sinusoids used in the fit with periods of 8.0 and 3.6 ps (blue and green). (b) Au nanorods in aqueous solution (mean length $L = 34$ nm and diameter $D = 10$ nm). The oscillating part is fitted with two damped sinusoids. The figure is taken from [11].

The temporal signal was accurately reproduced by the sum of two decaying exponentials and two damped sinusoidal functions. The two first contributions described fast electron cooling dynamics after excitation by the pump pulse, due to energy transfer to the lattice, and slow NP heat transfer to the glass matrix, respectively. At intermediate timescales (<30 ps), the signal exhibited clear oscillatory component, which resulted from the coherent vibrations of NPs. The oscillating part of the signal, obtained via subtracting the exponential contributions due to electron-lattice and NP-environment energy transfer from the raw data, was dominated by a damped oscillation with 8 ps period, and a smaller second oscillation mode with approximately half period, which were reproduced by two damped sinusoidal functions. These vibrational periods were attributed to the breathing mode and first harmonic radial modes of the nanosphere. Damping of the oscillating signal reflected both acoustic energy dissipation to the surrounding medium (homogeneous damping) and dephasing between the vibrations of the NPs composing the sample. The latter contribution depends on NP size and shape dispersion. It can be separated from the measured overall damping rate. Time-resolved signals measured in a colloidal solution of Au nanorods (mean 34 nm length and 10 nm diameter), and their analysis with the same procedure as for spheres are presented in Figure 1.3b. Two oscillations with very different periods (41 and 4 ps) are clearly visible, respectively corresponding to longitudinal and transverse vibrations of the nanorods.

The illustration of the computed acoustic modes excited on the NPs can be seen in Figure 1.4. For Ag sphere with $D = 26$ nm diameter, Figure 1.4a shows the semi-analytically computed frequency and excitation amplitudes of radial modes, and Figure 1.4b depicts the displacement profiles associated to $n = 0$ and $n = 1$ modes in any plane containing the sphere center. The computed frequency for the fundamental mode is 126 GHz (7.9 ps period), and for $n = 1$ mode is 276 GHz (3.6 ps period). As demonstrated, the dominant contribution of the former mode is well-accounted by the quick decrease of the excitation amplitude with n in the simulated vibrational spectra. For Au nanorods, dominant frequencies of about 24 and 246 GHz are computed (41.8 ps and 4.1 ps periods in Figure 1.4c) corresponding to the longitudinal and transverse motions, respectively (shown in Figure 1.4d).

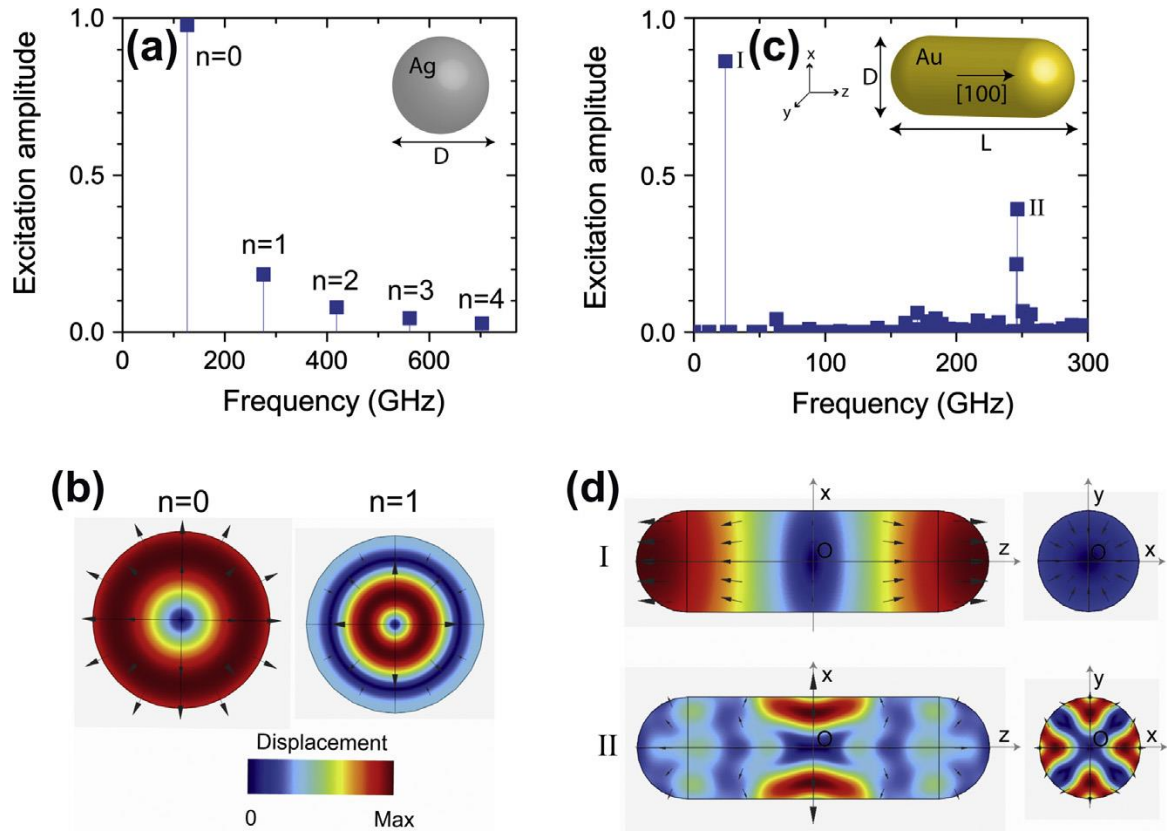


Figure 1.4 – Modeling NP acoustic vibrations. (a) Vibrational spectrum of Ag nanosphere. The frequency and excitation amplitude of radial modes were semi-analytically computed. (b) Displacement fields of $n = 0$ and $n = 1$ modes. (c) Vibrational spectrum of Au nanorod. Computations were performed using finite element method. (d) Displacement fields of mode (I) and the breathing mode with the largest excitation amplitude (II), in both longitudinal and transverse planes. The figure is taken from [11].

In case of NP ensembles, the dephasing between the vibrations of the different NPs is relevant. To demonstrate that, Figure 1.5 shows a comparison of the transient absorption traces from a single Ag nanocube (average edge length is 35.5 ± 3.4 nm) and a bulk sample (ensemble) [39]. Coherently excited vibrational modes can be seen in both traces, but the modulations in the single-particle trace are more pronounced and show a much longer damping time than the ensemble measurements. Fitting the modulations with damped cosine function yields a lifetime of 30 ps for the ensemble measurement, compared to 58 ps for the single-particle experiment. The faster damping rate in the ensemble studies is due to sample inhomogeneity: different sized particles have different periods, leading to a dephasing [40]. In contrast, the damping in the single particle studies is due to mechanical interactions between the particle and its surroundings [41]. The advantages of using single particle pump-probe experiments over ensemble measurements for studying vibrational dynamics are obvious from these measurements.

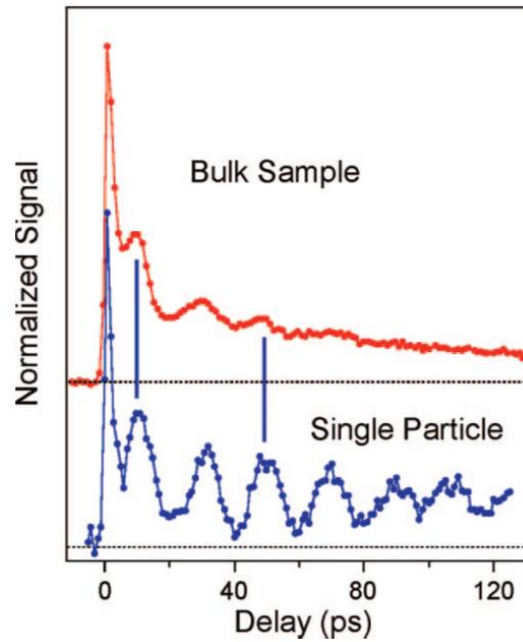


Figure 1.5 – Comparison of time-resolved traces from ensemble and a single Ag nanocube measurements. The two traces show very similar periods and phases (as shown by the vertical lines), but different damping times. The figure is taken from [39].

After the internal e-e scattering and e-ph coupling process are finished, the hot particle thermally equilibrates with its environment. This process has two components: heat transfer across the interface between the particle and its surroundings, and heat diffusion in the surroundings [42]. The modalities of heat transfer at macroscopic and nanometer scales differ in particular by the increased role played by interfaces on the nanoscale. These are characterized by a thermal interface resistance (Kapitza resistance), which describes the ratio between temperature jump and heat flux at the interface [43]. Time-resolved experiments investigated the rate of energy dissipation from Au NPs in aqueous solution with average sizes ranging from 4 to 50 nm in diameter [44]. The results demonstrated characteristic timescale for relaxation that varies from ~ 10 ps for the smallest particles examined (≈ 4 nm in diameter) to almost 400 ps for the 50 nm diameter particles. Additionally, the initial temperature of the particles evidenced no impact on the relaxation time. The two heat dissipation mechanisms depend on the NP sizes in different ways. The important factor is the surface-to-volume ratio of the particle, and the timescale for interface conductance-dominated relaxation scales as R , whereas, the heat dissipation-dominated cooling scales as R^2 [45], [46]. The size dependence is much stronger than that for the faster e-ph coupling process. For a spherical particle, the interface conductance component of heat dissipation is described by [10]:

$$\frac{\partial T_P}{\partial t} = -\frac{3G}{R\rho_P C_P}(T_P(t) - T_S(R, t)), \quad (1.15)$$

where T_P and T_S are the temperatures of the particle and the surroundings, ρ_P and C_P are the density and heat capacity of the particle, G is the interface thermal conductance defined as the inverse of Kapitza resistance, and R is the NP radius. One can neglect the heat diffusion within in metallic NPs. Heat diffusion in the surroundings is described by the diffusion equation, expressed for spherically symmetric particles in the form [10]:

$$\frac{\partial^2(rT_S)}{\partial r^2} = \frac{1}{\alpha_S} \frac{\partial(rT_S)}{\partial t}, \quad (1.16)$$

where α_S is the thermal diffusivity, and $r \geq R$ is the radial coordinate. Analysis of time-resolved signals yields an estimate for the thermal interface resistance between the initially heated metallic material and its environment (solid and liquid). Measurements have yielded interface thermal conductance G in the 20 - 400 MW/m²/K range [42], [45], [47] and addressed G sensitivity to the compositions of the metal, of the surrounding medium and of their interface [43].

1.4 NP shape transformations under intense laser excitation

The discussion about the ultrafast energy relaxation mechanisms detailed in the previous section is continued by the description of the mechanisms that account for Ag NP shape transformations when intense laser excitation is applied.

1.4.1 Photo-oxidation

When Ag NPs are in contact with a semiconductor matrix, such as TiO₂, the electron energy required to allow electrons to leave the NPs is lowered to the value of the Schottky barrier that is created at the interface between the metal and the semiconductor. Electrons excited through the LSPR of NPs at the laser wavelength can cross the Schottky barrier by injection or tunneling, as depicted in Figure 1.6A. Plasmon-induced charge transfer is of great importance in developing highly efficient photocatalysis and photovoltaic devices. The band bending prevents the injected electrons from escaping back to the NP. The positively charged NPs are unstable,

and tend to dissolve into Ag^+ ions, as shown in Figure 1.6B. This process is referred to as photo-oxidation, and it results in NP size shrinkage.

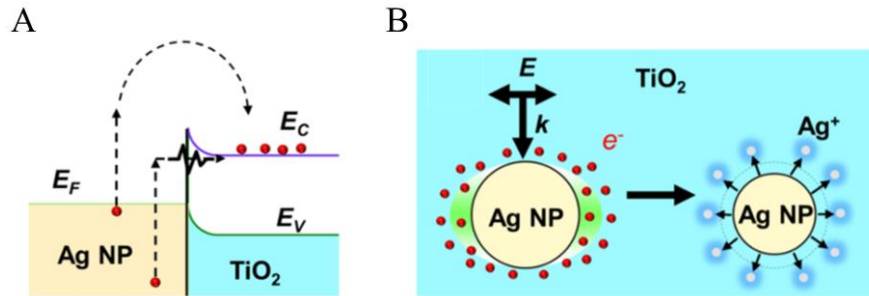


Figure 1.6 – Illustration of injection and tunneling of plasmon-induced hot-electrons (A), and photo-oxidation and subsequent dissociation phenomena (B) after laser excitation of Ag NPs embedded in TiO₂ matrix. E_C and E_V stand for the energy levels of the conduction and valence bands of TiO₂. The figure is adapted from [48].

1.4.2 Heat-assisted NP growth mechanisms

Several Ag NP growth mechanisms were described in the literature that are strongly promoted when the laser-induced temperature rise is high in the material. The mechanisms influence NP size as well as temporal evolution of Ag atoms between three forms: Ag^0 , Ag^+ and Ag NPs. First, a reduction reaction that converts Ag^+ to Ag^0 , *i.e.*, Ag^+ ions can diffuse in the surrounding - assuming that the Ag^+ mobility is sufficiently high - and recombine with electrons from the matrix conduction band (*e.g.* TiO₂, Figure 1.6) or from other compounds absorbed by the film [49]. The reduction process leads to increasing density of Ag^0 monomers that can contribute to the NP growth according to the following mechanisms. The growth of NPs can be driven by Ostwald ripening process, in which two phases are distinguished: clusters and monomers. The clusters are Ag NPs in the present case. The monomer is the Ag^0 whose concentration increases via the previous reduction step. In an Ostwald Ripening process, the growth of one Ag NP relies on the adsorption of Ag^0 monomer which is diffused by a force raised from the difference in Ag^0 volume concentration at macroscopic scale and at Ag NP surface. Therefore, thermal diffusion is an important initiator of the Ag NP growth in the matrix. The diffusion rate also depends on the temperature rise within the film and follows the Arrhenius' law [50].

Beside Ostwald ripening, NP coalescence process contributes to NP growth. In this mechanism, NPs contact and merge into a single nano-object. This process has been observed in many metallic systems. Molecular dynamics (MD) simulations of the NP coalescence process enable to obtain insight into the details. In such MD calculations, the temperature-dependent dynamics of NP coalescence between a pair of hollow Ag nanospheres [51] or Au nanodisks [52], [53] is monitored, or the shape transitions of a single Au nanorod [54] is investigated. In the case of a system of coalescing NPs, the radius of gyration r_g is monitored, which is defined as the root mean square distance of the NPs from the center of mass of the system. The coalescence process is characterized by the overall decrease of r_g depending on the temperature. The general description of the mechanisms driving the coalescence process at different temperature ranges is provided as follows.

The atom trajectory calculations revealed that atomic grain-boundary diffusion is the dominant mechanism at the first stage of the coalescence at lower temperatures (typically when $T < 400 - 500$ °C for initial NP diameters around 5 – 6 nm), where atoms migrate along the boundary between two contacted particles [52], [53]. At this stage, nearly constant or slight decreasing r_g is observed. Towards higher temperatures, the accumulation of amorphous layers leads to the so-called intermediate transition region [51], [54]. The accumulating portion of atoms in amorphous phase activates rapid viscous atomic flow, which is known as an important mechanism for amorphous materials. The viscous atomic flow is driven by surface curvature to reduce surface energy, which could lead to a faster decreasing r_g . For NPs, the surface energy becomes rather important factor, therefore this process results in a surface tension-driven atomic migration that is faster than normal force - free migration [53]. This is the reason for the faster decreasing r_g . Towards higher temperatures, the activation of the so-called “spherication” process driven by curvature-induced surface diffusion slows down the coalescence [51], [53]. The particles keep moving towards each other to form into one sphere. This slower process continues until reaching the melting point of the NPs resulting in a rapid collapse of the system into a single sphere [53]. The temperature ranges for the onset of the different mechanisms is not definite, *i.e.*, the melting temperature and the dynamics of the different diffusion processes exhibit strong initial NP size and heating rate dependence [51]–[53].

1.4.3 Competition between growth and shrinkage

The works of Liu *et al.* investigated experimentally and numerically the main physico-chemical mechanisms that influence the size of Ag NPs embedded in TiO₂ matrix loaded with Ag atoms (Ag), Ag ions (Ag⁺) and Ag NPs when exposed to continuous visible laser light [55]. In those experiments, the initial TiO₂ film was amorphous and mesoporous, and the initial Ag size distribution was a Gaussian distribution (centered at 3 nm diameter). They performed a series of laser scans at different speeds, and observed *ex situ* the final NP size and shape distributions as a result of irreversible NP shaping. The authors developed a numerical model describing the temporal evolution of the NP size during the beam passage. This model linked the transformations among Ag, Ag⁺ and Ag NPs in the composite system through the analysis of the involved physico-chemical mechanisms.

The demonstration of the course of mechanisms can be seen in Figure 1.7. One considers the oxidation reaction that decreases the Ag NPs size and increases the number of Ag⁺ ions, a reduction reaction that converts Ag⁺ to Ag⁰, Ostwald Ripening and inter-particle coalescence growth reactions. All these reactions are controlled by laser light and plasmon-induced temperature rise.

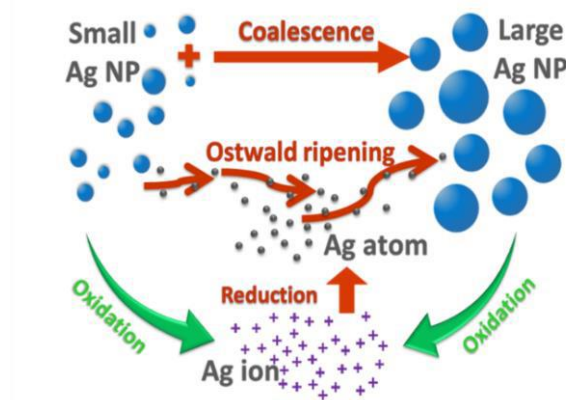


Figure 1.7 – Illustration of the main reactions that control the size distribution of Ag activated directly by the laser field or by the laser-induced temperature rise. The figure is taken from [55].

In general, provided that incident laser intensity is high enough, oxidation competes with growth, described by the temporal evolution of the system containing Ag⁺, Ag⁰ and Ag NP. The theoretical simulations were successfully compared to experimental results of NP distributions revealing the significant influence of each involved process.

These previous numerical studies suffered, however, from several limitations. Namely, they modeled the evolution of the system in a point without considering the effect of heating by the NPs grown few micrometers apart and still under the laser beam. The temperature was then calculated by assuming a homogeneous spatial size distribution of NPs under the laser spot. To overcome these limitations, Ma *et al.* proposed a two-dimensional model, which accounted for both thermal and spatial size distribution during laser writing to better investigate the NP growth kinetics [56]. In this model, NPs inside the laser spot acted as heat sources and contributed to the temperature field via thermal diffusion. As discussed previously, a portion of the absorbed laser energy decays via the e-ph and ph-ph interactions that thermalize the irradiated region. The electron relaxations and e-ph coupling occur on the timescale of few picoseconds, while ph-ph interactions take up to a few nanoseconds. Since Ag NPs grow more slowly than the e-ph interaction speed, the classical thermal diffusion equation was introduced in the model. The authors simulated the processes in cross-section (2D calculations). In the first step of the calculations, the temperature field is computed by finite element method. With the knowledge of the heat distribution, the growth, oxidation, and reduction are calculated. Additionally, solely diffusion-controlled NP growth mechanism was considered, which means that the coalescence process was not modeled. The extended 2D model provided new insights into the understanding of the writing speed-dependent phenomena, such as Ag NP growth in the laser front edge due to pre-heating by thermal diffusion, and the dynamical variations of the spatial size-distribution and temperature profile until a steady-state appeared.

1.4.4 Timescales of the different processes

A sketch of the time-dependent mechanisms following fs laser excitation of Ag NPs embedded in TiO₂ matrix is shown in Figure 1.8. The photon absorption by the NP generates a high density of excited electrons. e-e scattering results in a hot electron plasma typically within few hundreds of fs that is not in thermodynamic equilibrium with the environment (NP and matrix) [57]. Electrons with higher energy than the Schottky barrier formed at the Ag/TiO₂ interface can be injected into the conduction band of the TiO₂. This plasmon-induced electron transfer has been measured to be faster than 240 fs for Au NPs [58] and is expected to be of the same order of magnitude for Ag. Positively charged Ag NPs are created due to the high density of electrons leaving the NP, possessing strong electrostatic repulsion forces between neighboring ions, leading to Ag⁺ ejection. This charge-assisted atomic desorption results in NP size shrinkage, in opposition to the NP growth mechanisms described previously.

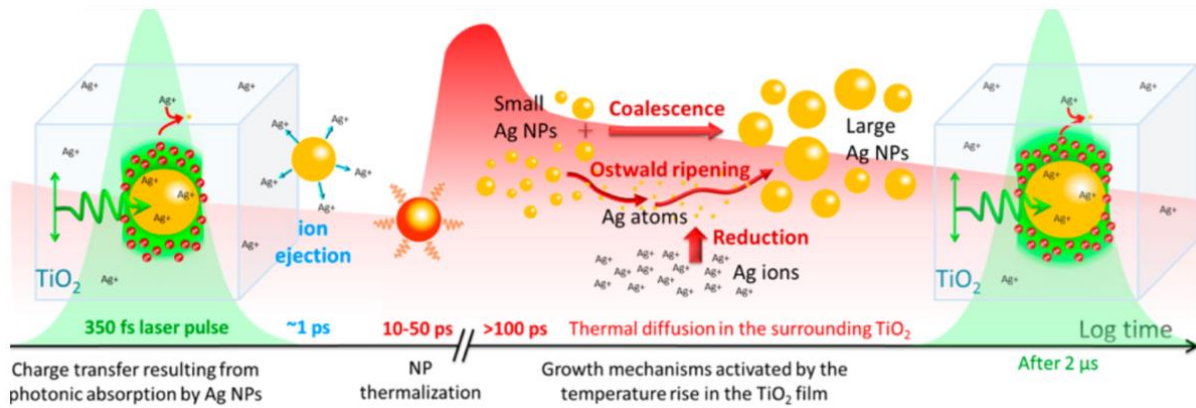


Figure 1.8 – Sketch of the mechanisms triggered in Ag/TiO₂ nanocomposite film under high-repetition-rate fs laser excitation. Image is taken from [57].

The remaining electrons on the NP did not cross the Schottky barrier relax via e-ph interaction over a timescale of typically a few tens of ps in case of such high excitations. In case of low perturbations, where the electronic temperature rise is less than 100 - 200 K, sub-ps typical e-ph relaxation times were demonstrated [59]. The equilibration of electron and lattice temperatures results in NP thermalization. Subsequently, on a timescale of 100 ps to 10 ns, heat is coupled to the TiO₂ matrix. The temperature rise of the matrix favors NP growth mechanisms. Coalescence, Ostwald ripening and reduction of Ag⁺ are the main mechanisms that control NP growth and reshaping, as described previously. High-repetition-rate laser irradiation leads to thermal accumulation in the matrix, which further boosts the growth of Ag NPs being diffusion-limited processes that requires longer times. They occur only above a temperature threshold, and their yield increases nonlinearly with temperature [57].

1.4.5 NP reshaping involving melting

Additionally to the previous investigations, heat-assisted reshaping mechanism involving NP melting was extensively studied. The work of Rodríguez *et al.* investigated Ag discontinuous films deposited on glass substrate, *i.e.*, ensembles of nanoislands transformations upon single excimer ns pulse irradiation [60]. Figure 1.9A shows that the initial Ag film sample is discontinuous but close to coalescence. Upon laser irradiation, the film is converted into big and rather spherical NPs shown in Figure 1.9B due to laser-induced melting followed by dewetting.

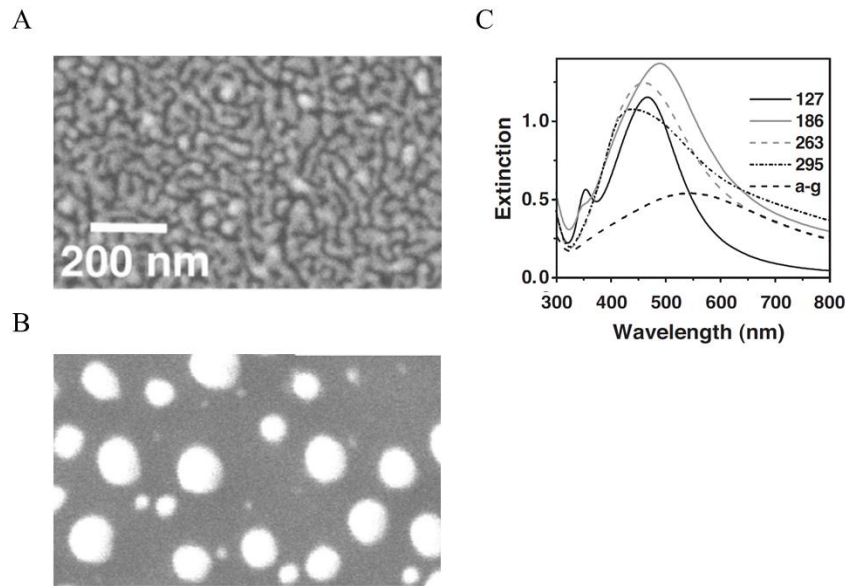


Figure 1.9 – Characterizations of samples containing Ag nanoislands on glass substrate. A: Electron microscopy image of the initial sample. B: The sample after irradiation by single ns laser pulse using a fluence of 127 mJ/cm². C: Extinction spectra of irradiated samples using various laser fluences, the numbers correspond to laser fluences in mJ/cm² and a-g stands for as-grown sample. The figure is adapted from [60].

The optical response of the laser-irradiated samples is dominated by significantly narrowed and blue-shifted LSPR. This is shown in Figure 1.9C by comparing the extinction spectra of the initial and irradiated samples using various laser fluences.

In another work of the same group, the dynamics of the discontinuous Ag films upon single-pulse ns laser irradiation was investigated by time-resolved measurements of the transmission and reflectivity of the sample [61]. The results showed that laser irradiation induces Ag melting within less than 10 ns. The aggregation and/or coalescence of the initially irregular metallic nanostructures is triggered upon melting and continues after solidification (estimated to occur at less than 80 ns) for a long time (> 1 μ s).

Similar shape transformations due to melting were reported in samples containing near-coalescence Ag nanoislands embedded in a dielectric matrix under single-pulse visible ns laser irradiation [62]. Additional exposure to multiple femtosecond laser pulses induced anisotropic shapes. Such nanoislands could be reorganized, shaped and aligned by exposure to exclusively ultrashort laser pulses [63].

1.4.6 Laser-induced anisotropic NP reshaping

There has been a great amount of literature regarding the mechanism of anisotropic reshaping of glass-embedded Ag NPs with ultrashort pulses [64]–[66]. In this section, a review of the process of shaping the initial Ag NP shape distribution into elongated shapes is provided. The graphical summary of the following description of different stages is shown in Figure 1.10 [2].

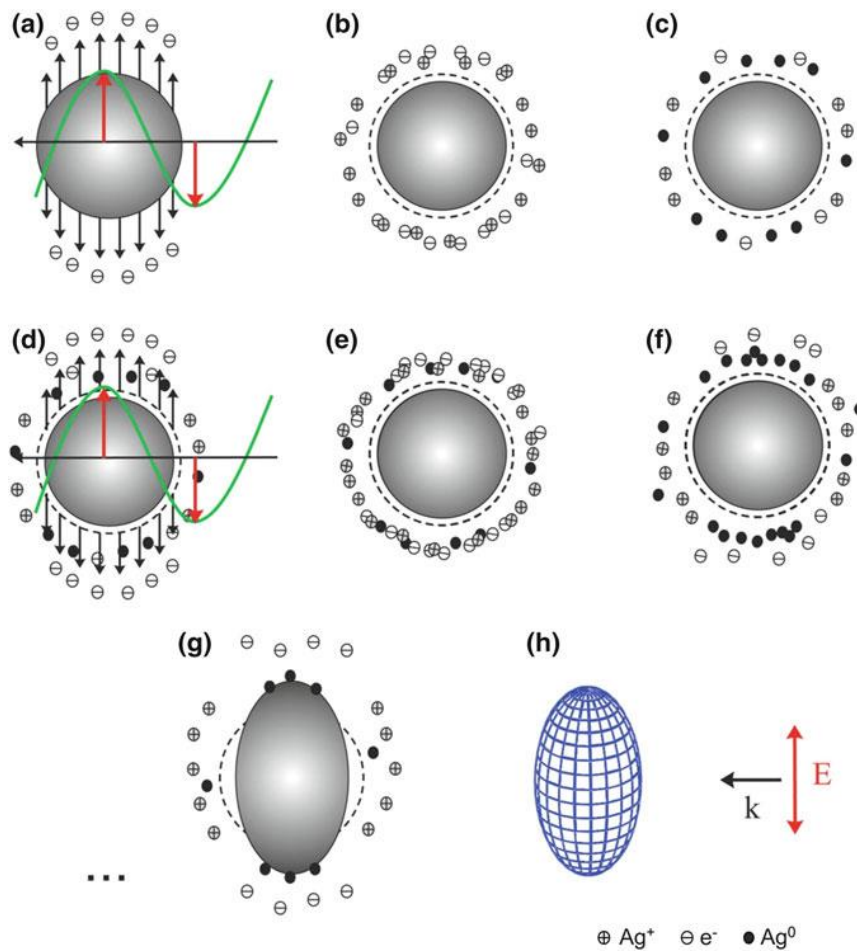


Figure 1.10 – Stages of laser-assisted shape transformation of Ag nanosphere into prolate shape under multiple linearly polarized ultrashort pulse irradiation. The description of stages (a) – (h) is provided in the text. Image is taken from [2].

The irradiation intensity is rather crucial parameter for the shape transformation, leading to characteristic intensity regions enabling the formation of either prolate or oblate shapes. In Figure 1.10, the stages leading to prolate NP shapes are demonstrated, as being relevant in the scope of the results discussed later in this thesis.

The LSPR enhances the electric field of the laser pulse close to the Ag particle by a few orders of magnitude, with the highest enhancement values close to the poles of the nanospheres with respect to the laser polarization [67]. This results in intense directed emission of electrons from the particle surface, preferentially parallel to the laser polarization (Figure 1.10a). The emission process occurs during the laser pulse. The anisotropy of the electron ejection is responsible for the final anisotropic NP shapes. The ejected electrons are trapped in the matrix forming color centers close to the poles of the sphere. Additionally, the optical breakdown threshold of the glass matrix can be exceeded due to the high electric field in the vicinity of the NP, which further increases the electron density in the matrix. Subsequently, the ionized NPs are likely to emit Ag ions in statistical directions when electron thermalization and heat transfer to the lattice are finished. Simultaneously, thermal electron emission is involved during e-ph interaction. The estimations for the maximal electronic temperature is provided in the range of 10^4 K, and lattice temperatures exceeding the melting temperatures of bulk Ag [2]. The real temperature of the NP can be expected to be much lower because of energy losses caused by electron and ion emission. The ionized positively charged NP becomes unstable, and the Coulomb forces lead to the ejection of Ag^+ , which form a cationic shell in the vicinity of the NP (Figure 1.10b) [2]. This charged shell of Ag cations around the particle experiences trapped electrons with high number density around the poles. After some picoseconds, they can recombine to form Ag atoms (Figure 1.10c), which finally diffuse back to the NP and precipitate mainly at the poles. Accumulating the effect of multiple pulses, remaining Ag ions may also act as trapping centers for the electrons being subsequently emitted by the laser pulses (Figure 1.10d–f). The high density of trapped electrons close to the poles and ions around the NP equator may cause local electric field distributions influencing the anisotropic nature of the electron and ion emission for the subsequent laser pulses. All these processes lead to a pulse-by-pulse elongation along the laser polarization, eventually leading to prolate spheroidal shape (Figure 1.10g, h). The irreversible shape transformation stops when the laser wavelength approaches the blue wing of the LSPR [2].

As a summary, for any type of shape transformation of spherical Ag NPs embedded in glass matrix induced by fs laser pulses, the main point of the reshaping is the anisotropic plasmon-assisted photoelectron emission from the metal surface, which defines the particle symmetry. The next steps of the mechanism determine solely the final NP shape depending on the laser intensity, *i.e.*, whether the NPs will be reshaped into prolate or oblate forms in an accumulative process, or they will be destroyed in case of too high laser intensities. In case of oblate forms, the very high local electric field at the poles of the sphere possibly results in a high density electron plasma via avalanche ionization of the glass [2]. The following plasma relaxation transfers energy to the NP on a faster timescale than the thermal diffusion. This can ultimately result in partial destruction of the NP at the poles (ablation).

In this analysis, the NPs are embedded in glass matrix. However, in case of a high-refractive index medium, excitation of guided waves can further enhance the NP shape transformations in periodic spatial regions leading to the formation of self-organized NP gratings. In the following section, the theory of self-organized NP reshaping is reviewed.

1.5 Laser-driven material organizations

In this section, the theories of laser-driven material organization are reviewed via, first, the discussion of the existing theories of surface modulations known as laser-induced periodic surface structures (LIPSS), and second, the theory behind laser-induced periodic arrangement of plasmonic NP ensembles.

1.5.1 Laser-induced periodic surface structures

Birnbaum reported for the first time the formation of LIPSS on polished germanium crystal surfaces irradiated with a ruby laser beam [68]. The phenomenon was attributed to diffraction effects and proposed that the surface modulation was caused by localized material removal. Subsequently, various theories emerged attempting to explain the physics behind such surface modulations. The currently existing theories can be divided in two major categories, *i.e.*, electromagnetic approaches considering the major role of optical energy deposition into the solid, and matter reorganization theories, which are based on the redistribution of surface matter.

1.5.1.1 Electromagnetic approaches

The basic idea behind the electromagnetic theories is that the incident light is scattered by the roughness of the sample surface leading to coherently driven elementary Huygens waves, or to the excitation of surface modes, such as surface plasmon polaritons (SPPs) [69]. SPP is an electromagnetic wave resulting from a collective oscillation of quasi-free electrons located at the interface between two different media. There is an interference phenomenon between the

incident field and fields excited by scattering or SPPs, which results in a spatial modulation of the local energy distribution that is transferred to the sample material. In case of high-enough laser excitation, the formation of the final periodic surface modulation is then triggered via, for instance, spatially modulated material removal (ablation). For materials exhibiting strong absorption, SPP-assisted LIPSS are usually formed with an orientation perpendicular to laser polarization, with periods close to the laser wavelength, known as low spatial frequency LIPSS (LSFL) [70]–[72]. This type of excitation attracts high level of interest due to the possibility that materials without initial plasmonic features (dielectrics and semiconductors) can be transformed transiently into metallic state once the density of the conduction band electrons exceeds a critical value after laser irradiation [69], which satisfies SPP excitation conditions. The LSFL periodicity Λ is often directly related to the SPP wavelength. For the case of a plane dielectric–metal interface and for normal angle of incident irradiation, the period of the surface modulation can be calculated from the complex bulk dielectric permittivity of the metal (ε_m) and dielectric medium (ε_d), and the laser wavelength λ as

$$\Lambda_{LSFL} = \Lambda_{SPP} = \lambda \cdot \Re \left(\sqrt{\frac{\varepsilon_m + \varepsilon_d}{\varepsilon_m \varepsilon_d}} \right). \quad (1.17)$$

Assuming pulsed laser excitation, for low number of laser pulses, the LSFL and SPP periods can be compared since the surface modulation depth is small at this stage (depth $\ll \lambda$). Subsequently, the positive feedback in the multipulse regime notably affects the LSFL formation. Therefore, the validity of the SPP model is limited.

The alignment of the LSFL relative to the linear beam polarization originates from the directional excitation of electrons in the material by the laser radiation [69]. Depending on the electrical properties of the metal or dielectric, this leads to a directional radiation feature and to an anisotropic field distribution of the induced surface electromagnetic fields.

The so-called efficacy factor theory developed by Sipe and his co-workers is actually the most universally accepted theory of LIPSS formation [73]–[75]. Based on the model, the irradiated solid can be divided into two parts, *i.e.*, a thin layer consisting of surface irregularities and a bulk material. The theory assumes transverse variation of an initial random surface, which can be decomposed into a sum of individual spatial frequencies. It is possible to calculate the amount of light scattered by each of these frequencies below the surface. Thus the total intensity on the material results from the superposition of the primary laser radiation and the scattered waves by surface roughness centers. This model consists of spatial frequency determination of the initial surface variation. The efficacy factor is thus calculated for each of the frequencies

and is generally represented in reciprocal space. In fact, it serves as a scalar function proportional to the inhomogeneous energy deposition into the irradiated sample [73], and describes the efficacy with which the surface roughness (represented by ripples wave vectors \mathbf{k}) can absorb optical radiation. The strength of this classical model is in its remarkable precise prediction of possible \mathbf{k} vectors of the surface. The surface modulation orientation and angle of incidence dependence are also correctly described.

Finite Difference Time Domain (FDTD) approaches open the way for investigating several aspects of LIPSS formation, such as the effects of polarization, surface roughness, refractive index variations, laser beam propagation, field enhancement, optical scattering, and interference phenomena, and can be used to reveal the spatio-temporal evolution of the irradiation material. The results demonstrated the electromagnetic origins of several structures, in case of both LSFL and high spatial frequency LIPSS (HSFL) structures. The latter exhibit periods considerably smaller than the irradiation wavelength (period smaller than $\lambda/2$).

One prominent demonstration of these approaches is the work of Zhang *et al.*, which calculated the contribution of the scattered near-field and far-field on the types of inhomogeneous energy absorption [76]. The authors found that the inhomogeneous energy absorption, which triggers LSFL formation results from the coherent superposition of the scattered far-field and the propagating, *i.e.* refracted waves. In contrast, HSFL in dielectrics originate from the coherent superposition between the scattered near-field and the refracted wave. Furthermore, Skolski *et al.* implemented inter-pulse feedback mechanisms by combining FDTD with ablation mechanisms, *i.e.*, the incident laser pulse was considered to modify the surface roughness by ablation, according to the profile of the absorbed energy [77]. Hereby, LSFLs, HSFLs were well-reproduced numerically by their approach.

1.5.1.2 Matter reorganization theories

Matter reorganization theories are based on considering the transport of laser-excited material in a liquid form that reshapes the surface topography. Explanations involve thermodynamic phase transitions and hydrodynamic effects of the transiently melted surface [69]. Possible mechanisms were proposed relying on surface tension gradients [78], thermoelastically generated surface acoustic waves [79], or capillary waves [80]. The detailed description of these mechanisms is beyond the scope of the present thesis. The relevant discussion can be found in the review article of Bonse and Gräf [69].

1.5.2 Self-organization of metallic NPs

Light-driven organized NP reshaping was demonstrated by several earlier works, evidencing the formation of homogeneous grating-like nanostructures composed of reshaped particles with tunable features. In the work of Destouches *et al.*, TiO₂ thin film homogeneously loaded with Ag precursors was investigated under continuous laser irradiation, and the emergence of periodic arrays of grown NPs was demonstrated [81]. In other works of the same group, fs laser-triggered self-organization was demonstrated in same initial sample [82]–[84]. The self-organized formation of periodic superstructures in thin plasma polymer films initially containing inhomogeneous metal nanoislands upon fs laser irradiation was reported by several other works [85]–[87]. Additionally, single ns laser pulse was used to trigger self-organized reshaping of a layer of plasmonic nanoislands deposited on top of Si₃N₄ membrane [88]. In this section, the general theory behind the formation of such periodic nanostructures is discussed.

When the sample is illuminated by the exciting laser, the initial NPs can be considered as oscillating electric dipoles radiating mainly in the plane perpendicular to the incident polarization [81]. This provides the explanation for the orientation of the NP grating lines reported in all above cited references: grating lines parallel to the linear laser polarization. In case of a high-refractive index host medium for the initial NP ensemble, the film acts as a waveguide, therefore a part of the field scattered by NPs remains confined in form of a quasi-guided mode. As initially the NPs are homogeneously distributed in the host matrix, the amplitude of the guided modes is small. Assuming the excitation of these guided modes, the interference with the incident wave gives rise to intensity modulations in the film along the direction perpendicular to the incident polarization. The optical interference pattern triggers the grating formation. The grating then creates a positive feedback loop by enhancing the coupling of the incident wave to the mode, *i.e.*, increasing the contrast of the interference pattern and finally promoting the grating formation itself. The spatial period of the interference pattern can be expressed as

$$\Lambda = \frac{\lambda}{Re(n_e) \pm \sin \theta_i} \quad (1.18)$$

where θ_i is the angle of incidence of the laser exposure and $Re(n_e)$ is the real part of the guided mode effective index. In Eq. (1.18), $-\sin \theta_i$ corresponds to the case where the projection of the wave vectors of the excited mode and incident wave, on the sample plane, are in the same direction, and $+\sin \theta_i$ to the case of opposite direction, as shown in Figure 1.11 a and b.

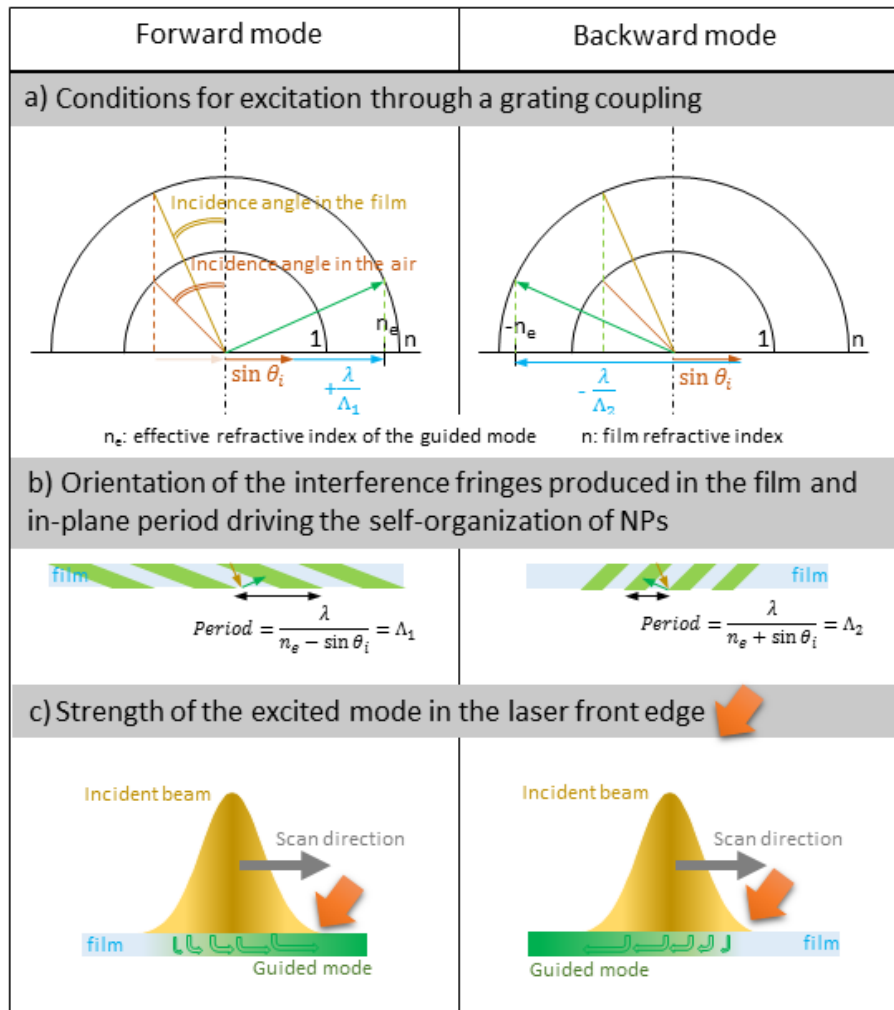


Figure 1.11 – Principles of guided mode excitation. a) Phase-matching condition at the origin of the positive feedback. b) Main features of the interference diagram produced when the incident beam interferes with the forward or the backward leaky mode in the layer. The orientation of fringes, not perpendicular to the interfaces, depends on the orientation of the wave vectors of the incident and guided waves, whose directions are depicted by the brown and green arrows, respectively. d) Selected mode vs. scan direction.

During static exposures, both directions can be excited equally, leading to two different periods that superimpose. In contrast, writing lines by moving the sample favors the mode excited in the forward direction, *i.e.*, the translation direction, and leads to a well-defined period [89]. Indeed, after initiating the sample movement, the grating is formed under the laser beam and mainly extends in the front edge of the focused spot. While the guided mode is excited to the right and left directions perpendicular to the grating lines under the beam, only the mode that propagates to the forward direction accumulates in the beam front edge (Figure 1.11c). So, the interference pattern that fixes the grating period in the front edge results from the interference

of the incident beam with the forward mode. Moreover, while the sample is moving, the interference pattern remains fixed relative to the sample. This interesting phenomenon originates in the way the modes are excited. The latter are excited through scattering, and their phase depends on the position of scatterers (Ag NPs). The phase of the wave that forms the forward guided mode consequently continuously changes when translating the sample under the laser beam and makes the interference pattern fixed relative to the sample. The latter extends over the laser beam. The scan direction therefore determines the sign before $\sin \theta_i$, and together with the laser wavelength, the incidence angle and the modal distribution of the structure, fixes the grating period.

Once formed, the grating of period Λ is responsible for efficiently coupling the incident light into the guided mode by diffraction and not only by scattering. In other words, scatterers are now organized and the scattered waves originating from the different periods constructively interfere in the direction of the guided mode. This means that the grating emerging from the excitation of the guided mode contributes to its own enhancement during the film transformation. This positive feedback mechanism is at the origin of the term self-organization. Finally, we should mention that what is called guided mode here should be more precisely named leaky mode since this mode is also scattered on Ag NPs and cannot propagate very far in the film. We initially assumed that scattering by metallic nanoislands was mostly in the direction perpendicular to the incident polarization. This angle selection actually results from the positive feedback, namely the diffraction by the grating, which is much more efficient when the incident laser polarization is parallel to the grating lines and which filters the direction in which the feedback is stronger [90].

2 Time-resolved techniques for characterizing laser-matter interactions

The investigation of the described physical phenomena in the previous chapter requires sophisticated experimental techniques capable of characterizing the photoexcited material with high spatial and temporal resolution. Optical techniques have been widely used in the study of nano-objects and nanomaterials. Optical time-resolved experiments take advantage of the transiently varying optical response of the sample to investigate the mechanisms underlying these optical changes, *e.g.* electron and lattice interactions, nano-object vibrations, thermal relaxation, material reorganization, damage, etc.

In this chapter, the methods used for characterizing the ground state and ultrafast transient optical responses of a single or ensembles of nano-objects upon photoexcitation are presented. In the first section, the technique of pump-probe spectroscopy is introduced followed by a review of relevant studies focusing on metallic nano-objects. The second section is dedicated to the presentation of the pump-probe microscopy configuration, which combines the temporal ability of spectroscopic approach with high spatial resolution. In the last section, a versatile and powerful experimental approach is presented applied for phase-sensitive measurements.

2.1 Ultrafast pump-probe spectroscopy of plasmonic nano-objects

In order to discriminate the different physical processes described in the previous chapter, time-resolved experiments are required with fs - ps time resolution allowing to temporally separate these processes, and study the overall dynamics of the system until the equilibrium condition is reached. This section is devoted to introduce the pump-probe experimental technique that has widely been used to study such kind of physical processes.

In a pump-probe experiments, two laser pulses are required, the pump and the probe. The former means a perturbation to the material. The time at which the maximum of the pump pulse intensity reaches the material is considered as the zero delay for the probe pulse. The role of the probe pulse is to monitor the modifications that are induced in the material by the pump. A high-precision mechanical linear translation stage is generally used to vary the delay between the pump and the probe pulses over a time range of several nanoseconds and with high temporal resolution. In such experiments, the probe beam is a broadband white light supercontinuum in

order to resolve the dynamics over a broad spectral range. The quantity that is monitored as a function of pump-probe delay time and probe wavelength is the spectral absorbance (including contributions from reflection, absorption and scattering) measured in a transmission configuration, which varies in the photoexcited system depending on the time after the excitation. The measured intensity of the probe pulse $I_1(\lambda, t)$ at delay t following the excitation by the pump pulse can be expressed as:

$$I_1(\lambda, t) = I_0(\lambda) * 10^{-A(\lambda, t)}, \quad (2.1)$$

where $I_0(\lambda)$ and $A(\lambda, t)$ are the incident spectral intensity of the probe pulse and the total spectral absorbance of the sample, respectively. Assuming that the incident intensity $I_0(\lambda)$ does not vary between two measurements, one can collect $I_1(\lambda, t)$ over a span of temporal delays t . The full time-resolved transient absorption spectrum is obtained, that can be expressed in dimensionless optical density (OD) units as:

$$\Delta OD(\lambda, t) = A(\lambda, t) - A(\lambda, t_0) = \log_{10} \frac{I_1(\lambda, t_0)}{I_1(\lambda, t)}, \quad (2.2)$$

where $A(\lambda, t_0)$ is the total spectral absorbance of the initial sample, and $I_1(\lambda, t_0)$ is the spectral intensity of the probe beam before the arrival of the first pump pulse. Pump-probe spectroscopy has experienced an intense growth in recent years, due to the technological progress in the generation of ultrashort light pulses and to the development of sophisticated spectroscopic techniques, which greatly increase the amount of information on the process under study. In the followings, the literature of pump-probe experiments investigating plasmonic systems is overviewed.

The transient changes of the metal dielectric function contain the signatures of the different ultrashort phenomena discussed in the previous chapter. The literature investigating the dynamics of different plasmonic nano-objects focusing on the temporal evolution of the transient LSPR bands is rather rich. In the early work of Del Fatti and Vallée, the physical origin and the dynamics of the ultrafast optical nonlinear response of plasmonic spherical NPs were analyzed around the LSPR central frequency [91]. The authors discussed that the pump-laser induced change in the electron distribution leads to modification of both the interband absorption spectrum and the electron optical scattering rate. As a result, the interband and intraband parts of the metal dielectric function are modified, and these effects are reflected in the transient optical measurements. In case of Ag nanospheres, a derivative type of shape for the transient spectrum was observed following photoexcitation of nanospheres with mean radii ranging from 2 to 15 nm. A demonstration can be seen in Figure 2.1 showing the spectral shape of the normalized transient transmission $\Delta T/T$ spectrum measured around the LSPR of single Ag NP with radius

of 13 nm embedded in glass for a fixed pump–probe delay of 1 ps. The excitation is performed by an infrared pump pulse with 25 fs pulse duration. The transient spectrum exhibits two distinct features in the spectral region around the ground state LSPR. A negative signal (induced absorption) is apparent on the long wavelength side of the steady-state LSPR peak, whereas positive feature (transient transparency) arises on the short wavelength side of the resonance. In case of Ag NPs, such transient spectrum can be described by a combined effect of a LSPR frequency shift $\Delta\Omega_F$ and broadening $\Delta\Gamma$ [92]. They are directly related to the alteration of the real and imaginary parts of the metal dielectric function due to the energy deposition into the electron plasma. In the work of Bigot *et al.*, the transient LSPR in Cu spherical NPs was demonstrated to have similar spectral features [93].

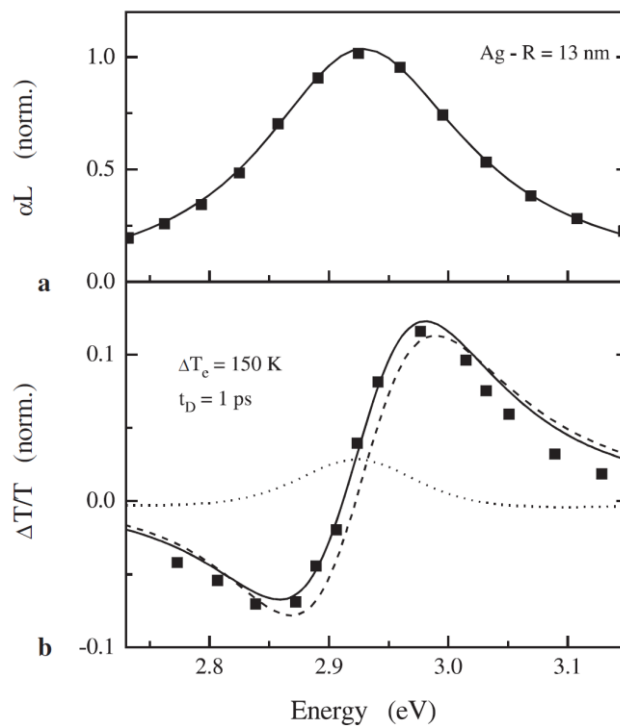


Figure 2.1 – Investigation of the characteristics of Ag nanospheres. **a**: Measured (squares) and computed (solid line) steady-state absorption spectrum of $R = 13$ nm Ag nanospheres embedded in glass. **B**: Measured transient spectrum of the transmission change around the LSPR for a fixed pump–probe delay of $t_D = 1$ ps (squares) following photoexcitation by a 25 fs near-infrared pump pulse. The dashed line is the calculated $\Delta T/T$ considering only the interband contribution and assuming an electronic temperature rise ΔT_e of 150 K, the dotted line is the intraband contribution. The solid line is their sum. Image is taken from [91].

In the case of multiple LSPR bands in the steady-state absorbance (which is the case in more complex nano-object geometries), the transient spectrum contains the additive contributions of the bleaching and induced absorption features of each resonance band resulting in a complex

transient spectrum with alternating negative and positive features, as demonstrated in the followings.

Several studies have investigated the optical relaxation dynamics of plasmonic nanorods using pump–probe techniques. The work of Wang *et al.* investigated the broadband spectral response of colloidal Au nanorods upon fs laser excitation [94]. The results evidenced complex spectral response that is very sensitive to the nanorod aspect ratio. The photo-induced modification of the metal dielectric function resulted in the alteration of the transverse and longitudinal localized plasmon modes. Figure 2.2 displays the dynamics of the transient absorption spectra of Au nanorod ensemble excited by 130 fs pulse at 550 nm. The vertical arrows denote the position of the transvers and longitudinal LSPR in the stationary spectrum. The final transient spectrum results from the superposition of the profiles associated with the two plasmon bands. Photo-induced absorption and transparency are alternately observed in the spectral window. This is due to the modification of the dielectric function of Au enhanced by the LSPR bands. Within the shortest times (sub-ps delays), the interband transition contribution was shown to be dominant in the whole spectral domain even for photon energies far below the threshold, whereas the intraband transition contribution could not be neglected at longer times. The relative weights of these contributions, and the spectral signature of the transient response, are affected by the ensemble effect in colloidal distributions.

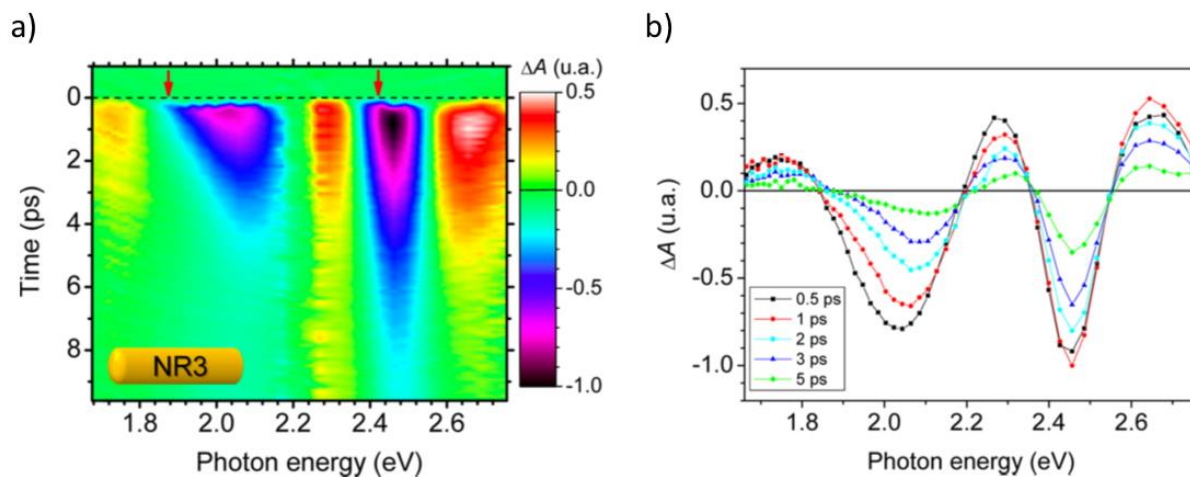


Figure 2.2 – Pump–probe spectroscopy performed on ensembles of colloidal Au nanorods with diameters of 12 ± 1 nm and length of 30 ± 4 nm excited by 130 fs and 550 nm pump wavelength. a) Time and spectral evolution of absorbance variation ΔA . The red arrows indicate the center of the transverse and longitudinal LSPR of the nanorods. b) Extracted transient absorbance spectra at different delay times. Figure is adapted from [94].

These spectral profiles are similar to the ones measured by other groups on a colloidal solution of Au nanorods [95], [96].

In the work of Otomalo *et al.*, complex spectral variations were observed in the transient spectra of bimetallic NPs [97]. The investigated sample contained core-shell Au-Ag nanocuboids characterized by numerous plasmon modes spanning on a broad spectral range in the steady-state regime. Additionally, higher-order modes were formed in the near-ultraviolet range where no plasmon resonance is possible to form with single noble metal NP. The work was supported by theoretical calculations that helped to assign the different contributions to that complex transient spectral profile. Each resonance mode identified in the stationary spectra was associated with a typical plasmon bleaching pattern (positive and negative spectral features) in the transient optical response following photoexcitation by 50 fs and 380 nm pulses. A typical transient spectral profile of the absorbance change ΔA with respect to the steady-state spectrum is demonstrated in Figure 2.3. Sets of transient induced extinction (positive features) and transparency (negative features) signals are demonstrated as a result of the transient modification of the dielectric function of the sample following the pump pulse absorption. Each transient feature is in direct relation to one of the ground state plasmon bands.

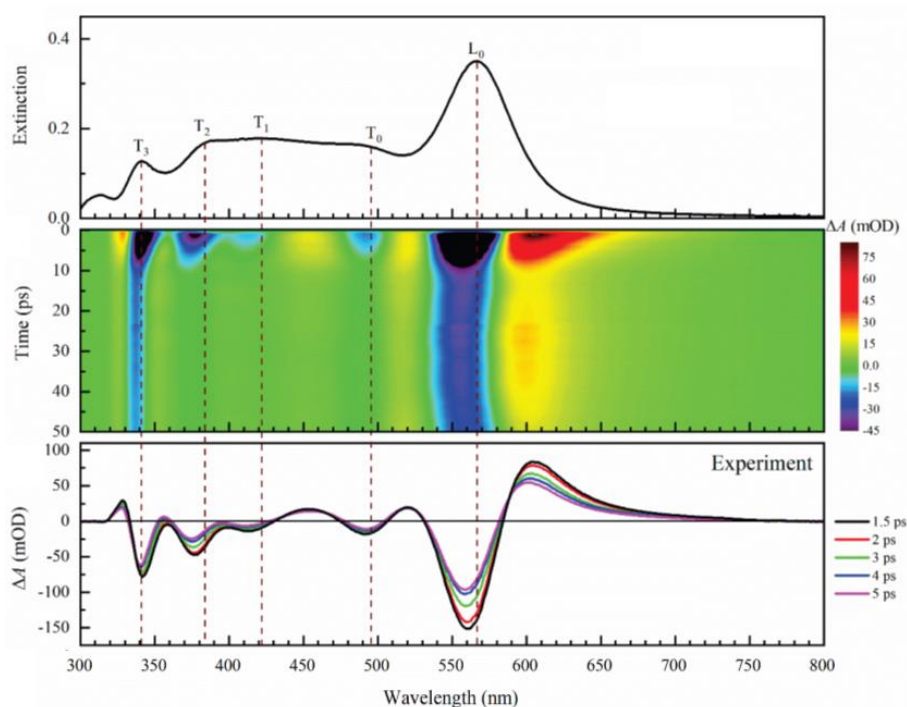


Figure 2.3 – Steady-state and transient spectra of colloidal core-shell Au-Ag nanocuboid. The steady-state extinction spectrum (upper image) contains several resonance bands that are transiently altered after photoexcitation by 50 fs and 380 nm pulse. The color map of the time and spectral dependence of the absorbance variation ΔA measured by pump-probe spectroscopy (middle image) exhibit several typical plasmon bleaching signals corresponding to the steady-state plasmon resonances. Extracted spectra at different time delays are shown in the lower image. The vertical dashed lines indicate the spectral position of the plasmon resonance modes. Image is adapted from [97].

Related to this work, the investigations of the transient optical response of other kinds of bimetallic nano-objects has been reported in the literature, *e.g.* Au@Ag and Au@Ag@Pt nanospheres [98]. In other experiments, the ultrafast dynamic process of aqueous solution of Au-Ag nanoshuttles was characterized by pump-probe spectroscopy [99]. The steady-state and transient absorption spectra are demonstrated in Figure 2.4, when the sample was excited by 400 nm and 190 fs pulses. It can be seen on the transient data that one prominent bleaching signal appeared around 500 nm, corresponding to the absorption peak around 500 nm in the steady-state sample. Additionally, a transient induced absorption signal was observed at roughly 560 nm. An additional bleaching signal is apparent above 700 nm that corresponds to the short wavelength side of the second ground state absorption peak centered at 800 nm. All the peculiar features of the transient absorption spectrum could be fairly described by the additive contributions of the individual transient plasmon bands.

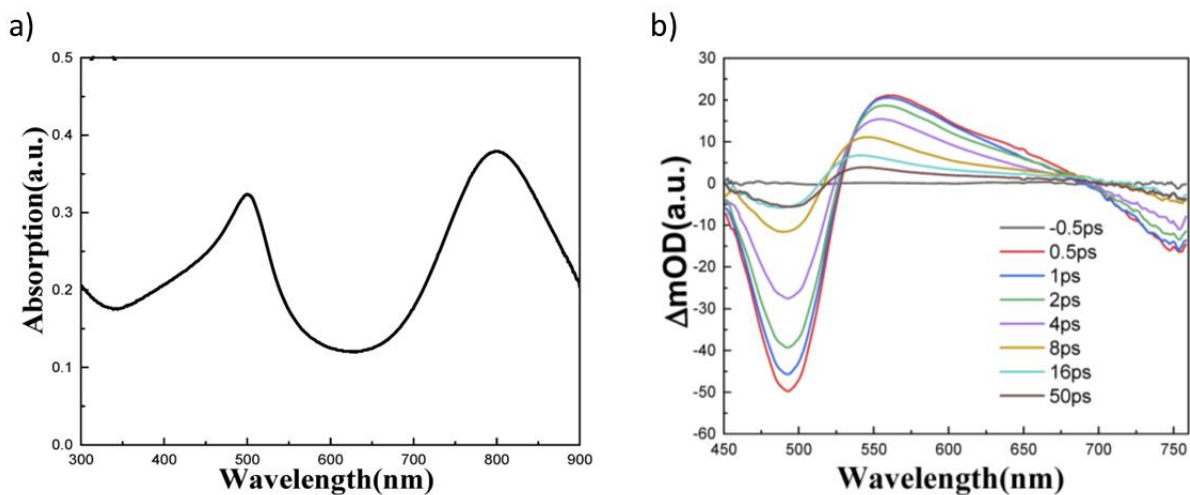


Figure 2.4 – Spectral characteristics of Au-Ag nanoshuttles. a) Steady-state absorption spectra and b) time-resolved transient absorption data upon 400 nm and 190 fs pulse excitation. Figure is adapted from [99].

2.2 Ultrafast pump-probe microscopy

Pump-probe microscopy combines the spatial resolution of optical microscopy with the temporal resolution of ultrashort laser pulses. This technique enables to investigate spatial variation in photo-excited ultrafast/fast phenomena triggered in nano-objects, revealing the role of structural properties, *e.g.* interfaces and inhomogeneities. Recently, significant developments of pump-probe microscopy have been realized aiming to characterize carrier dynamics with diffraction-limited spatial resolution in bulk semiconductors [100], individual nanostructures [101], as well as acoustic modes in metal nano-objects [102]. In diffraction-limited transient

absorption methods, the pump and probe pulses are focused to diffraction-limited spot sizes on the sample, and computer controlled mirrors vary the angle of incidence of the probe beam before the objective, allowing the probe beam to be focused to a point on the sample around the pump spot. However, the scanning (raster scanning) alters the path of the beam, the geometry of the system is developed the way that the path length introduced by tilting the beam results in a very little delay shift (<0.5 ps) [19]. In these experiments, a high level of sensitivity can be achieved, *i.e.*, $\Delta I/I$ in the range of 10^{-7} [103]. Several types of configurations are possible, providing complementary information on the temporal and spatial excited state dynamics.

2.2.1 Spatially-overlapped pump and probe beams

In the first group of experiments, the pump and probe beams are spatially overlapped and the pump–probe time delay is scanned using the delay line. This particular mode of operation is analogous to transient absorption spectroscopy measurements on ensembles, although with a diffraction limited pump and probe spot size, therefore enabling to select single items in the ensemble. Figure 2.5 shows results from an example pump–probe microscopy experiment and ensemble transient absorption experiments performed on different collections of Si nanowires [19].

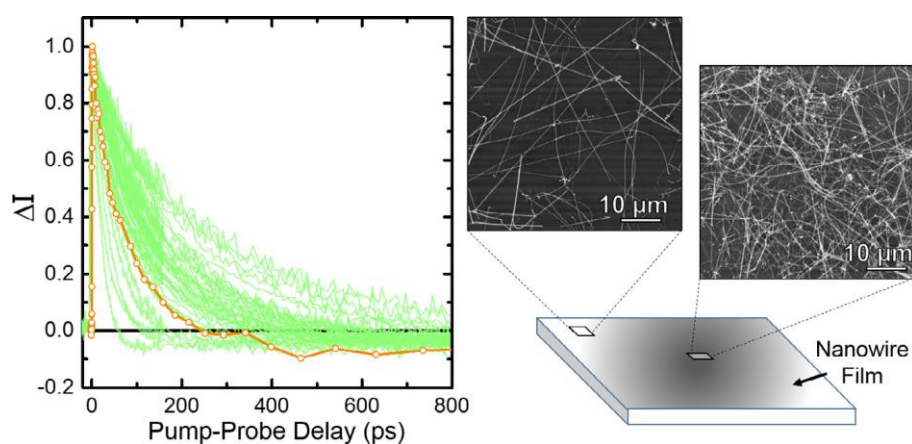


Figure 2.5 – Ultrafast dynamics of electron-hole recombination in Si nanowires. Left image: Pump–probe time traces, the green traces were obtained from 41 randomly selected individual points using pump–probe microscopy. Orange curve shows an average of decay kinetics measured by ensemble transient absorption spectroscopy with a broadband continuum probe. Right: Illustration of the nanowire film and electron microscopy images recorded in the center and on the edge of the sample. Image is taken from [19].

The nanowires were excited around 400 nm and the electron-hole recombination process was probed by monitoring changes in intensity of a near-infrared probe. The left image shows a collection of time delay scans obtained in the microscopy mode from a series of randomly selected single nanowires (green curves) on the edge of the sample. The orange curve shows an averaged decay kinetics measured on an ensemble of nanowires (in the center of the sample) using a traditional transient absorption spectroscopic setup with a broadband continuum probe. On average, measurements of individual nanostructures exhibit longer lifetimes than ensemble measurements, highlighting the important role of sample heterogeneity [104].

2.2.2 Raster scanning

The second mode of operation involves spatial scanning (raster scanning) of the dynamics either with spatially-overlapped pump and probe beams (both beams are raster scanned), or with keeping the pump beam fixed, and the probe is then spatially scanned. Results reveal the spatial position-dependent ultrafast material response of individual nano-objects. An example experiment investigated the electron-hole recombination dynamics within individual needle shaped ZnO nanorods at different spatial locations using raster scanning with spatially overlapped pump and probe beams [105]. The high spatial resolution enabled to characterize specific regions of the nanostructures. The photoexcitation promotes electrons from the valence band to the conduction band, resulting in high-density of free charge carriers. As shown in Figure 2.6, the dynamics at the end of the rod differs dramatically from the spatial locations inside the rod, with the ends showing faster recombination rates than any other point in the structure. The probe wavelength was 810 nm. The spatial variation is further demonstrated in images obtained by fixing the pump-probe delay and monitoring the transient signal as a function of position. The difference in recombination rates reflects two different decay pathways, with photo-generated carriers at the end of the rod recombining through a faster electron-hole plasma mechanism, and a slower trap-mediated recombination in the interior sections¹ [19].

The spatiotemporal imaging ability of ultrafast microscopy has enabled direct imaging of carrier transport phenomena in nano-objects. The interaction of charge carriers with the surfaces, localized defects, and electrical contacts in nanostructured devices can have a profound influence on the migration of electrons and holes through a semiconductor structure. The work of Gabriel *et al.* enabled to directly visualize the charge motion produced by photoexcitation at a localized spot as it spreads along a Si nanowire [101]. The motion of charge carriers is in the

¹ Further details can be found in Appendix.

focus of many emerging technologies in nanoscale electronics, optoelectronics, and solar energy conversion. The high spatial resolution achieved by the optical microscope provided insights into this complex electron–hole recombination and carrier migration dynamics.

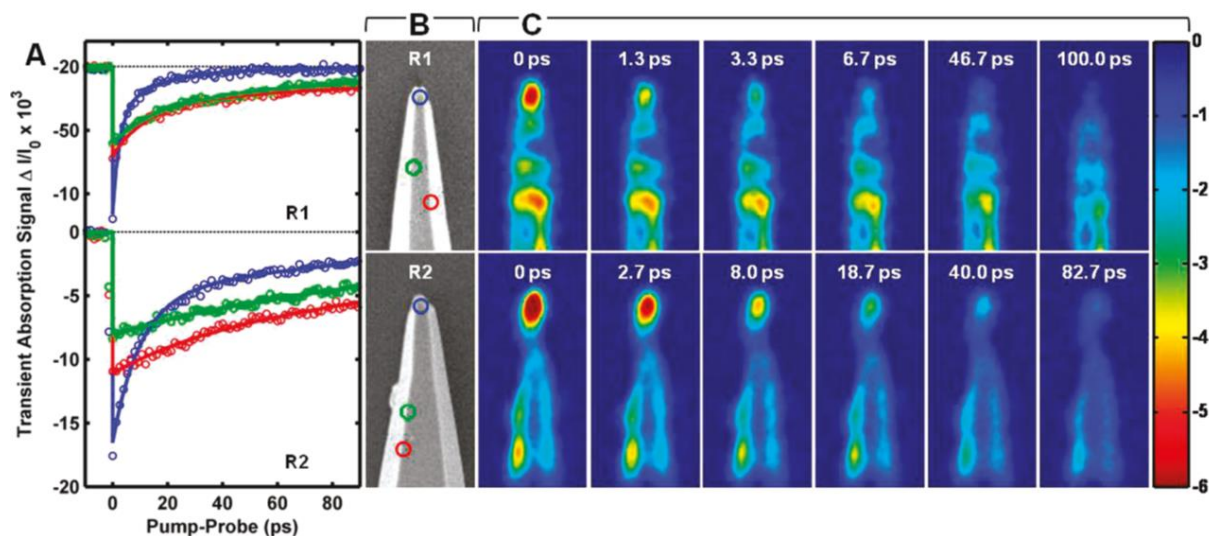


Figure 2.6 – Transient absorption microscopy of ZnO nanorods. (A) Time traces obtained with spatially-overlapped pump and probe beams at the end of the rod (blue curve) and interior points (red and green curves). (B) Electron microscopy images of two investigated nanorods with the locations of the delay scan marked by circles with the corresponding colors. (C) Transient absorption images showing the spatial decay of the photo-induced signal. Rapid decay was observed at the tip of the rod, while slower decay was apparent in the interior sections. The lateral resolution of the experiments was 350 nm. Image is taken from [105].

2.2.3 Optical microscopy approach

In other types of pump-probe microscopy, the probe beam illuminates the complete field of view homogeneously, and the magnified image of the sample is recorded using a detector (camera). This approach preserves the ability of investigating the dynamics with high spatial resolution, enables faster data acquisition (there is no need for raster scanning the investigated area), and avoids using complex electronic mirror systems. It can be used in case of stronger signal amplitudes than in the previously detailed experiments, typically in experiments triggering irreversible material reshaping. Using such technique, Von der Linde and coworkers investigated the ablation process in metals and semiconductors [106]. By exploiting the full potential of a

pump–probe imaging technique, they observed the formation and dynamic evolution of a transient Newton ring pattern in the nanosecond and sub-nanosecond time range after excitation. This pattern, formed by interference of the probe beam reflected at the front and back interfaces of the semi-transparent ablating layer, allowed a characterization of the propagation speed and its fluence dependence.

Subsequently, Garcia-Lechuga *et al.* could extend this work to several dielectrics also employing pump–probe microscopy [107], allowing to experimentally demonstrate and temporally characterize the transition from a single homogeneous layer into a shell structure. Beside investigating ablation, the same group performed imaging of the formation process of LIPSS produced by ultrashort laser pulses in Si [108]. Using a moving-spot, multiple-pulse irradiation approach, the authors were able to spatially and temporally resolve the birth and growth of individual LIPSS. They demonstrated that the formation process was initiated by free electron generation leading to non-thermal melting, liquid phase overheating and rapid solidification into the amorphous phase. In other experiments, Bhuyan and coworkers reported the ultrafast dynamics of high aspect ratio nanostructuring in bulk fused silica [109]. The authors proposed a description of mechanisms based on the axial energy deposition and subsequent material densification or rarefaction. The same group extended that work by describing the evolution of ultrafast-laser-excited bulk fused silica over the entire relaxation range [110], investigating local embedded modifications of the refractive index in the form of index increase in densified glass or in the form of nanoscale voids.

In the present thesis, pump-probe microscopic approach is applied with hyperspectral measurements and wavefront detection to characterize the ultrafast response of plasmonic nanocomposite materials under irreversible shape transformation conditions. The relevant results and discussion are presented in chapters 3-4. The principle of the wavefront detection used is explained hereafter.

2.3 Quadriwave lateral shearing interferometry

2.3.1 Measurement principles

Quadriwave lateral shearing interferometry (QLSI) is a quantitative phase imaging technique, capable of measuring both the intensity and the phase of a light beam. In case of simple lateral shearing interferometry, the incident wave front is replicated using diffraction gratings into two

identical but tilted wave fronts [111]. After propagation of the replicas, their interference pattern is recorded with a camera sensor. The phase gradients are recovered from the fringe deformation, by means of a Fourier deconvolution around the interferogram fringe frequency. However, this method lacks some gradient information to recover a full two-dimensional phase-field. Multiwave interferometry extends this principle to more than one gradient direction. In the case of QLSI, four replicas are created by a specific 2D diffraction grating. After propagation, two gradients along two perpendicular directions are measured, and then integrated to determine the spatial profile of the field intensity and phase. The interferogram deformation can be interpreted using either wave or geometrical optics. The principle of the interferogram formation is demonstrated in Figure 2.7.

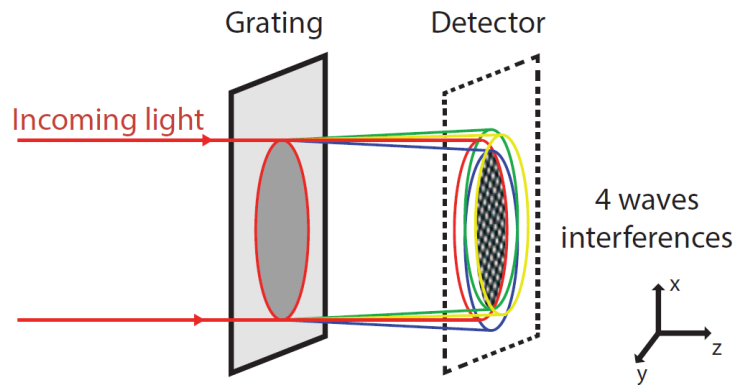


Figure 2.7 – Schematic of the principle of the QLSI technique. A diffraction grating forms four replicas of the incident wave, and the subsequent interferogram is recorded using a camera sensor. The spatial distribution of the phase and amplitude are then calculated from the four-waves interferogram. Image is taken from [112].

A diffraction grating replicates the incident beam. In the case of QWLS interferometer, the so-called modified Hartmann mask (MHM) is used [111]. It is made of the superposition of a Hartmann mask (amplitude grating with period p) and phase grating with period $2p$ as demonstrated in the Figure 2.8. The grating is optimized to diffract more than 90% of the light energy into the four first orders. The transmission of the MHM grating can be expressed as

$$t(x, y) = \cos\left(\frac{\pi}{p}x\right) \cos\left(\frac{\pi}{p}y\right). \quad (2.3)$$

Each diffracted order propagates along its own wave vector. After a propagation length z along the z -axis, if free space diffraction can be neglected, the electromagnetic field is coherent addition of the waves, which are displaced due to their deviation.

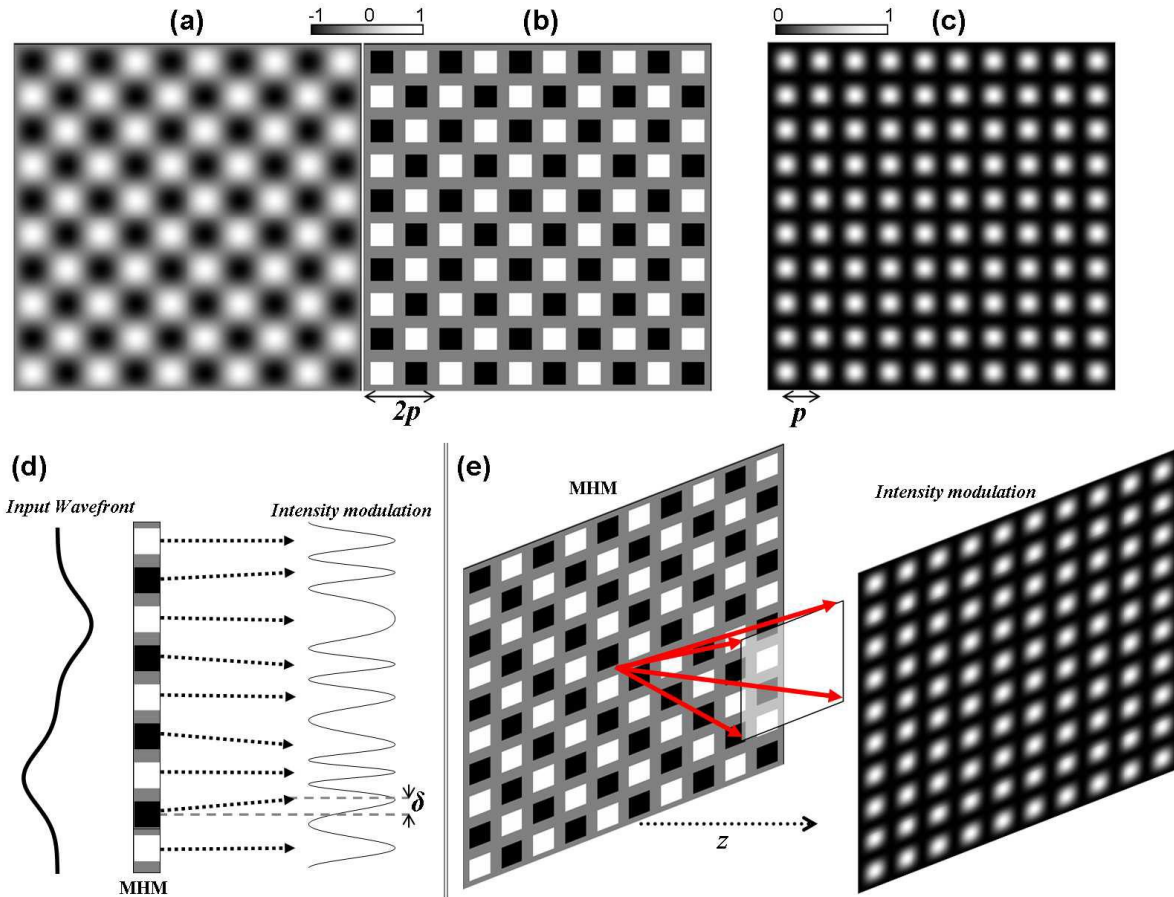


Figure 2.8 – Scheme of diffraction gratings associated with QLSI technique. (a) Ideal transmission for a four-wave-only 2D diffraction grating. (b) Transmission of MHM grating, which is an approximation of (a). (c) Intensity distribution of (a). (d) 1D interferogram formation by a MHM when a disturbed input wavefront is incident on the grating. (e) 2D interferogram formation by a MHM in the case of a plane input wavefront; visualization of the four diffracted waves (arrows). Image is taken from [111].

The intensity recorded by the camera sensor placed at a distance z from the diffraction grating is expressed as [111]:

$$\begin{aligned}
 I(x, y, z) &= I_0 \left\{ 1 + \cos \left(\frac{2\pi}{p} x + \frac{2\pi}{p} z \frac{\partial OPD}{\partial x} \right) + \cos \left(\frac{2\pi}{p} y + \frac{2\pi}{p} z \frac{\partial OPD}{\partial y} \right) \right. \\
 &\quad \left. + \frac{1}{2} \left[\cos \left(\frac{2\pi}{p} (x + y) + \frac{2\pi}{p} z \frac{\partial OPD}{\partial (x + y)} \right) + \cos \left(\frac{2\pi}{p} (x - y) + \frac{2\pi}{p} z \frac{\partial OPD}{\partial (x - y)} \right) \right] \right\}, \quad (2.4)
 \end{aligned}$$

where I_0 is the interferogram maximum of intensity in $z = 0$, and OPD stands for optical path difference, also referred to as optical thickness, linked to the phase ϕ of the incident electric field at a position with λ wavelength as

$$\phi = \frac{2\pi}{\lambda} OPD. \quad (2.5)$$

2.3.2 Example applications

This technique is used to determine the induced modification of the OPD due to the presence of an arbitrary sample. The OPD spatial profile is obtained via analyzing the interferogram *i.e.*, demodulating around specific carrier frequencies. Performing a Fourier transform on the interference image generates a pattern with 9 peaks. These peaks are distributed in a square area. There is a central peak, 4 lateral peaks and 4 peaks in the corner of the square. The 4 lateral peaks contain the phase gradient information along x and y . An inverse Fourier transform of these peaks enables to obtain phase gradient images along x and y . The final phase image is then retrieved by integrating the two phase gradient images. Making an inverse Fourier transform of the central peak gives the intensity of the incoming wave. A demonstration of the obtained intensity and OPD images after analyzing a raw interference image is shown in Figure 2.9 using a commercial wavefront sensor SID4-Element provided by Phasics. This first example shows the effect of single fs laser excitation of a Ag/TiO₂ nanocomposite sample, which is further investigated throughout the present thesis. The irradiation and illumination were performed using the experimental arrangement that is presented later in chapter 4, section 4.2.2. The intensity image was normalized by a reference image of the intact sample. The contrast in the intensity image is directly linked to the spatial distribution of the extinction of the sample, whereas the OPD image reveals information on the combined laser-induced refractive index and thickness change in the sample. The commercial QLSI wavefront sensor provided by Phasics was applied in the experiments described in chapter 4 instead of other phase techniques (*e.g.* Shack-Hartmann wavefront sensor, holographic methods, etc.), due to its achromatic design, noise insensitivity and very high phase resolution of 3 nm.

Historically, the QLSI finds its origin in the 90s by the work of Primot and his colleagues [113], [114]. There are many fields where this technology was applied, among those the work of Wattetliet *et al.* allowed the development of new applications in laser metrology [115]. In the followings, several works demonstrated that QLSI can be used in microscopic applications to investigate, *e.g.* low-contrast living cells [111].

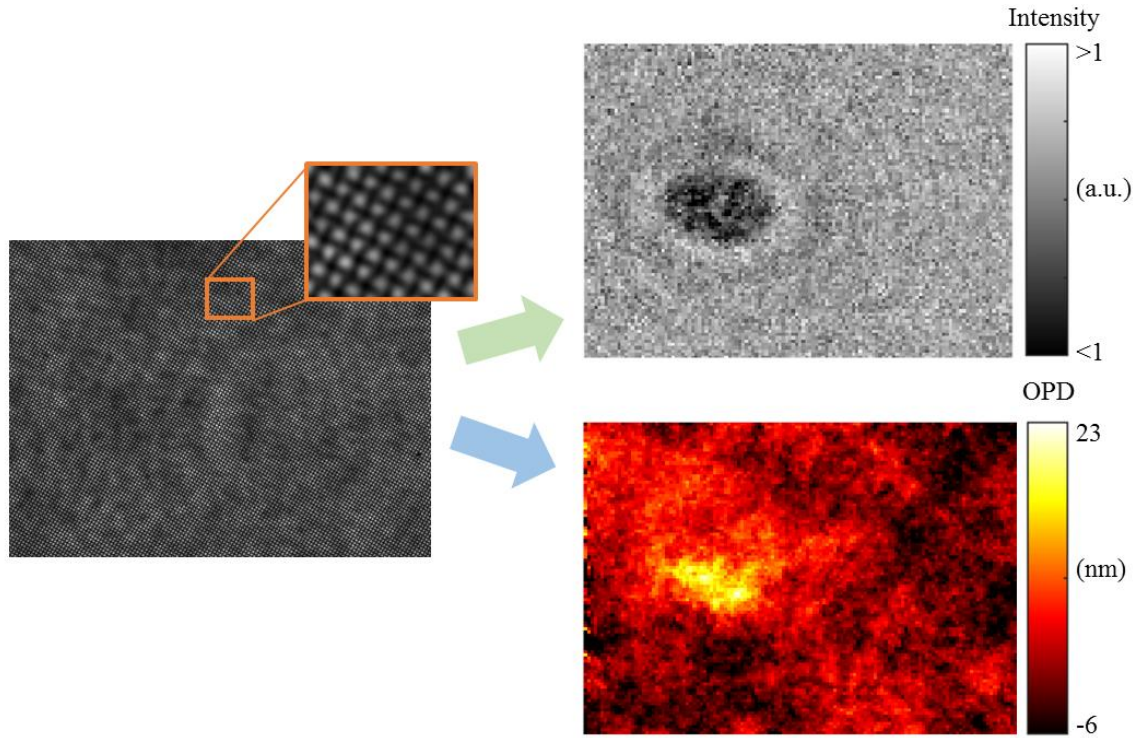


Figure 2.9 – Intensity and OPD images (right column) obtained from a raw interferogram image (left) obtained by QLSI technique using commercial SID4-Element wavefront sensor from Phasics. The images show the sample investigated in this thesis (described in chapter 3 section 3.2.1) observed in transmission configuration, excited by single ~ 200 fs pulse at 515 nm. The illumination wavelength was 450 nm. The details of the experimental setup are provided in chapter 4 section 4.2.2.

As the refractive index of a medium is temperature dependent, the QLSI is able to measure the wavefront distortion due to localized heating generated by laser excitation of different materials. For small temperature change, the refractive index variation Δn of a medium can be expressed as a linear temperature variation ΔT function such as:

$$\Delta n = \frac{\partial n}{\partial T} \Delta T. \quad (2.6)$$

For larger temperature variations, it is possible to approximate the temperature variation around with the Taylor's theorem [112]. Baffou *et al.* illustrated the abilities of the technique by mapping the laser-induced temperature distribution of Au NPs with diffraction-limited spatial resolution and 1 K thermal resolution, accompanied by retrieving the absolute absorption cross-section [116]. In other works, the QLSI technique was applied in ultrafast time-resolved experiments, for direct observation and quantitative measurement of the Kerr effect in fused silica, and free electron generation by photo-ionization process in optical coatings [117].

3 Mechanisms driving the self-organized reshaping of plasmonic metasurfaces

In this chapter, we report on a detailed study combining a broad range of experimental characterizations with numerical methods investigating the laser-matter interactions in ensemble of random plasmonic nanoislands encapsulated in a multilayer system. The interplay of the mechanisms detailed in the previous chapter results in a complex material response depending on the actual state of the gradually evolving system. The study explores the prominent roles of the direct interaction of the nanoisland ensemble with the electromagnetic field, the laser-induced temperature rise and the material relaxation on multiple timescales, eventually resulting in laser-induced anisotropy and emerging self-organized nanopatterns. The observed structural transformations are interpreted by numerical investigations of the laser-induced temperature rise considering the effect of thousands of pulses, and electromagnetic calculations revealing the quantitative origin of the self-organization phenomenon. Based on our results, laser-processed plasmonic metasurfaces could converge to realization in applications that strongly rely on laser-induced optical dichroism, such as the technique of printed image multiplexing, data storage and digital fabrication of nanoscale electronics. The results presented in this chapter are published in reference [118].

3.1 Introduction

Laser irradiation of metallic NP ensembles enables to control the optical properties on large-extent areas with sub-micrometer resolution leading to realization of complex metasurfaces [3], [4]. The LSPR band of metallic NPs is highly sensitive to the NP size and shape distributions, electromagnetic coupling effects and surrounding medium refractive index. This property enables the realization of rewritable media with photochromic Ag/TiO₂ films [5], [119]–[126] or ink-less color printing mediated by reshaping Al [127], Au [128], [129] and Ag [130], [131] NPs. Laser-generated assemblies of NPs provide dichroic spectral responses [1], [83], [132]–[134], enable to realize secure diffracting patterns [135] and multiplexed images [3], [4]. There is a great potential in laser-assisted reshaping of metallic NPs for low temperature, high-resolution fabrication of electrically conductive nano- and micropatterns without using expensive vacuum deposition techniques [136]–[138]. In this technology, the application of fs lasers enables to surpass the light diffraction limit, and the direct fabrication of metal nanopatterns smaller

than the excitation wavelength becomes possible. Submicron metal patterns on flexible polymer substrate is demonstrated as well owing to the localized heat deposition properties of ultrashort pulses [139]. In order to optimize the parameters of the laser processes for each kind of applications, it is required to deeply understand the physical and chemical mechanisms triggered in the material following the absorption of photon energy eventually leading to material transformations. In case of pulsed-laser irradiation, the material transformations usually require many pulses to reach new physical properties, like optical anisotropy [12], [140]–[142], therefore studying the intermediate states of the material throughout the evolution is crucial to reveal the mechanisms driving the reshaping.

In this chapter, we characterize the multipulse shape transformations of Ag nanoislands ensembles encapsulated between two TiO₂ thin films when the material is submitted to high-repetition rate, visible fs laser irradiation. The variety of laser-induced nanostructures in different ranges of cumulative pulse numbers sheds light on the interplay between different laser-induced physico-chemical mechanisms. A chronology of the mechanisms is proposed by completing the experimental characterizations by numerical modeling of the spatial distribution of the laser-induced temperature rise in the multilayer stack on multiple timescales, and by theoretical investigation of the self-organization phenomena.

3.2 Experimental methods

3.2.1 Preparation of Ag/TiO₂ multilayer nanocomposite by physical vapor deposition

Three-layer structures composed of a 15 nm-thick layer of non-spherical near-coalescence Ag nanoislands sandwiched between two 30 nm-thick TiO₂ layers are prepared via physical vapor deposition using a Bühler SYRUSpro 710 machine. Ag layers are obtained from Ag granules and TiO₂ layers from pure TiO₂ material. A focused electron beam is used to heat-up the material with a typical current of a few tens of mA for both materials. A specific e-beam pattern is developed in order to ensure uniform evaporation of the material. Samples are placed onto a rotating calotte, situated at a distance of about 600 mm from the crucible, to achieve layers with good uniformity over the an area of ~ 15 cm² on a microscope slide substrate. Depositions are carried out at room temperature at an initial pressure of about 10^{-6} mbar. Ag is deposited at a low rate of 0.1 nm/sec and TiO₂ at an even lower rate of ~ 0.01 - 0.02 nm/sec. Layer thicknesses and deposition rates were controlled with a quartz crystal microbalance. The samples are prepared by the team RCMO from Fresnel Institute in Marseille.

Ag/TiO₂ nanocomposite material is investigated due to its recently demonstrated excellent performance in laser-printed image multiplexing [3], [4]. These two materials form an ideal couple to get a large variety of colors by laser processing and also to create very particular optical properties that enable image multiplexing. Among noble metals, Ag is the one that gives rise to the largest color range with NPs smaller than 100 nm thanks to the spectral shift of the LSPR in the visible range. TiO₂ is chosen for two main reasons. Firstly, its high refractive index allows to sustain a guided mode with a relatively low overall thickness (taking into account the two layers). Secondly, the electrochemical response of Ag/TiO₂ couple efficiently contributes to Ag NP growth via ultrafast electron transfer into the TiO₂ conduction band and subsequent ionic Ag reduction in the matrix.

The thickness of the Ag layer is empirically adjusted in order to obtain a layer of nanoislands in the physical vapor deposition. Towards thicker Ag layer, the transition from separate nanoislands into homogeneous film layer was observed resulting in the disappearance of the LSPR. The unpolarized transmission spectrum and the scanning electron microscope (SEM) image of the initial sample are shown in Figure 3.1. The spectrum is measured using a commercial spectrophotometer (Cary 5000 from Agilent) with 2 nm spectral resolution in the visible and near-infrared region, and FEI Nova nanoSEM 200 scanning electron microscope with a helix detector is used in low vacuum mode to observe the morphology of the sample.

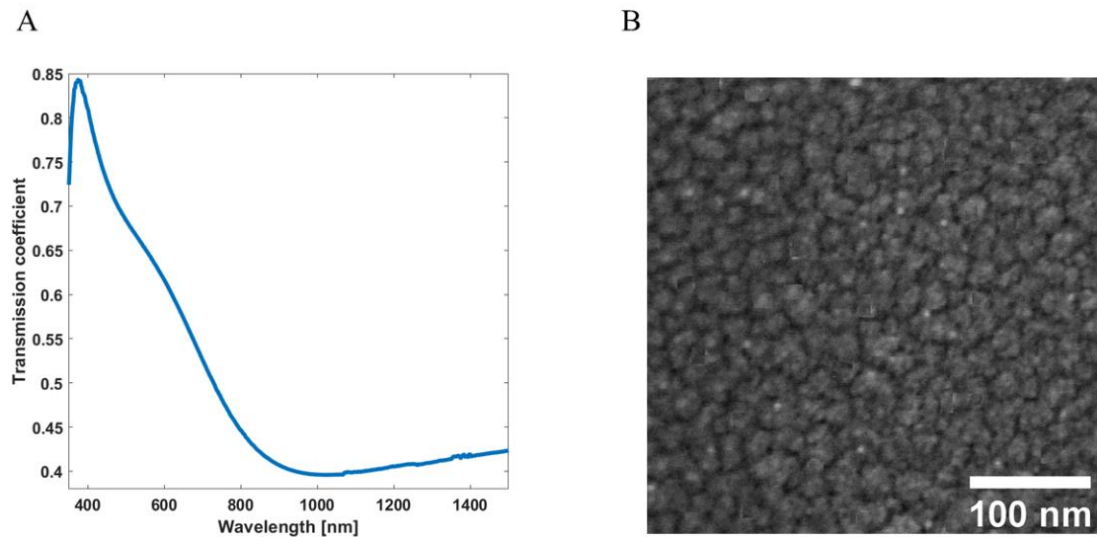


Figure 3.1 – *Ex situ* characterizations of the initial sample. A: Unpolarized transmission spectrum of the initial film in the visible and near-infrared region. There is no polarization anisotropy present before laser inscription. B: SEM image of the initial film showing the morphology of the tightly-packed, non-spherical Ag nanoislands.

3.2.2 High-repetition-rate pump-probe microscopy setup

High-repetition-rate pump-probe microscopic arrangement is applied to follow the pulse-to-pulse evolution of the anisotropic optical response of the material. The setup consists of two laser sources and an ultrahigh-speed camera, electronically synchronized with the former by means of an electronic delay generator. The sketch of the arrangement is shown in Figure 3.2.

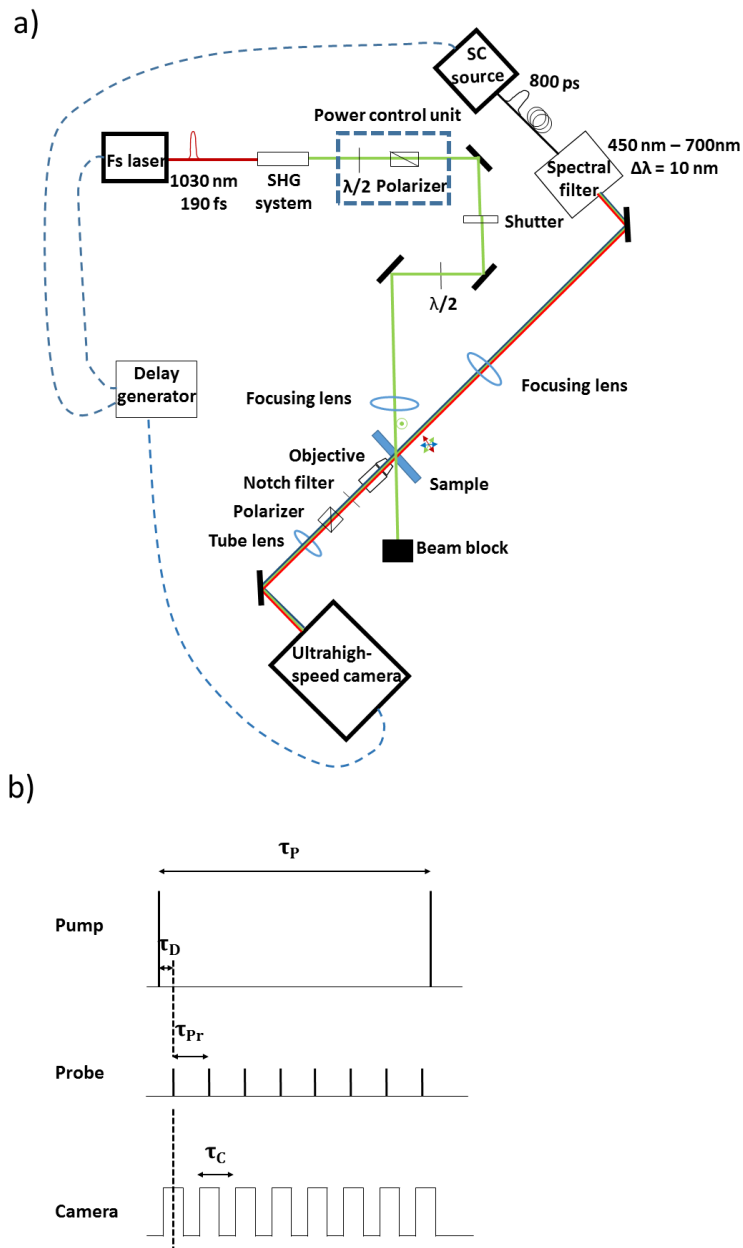


Figure 3.2 – The experimental setup for the *in situ* spectral measurement. (a) Sketch of the high-repetition-rate fs pump – supercontinuum (SC) probe imaging arrangement. The fs laser-triggered mechanisms are probed in transmission by the SC source, whose output is filtered to a narrow spectral band and tuned over the visible spectral range, imaging the sample surface onto an ultrahigh-speed camera.

Synchronization of the pump and probe laser pulse trains and the camera frame rate is controlled by a delay generator. (b) Principle of the synchronization of the pump and probe pulse trains and the camera frame rate; $\tau_P = 1/f_{\text{rep}}$: time between consecutive pump laser pulses, τ_{Pr} : time between consecutive probe laser pulses, τ_D : pump-probe delay, τ_C : time between consecutive camera frames, $\tau_C = \tau_{Pr}$. Each probe laser pulse is synchronized with the center of the exposure time window of the camera.

The pump laser system (PHAROS from Light Conversion) is based on a mode-locked oscillator with regenerative amplifier providing laser pulses of 190 fs duration (FWHM) at 1030 nm fundamental wavelength. The laser pulses are frequency doubled to 515 nm by a commercial harmonic generator system (HIRO from Light Conversion) based on a BBO crystal to work in the visible wavelength range.

The pulse duration of the visible wavelength is measured using a commercial intensity autocorrelator provided by Light Conversion to characterize the temporal broadening of the initial 190 fs pulse duration. In the experiment, two replicas of the beam are generated with a variable delay, then focused in a second-harmonic-generation crystal. The intensity of the second-harmonic signal is monitored as a function of the time delay between the two replicas. The second-order autocorrelation signal measured by a slow photodiode is expressed as $A(\tau) = \int_{-\infty}^{\infty} I(t) * I(t - \tau) dt$, where I is the intensity of the beams, and τ is the delay between the two replicas. The normalized measured autocorrelation can be seen in Figure 3.3.

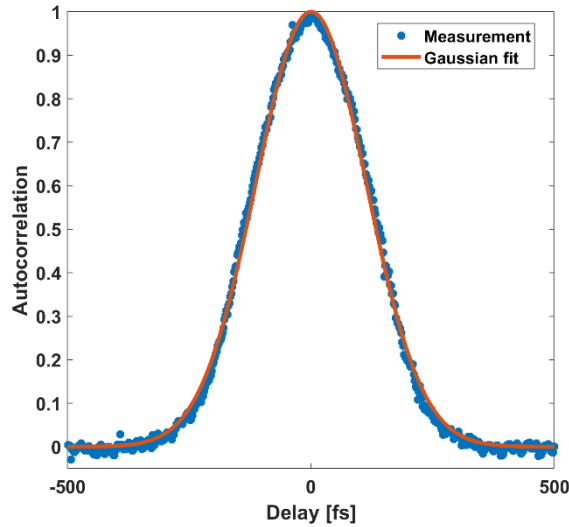


Figure 3.3 – Normalized autocorrelation function of the laser output after the second harmonic generation, and the Gaussian fit. From the Gaussian fit, the measured pulse width is obtained as 196 fs (FWHM).

It is known that the intensity autocorrelation of a Gaussian pulse has a temporal profile of a Gaussian function. Therefore, the fit of the autocorrelation function provides the pulse duration. The measured pulse width of 196 fs demonstrates that the broadening due to the second harmonic generation is negligible.

The pulse energy is adjusted by a half-wave plate and polarizer combination, and the polarization incident on the sample is controlled by an additional half-wave plate. The laser beam is focused with a 30 cm focal length lens at the sample surface under a 45° incidence angle, resulting in an elliptical focal spot, whose horizontal and vertical 1/e radii are measured as described in the followings.

Liu's method is a simple experimental approach that allows to determine the focal spot radius by measurements of the sizes of laser-induced modifications at different irradiation energies [143], without the need for imaging the beam profile. This methodology assumes a Gaussian laser beam profile expressed as

$$F(r) = F_0 e^{-\frac{2r^2}{\omega_0^2}}, \quad (3.1)$$

where $F(r)$ is the local fluence at a given radial position r , F_0 is the peak fluence value and ω_0 is the radial Gaussian beam waist at 1/e² the peak value. In our case, the beam quality has been validated by beam profiling method (CCD). One can define the marking fluence threshold F_{th} as the local fluence corresponding to the border of the laser marking, exhibiting a radius equal to R . Therefore, Eq. (3.1) can be written as

$$F_{th} = F_0 e^{-\frac{2R^2}{\omega_0^2}}, \quad (3.2)$$

which can be further transformed into a linear relationship by taking its logarithm, leading to:

$$R^2 = \frac{\omega_0^2}{2} \ln \frac{F_0}{F_{th}}. \quad (3.3)$$

However, the experimental parameter that is usually measured is not the peak fluence but the integrated pulse energy E . Generally, independently of the beam shape, the relationship between those parameters is linear, related with the effective beam area [144]. Therefore, Eq. (3.3) can be expressed as

$$R^2 = \frac{\omega_0^2}{2} \ln \frac{E}{E_{th}}, \quad (3.4)$$

where E and E_{th} are the pulse energy and the pulse energy threshold for the laser marking. As a result, the Gaussian beam waist ω_0 can be determined through the slope of a linear regression. In case of elliptical spot, the linear regressions can be performed for both vertical and horizontal laser marking radii.

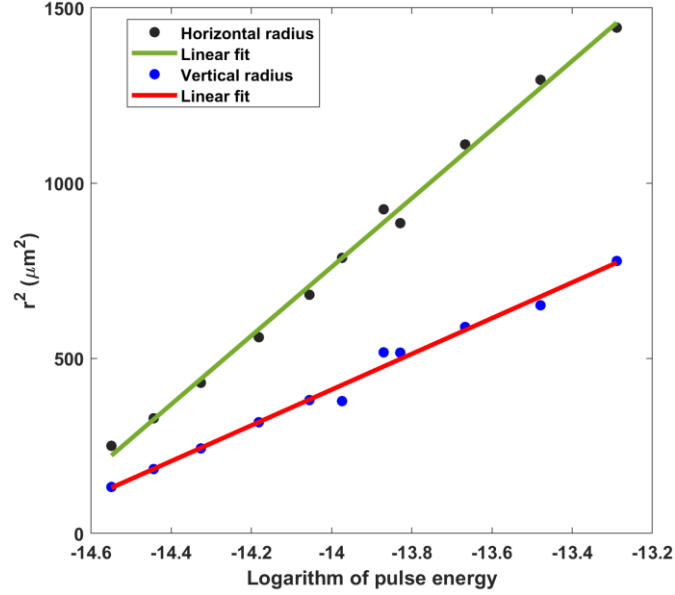


Figure 3.4 – Beam size measurement based on Liu’s method. The slopes of the linear regressions for the horizontal and vertical radii of the laser markings at various pulse energies provide the 1/e spot radii.

From the two slopes of the linear regressions, the 1/e spot diameters ($2\omega_0/\sqrt{2}$) for the horizontal and vertical dimensions are determined as 63 μm and 45 μm , respectively. The laser fluence F can be calculated based on the formula

$$F = \frac{2P}{f_{rep} \cdot \pi\omega_{0,h}\omega_{0,v}}, \quad (3.5)$$

where P is the laser power, f_{rep} is the laser repetition rate, $\omega_{0,h}$ and $\omega_{0,v}$ are the 1/e² horizontal and vertical spot radii.

A New Wave (Leukos) supercontinuum (SC) source equipped with a tunable filter (BEBOP filter, Leukos) is used as an unpolarized quasi-monochromatic (10 nm spectral width) probe laser with 800 ps pulse duration and a tunable wavelength in the range 450 nm – 700 nm. Probing in the visible wavelength range is necessary to spectrally resolve the transformation of the final LSPR. The beam is weakly focused with a 50 cm focal length lens in order to illuminate the entire fs laser excited area.

The fs laser-induced changes in the material are studied by the probe laser in transmission, imaging the sample surface by means of an infinity corrected objective (Mitutoyo, NA = 0.42 and M = 20x) and a tube lens ($f = 200$ mm) onto the CMOS detector of the ultrahigh-speed camera (Phantom V1212). A Notch filter is used to block scattered pump light (inevitably the probe light also at 515 nm), and a polarizing cube is applied in a rotation mount to measure the different polarized transmission spectra. The pixel size of the CMOS detector is $28\ \mu\text{m}$, yielding a detector-limited spatial resolution of $1.4\ \mu\text{m}$ of the sample image. The image acquisition rate is 600 kHz that is the maximum repetition rate of the ultrahigh-speed camera, and the dimensions of the recorded images are $179\ \mu\text{m}$ and $44\ \mu\text{m}$ in the horizontal and vertical directions.

The synchronization of the three main parts is controlled by a delay generator (Berkeley Nucleonics; Model 577), which is triggered externally by the TTL signal synchronized to the laser pulses of the supercontinuum source. One output signal of the generator synchronizes the camera at the same repetition rate, resulting in one probe pulse per acquired image (recorded with a typical exposure time of 600 ns.) Another output signal is used to synchronize the laser pulses of the pump laser. The frequency of the probe laser is divided by eight to obtain a 75 kHz repetition rate for the pump laser. This value is used to achieve heat-accumulation effect promoting the NP growth mechanism. A third, low frequency signal synchronized to the master frequency is shared between the pulse picker of the fs laser and the camera's trigger input, and used to start the data acquisition of the camera, and initiate the fs pulse train. The overall jitter between pump and probe laser pulses originating from the sum of the individual jitters (both lasers and the delay generator) is measured to be 15 ns at the plane of the sample, using a fast photodiode from Thorlabs. This value corresponds to the temporal resolution in our experiments.

The workflow starts with fixing the repetition rate of the probe and the pump laser pulses. The repetition rate of the probe is always divided by an integer value to reduce the pump laser frequency and thus record multiple frames between two consecutive pump pulses. The next step is setting the delay between a pump pulse and the first probe pulse. One pump pulse is always followed by a probe pulse train with a given number of pulses, whose first pulse arrives at a fixed time delay (with a 15 ns jitter). Finally, the desired probe wavelength is selected by means of the spectral filtering unit.

A video file containing all probing frames of the laser-excited area is recorded, beginning with the x^{th} probe pulse (typically $x = 100$) before the first pump pulse and ending by the y^{th} probe pulse after the N^{th} pump pulse, with y and N being limited by the physical memory size of the camera (72 GB). Results are averaged over five video files recorded within the same conditions in a fresh area of the sample. Probe wavelength scans are performed with the $\Delta\lambda = 10$ nm bandwidth from 450 nm up to 700 nm, by steps of 10 nm. The data evaluation is composed of

image processing routines developed in Matlab environment. The quantity that is shown in the results section corresponds to the absolute transmission coefficient of the sample in the center of the laser-processed area.

As a first step, the average pixel intensity of an area of reference located outside the pump laser spot is determined in the frame recorded just before the arrival of the first pump laser pulse. The average intensity of the reference area is denoted by \bar{I}_{AoR_IF} . The average pixel intensity of exactly the same area is measured in each of the recorded frames M and denoted by \bar{I}_{AoR_M} . These values are used to normalize the intensity of all pixels in each frame M , which shows small variations caused by fluctuations of the probe laser pulse energy. It is assumed that the fluctuations of the laser source are visible in an equal manner over the whole frame. So, each frame I_M is divided by the ratio $\bar{I}_{AoR_M} / \bar{I}_{AoR_IF}$, as to normalize each frame with respect to the fluctuations of the probe laser pulse energy.

The subsequent step is a division of each frame I_M , pixel-by-pixel, by the frame I_{IF} recorded just before the arrival of the first pump laser. This division removes the static speckle pattern coming from the illumination conditions, and yields the relative transmission value in each pixel, relative to the initial state of the material.

The next step is multiplying the whole image by the transmission coefficient of the initial film at the current wavelength $T_{if}(\lambda)$, whose value is measured with the spectrometer before carrying out the *in situ* pump-probe experiment. With these steps, one obtains the absolute value of the film transmission coefficient T over the whole frame for each pixel, as

$$T = \frac{I_M}{I_{IF}} \frac{\bar{I}_{AoR_IF}}{\bar{I}_{AoR_M}} T_{if}(\lambda). \quad (3.6)$$

Finally, the transmission coefficient is calculated by averaging T over an area of 6x6 pixels at the laser spot center, which corresponds to circular area of 8.4 μm in diameter on the sample. This transmission coefficient of the sample at the center of the laser processed area T_C , is the one that is reported in the results section.

The demonstration of the image normalization effect recorded at 640 nm probe wavelength can be seen in Figure 3.5. The reference image is the video frame taken before the arrival of the first fs pulse, and used to divide every subsequent video frame. The red dashed and solid rectangles indicate the regions used for filtering the image intensity fluctuation and for determining the value of the transmission coefficient at the focal spot center, respectively.

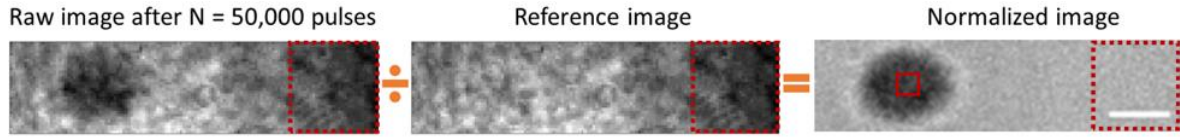


Figure 3.5 – Demonstration of the image normalization using the example illumination wavelength of 640 nm. The reference image is captured before the arrival of the 1st fs pulse, and used to divide every video frame containing the laser excited area after each fs pulse. The solid rectangle shows the area of interest to obtain the transmission coefficient value, and the dashed rectangle indicates the region used to normalize the probe laser energy fluctuations. The scale bar in the normalized image is 30 μm .

3.3 Numerical approaches

3.3.1 Modeling the laser-induced temperature profile

Laser-induced temperature simulations are carried out by the team CONCEPT from Fresnel Institute in Marseille with a model recently developed during the PhD thesis of Paul Rouquette to predict the photo-induced temperature in planar multilayer systems illuminated by a pulsed optical source [145]. The temperature is calculated from the Fourier equation, provided in the form:

$$\Delta T_i(\vec{r}, z, t) - \left(\frac{1}{a_i}\right) \partial_t T_i(\vec{r}, z, t) = -\left(\frac{1}{b_i}\right) S_i(\vec{r}, z, t), \quad (3.7)$$

where T_i is the photo-induced temperature in the medium of index (i) of the multilayer system, t represents the time variable, $\vec{r} = (x, y)$ the transverse space coordinate and z the direction perpendicular to the multilayer interfaces. The thermal parameters are the diffusivity a_i and the conductivity b_i . The thermal source in the medium (i) is named S_i , and corresponds to the volume density of optical losses.

Once the thermal source S_i is known, Eq. (3.7) is solved through a double Fourier transform versus time t and space coordinate \vec{r} . In the second Fourier plane, thermal admittances and thermal effective indices [146] in the multilayer are used according to a procedure similar to that used in optics to calculate the stationary electromagnetic field in the component [147], [148]. Finally, as the thermal source can be considered as a volume current, the resolution method is based on that used for the scattering of light by heterogeneous volumes in multilayer systems [149].

Under these conditions, the specificity of the photo-induced temperature problem lies in the expression of the source $S_i(\vec{r}, z, t)$. The expressions are greatly simplified if we assume that the incident optical source, which creates the absorption and therefore the temperature rise, is quasi-monochromatic around the temporal frequency $f_0 = \frac{c}{\lambda}$ and only slightly divergent around the spatial frequency \vec{v}_0 , which is consistent with our experimental conditions.

To take into account the interference pattern that arises between the incident wave and a guided wave excited by scattering [150], a sinusoidal spatial modulation is added to the optical source. The contrast $\frac{2\beta}{1+\beta^2}$ of this modulation is fixed to a low value by taking $\beta = 0.1$ to simulate a limited coupling of incident light into the guided wave. Finally, it must be underlined that the time simulations of the temperature rise are carried out by considering that all the system parameters are fixed, which is, obviously, a strong approximation. With these hypotheses, the source (in 2D geometry) writes, for TE polarization, in the first Fourier plane:

$$\tilde{S}_i(x, z, f) = \frac{\partial \mathcal{A}_i}{\partial z}(\vec{v}_0, z, f_0) \frac{2}{\Re\{\tilde{n}_0\}} \left(\frac{\partial W}{\partial S} \right) e^{-\frac{(\pi\tau f)^2}{2}} |e^{j2\pi v_{0x}x} + \beta e^{-j2\pi v_{0x}x}|^2, \quad (3.8)$$

where $v_{0x} = \frac{\sin\theta_i}{\lambda}$, with θ_i and λ and the incidence angle and the wavelength of the femtosecond laser, $\frac{\partial W}{\partial S}$ is the laser fluence, the temporal Gaussian function describes the limited pulse duration τ , and

$$\frac{\partial \mathcal{A}_i}{\partial z} = \left(\frac{\omega}{2} \right) (\epsilon_i'' |E_i(z)|^2 + \mu_i'' |H_i(z)|^2) \quad (3.9)$$

is the linear absorption density at frequencies (f_0, \vec{v}_0) . This source function is repeated each $\tau_p = \frac{1}{f_{rep}}$. Strictly speaking, the heat equation must be solved in a 3D geometry at different timescales. However, because the calculation is time-consuming, a 2D geometry is considered, so that the temperature may be slightly overestimated with a slower cooling.

Our model is compared with success to other results of the related literature [151]. The comparison between the result of temperature modelling in reference [151] and our model is demonstrated in Figure 3.6. HfO₂/SiO₂ multilayer mirror system deposited on K9 glass is considered, and the temperature distribution along the direction of depth in the films for 10 ns and 1 ms laser illuminations under normal incidence are calculated. In our calculations, we considered the same system for the 10 ns laser illumination case. The temporal shape of the laser pulse is assumed to be Gaussian function, and the temperature profile is calculated at the time when the

laser intensity is maximum. The good agreement between the two results validates our approach.

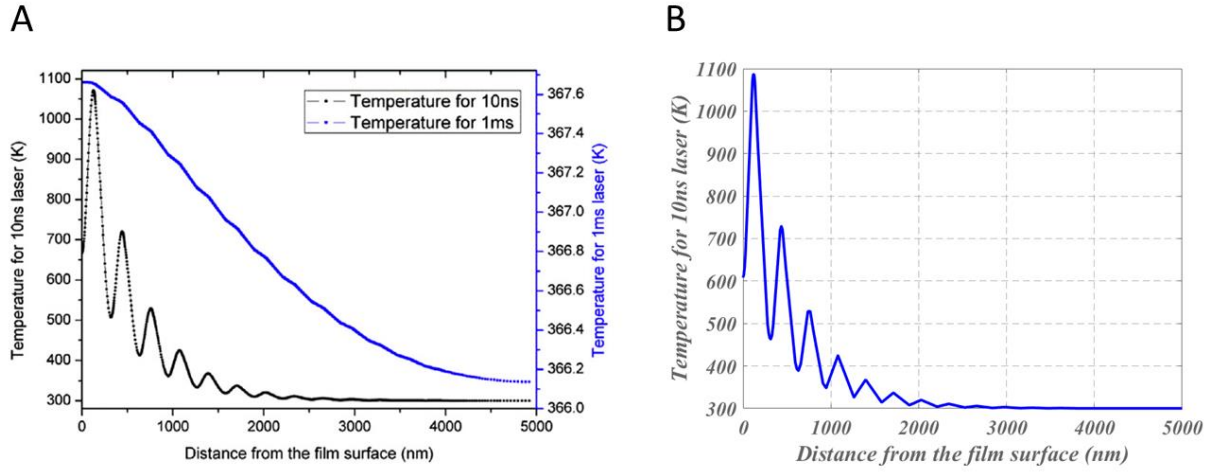


Figure 3.6 – Comparison of the result of our temperature model to the thermal calculation in reference [151]. A: Temperature along the direction of depth of the film induced by 1 ms long-pulse and 10 ns short-pulse lasers under normal incidence. The figure is reused from [151]. B: Temperature along the direction of depth of film induced by 10 ns short-pulse lasers under normal incidence calculated by our model. In both calculations, the temperature is calculated at the time when the laser intensity is maximum.

3.3.2 Electromagnetic calculations

These simulations are also carried out by the team CONCEPT from Fresnel Institute based on our suggestions for the design of the system and the choice of parameters. Self-organization phenomena are investigated by calculating the guided mode effective refractive index and electric field depth profile in a multilayer system using reflection pole method [147], [152], [153]. The model is a waveguide structure composed of three layers with e_i thickness and n_i refractive index for each layer i as shown in Figure 3.7a, where n_0 and n_S are the refractive indices of the superstrate and substrate, respectively. If the system is illuminated by the electromagnetic field with λ vacuum wavelength and angle of incident A_i , the complex reflection coefficient at the first interface is provided as [147]

$$r_0 = \frac{\tilde{n}_0 - Y_0}{\tilde{n}_0 + Y_0}, \quad (3.10)$$

where $\tilde{n}_0 = \frac{1}{\eta_0 \mu_{r0}} n_0 \cos \theta_0$ with $\theta_0 = A_i$ angle of refraction in the superstrate, Y_0 is the admittance at the first interface, η_0 is the vacuum impedance and μ_{r0} is the relative magnetic permeability of the superstrate. Y_0 is defined as the ratio of the tangential magnetic field to the tangential electric field. $Y_0 = \tilde{n}_0$ holds for a progressive wave (along the z axis), and $Y_0 = -\tilde{n}_0$ holds for a retrograde wave (along the $-z$ axis), with the wave components demonstrated in Figure 3.7b. r_0 is defined as the ratio of the up-going component of the electric field to the down-going component. For confined waves within the multilayer structure, only retrograde wave exists in the superstrate, implying that $|r_0| \rightarrow \infty$ (Eq. 3.10). Thus, the mode indices are those that make $|r_0|$ infinite. Mathematically, the confined mode indices are the poles of r_0 . This is the basic foundation of the method. In general, r_0 is the reflection coefficient for the complex wave amplitude, and it is a mathematical factor that can take any value. It should not be confused with the Fresnel amplitude reflectance at an interface. In practice, it is more convenient to invert r_0 and work with its reciprocal.

It can be shown, that the admittance Y_0 can be obtained by a recursive formula [147]

$$Y_{i-1} = \frac{Y_i \cos(\alpha_i e_i) - j \tilde{n}_i \sin(\alpha_i e_i)}{\cos(\alpha_i e_i) - j \frac{Y_i}{\tilde{n}_i} \sin(\alpha_i e_i)}, \quad (3.11)$$

where $\tilde{n}_i = \frac{1}{\eta_0 \mu_{ri}} n_i \cos \theta_i$ with θ_i and μ_{ri} the angle of refraction in layer i and relative magnetic permeability of layer i , respectively, and $\alpha_i = \sqrt{\left(\frac{2\pi n_i}{\lambda}\right)^2 - (2\pi \nu)^2}$ with $\nu = n_0 \sin \theta_0 / \lambda$. To initialize the recursion, it can be shown, that the admittance at the last interface is provided as $Y_3 = \tilde{n}_s$. As a summary, to obtain the complex effective index of a guided mode supported by the multilayer structure, the minimum of the inverse reflection coefficient at the superstrate $r_0(\nu)$ needs to be calculated. Once $\nu = \nu_g$ is obtained, the guided mode effective refractive index is provided as $n_g = \lambda \nu_g$.

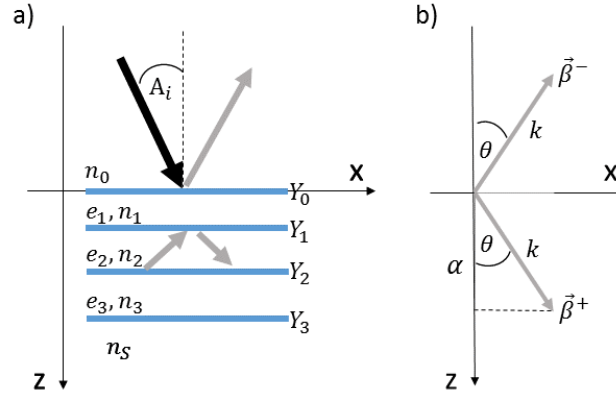


Figure 3.7 – a) Sketch and notation for the waveguide structure. n_i : refractive index of the medium i ; e_i : thickness of the layer i ; A_i : angle of incident; Y_i : admittance at the interface i . b) Progressive ($\vec{\beta}^+$) and retrograde ($\vec{\beta}^-$) wave components at an arbitrary spatial point; $k = 2\pi n/\lambda$.

Finally, provided that the mode effective refractive index is determined, an additional recursive formula enables to compute the spatial intensity profile of the guided mode for S polarization [147]:

$$\hat{E}_{i,tg}(v_g) = \left[\cos(\alpha_i(v_g)e_i) + j \frac{Y_{i-1}(v_g)}{\tilde{n}_i(v_g)} \sin(\alpha_i(v_g)e_i) \right] \hat{E}_{i-1,tg}(v_g), \quad (3.12)$$

with

$$\hat{E}_{0,tg}(v_g) = 1 + r(v_g). \quad (3.13)$$

3.4 Experimental results

This section details the wide range of experimental results aiming to characterize the irreversible transformations of the multilayer system in the multipulse regime using different experimental conditions. *In situ* spectral measurements reveal the multipulse evolution of the optical response of the material, and *ex situ* electron microscopy investigations provide the corresponding structural transformations. In the last part of this section, *in situ* electron microscope experiments are performed by Dr. Matthieu Bugnet from MATEIS laboratory of University of Lyon revealing the morphological transformations of Ag nanoislands upon thermal annealing (no laser irradiation is performed).

3.4.1 Laser fluence-dependent spectral kinetics

The experimental results investigating the optical response at different pump laser fluences are detailed first. In Figure 3.8a, the multipulse evolution of the transmission coefficient probed at 570 nm is demonstrated at selected laser fluences. At the two highest fluences, a transmission increase is followed by a considerably slower transmission decrease, and a final increase repeats on the slowest rate. Towards lower laser fluences, an extra fast transmission decreasing period occurs before the first increase. For any case, the most important observation is that characteristic pulse number regions can be assigned (3 or 4 regions), where the kinetics of the evolution exhibits considerably different rates suggesting different mechanisms driving the NP transformations, and therefore the optical response.

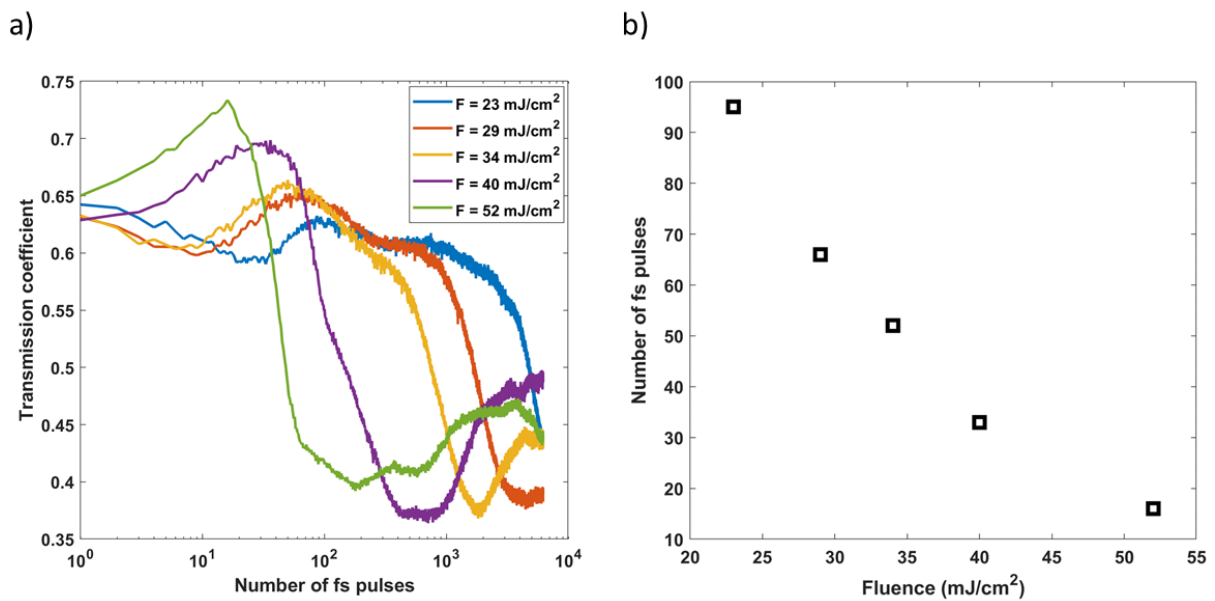


Figure 3.8 – Laser-fluence-dependent spectral kinetics. a) The evolution of the transmission coefficient probed at 570 nm at different laser fluences. b) The estimated number of pulses needed to reach the transmission maximum at each laser fluence.

The kinetics at each region is highly sensitive to the laser fluence, additionally, the onset of the individual regions can be efficiently tuned, *i.e.* the higher fluence results in that the different regions occur at lower pulse numbers. This is demonstrated in Figure 3.8b, where the number of pulses needed to reach the transmission maximum is estimated at each fluence, revealing non-trivial scaling. All of these observations suggest the triggering of heat-sensitive reshaping mechanisms described in chapter 1, and are further characterized in the subsequent sections.

3.4.2 Multipulse evolution of the optical anisotropy

An intermediate laser fluence value of 31 mJ/cm^2 is selected based on the observations of the laser markings at various fluences (previous section) under optical microscope, and complete spectral measurements are conducted with the selected value. The pulse-to-pulse evolution of the polarized transmission spectrum measured with the setup described in the Experimental methods section, up to $N = 50000$ pulses, is shown in Figure 3.9. Columns a) and b) show the results for polarization states of the probe laser incident at 0° , respectively parallel or perpendicular to the pump laser polarization (S polarization). Row 2 displays spectra for selected pulse numbers N , extracted from the 2D plots shown in row 1.

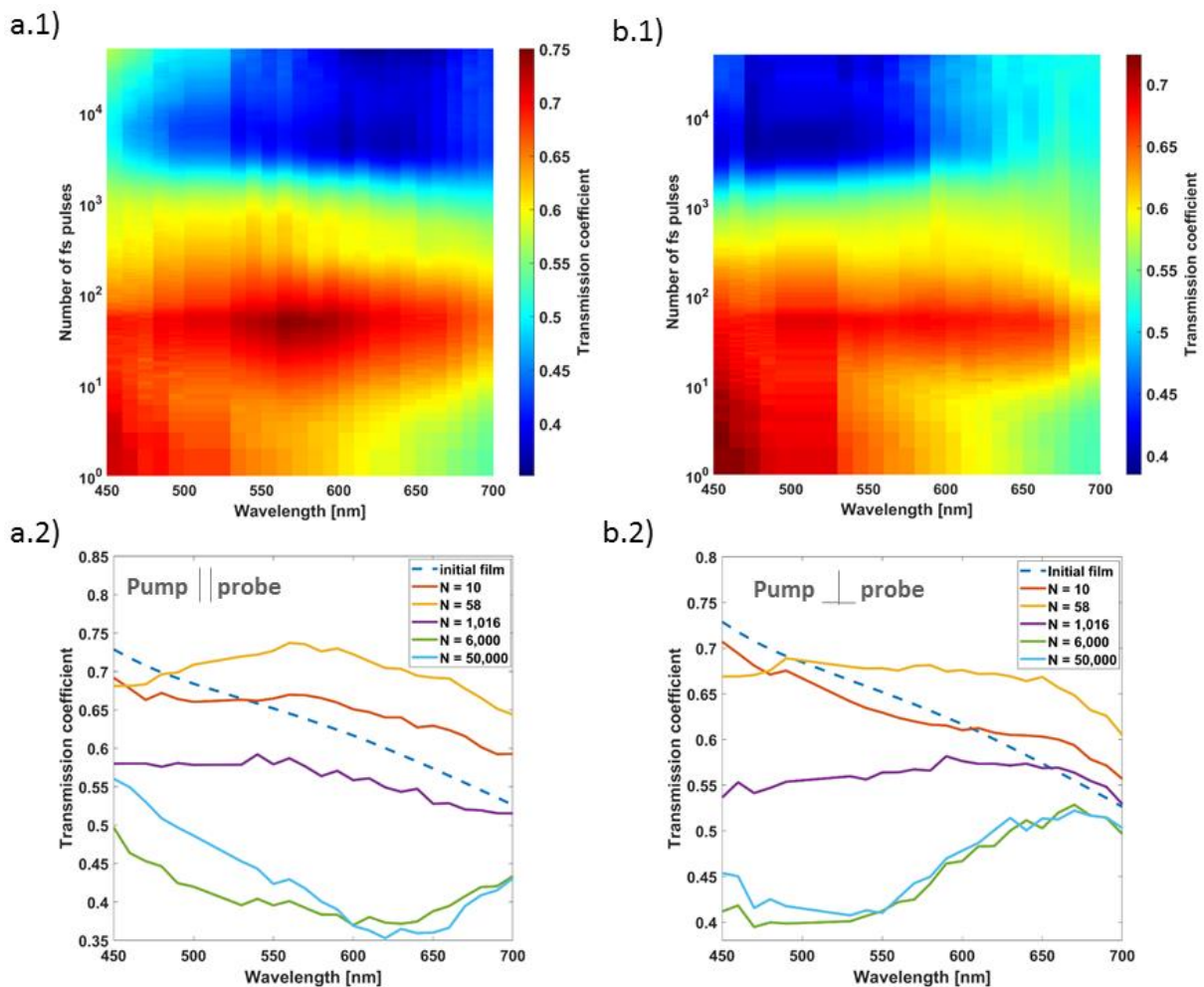


Figure 3.9 – Pulse-to-pulse evolution of polarized transmission spectra recorded *in situ* at the center of the fs-laser-processed area over the first 50000 pump laser pulses. a.1) and b.1) 2D plots of the transmission spectra versus the fs laser pulse number N for a probe polarization parallel or perpendicular, respectively, to the pump laser polarization. A logarithmic scale is used for the pulse number. a.2) and b.2) Extracted spectra from a.1) and b.1) at characteristic pulse numbers N .

The delay between each fs pump pulse and the first probe pulse is set to 15 ns in this figure. Each fs pulse, beginning from the very first one, causes a permanent change in the sample transmission spectrum. During the first ~ 10 pump pulses, the original absorption of the LSPR band, with a transmission minimum at around $\lambda = 1000$ nm wavelength (Figure 3.1 in Experimental methods), is weakened at long wavelengths and strengthened at shorter wavelengths. Moreover, significant differences are observed for the two probe polarization states as a result of laser-induced dichroism in the sample. This trend continues and leads to a flattening of the spectrum during the next ~ 50 pulses, yielding an overall increase in transmission for both polarizations, with an average value of about 70% over the whole spectral range probed. Upon further increasing the number of pulses, the transmission over the entire spectrum constantly decreases at a slow rate, up to about $N = 1000$. Subsequently, up to $N = 6000$ pulses, a broad dip emerges, centered at $\lambda = 530$ nm for perpendicular polarization, and $\lambda = 600$ nm for parallel polarization, which sharpens and redshifts until the end of the recorded evolution ($N = 50000$).

These experiments are performed at a fixed pump laser repetition rate of 75 kHz. In order to evaluate the sensitivity of the kinetics of the spectral transformation to the rate of the heat accumulation, repetition rate scan is performed at constant pump laser fluence. The results are presented in the following section.

3.4.3 Effect of the heat accumulation

Figure 3.10 shows the shot-to-shot evolution of the transmission coefficient at a constant probing wavelength ($\lambda = 530$ nm), plotted for three different pump laser repetition rates and constant fluence of 31 mJ/cm^2 . Figure 3.10a shows in all cases an initial fast decrease during the first 10 pulses, followed by a strong increase over the next 80 to 90 pulses, before decreasing again abruptly until around $N = 130$ (dashed line), where the evolution is slowed down. Up to this point, the overall evolution of each pulse does not depend significantly on the repetition rate. For higher pulse numbers, the kinetics of the spectral changes is slowed down strongly and the influence of the repetition rate increases, which is a signature of thermal accumulation, playing an important role on the sample evolution on this timescale. Figure 3.10b highlights the decreasing effect of each fs pulse on the transmission coefficient after hundreds of pulses at 75 kHz repetition rate. During the very first fs pulses, each laser pulse decreases the transmission coefficient by about 1 %, while after 920 pulses, the effect of each single pulse falls in the sensitivity level of the camera and 10 successive pulses decrease the transmission coefficient by less than 0.1 % typically.

When looking at the evolution of the transmission coefficient over a probe pulse train between two consecutive fs pulses, only the first probe pulse arriving 15 ns after a given pump pulse shows a significant change (Figure 3.10/b.1). The subsequent 7 probe pulses before the next pump pulse arrives do not show any detectable transmission change, indicating that the sample does not evolve between two probe pulses (temporal separation = 1.67 μ s) without further pumping.

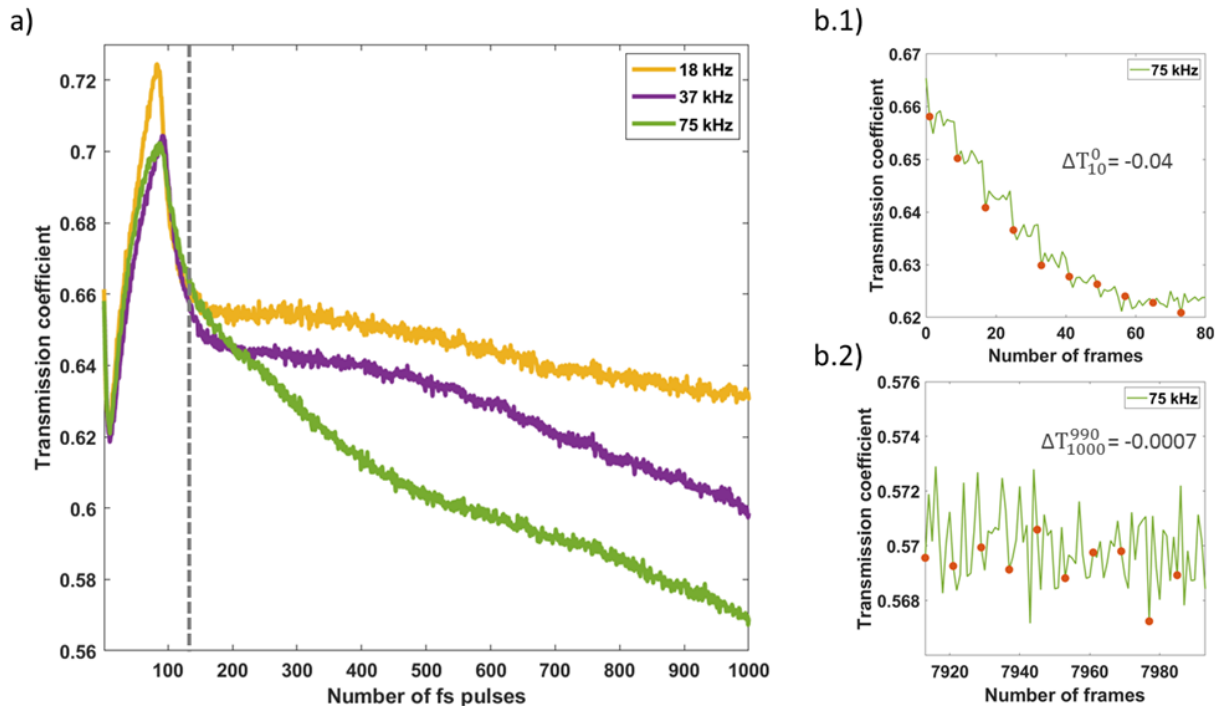


Figure 3.10 – The effect of the repetition rate. a) Transmission coefficient probed at 530 nm wavelength after each fs pulse ($N = [1, 1000]$) for different pump laser repetition rates (see legend) and constant fluence of 31 mJ/cm^2 . The dashed line at $N = 130$ indicates the change in kinetics, from which the sample evolution strongly depends on the repetition rate. The plots displayed in b.1) and b.2) show the variation rate of the transmission coefficient for $f = 75$ kHz, over the first and the last 10 pump pulses of the series. The transmission values corresponding to the eight intermediate probe pulses between consecutive fs pulses are also plotted (600 kHz camera frame rate was used). The filled circles indicate the values corresponding to the first probe pulse after each fs pulse (with 15 ns temporal delay).

To further evaluate the importance of heat accumulation in our sample, the *in situ* spectral measurement is repeated at a considerably smaller repetition rate of 5 kHz. The laser fluence at both repetition rates (75 kHz and 5 kHz) is 52 mJ/cm^2 in these experiments. Additionally, the polarizer is removed from the microscope setup, therefore the unpolarized transmission is measured. The comparison of the results from the two experiments is demonstrated in Figure 3.11. In images a.2 and b.2, the solid and dotted lines indicate the spectrum flattening and subsequent decreasing tendencies, respectively, and the colors encode the number of pulses. In general, the

lower repetition rate results in a considerably slower spectral transformation as an indication of the lower rate of heat accumulation induced in the TiO₂ matrix, which determines the kinetics of the heat-assisted NP reshaping mechanisms. This is clearly observable by the flattening tendency in both cases, which lasts for 50 and 10 pulses for the lower and higher repetition rates, respectively.

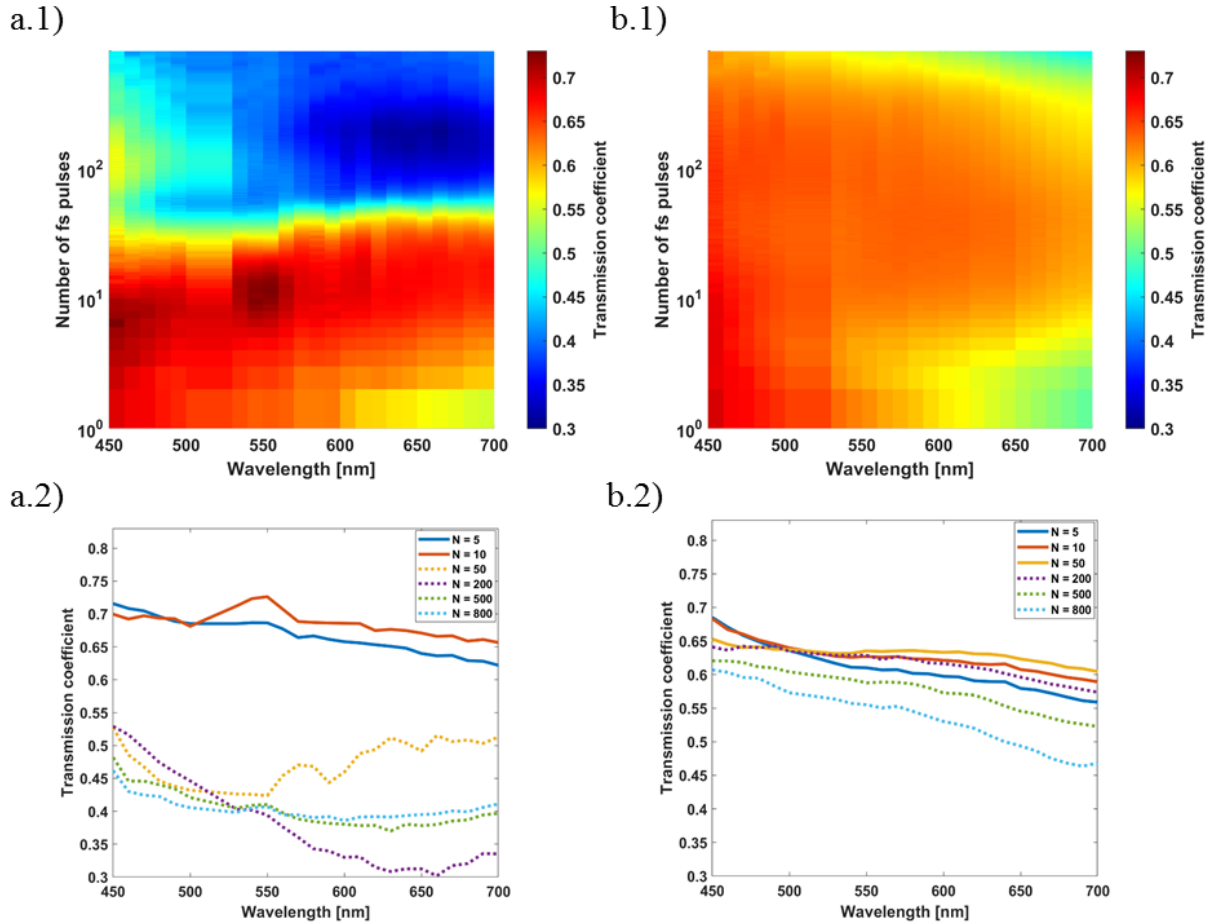


Figure 3.11 – Repetition rate-dependence of the pulse-to-pulse evolution of the unpolarized transmission spectra recorded *in situ* at the center of the fs-laser-processed area over the first 800 pump laser pulses. The laser fluence is 52 mJ/cm². a.1) and b.1) 2D plots of the transmission spectra versus the fs laser pulse number N for the laser repetition rates of 75 kHz and 5 kHz, respectively. a.2) and b.2) Extracted spectra from a.1) and b.1) at characteristic pulse numbers N . The solid and dotted lines indicate respectively the spectrum flattening and subsequent decreasing spectral tendencies in both images.

Additionally, the subsequent formation of the transmission dip is by far not finished within the first 800 pulses at 5 kHz, in contrast to the higher repetition rate observation at 200 pulses. In consequence, substantially different NP structures could be achieved by solely tuning the laser repetition rate. In the following investigations, the sample response in the first conditions is investigated in details, *i.e.*, 75 kHz repetition rate and 31 mJ/cm² laser fluence.

3.4.4 Time-resolved experiments on short timescale

A more accurate investigation of the sample evolution over the first hundreds of ns after each pump pulse has been carried out with the 15 ns temporal-resolution of the experiment. Figure 3.12 shows that the unpolarized transmission coefficient at $\lambda = 530$ nm remains fairly constant from 15 ns to 1 μ s, independently of the pulse number N , for which we plot the time variations. This implies that all significant permanent transformations in the sample occur in less than 15 ns.

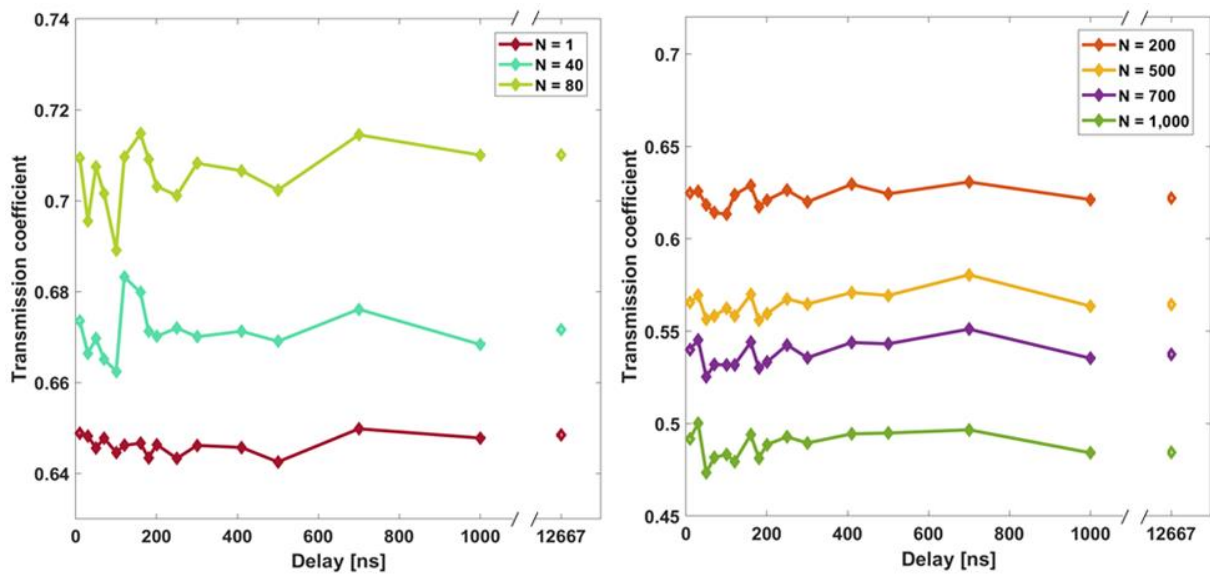


Figure 3.12 – Variations of the unpolarized transmission coefficient at $\lambda = 530$ nm after different numbers of pump pulses, N , probed at different delays with respect to the pump pulse and covering a delay range from 15 ns to 12.7 μ s. The time between consecutive pump pulses is 13.3 μ s.

A short summary of the results from the *in situ* spectral measurements is provided as follows. The experiments conducted at different laser fluences and probed at single wavelength revealed that the kinetics of the sample response is strongly sensitive to the laser fluence, which indicated heat-sensitive NP reshaping mechanisms. This was further supported by experiments using different laser repetition rates, revealing the sensitivity of the spectral transformations on heat accumulation. Pump-probe experiments conducted on the ns- μ s timescale revealed that the sample relaxation is faster than ~ 15 ns independently from the fs pulse number. Additionally, the pulse-to-pulse evolution of the polarized transmission spectrum evidenced the formation of laser-induced dichroism, which implies anisotropic NP shapes and nanostructures.

3.4.5 *Ex situ* electron microscopy of structural changes

Laser-induced changes have been investigated by SEM and high-angle annular dark-field scanning transmission electron microscopy (HAADF-STEM). HAADF-STEM characterizations are performed with a Jeol Neo ARM 200F operated at 200 kV on cross-sections and top-view FIB thin lamellas made using an FEI Strata DB 235 instrument. Laser-processed regions are investigated resulting from a static laser exposure at characteristic pulse number N , as well as in line regions drawn by moving the sample at constant speed upon laser irradiation. The scanning speed V was chosen to correspond to an effective number of pulses N_{eff} calculated as $V = \frac{2rf}{N_{eff}}$, with r and f indicating the horizontal $1/e$ spot radius and laser repetition rate, respectively.

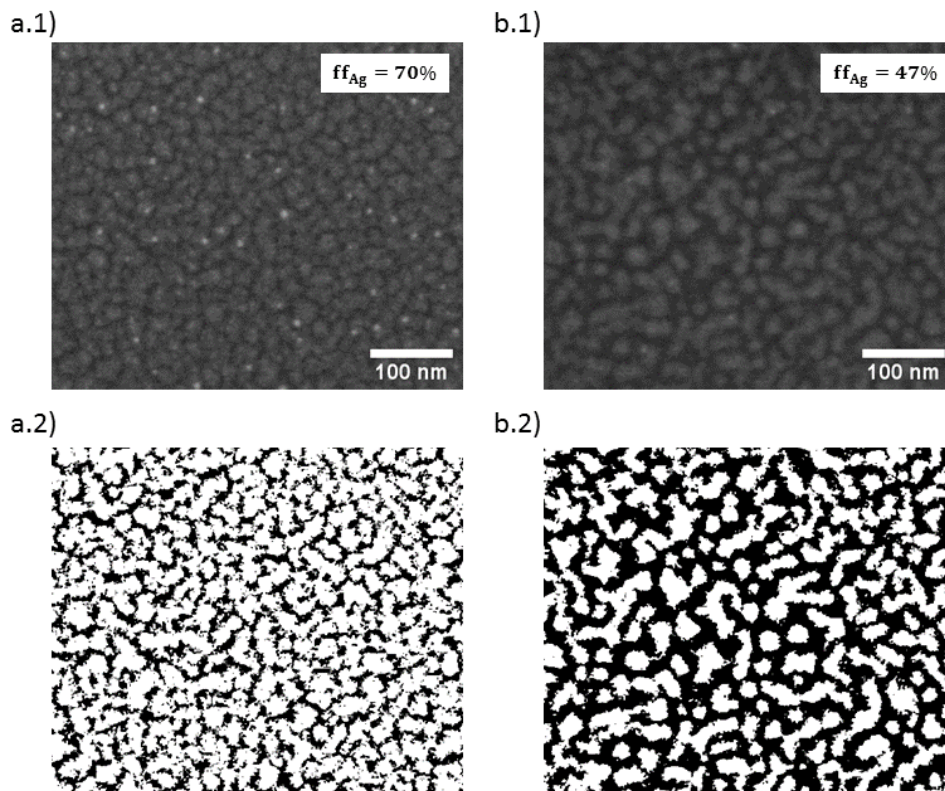


Figure 3.13 – SEM characterization I. a.1) SEM image of the initial film. a.2) Binary image of a.1) after image processing to better visualize the Ag nanoislands. b.1) SEM image of the laser spot after $N = 10$ pulses. b.2) Binary image of b.1) after image processing. ff_{Ag} stands for Ag filling factor.

Figure 3.13 shows SEM images of the film before and after irradiation with 10 pump laser pulses. As the Ag nanoislands are buried under a 30 nm thick TiO_2 layer, the image contrast is

low. The comparison of the two images after image processing reveals an overall laser-induced decrease of the filling factor from 70% to 47%.

Characteristic SEM images of the laser processed lines and same for the laser processed dots with an increasing effective pulse number are shown in Figure 3.14 and Figure 3.15, and compared to the corresponding image before irradiation ($N_{eff} = 0$) at the same magnification.

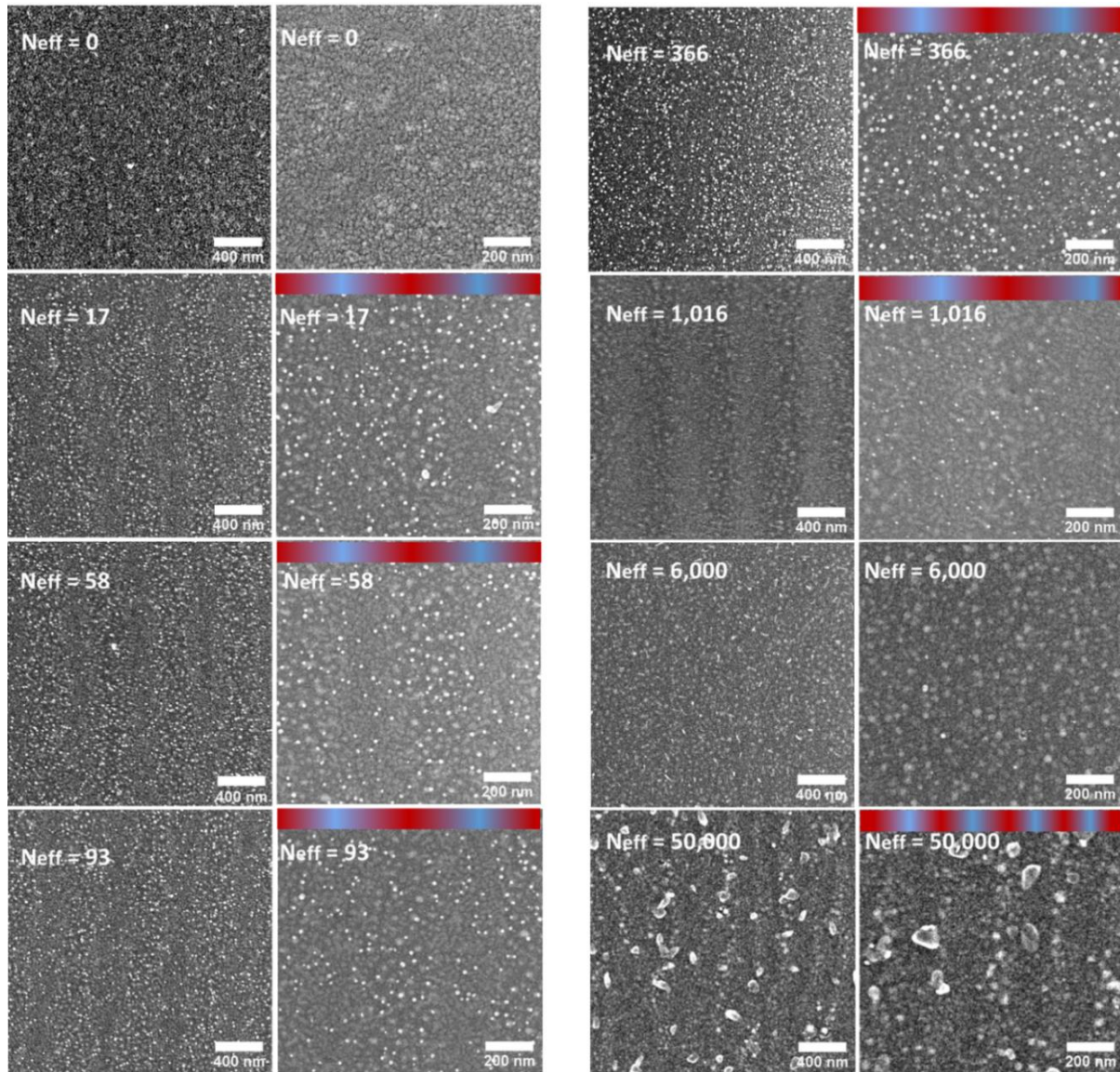


Figure 3.14 – SEM characterization II. SEM images of the center of lines written with the fs laser at different scan speeds, corresponding to the indicated effective numbers of pulses N_{eff} . For each pulse number, the left frame corresponds to 60,000x magnification and the right one to 120,000x magnification. The red and blue colors are a guide for the eyes to aid identifying the grating structures.

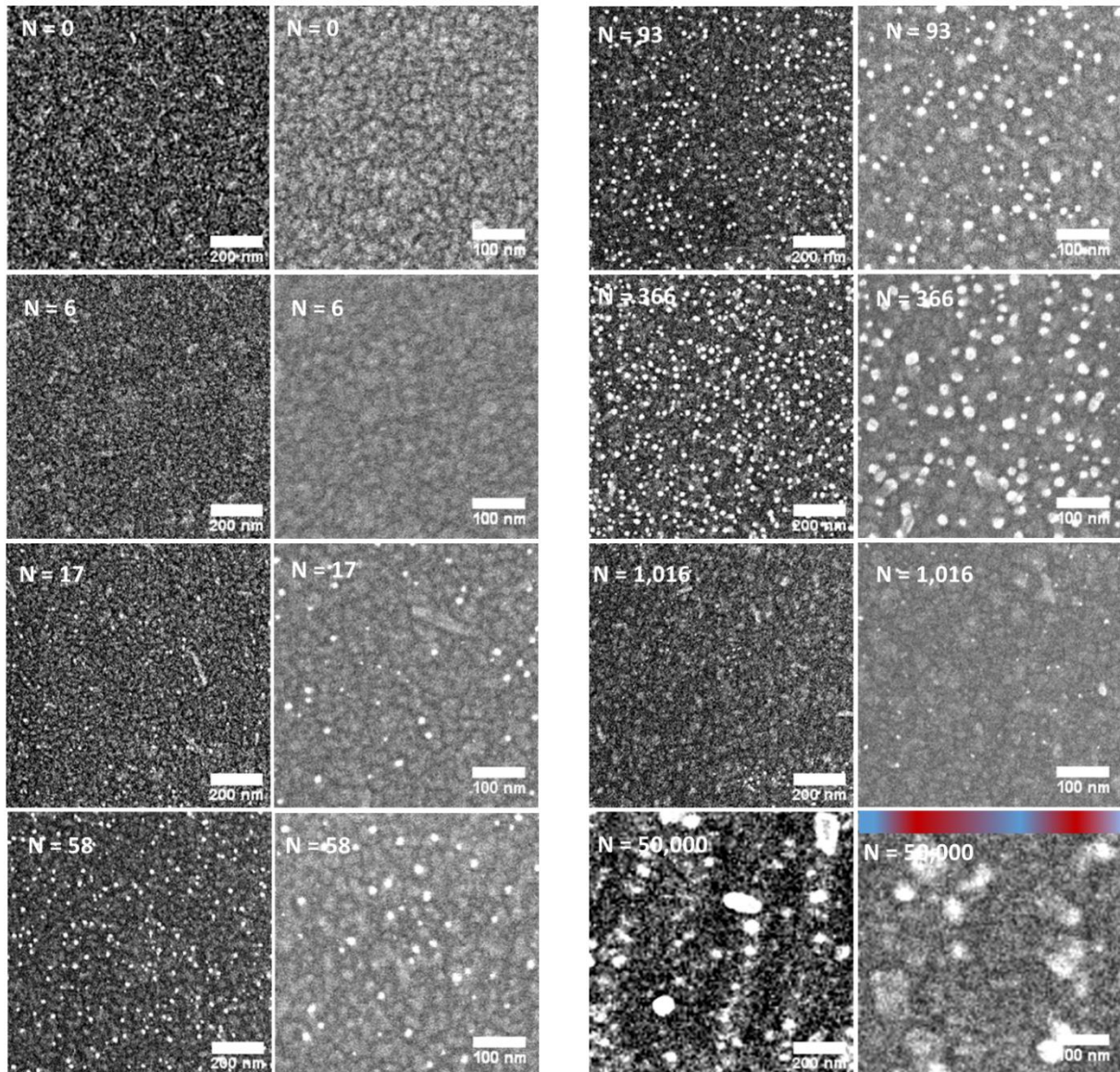


Figure 3.15 – SEM characterization III. SEM images of laser spots marked at different pulse numbers N . In each case, the left image corresponds to 60000x magnification and the right one to 120000x magnification. The red and blue colors are a guide for the eyes to identify the gratings structure.

The SEM characterizations evidence the migration of Ag towards the surface after $N_{eff} = 17$, where it forms small (diameters typically between 7 nm and 30 nm) Ag NPs with rather circular shape. These NPs were not present initially or after $N = 10$ (Figure 3.13), and their density and size slightly increase with pulse number, before disappearing at $N_{eff} = 1016$ pulses approximately.

The presence of an embedded self-organized grating can also be observed in the same range of effective pulse numbers ($N_{eff} = 17$ to $N_{eff} = 1016$) in the laser-written lines. The fringes of the

grating are aligned parallel to the fs laser polarization and the grating period is 525 ± 40 nm. One can note that Ag NPs at the top surface of the film seem to concentrate more in the lines, where Ag nanoislands are reshaped into bigger and more spherical NPs. At $N_{eff} = 1016$, all NPs seem to be embedded. At $N_{eff} = 6000$, the grating and all nanoislands have disappeared to make way for larger and more regular NPs. At the very end of the laser exposure, after 50000 pulses, another type of self-organized grating emerges. Its orientation is also parallel to the laser polarization, it is less regular and in some areas its period is 235 ± 20 nm. Some large particles (with diameters in the range of 70 - 130 nm) are visible along the periodic lines and all particles seem to be embedded. The comparison of SEM characterizations of nanostructures produced upon line writing with those of static irradiations confirms their similarity in terms of NP sizes, except for their self-organization, which is found to be more regular in lines.

More accurate information on the NP shape and location is provided by STEM characterizations of four selected samples demonstrated in Figure 3.16. HAADF-STEM images of the top and cross-sectional views combined with EDS chemical maps give a deeper insight into the material transformations.

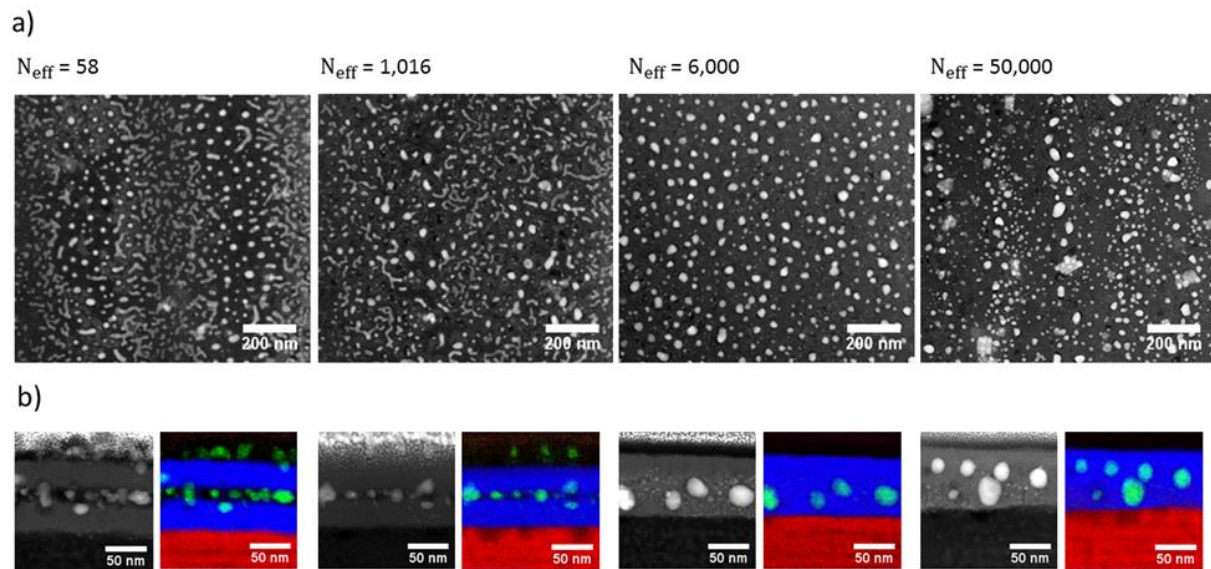


Figure 3.16 – STEM characterizations of the center of laser-written lines for $N_{eff} = 58$, 1016, 6000, and 50000. (a) Plan-view HAADF-STEM images and (b) HAADF-STEM images of the corresponding cross-sections and EDS chemical mappings indicating Ag (green), Ti (blue), and Si (red).

At $N_{eff} = 58$, the self-organized grating clearly originates from the localized reshaping of the initial Ag nanoislands into more spherical Ag NPs within periodically spaced fringes. This figure also demonstrates that Ag nanoislands remaining in the other half-periods have begun to coalesce, leading to wider spaced smaller nanoislands with worm-like shape. The cross-sectional chemical maps reveal Ag NPs sandwiched between two TiO_2 thin films, together with

Ag NPs located on top of the TiO₂ surface. At $N_{eff} = 1016$, the NP shapes and locations are very similar to the previous ones, except that overall the Ag NPs appear larger, the fringes seem less regular and begin to merge, and the distance between the two TiO₂ films is smaller. At $N_{eff} = 6000$, the fringes have merged completely yielding a homogeneous distribution of large NPs, with small ones in between. The exact shape properties of this sample is investigated using image processing routines. The center of the NPs are detected, and ellipses are fitted to the contours of each with the free variables of the minor and major axes, and the orientation of the major axis, *i.e.*, its angle compared to the laser polarization. The histograms of the NP aspect ratio and the angle of the major axis are demonstrated in Figure 3.17.

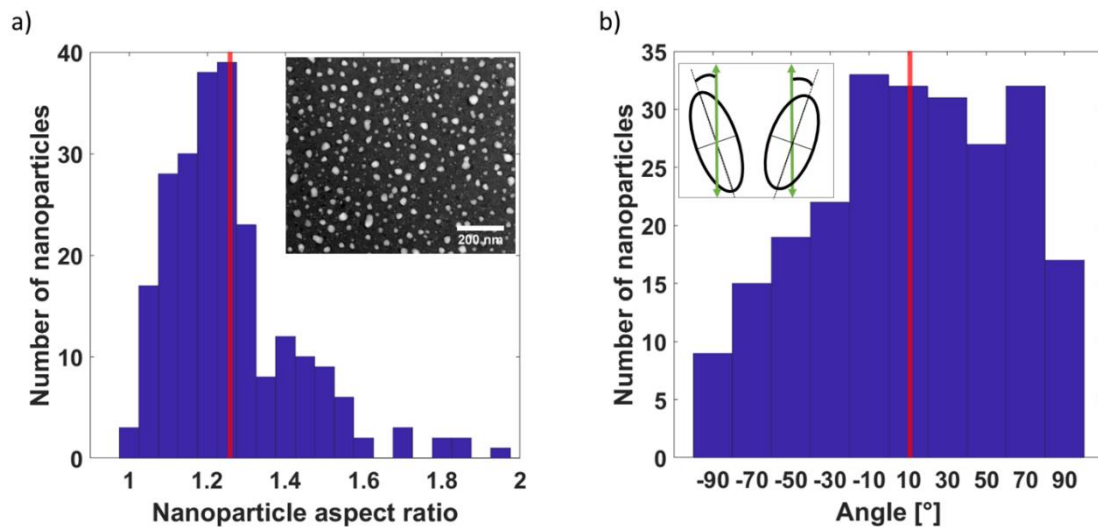


Figure 3.17 – Structural investigation of the sample marked with $N_{eff} = 6,000$ pulses. a) Histogram of the NP aspect ratio, defined by the ratio of the major to the minor axes of the fitted ellipses. The red vertical line indicates the mean value: 1.28. The inset shows the STEM image of the center of the laser-written line. b) Histogram of the angle distribution, which is defined between the direction of the laser polarization (shown by the green double arrows in the inset image) and the principal axis of an elliptical NP. The average value is indicated by the red vertical line: 10.9°. The inset demonstrates the angle sign convention; left image: positive angle, right image: negative angle.

The NPs have a prolate shape with an average aspect ratio of 1.28, whose longer axis lies along the polarization of the fs laser pulses. The average value of the major axes is determined as 10.9°. Based on the cross-section images, the two TiO₂ films have merged into a single one, and all NPs are embedded.

At $N_{eff} = 50000$, the small-period NP grating can be appreciated in the top view image. It seems to originate from a modulation of the NP density in the direction perpendicular to the long period fringes. Compared to the case of $N_{eff} = 6000$, the cross-section is very similar but the NP

size distribution is more heterogeneous. It is worth noting that no modulation of the upper TiO₂ layer topography is observed, whatever the pulse number is.

A short summary of the results from all the electron microscopic investigations of the laser-irradiated sample is provided as follows. At low number of pulses ($N \leq 10$), the images revealed a decrease of the Ag filling factor from 70% to 47%. After a few tens a pulses, self-organized grating formed that was aligned parallel to the fs laser polarization, and the grating period was 525 ± 40 nm. The cross-sectional chemical maps revealed Ag NPs sandwiched between two TiO₂ thin films, together with Ag NPs located on top of the TiO₂ surface. At $N_{eff} = 1016$, the NP shapes and locations were very similar to the previous ones, except that the fringes seemed less regular, and the distance between the two TiO₂ films was smaller. At $N_{eff} = 6000$, the fringes merged completely yielding a homogeneous distribution of large NPs possessing prolate shapes with an average aspect ratio of 1.28, whose longer axis lied along the polarization of the fs laser pulses. The multilayer system merged into a single one, with all NPs embedded. At $N_{eff} = 50000$, the small-period NP grating reformed, its orientation was also parallel to the laser polarization, and its period was 235 ± 20 nm.

3.4.6 Comparison of *in situ* thermal annealing to laser-induced heating

In the previous section, the morphological transformations of nanoislands ensemble upon laser-induced heating were revealed. In order to establish a link between the structural observations and the spatial temperature profile, *in situ* thermal annealing experiments are conducted in TEM, and the evolution of the nanoisland morphology is compared to the laser-heated sample. In these experiments, similar Ag/TiO₂ multilayer sample with Ag thickness of 5 nm and TiO₂ thicknesses of 20 nm is directly deposited on a TEM grid, and *in situ* heated gradually in the range 100 – 1000 °C in an image-corrected FEI Titan ETEM G2 transmission electron microscope. The structural evolution of the nanoislands is monitored using “Z-contrast” annular dark-field (ADF) imaging conditions in scanning transmission electron microscopy mode, at 300 kV, and under high vacuum conditions ($\sim 10^{-6}$ mbar). A slow ramping time of 5 minutes is used. A sequence of plan-view STEM-ADF images of the nanoislands at different annealing temperatures is shown in Figure 3.18, accompanied by the sample at room temperature for comparison.

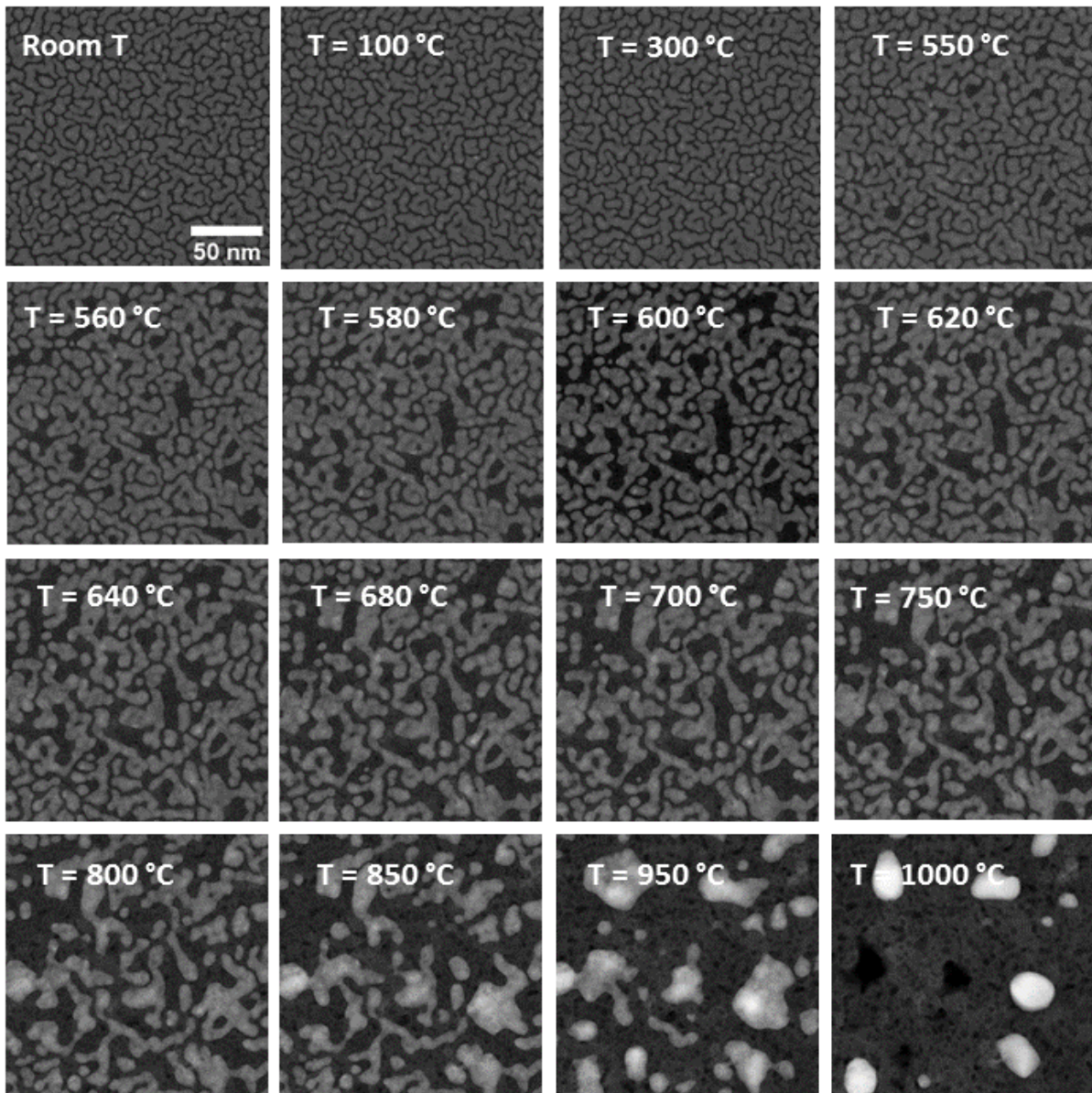


Figure 3.18 – The effect of the *in situ* thermal annealing in TEM to the nanoisland morphology.

There are two major effects of the high-temperature treatment to the nanoislands morphology. In the first place, dark areas appear in the STEM-ADF images from 550 °C, suggesting that the average interparticle distance increases towards higher temperatures. Additionally, nanoisland edges progressively get rounded to reach nearly circular shapes at high temperatures. In the final state at 1000 °C, mostly large spherical NPs are observed. These observations already enable to draw the first conclusion about the temperature profile in the STEM images of the laser-heated samples shown in Figure 3.16. In the spatial regions of spherical particles in the sample marked with $N_{eff} = 58$, the temperature rise is supposed to be higher than in the regions

containing nanoislands with decreased size and interparticle distance. The threshold for reshaping into spherical particles is reached at least for a short time after the pulse excitations in those regions. Additionally, the temperature threshold in the sample marked with $N_{eff} = 6000$ is homogeneously reached everywhere, which can be attributed to the heat accumulation upon the high-repetition-rate laser irradiation.

In order to quantitatively investigate the evolution of the morphology with the temperature, the Ag filling factor and the number of nanoislands are determined in each image using image processing routines. The evolution of these two quantities is shown in Figure 3.19. The number of nanoislands evolves on characteristic temperature regions, the end of each region is labeled by letters A-C.

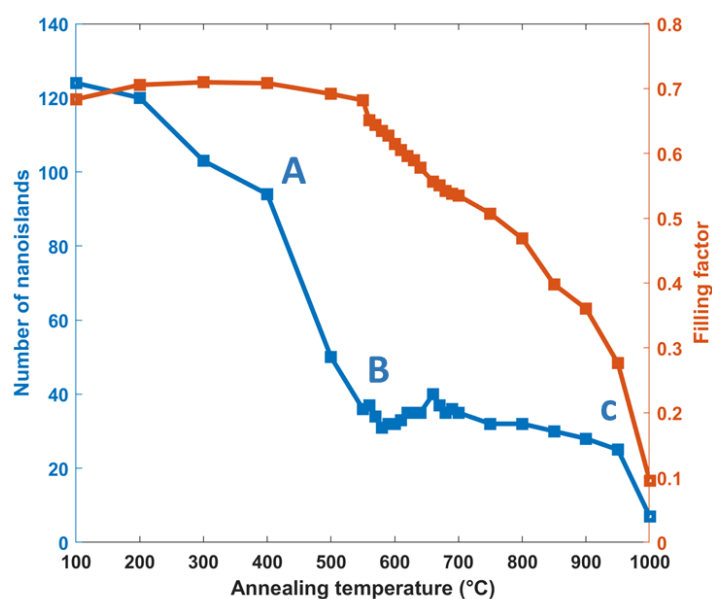


Figure 3.19 – Investigations of the temperature-dependent NP morphology. Evolution of the number of nanoislands and Ag filling factor determined in the TEM images in Figure 3.18. Letters A-C indicate the onset of different mechanisms described in the text.

The number of nanoislands gradually decreases until 400 °C (A), from which point on a faster decrease is observed until 580 °C (B). Then, a nearly constant evolution with slight decreasing tendency is observed up to 950 °C (C), where the onset of another fast decreasing tendency follows up to 1000 °C (D). The Ag filling factor exhibits two distinct temperature regions. It remains constant until ~ 580 °C, a temperature above which a gradual decreasing is observed.

The description of the mechanisms driving the coalescence process provided in section 1.4.2 in chapter 1 can be adapted to interpret these regions. Until point A in Figure 3.19, the nanoisland number decreases due to the neck formation between adjacent nanoislands via the mechanism of grain-boundary diffusion. The onset of the more rapid decrease at point A can be explained

by the intermediate transition mechanism resulting in faster neck formation via the activation of viscous flow. The filling factor remains rather constant, because of the small contribution of the forming connections between the nanoislands. From point B, the filling factor starts decreasing due to the strong nanoisland reshaping via the spherification process driven by the curvature-induced surface diffusion. Between B and C, the number of nanoislands is rather constant with slight decreasing tendency, because of the increasing average interparticle distances during the spherification process. Around point C, the melting and merging of the remaining small NPs, and possible vaporization result in the further decreasing number and filling factor.

It is important to emphasize that the NP sizes and shapes are rather heterogeneous in our sample. The comparison with the MD simulations in section 1.4.2 in chapter 1 provides important information about the NP coalescence in our sample, but additional factors might be important to consider, *e.g.* possible changes in the solid-liquid interfacial energy due to curvature effects [154], and the presence of the TiO₂ matrix (Ag encapsulation). To further evaluate the mechanism of coalescence in similar samples to the present one, MD simulations with more complex NP shapes would be needed. Additionally, it is important to mention that in our laser-treated sample, the different processes possibly occur at a lower temperature than in the *in situ* annealing experiment due to the different pressure.

3.5 Discussion

The multipulse evolution of the polarized transmission spectrum of the sample and the obtained information about the morphology and distribution of NPs for a few selected pulse numbers shed light on the different mechanisms that successively play a role in the laser-induced transformations and self-organization of Ag nanoislands. The following discussion first focuses on the laser-induced physical chemical mechanisms at the origin of the morphological changes in the film. In the second part, the optical phenomena involved in the occurrence of self-organized periodic nanopatterns are discussed.

3.5.1 Morphological transformations

Since TiO₂ does not absorb the incident pump laser wavelength (515 nm), the fs laser-induced mechanisms are triggered by the absorption of light by Ag nanoislands through their LSPR,

which transfers photon energy to the electrons. The linear absorption coefficient at the pump wavelength is rather high (initial transmission at 515 nm is approximately 0.69 as shown in Figure 3.9), therefore, linear absorption is expected to dominate. Ultrafast electron–electron scattering gives rise to hot electrons that are not in thermodynamic equilibrium with the Ag lattice [155]. Their ballistic velocity is estimated to be $\approx 10^6$ m/s, and their energy lies in the range between 1 eV and 4 eV [156], [157]. Electrons having high enough energy to overcome the Schottky barrier (>1 eV) at the metal nanoislands/ TiO_2 interface are injected in the conduction band of TiO_2 , leaving behind positively charged ions at the surface of the nanoisland [158], [159]. This plasmon-induced electron transfer has been measured to be faster than 240 fs for Au NPs [58] and is expected to be of the same order of magnitude for Ag nanoislands. The strong repulsive force between neighboring Ag^+ ions can lead to ion ejection, which has been reported as Coulomb explosion in works with ultrafast lasers [160] or as ionic release when continuous wave light is used [161], [162]. The Coulomb explosion occurs typically over a timescale of 1 ps. The ion ejection results in a shrinkage of NPs and seems to be the main mechanism that drives the nanoisland reshaping during the very first pulses, where a shrinkage is observed (Figure 3.13). The latter well explains the pulse-to-pulse decrease of the broad LSPR (flattening of the transmission spectrum) of the initial nanoislands, reported in Figure 3.9. The time-resolved pump-probe experiments also confirm that during the first fs laser pulses, the reshaping mechanism occurs in less than 15 ns after each pulse because the transmission remains constant afterward until the next fs laser pulse.

Hot electrons that do not pass the Schottky barrier relax via electron–phonon coupling, leading to NP thermalization on a timescale of a few picoseconds, according to the literature [10]. The temperature rise in the nanoislands features a peak value that depends on the laser fluence and on the initial temperature of the material. This initial peak temperature is gradually reduced via heat transfer toward the vicinity by two mechanisms: thermal conduction across the NP-surrounding interface and heat diffusion to the surrounding material [10]. The transferred heat energy results in a temperature rise in the thin TiO_2 film usually within less than 10 ns [30]. This temperature rise relaxes over a timescale that depends on the thermal parameters of the system, the fluence, and the laser beam diameter on the film. According to the experiments, the relaxation time appears to be longer than the temporal period between two successive fs laser pulses (13.3 μs), as the effect of pulse accumulation has been observed to depend on the laser repetition rate.

In order to support the above interpretations of the experiments based on the results reported in the literature, simulations of the laser-induced temperature rise in the multilayer system were carried out using a model that is described in section 3.3.1. As Ag nanoislands cover a large part of the intermediate layer, which resembles a near-coalescence metallic film, the model

considers a homogeneous layer with averaged optical and thermal parameters resulting from a mixture of Ag and air. The simulations are carried out for a 15 nm-thick absorbing layer sandwiched between two 30 nm-thick TiO₂ layers. The multilayer is supported by a semi-infinite glass substrate, illuminated at 515 nm wavelength, with 190 fs long light pulses at 75 kHz repetition rate. The field intensity is modulated with a 525 nm period of spatial modulation along the x direction to take into account the interference phenomenon, which takes place in the film between the incident wave and a guided wave and which leads to the self-organized structures, as explained in the next subsection. This model does not account for the film transformations pulse after pulse, but it helps to estimate the time during which thermal modulation induced by light modulation sustains in the film after each pulse and the effect of thermal accumulation in this multipulse process.

The optical and thermal coefficient of each medium are assumed to be constant over the temperature rise and are chosen as follows. $n_{TiO_2} = 2.43$ [163], $a_{TiO_2} = 8.47 \cdot 10^{-7} \text{ m}^2/\text{s}$ [164], $b_{TiO_2} = 2.5 \text{ W/m/K}$ [164], $n_{glass} = 1.52$ [165], $a_{glass} = 0.62 \cdot 10^{-6} \text{ m}^2/\text{s}$ [165] and $b_{glass} = 1.14 \text{ W/m/K}$ [165]. The refractive index of the absorbing layer is calculated using the Maxwell Garnett equation,

$$n = n_{air} \sqrt{\frac{n(Air)^2 + \frac{(1+2\eta)(n_{Ag}^2 - n_{air}^2)}{3}}{n(Air)^2 + \frac{(1-\eta)(n_{Ag}^2 - n_{air}^2)}{3}}}, \text{ with } n_{Ag} = 0.05 + j * 3.2695 \text{ [166]}, n_{air} = 1; \text{ and } \eta$$

the filling factor of Ag equals 0.7 obtained based on the SEM image of the initial sample, leading to $n = 6.9498 + j * 0.5575$. While the thermal coefficients of this layer is defined as the following weighted averages: $a = 0.7 a_{Ag} + 0.3 a_{air}$ with $a_{Ag} = 173 \cdot 10^{-6} \text{ m}^2/\text{s}$ [165] and $a_{air} = 20.5 \cdot 10^{-6} \text{ m}^2/\text{s}$ [167], leading to $a = 127.3 \cdot 10^{-6} \text{ m}^2/\text{s}$ for the diffusivity; $b = 0.7 b_{Ag} + 0.3 b_{air}$ with $b_{Ag} = 427 \text{ W/m/K}$ [165] and $b_{air} = 0.025 \text{ W/m/K}$ [167], leading to $b = 298.9 \text{ W/m/K}$ for the conductivity.

The transmission coefficient considered for the simulations is very close to the one of the initial film at 515 nm, *i.e.*, 69%. According to Figure 3.9, after few hundreds pulses, the transmission coefficient of the film at the pump laser wavelength decreases below this value, and the film absorbs more incident photons. It is thus reasonable to consider that the following simulated temperature rise underestimates the real temperature rise in the film. However, the simulation results shown hereafter are consistent with changes observed in the sample.

Figure 3.20a illustrates the time variations of the temperature simulated at four points of the multilayer located either in the middle of the Ag layer or at the TiO₂/glass interface at two locations, where the intensity in the film is assumed to be either maximum or minimum (as

described in in section 3.3.1, a 10% contrast of the interference signal is used for these simulations).

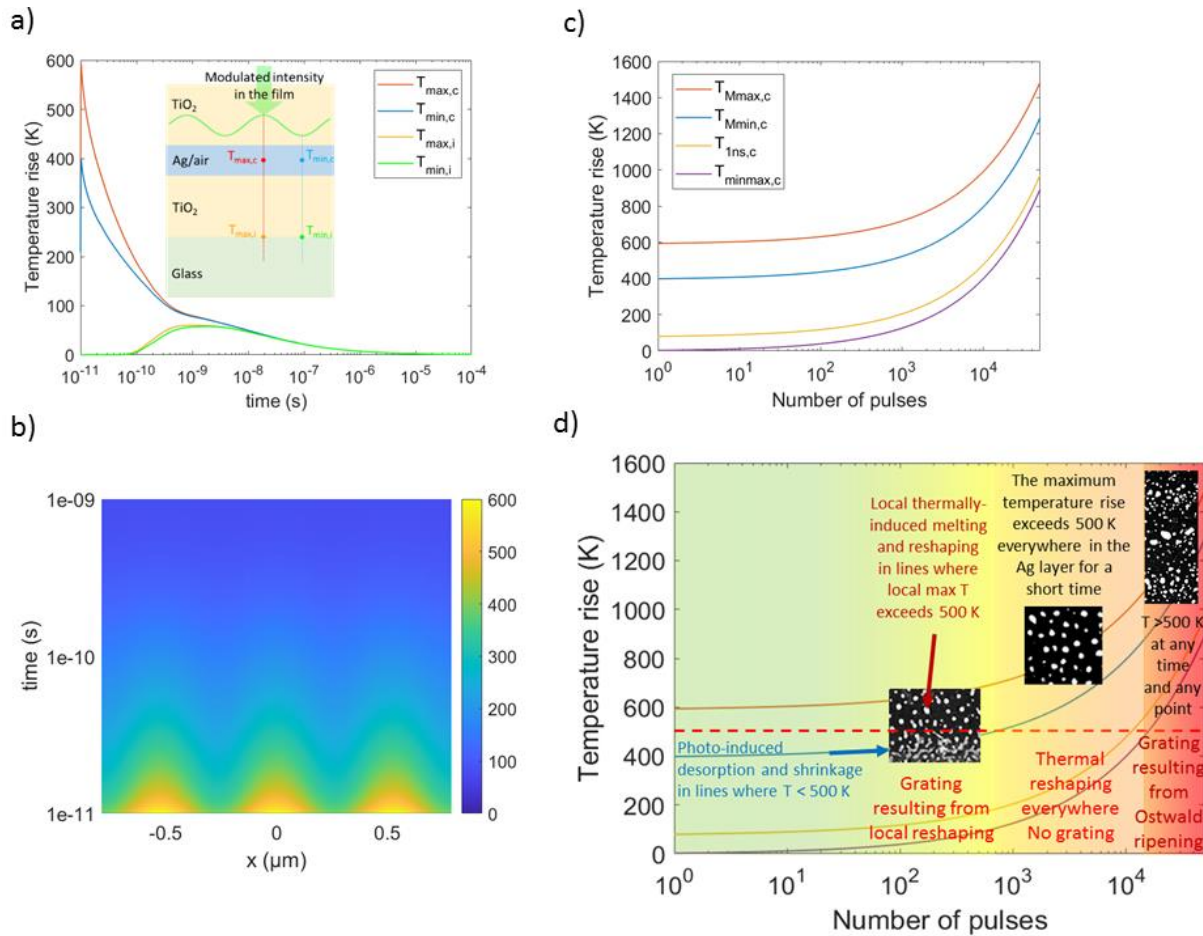


Figure 3.20 – Simulation of the temperature rise at different positions and times in the multilayer system. (a) Time variations of the temperature increase simulated after the first fs laser pulse in the middle of the Ag/air layer where the modulated intensity is maximum ($T_{max,c}$) or minimum ($T_{min,c}$) and at the TiO₂/glass interface, where the intensity is maximum, ($T_{max,i}$) or minimum, ($T_{min,i}$). The sketch in the inset shows the location of the four points in the multilayer system. (b) 2D colormap of the temperature in the middle of the Ag/air layer as a function of time and space along the direction of modulation of intensity. (c) Pulse-to-pulse evolution of the maximum values of $T_{max,c}$ and $T_{min,c}$ (curves $T_{Mmax,c}$ and $T_{Mmin,c}$), the temperature rise in the middle of the film after 1 ns when $T_{max,c}$ already equals to $T_{min,c}$ (curve $T_{1ns,c}$), and the minimum value of $T_{max,c} = T_{min,c}$ just before the next pulse (curve $T_{minmax,c}$). A laser repetition rate of 75 kHz is assumed in the calculations, as used in the experiments. (d) Synthetic diagram of the main physical–chemical mechanisms driving the NP reshaping pulse after pulse.

The temperature increases very rapidly in the absorbing Ag layer, it reaches a maximum at the TiO₂/glass interface located 30 nm away from the Ag/TiO₂ interface after about 10 ns, which is consistent with the literature [161]. The maximum temperature reached at the bottom interface is much lower than the maximum temperature reached in the Ag layer, and the temperature

gradient induced by the intensity modulation in the Ag layer does not exist at the bottom interface. The simulations after the first fs laser pulse (Figure 3.20a and b) show that the temperature rise in the absorbing layer varies between 400 K and 600 K over one period of the interference pattern. However, the temperature modulation in this layer vanishes after about 1 ns, when the maximum and minimum temperatures converge to a temperature rise below 100 K. This confirms that the time for atoms to move due to thermal energy is short during the first pump laser pulses. This is consistent with the time-resolved measurements, which do not detect any change in the material between 15 ns and the next pulse.

According to the periodic shape distribution of nanoislands observed in Figure 3.16 after $N = 58$ laser pulses, the fringes showing a shrinkage of nanoislands must correspond to the regions where the temperature lies below the melting point of Ag, whereas it lies above in the regions where the nanoislands coalesce and reshape to form larger and more regular NPs. The melting temperature of Ag is known to depend on the radius of curvature of NPs [168], [169]. Around 1000–1200 K (depending on the NP shape) for radii larger than 7 nm, the melting temperature can decrease down to less than 500 K for radii smaller than 2 nm.

In this sample, the nanoislands are rather large but flat and heterogeneous in shape, which may locally lead to very small radii of curvature. By comparing the experimental results (Figure 3.16) with the simulated temperature rise (Figure 3.20), it can be inferred that the range of temperature rises required for Ag NP reshaping is between 400 K and 600 K in the sample. For the next demonstration, it is estimated to be around 500 K. During the first tens of pulses, the maximum temperature rise in the middle of the Ag layer does not evolve significantly, and the time during which the temperature rise lies above 500 K after each pulse is less than 20 ps. The very short time may explain the fact that only fs laser-induced atomic desorption occurs during the first fs laser pulses, leading to a slight shrinkage of all NPs [142]. Thermal reshaping due to $T_{Mmax,c} > 500$ K is only observed after few tens of pulses in localized periodic patterns. After almost 1000 pulses, $T_{Mmin,c}$, the maximum temperature rise in the low-intensity fringes in the middle of the Ag layer also exceeds the melting temperature of Ag for a very short time. This means that thermally induced reshaping can start almost everywhere in the Ag layer and can lead to less regular grating lines.

The higher temperature in the fringes, where the coalescence occurs before 1000 pulses, also promotes ionic Ag diffusion [170], [171], and can explain the higher concentration of small Ag NPs on top of the TiO₂ surface in these regions, as observed in Figure 3.14 and Figure 3.16. The Ag⁺ ions released by atomic desorption from the nanoislands [142] exhibit large diffusion coefficient and mobility, which increase by orders of magnitude at high temperatures [172]. Following the chemical potential gradient in the material, Ag tends to migrate toward the air/

film interface up to few hundreds fs pulses. During the first tens of pump pulses, the nanoisland shrinkage tends to decrease their initial absorption in the infrared, and the growth of very small particles (<10 nm) on the top surface contributes to increase the absorption at low wavelength (<460 nm), as predicted by Mie theory [173]. These mechanisms lead to a flattening of the transmission spectrum with a relatively high average transmission, as observed in Figure 3.9.

Upon further increase in pulse number, the coalescence and reshaping of nanoislands into larger NPs is likely to cause an increase in the absorption observed. Previous studies investigating NP coalescence discussed that the particle–substrate adhesion might have an important role in the characteristic timescale for the coalescence process. The interaction between the atoms of the metallic NPs and the substrate can be described by Lennard–Jones type potential [52]. Taking into account the moderate adhesion, the molecular dynamic simulations revealed that reduced particle–substrate interaction results in faster coalescence dynamics [52]. The substrate thermal properties also have a significant impact on the coalescence/sintering process via heat loss through heat conduction to the substrate. In general, higher thermal conductivity for the substrate results in the need for higher processing laser intensity. This was demonstrated by the numerical comparison of sintering dynamics of Ag NPs on boron-doped silicon wafer and glass [138]. The results revealed that considerably longer time is needed to reach the sintering temperature (about 6.5 times longer) on silicon wafer due to its high thermal conductivity (90.76 W/m/K). Owing to the low thermal conductivity of TiO₂ (2.5 W/m/K) in this study, the sintering/coalescence of NPs is triggered efficiently and finishes in less than ~15 ns, as confirmed by the time-resolved measurements. Additionally, it is important to note that the non-wettability of the Ag/TiO₂ interface related to the roughness of TiO₂ and the cohesion between the Ag atoms being larger than the adhesion between Ag and TiO₂ further promote efficient merging process of the melted NPs.

Starting at about 6000 fs pulses, the periodic nanopatterns disappear, and larger and regular NPs are being formed over the whole film rather homogeneously. Figure 3.20c and d show that after few thousand pulses, $T_{Mmin,c}$ largely exceeds 500 K, which explains why the NP shape homogenizes everywhere in the film. The high temperature and the thermal diffusion toward the substrate trigger another atomic diffusion mechanism involving the substrate. High temperatures at the substrate/film interface promotes Na⁺ diffusion toward the film and reverse diffusion of Ag⁺ from the top surface toward the substrate [172]–[174]. EDS chemical maps for $N_{eff} = 6000$ indicate the presence of Na within the TiO₂ layer, demonstrated in Figure 3.21. At this stage, Ag NPs are concentrated within the TiO₂ film that has merged into a single layer.

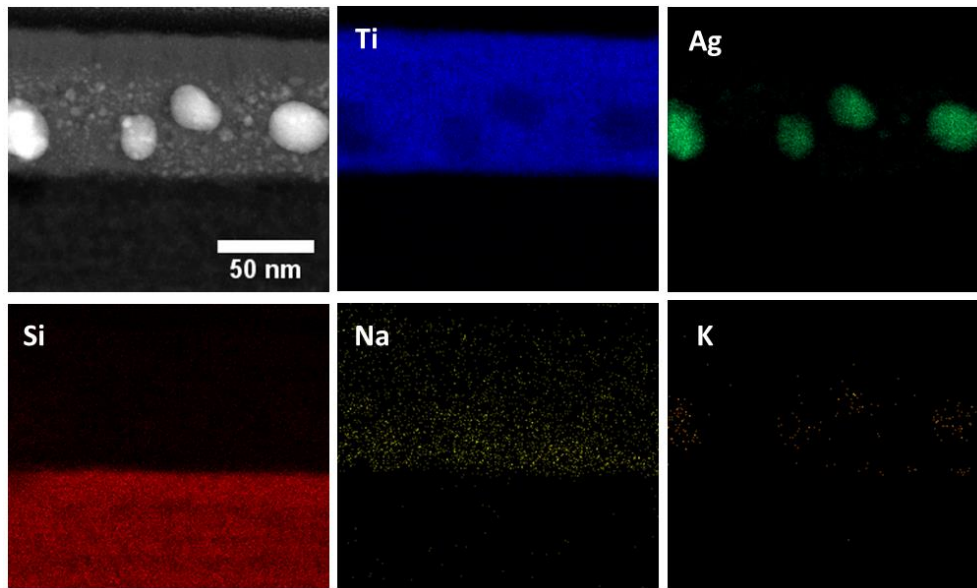


Figure 3.21 – STEM cross-section image and individual EDS chemical maps of the laser line written with $N_{eff} = 6,000$ pulses.

After about 20000 pulses, $T_{minmax,c}$ also exceeds 500 K (Figure 3.20), meaning that the temperature rise never decreases below the melting point of Ag between two successive fs laser pulses. This allows the emergence of another periodic pattern in the Ag layer (Figure 3.16). Lateral gradients of light intensity can govern the physical-chemical mechanisms. In such a configuration, ionization and Ag^+ ion ejection can be invoked, but mostly in the fringes of maximum light intensity. Ag ionic diffusion toward areas where less Ag^+ ions are released (lower intensity fringes) can occur. Similarly to the Ostwald ripening mechanism and following the Fick's laws [175], [176] smaller Ag NPs present in the high intensity regions begin to disappear. This process also feeds Ag NPs present in the low intensity regions, which eventually leads to the grating observed after 50000 fs pulses. Due to the weak in-plane thermal gradient, the grating forming process is not efficient and requires such a high pulse number.

3.5.2 Optical origin of self-organized reshaping

In this section, we consider the optical mechanisms that occur at the same time as the physical-chemical mechanisms, and which lead to modulate the incident light intensity in the multilayer. The multilayer acts as a waveguide, and the effective index of its guided modes can be calculated by searching the complex poles of the reflection coefficient of the system, as described in references [147], [150] and section 3.3.2. The field of the guided mode can be described as:

$$E(x, z) = A(z) \exp(j\beta x) = A(z) \exp(j\beta' x) \exp(-\beta'' x), \quad (3.14)$$

where $\beta = \beta' + j\beta''$ is the complex propagation constant, $\beta' = \frac{2\pi}{\lambda} \text{Re}(n_e)$, with $\text{Re}(n_e)$ the real part of the effective index, and $2\beta''$ the attenuation coefficient. Here, two effective indices are successively estimated by considering the opto-geometrical parameters given by STEM characterizations after 58 and 50000 pulses, which are the stages where the two gratings are observed, respectively. The following parameters are deduced from the analysis of STEM images of Figure 3.16. After 58 pulses, the simulated system is composed of three layers, $\text{TiO}_2/\text{Ag}/\text{Air}/\text{TiO}_2$, whose thicknesses are 30 nm / 15 nm / 30 nm. The Ag filling factor in the middle mixed layer is $\eta = 25 \pm 7 \%$. After 50000 pulses, the simulated system is composed of a single layer, Ag/TiO_2 , whose thickness is 70 nm. In this single layer, the Ag filling factors of $\eta = 8 \pm 2 \%$ and $\eta = 4 \pm 1 \%$ were used. As the two TiO_2 layers have merged into a single one whose thickness is 10 nm larger than the sum of the two initial TiO_2 layers, the layer may be less dense than the initial layers and its refractive index lower than $n_{\text{TiO}_2} = 2.43$.

After 58 pulses, the inverse of the reflection coefficient of the structure exhibits a sharp and pronounced minimum value for a complex propagation constant equal to $\beta = \frac{2\pi}{\lambda} (1.750 + j 7.430 * 10^{-4})$ as demonstrated in Figure 3.22, a.1. The distribution of the modal intensity along the z direction (Figure 3.22, a.2) for this propagation constant confirms the presence of a fundamental mode with a maximum intensity located in the TiO_2 bottom layer, few nanometers from the Ag interface.

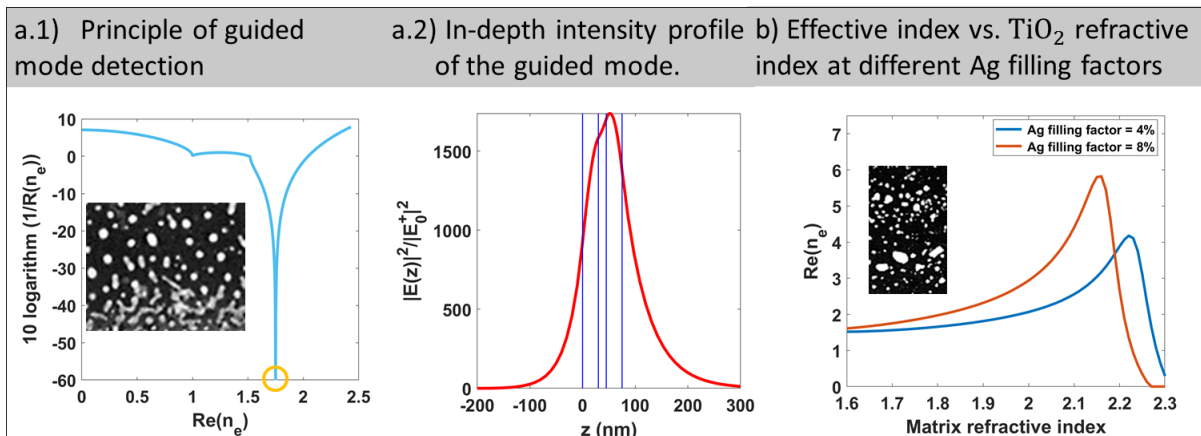


Figure 3.22 – Quantitative investigations of the self-organized phenomena. (a.1) Inverse of the reflection factor after $N_{\text{eff}} = 58$ (inset from Figure 3.16). It exhibits a minimum for a particular real part of the effective index of the structure. The parameters of the latter are defined from the HAADF-STEM characterizations. The presence of a minimum means that a mode with the corresponding effective index (highlighted by the yellow circle) can be guided in the structure. (a.2) Intensity profile of the corresponding guided mode as a function of the depth inside the multilayer stack. Blue vertical lines indicate

the interfaces of the sample with $z = 0$ nm being the air/TiO₂ interface. (b) After 50,000 pulses (inset, same as in Figure 3.16), Ag NPs progressively diffuse in the TiO₂ whose layers merge in a single layer. Calculation of the effective index of the guided mode for two volume fractions of Ag NPs in a single layer whose refractive index is varied to show the presence of a resonance at the pump wavelength λ when the NPs diffuse from a low-index medium to a high-index one.

As described in the first chapter, assuming the excitation of guided mode, by means of scattering on the metallic nanoislands in the direction perpendicular to the TE incident polarization, its interference with the incident wave impinging under incidence angle $\theta_i = 45^\circ$ gives rise to intensity modulations in the film along the direction perpendicular to the incident polarization. The spatial period of the interference pattern can be expressed with Eq. (1.18). During static exposures, both forward and backward modes can be excited equally, leading to two different periods that superimpose. This is probably the reason for the weaker self-organized nanopatterns observed in static exposure (Figure 3.15). Writing lines by moving the sample favors the mode excited in the forward direction, *i.e.*, the translation direction, and leads to a well-defined period. In the experiments, all lines are written in the forward direction and should lead, when using $\text{Re}(n_e) = 1.75$ to a grating period of 494 nm. This period matches well the grating period, 525 ± 40 nm, measured in the lines written at $N_{\text{eff}} < 6000$.

At 50000 pulses, the three initial layers have merged and Ag NPs are embedded in a single TiO₂ layer whose thickness is slightly larger than the sum of the two initial TiO₂ layers. Consequently, the TiO₂ layer may be expected to be less dense than the initial layers and its refractive index lower than the one considered up to now for this material ($n_{\text{TiO}_2} = 2.54$). The filling factor of Ag inside the TiO₂ is also less easy to estimate since the NPs are not aligned in the same plane but distributed in a 70 nm thick layer. For these reasons, we consider the variations of the real part of the mode effective index with the matrix refractive index for two Ag filling factor. Figure 3.22b shows that the real part of the mode effective index encounters a maximum when the matrix refractive index varies around 2.2-2.3. The latter is due to the LSPR of Ag NPs, which reaches the femtosecond laser wavelength when the matrix refractive index increases to a value larger than 2 (merging of the two TiO₂ layers). According to Figure 3.22b, it appears reasonable that the real part of the mode effective index can reach the value of 2.89, which leads, according to Eq. (1.18), to the period of 235 ± 20 nm observed experimentally. The main reason for explaining the smaller period of the grating pattern that forms after a long exposure time is therefore the merging of the two layers, which results from a temperature rise that exceeds the melting temperature of Ag at any time between the fs laser pulses.

Few remarks can be added to better describe the modes supported by the structure. For matrix refractive index values varying from 2.16 to 2.30, two guided modes are supported by the structure. In our calculations and in Figure 3.22b, only the fundamental mode having a single maximum in its depth intensity profile was considered. The first-order mode exhibits two maxima located near the interfaces. The variation in the real part of the fundamental and first-order guided modes effective indices with the matrix refractive index for two Ag filling factors is reported in Figure 3.23.

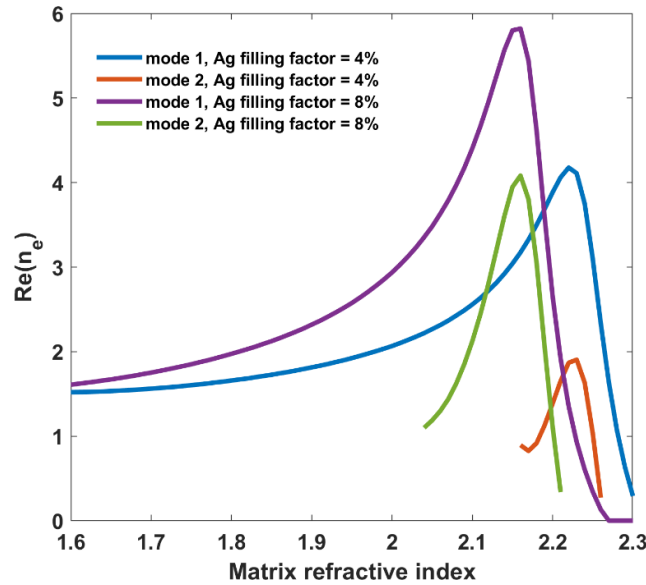


Figure 3.23 – The variation of the real part of the fundamental (mode 1) and first order (mode 2) guided modes’ effective indices with the matrix refractive index for two Ag filling factors in the sample marked by $N = 50,000$ pulses.

The formation of self-organized structures for $N_{eff} > 17$ is certainly at the origin of the polarization-dependent transmission spectrum of the sample observed in Figure 3.9 up to about $N = 1016$, which leads to a blue-shifted resonance for the TE polarization compared to the TM one. While the grating structure vanishes at higher effective pulse numbers, the dichroism is reinforced. At $N_{eff} = 6000$, the NPs grow in size and transform into prolate spheroids aligned along the linear laser polarization, as demonstrated in Figure 3.17. Correspondingly, two LSPR bands emerge in the transmission spectra (Figure 3.9), which correspond to the major and the minor axes of the spheroid. Such a shape anisotropy upon fs laser irradiation has also been reported in works of Stalmashonak *et al.* [142], [177]. Upon further increasing the pulse number, the evolving grating features a sharpening and slight redshift of both resonances, a process that continues up to 50000 pulses.

3.6 Conclusion

By combining *in situ* and *ex situ* characterizations with simulations of the temperature rise and guided-mode effective indices in the multilayer, our results unveiled different mechanisms that successively drive the reshaping and self-organization of Ag NPs embedded between two TiO₂ layers. The description of the mechanisms at different pulse number regimes is provided as follows.

During the very first fs laser pulses, photo-oxidation and atomic desorption mechanisms shrink the NPs. Between about 10 and 1000 pulses, self-organized gratings forms, resulting from essentially two mechanisms. First, the presence of a spatially modulated intensity distribution due to the interference of the incident wave with the forward-guided mode excited by scattering on the NPs. Second, a resulting transient spatial temperature modulation in the Ag layer, whose maximum exceeds the melting temperature of Ag, while the minimum stays below, leading to local reshaping and coalescence of Ag NPs within sub-micrometric periodic fringes.

After a few thousands of pulses, the temperature modulation in the film transiently exceeds the melting temperature of Ag everywhere, including where it is minimum, leading to a homogeneous spatial distribution of larger ellipsoidal NPs. Anisotropic NP shapes arise from the interaction with the strong electric field of the ultrashort laser pulses and the limited time of the temperature increase.

After tens of thousands of pulses, the temperature rise is permanently higher than the melting temperature of Ag. The Ag NPs disperse in the TiO₂ layers that merge, and their LSPR approaches the pump laser wavelength. The increased effective refractive index of the guided mode results in the emergence of an interference pattern with smaller period. The high temperature at any time and everywhere in the film then promotes Ostwald ripening mechanisms that very slowly form low-period gratings, where Ag NPs grow in the low-intensity lines, and shrink in the high-intensity lines.

As a conclusion of the chapter, following the pulse-to-pulse evolution of plasmonic materials appears as a powerful strategy to unravel the complex material transformation pathways, thus providing key information for process optimization, *e.g.* in identifying specific dichroic and spectral properties. Important investigations of the ultrafast dynamics of the NP reshaping was not possible to conduct due to the temporal resolution of the setup being limited to 15 ns. To overcome this limitation, the setup was subsequently improved by installing a mechanical delay line. The results obtained by the updated setup are detailed in the next chapter of the thesis.

4 Ultrafast dynamics of plasmonic NP shape transformations

In the previous chapter, the multipulse shape transformation of Ag NP ensemble encapsulated between two titania layers under fs laser irradiation was investigated in details. The time-resolved pump-probe experiments performed on the ns - μ s timescale evidenced that all the relaxation dynamics finishes in shorter timescales independently from the pulse number. The present chapter can be regarded as a continuation of the previous chapter aiming to explore the ultrafast timescales of the material shape transformation in the multipulse regime. Similarly to the complex evolution of the optical response of the material probed at a fixed delay (15 ns in the previous chapter) at different pulse number regimes, the ultrafast dynamics of the sample response exhibits strong pulse number-dependent features. Here, the ultrafast time-resolved experiments are further extended to investigations above the single-pulse film ablation threshold and below the reshaping threshold. The latter is performed using commercial transient absorption spectroscopy, whereas the former is supported by dynamical phase measurements using QLSI technique. Furthermore, *ex situ* electron microscopy investigations of the irradiated samples provide direct evidences for ultrafast phenomena dominating the size reduction process in the investigated low pulse number regime, as well as self-organization

4.1 Introduction

Most of the ultrafast time-resolved experiments of fs laser-excited plasmonic NPs are conducted in the weak excitations regime, where NP shape transformation is not triggered by the laser excitation [28], [97], [178], [179]. The literature of the time-resolved ultrafast NP reshaping is rather limited. In the followings, the relevant studies are summarized.

Warth *et al.* investigated the ultrafast dynamics of fs laser-induced reshaping of initially spherical Ag NPs embedded in glass matrix into uniformly oriented spheroids [12]. The results of that study are summarized as follows. The emission of electrons and Ag^+ ions from the NPs into the glass matrix, and subsequent recombination and diffusion at the NP poles were described as the driving mechanisms behind the reshaping. The temporal dynamics below one ns time delay could be described by the shot-to-shot development of the persisting spectral changes, but its time dependence between two pulses did not exhibit peculiar features. All transient evolutions in connection with the LSPR reached their maxima in a few ps, followed by the indication of electron and ion emission, and e-ph coupling until 20 ps. At longer delays,

during the ph-ph interaction, a much slower decay on the timescale of several hundred picoseconds was detected, which was contributed to heat conduction and the shape transformation processes like recombination and diffusion. The transient absorption spectrum revealed the ultrafast dynamics of the transient LSPR very similar to other experiments conducted in the weak excitation regime, *i.e.*, ultrafast red-shift and broadening of the ground state LSPR. The transient absorption spectrum exhibited plasmon bleaching and photo-induced absorption features.

Another relevant experiment investigated the ultrafast time-resolved fs-laser-induced fragmentation process of Au NPs in aqueous medium [180]. The illustration of the fragmentation process is shown in Figure 4.1, and the description provided by authors is summarized as follows. Following e-e thermalization, Fermi distribution at an elevated electron temperature is established, accompanied by electron emission. Simultaneously, the hot electrons relax via e-ph scattering, and contribute to increasing lattice temperature. In this stage, NP reshaping occurs as a result of surface melting. A further increase in the lattice temperature to the melting point results in phase transformation from solid to liquid, reducing the surface tension (surface energy) of Au NPs. When the critical charge of a liquid Au NP exceeds the Rayleigh instability threshold (Coulomb energy > surface energy) [181], the liquid droplet breaks up into many smaller nanodroplets. These fragmented nanodroplets move away from each other because of the repulsive forces providing them a certain kinetic energy. The timescale to reach the melting point is a few ps, depending on the laser fluence. The entire fragmentation process can take place in ~ 100 ps, until the fragmented Au NPs remain far apart owing to the kinetic energy. In general, this model for the NP fragmentation is generally accepted, and considered to describe other systems, *e.g.* Au NPs encapsulated in a silica shell exhibited similar fragmentation process [182].

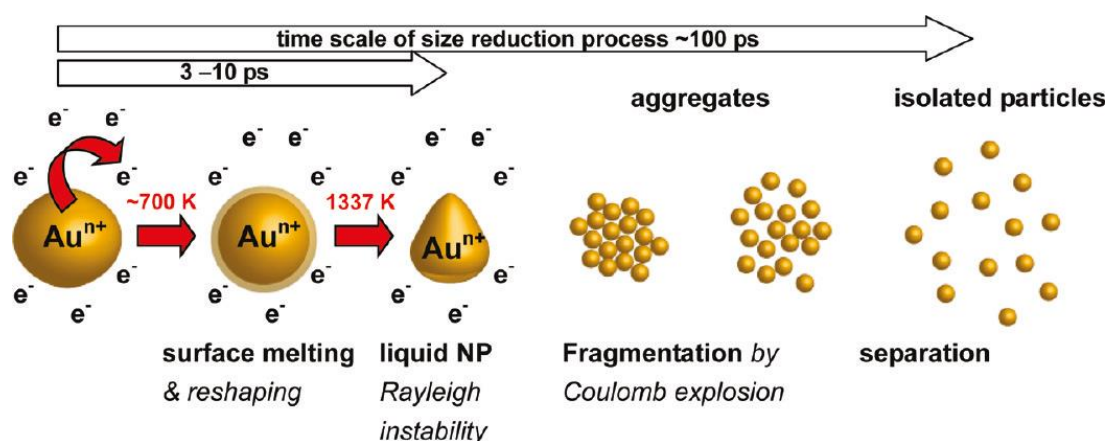


Figure 4.1 –Illustration of fs-laser-induced fragmentation process of aqueous Au NPs. Image is taken from [180].

In other study, the ablation of Au NPs below the melting point was characterized using ps scattering technique [183]. This process was induced by the optical near-field enhancement close to curved surfaces.

In this chapter, the ultrafast dynamics of photoexcited Ag nanoislands encapsulated in multi-layer stack is investigated in three groups of experiments. In the first part, transient absorption spectroscopy reveals the relaxation dynamics of transient plasmon bands, when excitation below the shape transformation threshold is applied. This study is followed by the investigation of ultrafast dynamics of shape transformations in the multipulse regime using pump-probe microscopy setup. Furthermore, the morphological transformations are *ex situ* characterized by STEM measurements directly evidencing the ultrafast phenomena. In the third group of experiments, the ultrafast dynamics of sample transformations above the ablation threshold is investigated, defined as a partial film removal process.

4.2 Experimental methods

4.2.1 Transient absorption spectroscopy for reversible excitation

The sketch of the transient absorption spectroscopy setup can be seen in Figure 4.2. The setup is based on the fs laser PHAROS described in the previous chapter operating at 60 kHz. The pump beam is obtained from an OPA and a subsequent stage of harmonic generator (both from Light Conversion) capable of tuning the pump wavelength from 210 nm to 20 μm . Pump wavelength of 1000 nm and 1100 nm are chosen to directly excite the broad LSPR of the investigated samples (shown later in Figure 4.6b and Figure 4.9a). The time-resolved experiments are conducted in a commercial pump-probe arrangement (HARPIA from Light Conversion). The pump is chopped and focused on the sample at nearly normal incident angle. The probe is time-delayed with respect to the pump with a maximum time delay up to ~ 7 ns, and then frequency-doubled to produce 515 nm beam using a beta barium borate crystal. Spectrally broad white light continuum (350 nm – 650 nm) is generated in a 4 mm thick sapphire crystal, subsequently the beam is focused on the sample by a parabolic mirror at normal incidence. The pump and the probe beam spot diameters are around 100 μm and 90 μm , respectively. The transmitted probe light is collected using the imaging spectrograph (Kymera 193i, OXFORD instruments) equipped with a NMOS linear image sensor (HAMAMATSU S8380-256Q). The spectral resolution is ~ 1.7 nm. The chopper allows the pump beam to be blocked half of the time to ensure the measurement of probe pulse intensity with and without pump pulse, at both states using 0.5

ms acquisition time (integrating over 32 probe pulses). One differential absorption spectrum at a fixed delay $\Delta A(\lambda, t)$ is a result of averaging 10,000 spectra.

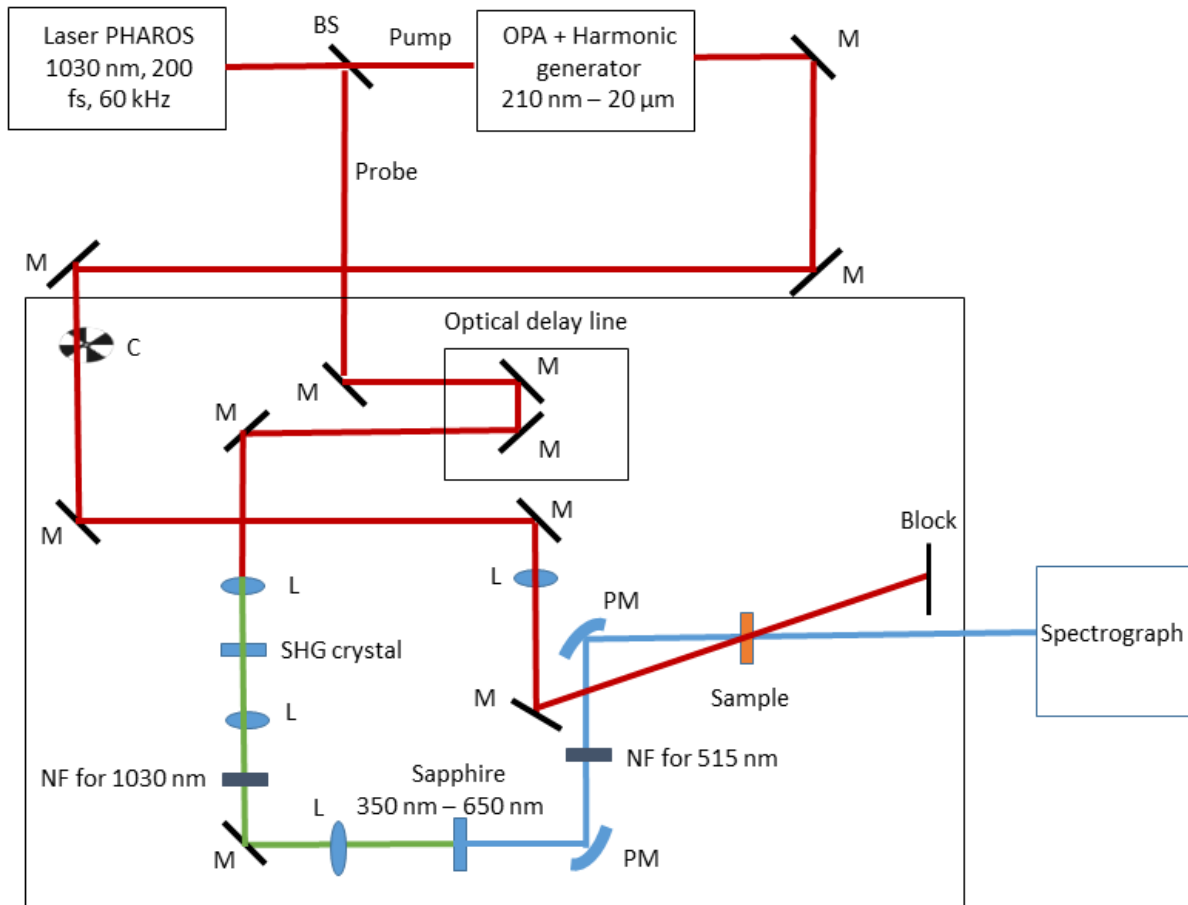


Figure 4.2 – Sketch of the transient absorption spectroscopy setup. M: mirror, BS: beam splitter, C: chopper, L: focusing lens, PM: parabolic mirror, NF: Notch filter.

The temporal overlap of the pump and probe pulses and the temporal resolution of the setup are determined by recording the transient absorption spectra of a glass substrate (N-BK7) without film deposited on the surface. The raw transient absorption 2D map is demonstrated in Figure 4.3a. Here, the pump wavelength of 1000 nm is used. The response of the glass substrate excited by the pump pulse is considerably faster than the characteristic timescale of the convolution of the pump and probe pulses, therefore one can expect detectable signal just around the temporal overlap region. The origin of the detected signal is attributed to cross-phase modulation, in which the pump pulse modulates the real part of the refractive index of the medium experienced by the probe pulse, resulting in a spectral re-distribution of it. The complete description of this nonlinear effect can be found elsewhere [184].

Such a measurement also provides information about the dispersion of the pump-probe setup. Due to the different phase velocities of the spectral components of the white light probe, one can observe a time difference between the times of arrival at each probe wavelength.

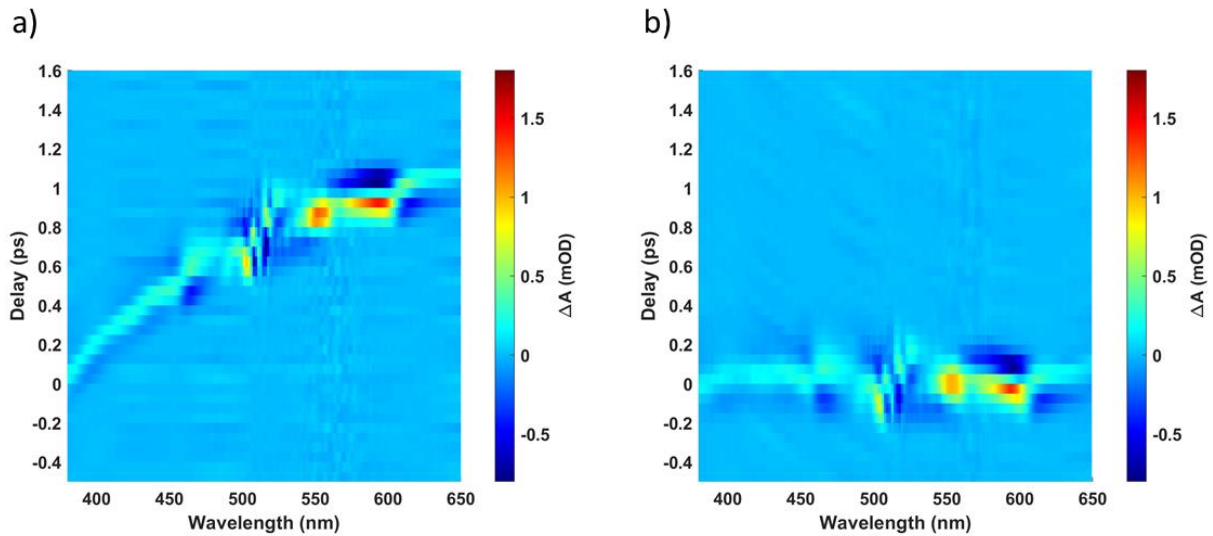


Figure 4.3 – Transient absorption measurement on the N-BK7 glass substrate. a) The ultrashort raw signal around the temporal overlap of the pump and the probe pulses. The pump wavelength is 1000 nm. b) The signal after dispersion-correction.

The dispersion is acquired during the white light generation and propagation in the different media (including air). As a result, the broadening of the initial 200 fs pulse duration can be expected. The temporal resolution of the experiment is defined as the width of the signal, which is measured to be ~ 700 fs. However, this value exhibits slight wavelength-dependence, *i.e.*, varying in the range of ~ 500 fs – 700 fs (Figure 4.3). The same measurement was performed for all pump wavelengths used in the later experiments (1100 nm in this chapter, 700 nm and 540 nm in chapter 5). The dispersion correction is manually performed by fitting a polynomial function on the estimated center of the signal at each wavelength. The dispersion corrected data can be seen in Figure 4.3b. This manual correction is performed in each raw data.

4.2.2 Pump-probe microscopy for irreversible excitation

The sketch of the ultrafast pump-probe microscopy setup is demonstrated in Figure 4.4. The central laser and the beam path of the pump arm are the same as the arrangement described in chapter 3 in Figure 3.2a, with an extra element of a KD*P crystal-based Pockels cell (EM510M-D-AR400-700 from Leysop) to trigger solely this arm.

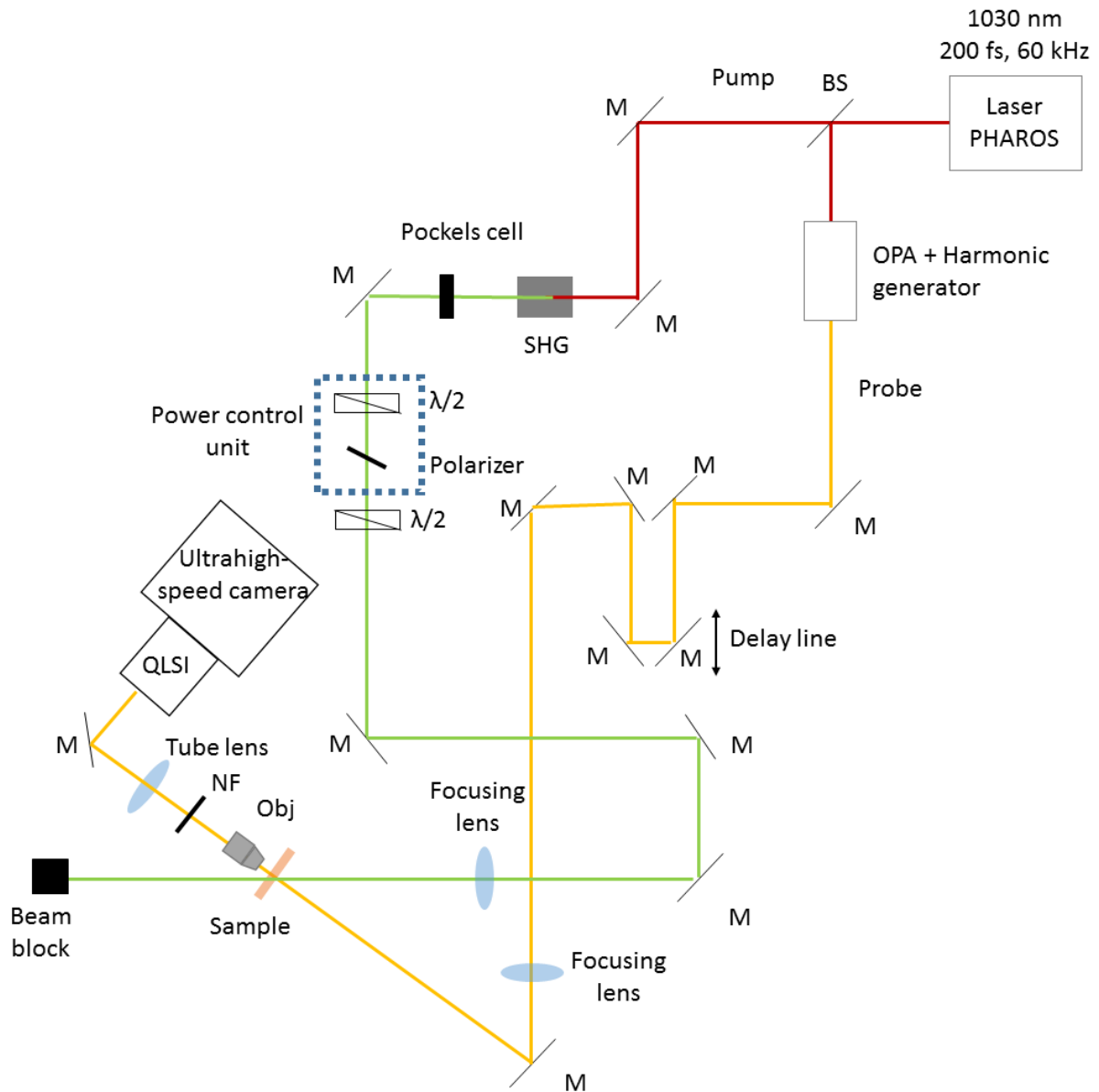


Figure 4.4 – Sketch of the ultrafast pump – probe microscopy setup. M: mirror, BS: beam splitter, NF: Notch filter, SHG: second harmonic generation, Obj: objective, QLSI: quadriwave lateral shearing interferometer.

The important modifications concern the probe beam. The probe beam is the output of the OPA and harmonic generator described in the previous section (in that experiment, it was used as the pump beam). The laser repetition rate is fixed by the OPA and harmonic generator to 60 kHz. The output of the OPA and harmonic generator is sent into a single-pass mechanical delay line installed manually in this setup (the commercial HARPIA pump-probe spectroscopic arrangement is not used). The maximum delay is ~ 3 ns. The optical alignment of the delay line is carefully conducted by observing the beam directional stability throughout the full delay range

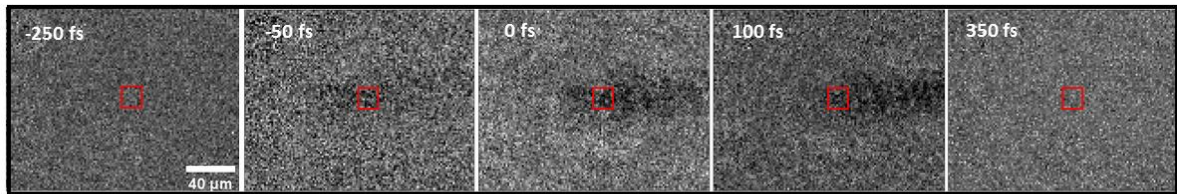
of 3 ns, far from the output of the delay line. Subsequently, the probe beam is weakly focused on the sample by a lens with a focal distance of 40 cm. The pump laser-induced changes are observed using optical microscope in transmission configuration (same objective, tube lens, Notch filter and ultrahigh-speed camera as in Figure 3.2a, without the polarizer). In the image plane of the microscope, an achromatic quadriwave lateral shearing interferometer (Phasics SID4-Element) is used to perform phase-sensitive experiments, as described in chapter 2. The operational wavelength range of the interferometer is 450 nm – 800 nm. In all the following experiments, S polarization is used for the pump beam, and the probe polarization is perpendicular to it.

The workflow begins with selecting a probe wavelength in the range of 450 nm – 800 nm, and recording a video file with each frame containing the interference image of the laser-affected area after each pump pulse (with the fixed 60 kHz repetition rate), using single probe pulse per image acquisition. The same is repeated at each selected delay value. The intensity (transmission) and phase information is obtained from the raw interference images using commercial evaluation software SID4-BIO provided by Phasics. Once obtained, the same image treatment routines are used as described in chapter 3. Results were averaged over three video files recorded within the same conditions in a fresh area of the sample. Same as in the experiments in chapter 3, one video file is recorded with one selected probe wavelength ($\Delta\lambda \sim 4$ nm). In the following experiments, the probe wavelengths of 450 nm and 630 nm are used.

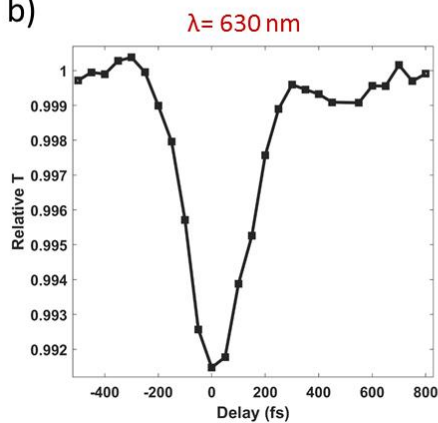
The temporal overlap of the pump and probe pulses is determined by characterizing the response of a glass substrate (N-BK7) without film deposited on the surface. A sequence of intensity images (normalized by the frame before the arrival of the first pump pulse) recorded at 630 nm probe wavelength around temporal overlap is demonstrated in Figure 4.5a. Pump laser fluence of 70 mJ/cm² was used in these experiments. The red rectangles indicate the area of averaging in the beam center in each image (area of 7-by-7 pixels). The trace of the pump beam propagation in the bulk substrate can be observed in the images (dark line area; the pump beam propagates from left to right in the images). The dynamics of the relative transmittances at 630 nm and 450 nm are shown in Figure 4.5b and Figure 4.5c, respectively. The relative transmittance at each pixel is defined by the ratio I_d/I_0 , where I_d and I_0 are the pixel intensities at a fixed time delay d and the initial film, respectively. Solely in these experiments, the averaging of 100 measurements was possible due to the reversible material relaxation (no need to move the sample). Similarly to the transient absorption spectroscopic measurements, signal is detected solely around the temporal overlap region. Similarly to the results shown in Figure 4.3, the origin can be attributed to nonlinear optical effects, such as cross-phase modulation [184].

In both cases, signal contribution is detected in the time window of -200 fs to ~600 fs. Therefore, the estimated temporal resolution of the setup is 800 fs. The corresponding phase images are less reliable to investigate due to the considerably stronger signal fluctuation.

a)



b)



c)

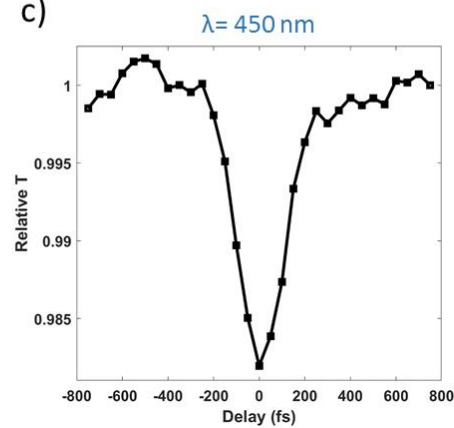


Figure 4.5 – Ultrafast dynamics of the relative transmittance measured on the N-BK7 glass substrate. a) Sequence of intensity images recorded using 630 nm probe wavelength at different time delays around 0 ps. The red rectangles indicate the area of averaging in the beam center. b) Variation of the relative transmittance in the beam center probed at 630 nm. c) Variation of the relative transmittance in the beam center probed at 450 nm. In these experiments, the pump laser fluence is 70 mJ/cm².

4.3 Results and discussions

This section summarizes the wide range of experimental results about the ultrafast dynamics of the photoexcited multilayer system using two experimental conditions. At the first part, the ultrafast energy relaxation below the reshaping fluence threshold is characterized using the transient absorption spectroscopic setup. Subsequently, the ps dynamics of the irreversible shape transformations is demonstrated either below or above the ablation threshold.

4.3.1 Reversible energy relaxation

The reversible ultrashort and short dynamics of ensembles of photoexcited plasmonic nanoislands are investigated using the transient absorption spectroscopic setup. In these experiments, pump laser fluence of 0.8 mJ/cm^2 and 60 kHz repetition rate were used. Similar Ag/TiO₂ multilayer samples are investigated as in chapter 3, with different nominal Ag thicknesses prepared on N-BK7 glass substrate using the same preparation method and conditions described in the Experimental methods section of chapter 3. The TiO₂ layer thicknesses are fixed at 30 nm in all cases.

We start the data analysis with the sample that contains a Ag layer of 5 nm. The plan-view electron microscopy image and the corresponding steady-state absorbance spectrum of the sample can be seen in Figure 4.6.

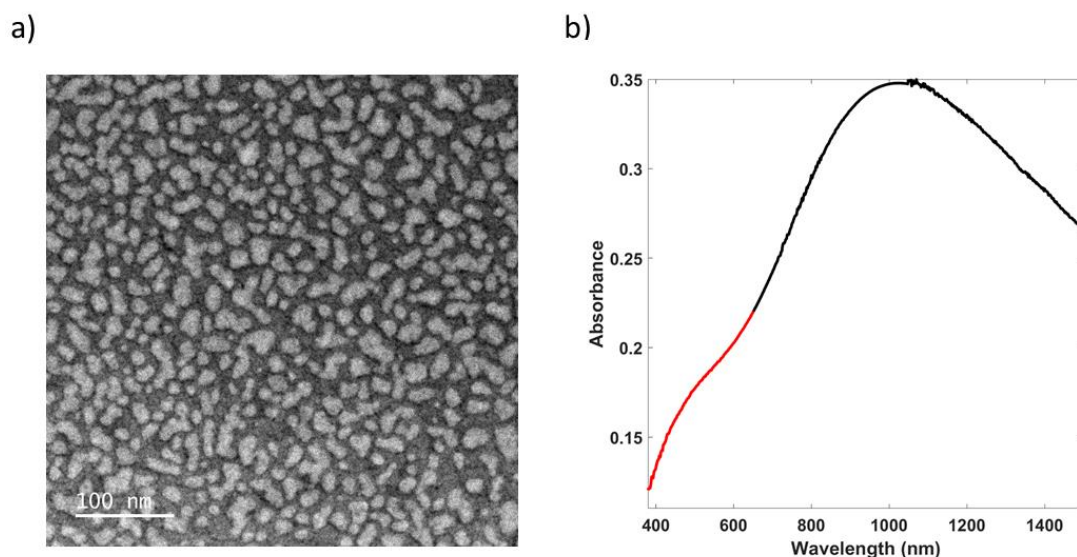


Figure 4.6 – Steady-state characterizations of the sample with Ag layer thickness of 5 nm. a) Plan-view electron microscopy image of the Ag nanoislands. b) The steady-state absorbance spectrum of the sample. The red region indicates the spectrum on the probe wavelength region.

The red segment of the spectrum indicates the region of the probe spectrum: 380 nm – 650 nm. The absorbance spectrum contains two relevant features from the point-of-view of the transient experiments. Broad LSPR centered at 1000 nm, that dominates the absorbance over several hundreds of nanometers, and a secondary, weaker resonance in the spectral region of interest (red part of the spectrum), which is overlaid with the broad, primary resonance. In the followings, the broad resonance and the weaker resonance are denoted as R_0 and R_1 , respectively.

As the probe wavelength range covers the spectral region of both resonances, the transient absorption spectrum reflects the temporal dynamics of each individual contributions. This is demonstrated in Figure 4.7.

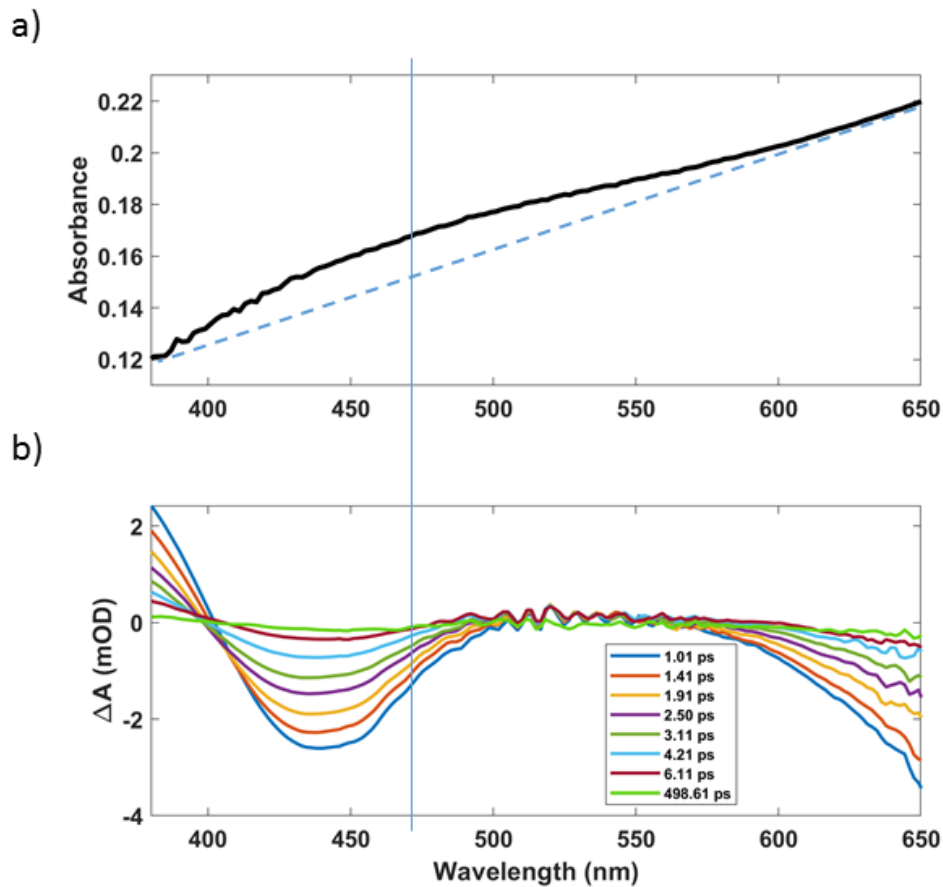


Figure 4.7 – Spectral characterizations of the sample with Ag layer thickness of 5 nm. a) The steady-state absorbance spectrum on the probe wavelength region. The blue dashed line is a guide for the eye highlighting the presence of a second, weaker resonance in the absorbance spectrum overlaid with the broad resonance centered at 1000 nm. The vertical blue line indicates the estimated center position of the weaker resonance. b) Transient absorption spectra at different time delays indicated by the colors.

The steady-state absorbance in Figure 4.7a is compared to the transient absorption spectra at various time delays in Figure 4.7b. The pump laser wavelength of 1000 nm is used to excite directly R_0 .

The transient absorption spectra reflect four distinct spectra regions with different transient behaviors due to the modification in the dielectric function of Ag after pump-photon absorption [25]. A positive signal below 400 nm, which is referred to as photo-induced absorption (PIA) [178], the negative signal between 400 nm and 500 nm, known as plasmon bleaching [12],

rather flat transient between 500 nm and 550 nm, and finally an additional negative feature above 550 nm. These features result from the sum of the transient responses of the two LSPR modes associated with the Ag nanoislands. The relaxation of the four types of signal is demonstrated at different time delays from 1 ps until 500 ps.

The vertical blue line indicates the approximated spectral position of R_1 , for a comparison with the first negative feature of the transient spectra. The dashed blue line is a guide for the eye helping to identify the presence of the resonance overlaid to the slowly varying background. Figure 4.8 demonstrates ultrafast time traces at selected probe wavelength ranges, either in the vicinity of R_1 or in the bleaching signal above 600 nm.

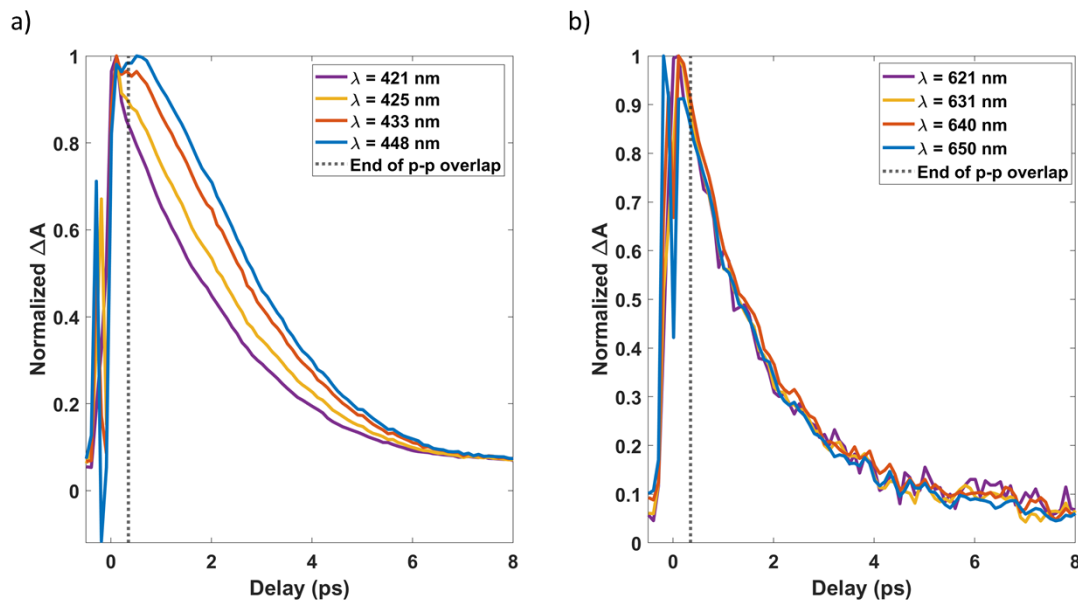


Figure 4.8 – Ultrafast time traces at different spectral regions. a) Normalized time traces in the vicinity of R_1 , and in the spectral region of the bleaching signal above 600 nm in b). The dashed line indicates the end of the pump-probe temporal overlap.

In both images in Figure 4.8, the vertical dashed lines at 350 fs indicate the time delay until when the signal originating from the temporal overlap of the pump and the probe pulses has disturbing effects. The signal measured at higher delay than 350 fs reflect the response from the Ag layer without any intrinsic artifacts overlaid [184]. The time traces were normalized to the same signal level to compare their temporal behaviors. The time traces in the spectral region of R_1 reflect strong wavelength-dependent rise time and decay. The longer wavelength experiences longer rise time, and subsequently faster decay until 8 ps. Attempts were made to fit the time traces by sum of three exponentials in order to assess the characteristic time constants of the e-e, e-ph and ph-ph interactions, but the quality of the fits were not satisfactory suggesting additional mechanisms. At longer delays than 8 ps, the relaxation shows no wavelength de-

pendence, the individual time traces relax to equilibrium values at the same rate. On the contrary, the time traces recorded in the bleaching signal in the red spectral region far from the weaker resonance (Figure 4.8b), which is the short wavelength wing of R_0 , show no probe wavelength dependent temporal evolution. The observation holds for the rise times as well as for the decay times.

Essentially, the transient spectra of the different samples revealed similar spectral features described previously with slight differences. The steady-state and transient spectra of the sample containing 10 nm thick layer of Ag nanoislands is demonstrated in Figure 4.9. The transient spectrum is measured at 2.5 ps delay. In this experiment, the pump wavelength of 1100 nm is used to directly excite R_0 in this sample.

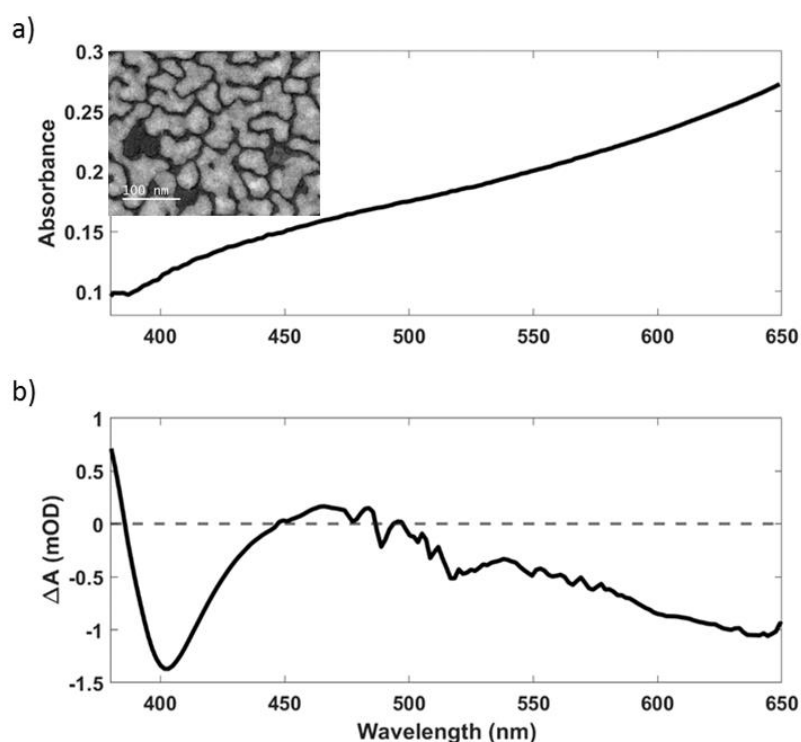


Figure 4.9 – Spectral characterizations of the sample with Ag layer thickness of 10 nm. a) The steady-state absorbance spectrum. The inset shows the plan-view STEM image of the sample. b) Transient absorption spectrum at 2.5 ps time delay.

Compared to the previous sample (Figure 4.7), the PIA signal below 390 nm side of the spectrum is slightly blue-shifted, and the bleaching signal around ~ 400 nm is narrower. The bleaching signal is directly linked to the narrower R_1 in the steady-state spectrum. Corresponding to the narrower bleaching signal, the flat transient feature on the long wavelength wing of the bleaching signal extends on a shorter wavelength region.

4.3.2 Discussion on transient absorption spectra

The spectral shape of $\Delta A(\lambda, t)$ around a LSPR band exhibits transparency feature (negative differential absorption signal referred as bleaching) and a photo-induced absorption (positive signal) feature previously demonstrated by several works in various materials such as Au [185]–[187], Ag [12], [25], [188] and Cu [93]. It is a consequence of the enhancement of the nonlinear optical response around the LSPR due to the dielectric confinement, as discussed in chapter 2. In the case of multiple resonances in the steady-state absorbance spectrum, the transient spectrum around each resonance reflects the sum of the individual effects, the contributions of the bleaching and induced absorption features add together resulting in a complex transient spectrum with alternating negative and positive features [97], [187].

First, we examine the transient features above 400 nm in the spectra shown in Figure 4.7. There are two overlaid resonances in the steady-state absorbance referred to as R_0 and R_1 , each owing its contribution in the transient spectrum. The bleaching around 450 nm and its positive long wavelength wing are superimposed with the bleaching of R_0 . The induced absorption wing from transient R_1 decays above 560 nm, leading to the second negative transient observed between 560 and 650 nm. Analyzing the transient absorption spectrum is shown to reveal resonance modes weakly detectable in the stationary spectra, that is R_1 in the present case. The same considerations hold for the interpretation of the transient spectrum of the sample with 10 nm thick Ag layer. In that sample, the presence of a resonance R_1 is strongly manifested in its transient spectrum, however somewhat hidden in its steady-state absorbance (Figure 4.9).

The photo-induced absorption signal below 400 nm is detected in all samples regardless to the steady-state LSPR spectrum. It is important to note that this band is definitely correlated to the presence of metal NPs, since the experiments on the substrate with no Ag layer does not exhibit any signs of transients outside the temporal overlap region. It is suggested that the nature of this band is not directly related to LSPR. A possible explanation is transient modification of the energy transitions from the d -bands below the Fermi energy to the s - p conduction band of Ag as a result of smearing of the Fermi level due to heating of the conduction electrons [12], [189], [190]. Increased density of interband transitions could result in a transient increase of absorption rather far from the interband transition threshold of Ag (~ 300 nm), in our experiments expanding until ~ 400 nm.

As a summary, the complex transients are results of the sum of contributions of different resonances in the material. The individual spectral regions can be well-described by the combination of photo-induced absorption and plasmon bleaching contributions. Additionally, resonances hidden (or rather weakly exhibited) in the stationary spectra can be revealed by the

ultrafast differential transient signal. In the following sections, the ultrafast dynamics of the NP reshaping in the sample containing 10 nm thick Ag layer is investigated further.

4.3.3 Ultrafast dynamics of irreversible transformations below the single-pulse ablation threshold

At first, the results of the reshaping dynamics are presented by the temporal response of the material probed at 630 nm and 450 nm using the pump-probe microscopy setup. Figure 4.10 shows the evolution of the relative transmittance in the center of the laser-irradiated area on short (< 9 ps) and longer timescales until 1000 ps using pump laser fluence of 43 mJ/cm^2 at 515 nm wavelength. As mentioned, the relative transmittance at each pixel is defined by the ratio I_d/I_0 , where I_d and I_0 are the pixel intensities at a fixed time delay d and the initial film, respectively.

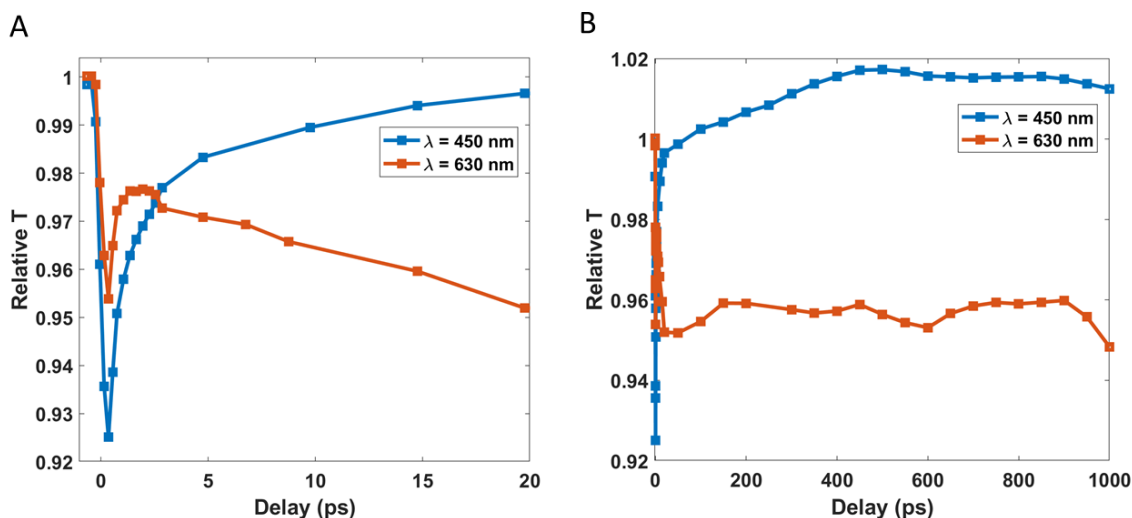


Figure 4.10 – Ultrafast time traces of the relative transmittances recorded at 450 nm and 630 nm. A: Ultrafast dynamics of relative transmittance probed at 450 nm (blue curve) and at 630 nm (red curve). B: The same as image A showing the longer delay behaviors.

The intraband pump photon absorption results in instantaneous excitation of hot electrons [10], [28]. The first, sudden signal decrease at $\tau = 0$ ps corresponds to the energy equilibration between the electrons in the Ag NPs via e-e collision. Thermalized, hot Fermi electron distribution is established which is not in thermal equilibrium with its environment. The amplitude variation of the signal reflects the increasing electron temperature, which can reach the temperature region of 10^4 K in the laser fluence region where irreversible NP reshaping occurs [12]. The

characteristic timescale for the internal energy redistribution is a few hundreds of femtosecond in noble metals [25]. In Figure 4.10, the signal decreases until $\tau = 600$ fs, from which point it exhibits a slower, increasing trend until $\tau = 3$ ps for both wavelengths. During and after the electron interaction, the energy is transferred to the lattice by e-ph interaction. In consequence, the temperature of the metallic NP strongly increases. This causes the signal increase observed after $\tau = 600$ fs.

The coupling interaction between the electrons and the lattice can be described by the two-temperature model (TTM) taking into account the temperature-dependent electronic heat capacity, and the coupling constant of the electron-phonon system [10], [32]. The temperature dependence of the electron heat capacity results in that the timescale for e-ph coupling depends on the initial electronic temperature, *i.e.*, on the injected energy into the electron plasma. The higher laser fluence results in a faster energy exchange between the electrons and the phonons. The model is suitable for providing the temperature evolution of the two-particle system during the thermalization process. As a consequence of the considerably higher lattice heat capacity at room temperature than the electronic heat capacity, the initial electronic temperature after laser excitation is much higher than the temperature of the equilibrated electron-phonon system. In the low excitation regime, the typical timescale for this process is a few ps [191]. In the present case, the process is not finished until $\tau = 20$ ps where a considerably slower signal decays are observed for both cases. This overly longer e-ph interaction is consistent with the earlier findings reported at comparable laser excitation fluences [12].

The slowest decay observed above $\tau = 20$ ps corresponds to the hot particle equilibrating with the environment matrix. The change of relative transmittance is considerably smaller compared to the change during the fastest relaxation processes (e-e and e-ph interactions) indicating that the main reshaping mechanisms finishes before the cooling of the NP. Until $\tau = 20$ ps, the fast and strong changes to the transmittances are finished, compared to the slight evolution at longer time delays for both wavelengths. The signals do not recover to 1 even before the next pulse ($\tau = 16.7$ μ s) indicating the persistent change in the LSPR band due to the irreversible shape transformation already after single pulse excitation (results showing the signal recovery to 1 far from the laser spot are discussed in section 4.3.5). However, the sign of transmittance change is different, *i.e.*, there is a persistent transmittance decrease for the red wavelength and a slight signal increase in the blue wavelength. The evolution of the LSPR band strongly depends on the wavelength of the probe beam. It will be further examined in the discussion session.

4.3.4 Local laser fluence-dependent dynamics

The use of the microscopic approach enables to investigate the temporal response of the material at different spatial positions corresponding to different local laser fluences. The radial spatial profile of the focused laser spot follows a Gaussian profile. The local laser fluence decays with distance from the peak laser fluence being 43 mJ/cm^2 in the center of the focused spot. Figure 4.11 shows the temporal dynamics of the relative transmittance at 630 nm probe wavelength at four different spatial positions represented by the colored curves.

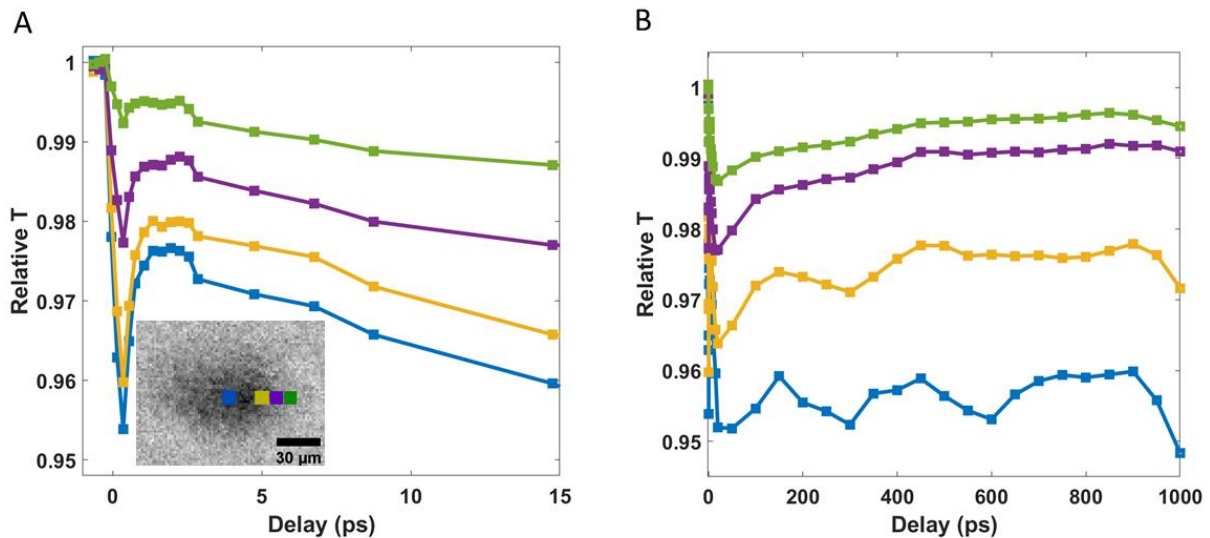


Figure 4.11 – Demonstration of the local laser fluence-dependent dynamics. A: Ultrafast dynamics of relative transmittance at different sample positions. The probe wavelength is 630 nm. The inset shows the transmission image of the sample at $\tau = 0.35$ ps. The colors of the curves in each image correspond to the colors of the filled rectangles in the inset image. B: Same as image A on longer time delays.

The signal amplitudes at the minimum of the transmittance reflect the rate of the electron plasma heating. From the direct comparison of the signal amplitudes in the minimum, it is obvious that the higher local fluence results in a stronger electronic heating in consequence of the higher amount of deposited energy that is reflected by the optical signal change. With increasing laser fluence, the buildup of the hot Fermi distribution becomes faster [192], however, this is not reflected in our data because of the poor sampling of the time delays. The “memory” of the stronger initial electronic heating is preserved during the e-ph and ph-ph interactions, *i.e.*, it is reflected in higher signal amplitudes at any further time delays. Each example signal exhibits persistent spectral changes at the longest delay of $\tau = 1000$ ps. The higher local fluence results in a stronger rate of NP reshaping, which is indicated by the change in the relative transmittance.

The spatial scan reveals that the strongest spectral changes finish during the e-e and e-ph interactions, independently from the local laser fluence.

At the end of the e-ph interaction around 20 ps, the temperature of the heated NP ensemble can be estimated to several hundreds of degrees, as revealed by the temperature simulations in the previous chapter (Figure 3.20). Towards longer delays, considerably slower and smaller spectral variations are observed at different sample positions governed by heat flow through the nanostructure interfaces and heat diffusion in the surrounding medium. The characteristic time-scales for these two processes are in general similar, which makes it complicated to distinguish them. For any case, the heat coupling into the environment transiently alters the dielectric function of the surrounding medium, that results in tuning LSPR band spectral properties, thereby significantly contributes to time-resolved signals [43].

It was earlier demonstrated for Au NPs in aqueous solution (without persistent NP reshaping) that the rate of the heat dissipation does not depend on the initial temperature of the NPs [193]. Our data supports this observation, as no characteristic distinction between the relaxation dynamics at different local fluences is detected except the amplitude variation that seems to decrease towards lower local fluences (*e.g.* the comparison of yellow and green curves).

4.3.5 Temporal dynamics of NP reshaping in the multipulse regime

In these experiments, the accumulating shape transforming effect of each fs pulse is investigated. Figure 4.12 shows the evolution of the ultrafast dynamics of the relative transmittance with increasing fs pulse number recorded at 630 nm probe wavelength. The first important observation is the persistent transmission decreasing effect of each fs pulse during the first five pulses. Each curve starts from gradually lower transmittance value relative to the initial sample, as one can observe in the negative delay data points. Further increasing pulse number results in a change of tendency, *i.e.*, persistent transmittance increase is observed. Additionally, peculiar transformation of the dynamics during the e-e interaction is detected. The decreasing signal observed in the case of $N < 2$ subsequently transforms into increasing transients at higher fs pulse numbers. The gradually decreasing transmittance at $N < 5$ and the transformation of the optical dynamics during the e-e interaction are clear indications of the LSPR band transformation due to irreversible reshaping effect of each fs laser pulse, and it will be further discussed in the discussion section.

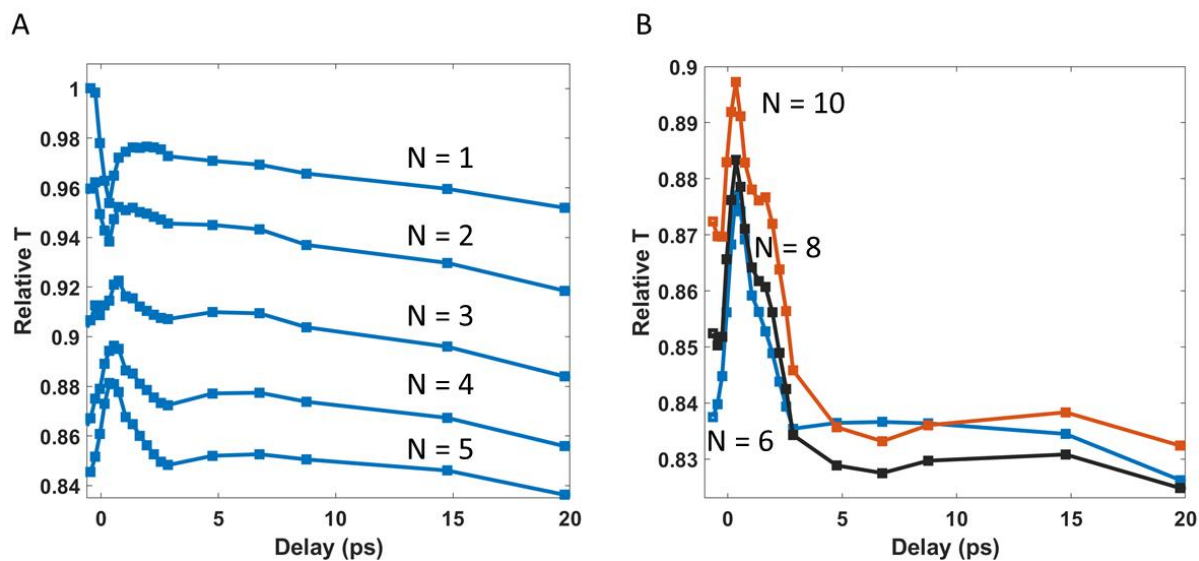


Figure 4.12 – The effect of increasing fs pulse number N on the ultrafast dynamics of the relative transmittance at 630 nm. The transmittance decreases after each fs pulse when $N < 6$ (image A) and increases when $N > 5$ (image B). In image B, different colors are used for easier distinction between each curve. The pump laser repetition rate is 60 kHz.

The longer timescale dynamics of the ph-ph coupling exhibits additional peculiarities, as demonstrated in Figure 4.13.

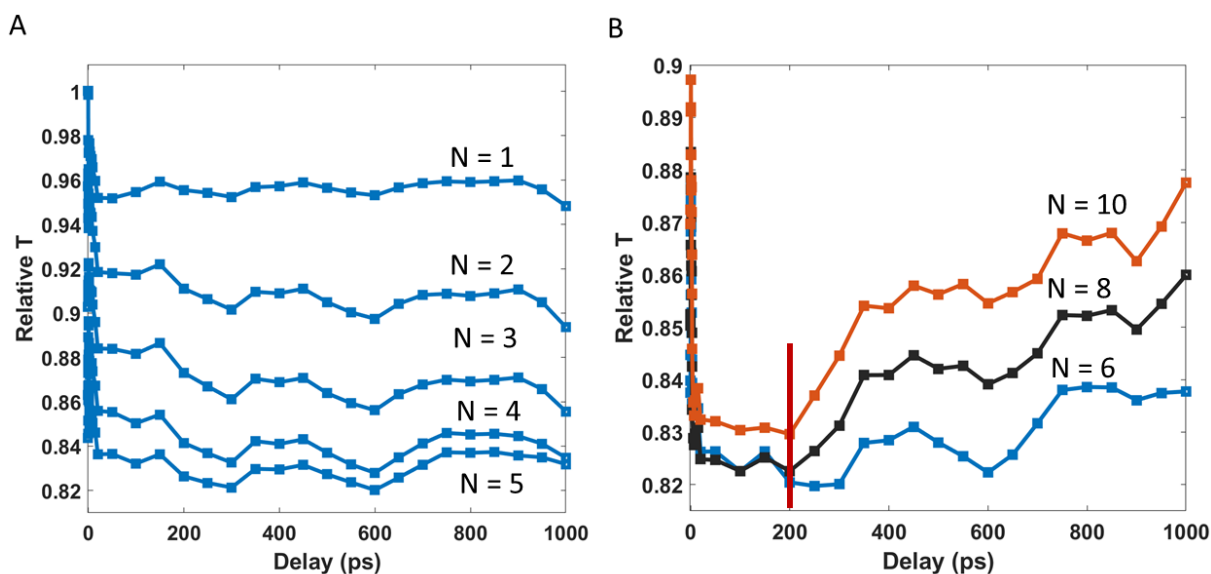


Figure 4.13 – The effect of increasing fs pulse number N on the ultrafast dynamics of the relative transmittance at 630 nm, same as in Figure 4.12 but plotted on long timescale. The transmittance persistently decreases after each fs pulse when $N < 6$ (image A), and increases when $N > 5$ (image B). In image B, different colors are used for easier distinction between each curve. The red, vertical line at 200 ps indicates the onset of a transient signal increase, suggesting the activation of a slower NP reshaping process.

In the regime where the transmittance decreases (left image), the cooling of the thermalized NPs and the heating of the TiO₂ matrix are reflected by the slow signal relaxation on hundreds of ps. On this timescale, the increasing number of pulses does not exhibit any relevant differences in the relaxation dynamics. However, important feature can be seen when $N > 5$ (right image). The red vertical line at $\tau = 200$ ps indicates strong transmittance rise evidencing the activation of a delayed NP reshaping mechanisms that is eventually responsible for the persistent transmittance increase. Except the fluctuations in the signal, the increasing trend seems monotonous and rather slow, since it does not seem to finish until 1000 ps.

The ultrashort and longer time delay dynamics at lower local laser fluence are demonstrated in Figure 4.14. In contrast to the beam center (Figure 4.13), persistent transmittance decrease is detected even after $N = 5$, however the dynamics of the e-e coupling exhibits the same positive signal. Another important difference is that the long timescale dynamics does not evidence the onset of the transmittance increase at 200 ps as discussed and demonstrated in Figure 4.13. It suggests the existence of fluence threshold for triggering that slower NP reshaping process.

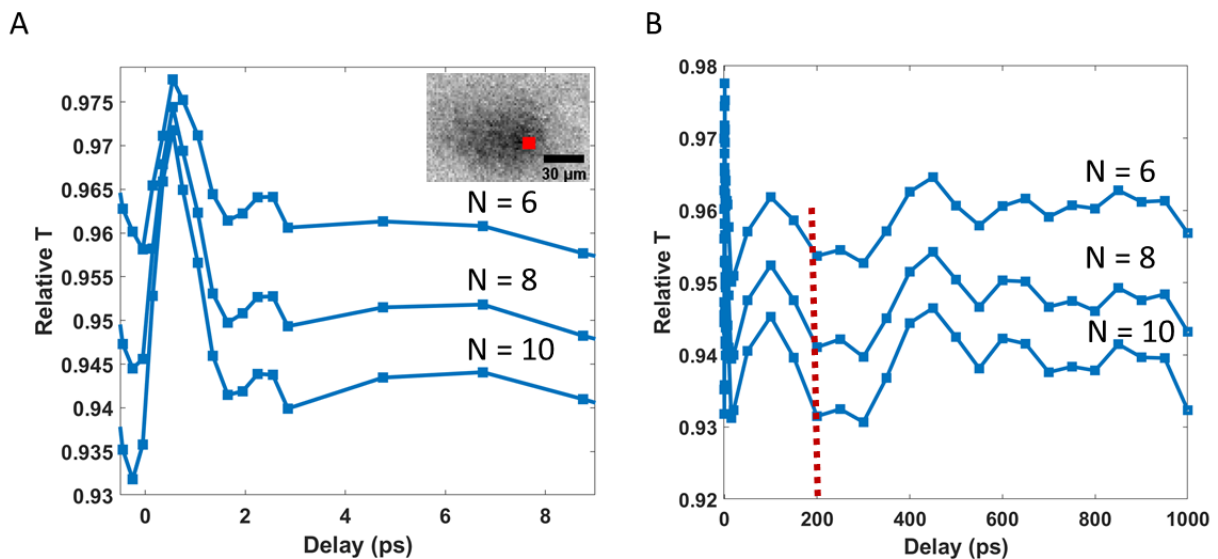


Figure 4.14 – The effect of increasing fs pulse number $N > 5$ on the ultrafast dynamics of the relative transmittance at 630 nm away from the beam center. A: The dynamics on ultrashort time delays. The inset shows the transmission image of the sample at 0.35 ps after the first pulse. The red rectangle shows the position of the analysis. B: Long time delay plot of the curves in image A. The vertical dashed, red line indicates the delay at which the slow reshaping process started at higher laser fluence (Figure 4.13).

For comparison, the multipulse evolution of the transmittance in the beam center probed at 450 nm can be seen in Figure 4.15. In opposite to the multipulse tendency observed at the red wavelength in Figure 4.13, persistent transmittance decrease is evidenced independently from the pulse number.

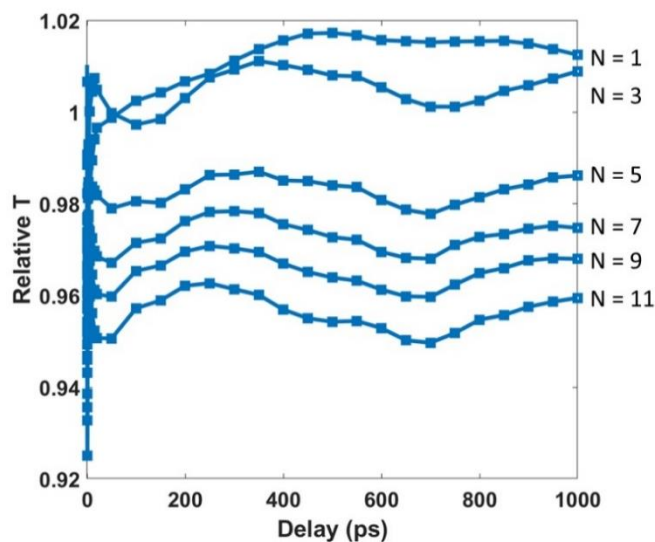


Figure 4.15 – The effect of increasing fs pulse number N on the ultrafast dynamics of the relative transmittance probed at 450 nm.

4.3.6 Ultrafast response below reshaping threshold

Far from the beam center, where the local laser fluence is too low to trigger the irreversible NP shape transformation, the transmittance is expected to relax back to the initial value. This is demonstrated in Figure 4.16 using the example of the 450 nm probe wavelength. The transmittance evolution is compared at different sample positions in the vicinity of the spot. When the local fluence is high enough to sufficiently heat the NPs, the heat coupling into the matrix via ph-ph interaction is observed as slow signal decaying on hundreds of ps (blue and green curves). The higher laser fluence results in higher initial signal amplitude at the beginning of the e-ph interaction. Further from the beam center, where the initial electronic heating is lower, the disappearance of the signal from the ph-ph interaction can be observed (cyan and purple curves). There is an indication of the perturbation of the electron plasma around 0 ps delay, and the deposited energy decays via e-ph interaction on a few ps without detectable heat coupling into the environment. In these cases, the increase in electron temperatures can be estimated below 300 K [12].

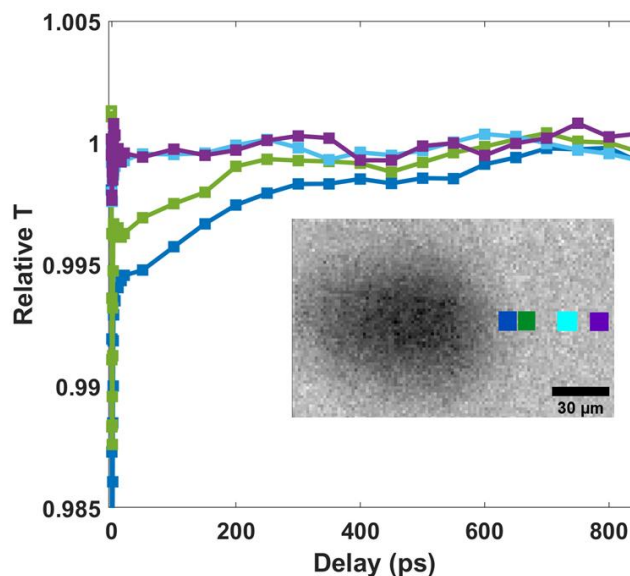


Figure 4.16 – Ultrafast dynamics of relative transmittance at 450 nm at different spatial locations far from the beam center where no NP reshaping is expected. The inset shows the transmission image of the sample at 0.35 ps. The colors of the rectangles correspond to the colors of the curves.

4.3.7 Discussion on irreversible sample transformations

4.3.7.1 Electron microscopy revealing NP shape transformations

As revealed by the short dynamics at the two investigated probe wavelengths (Figure 4.12 and Figure 4.13), the transmittance exhibits persistent change on long delays (16.6 μs), already after the first pulse, and the effect accumulates with increasing number of pulses. It clearly indicates that the LSPR band (peak position and spectral width) of the initial sample centered at 1100 nm gradually transforms upon each fs pulse. This can be interpreted as a result of irreversible shape transformation of the NPs due to the high laser intensity (laser peak fluence of 43 mJ/cm²). To demonstrate that, Figure 4.17 shows a comparison of HAADF-STEM images of the initial sample and the laser irradiated samples with different pulse numbers ($N = 4$ and $N = 10$).

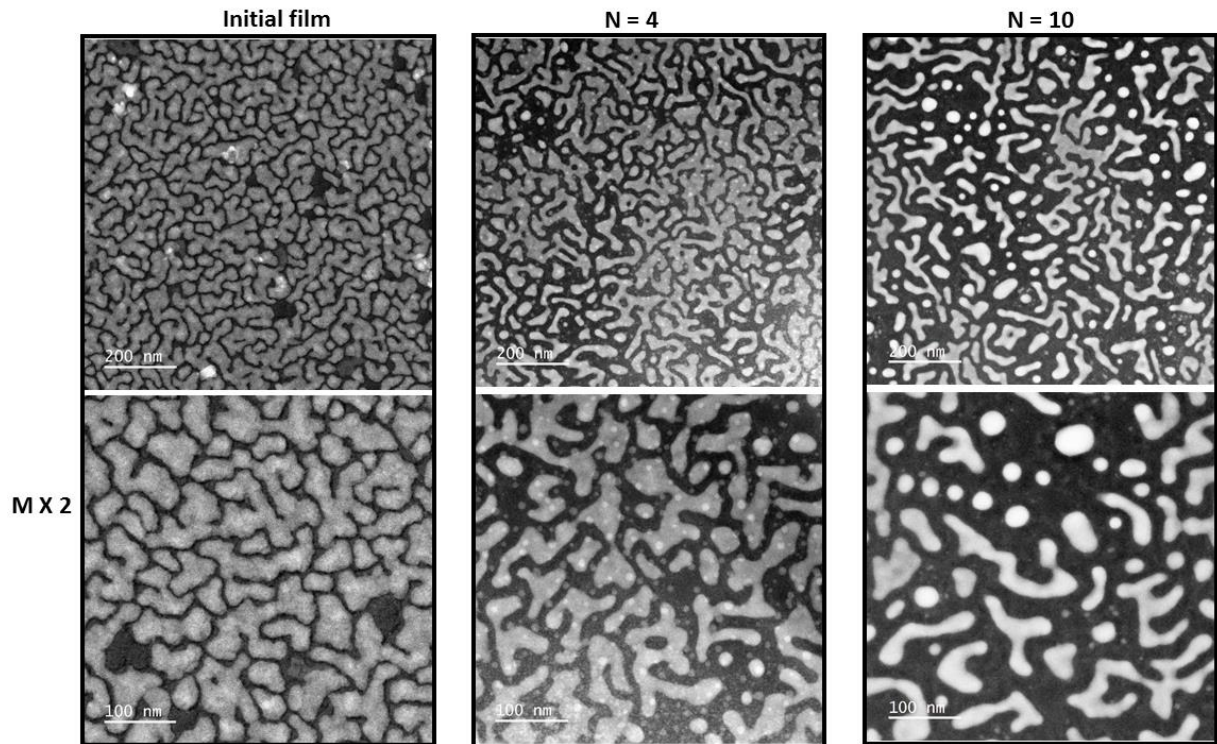


Figure 4.17 – HAADF-STEM images of the initial film compared to the laser-marked sample with different number of pulses N . The second row contains images recorded at double magnification.

The first relevant observation is that the increasing number of pulses results in a decrease of the Ag surface filling factor, similarly to the observations in the previous chapter. It is clearly visible at both magnifications. Additionally, the initial sample contains rather homogeneous distribution of nanoislands exhibiting complex shape distribution without the presence of spherical NPs. On the other hand, both samples, especially the one after $N = 10$ pulses, show the presence of spherical particles as an indication of NP melting. In some places of the sample, the local melting is observed in a periodic structure, as shown in Figure 4.18. The period of the self-organized pattern indicated by Λ is approximately 540 nm. It was demonstrated in the previous chapter that the periodic NP reshaping can be attributed to the excitation of embedded guided modes within the multilayer that interferes with the incident laser light giving rise to a periodic intensity and temperature modulation [57], [86], [90].

Here, the period of the self-organized grating $\Lambda = 525 \pm 40$ nm matches very well with the observations from the previous experiment discussed in chapter 3, because of the same illumination conditions (angle of incident, laser polarization and wavelength).

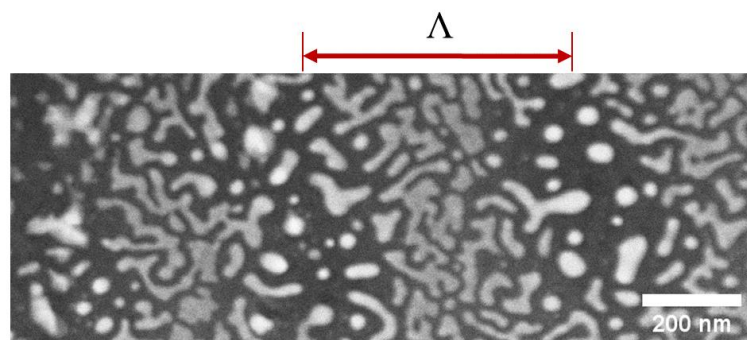


Figure 4.18 – HAADF-STEM image of an area of the sample after $N = 10$ pulses indicating local self-organized reshaping. The period Λ is estimated to be 540 nm.

The spherical NPs are found in spatial positions, where the local temperature rise is high enough to exceed the melting point of the Ag NPs, *i.e.*, where constructive interference occurs between the guided wave and the incident wave. The next important observation from the HAADF-STEM images is the high density of small, spherical particles in the sample marked with $N = 4$ pulses. To highlight them, Figure 4.19 left image shows a section of Figure 4.17, where some small NPs are indicated by red arrows.

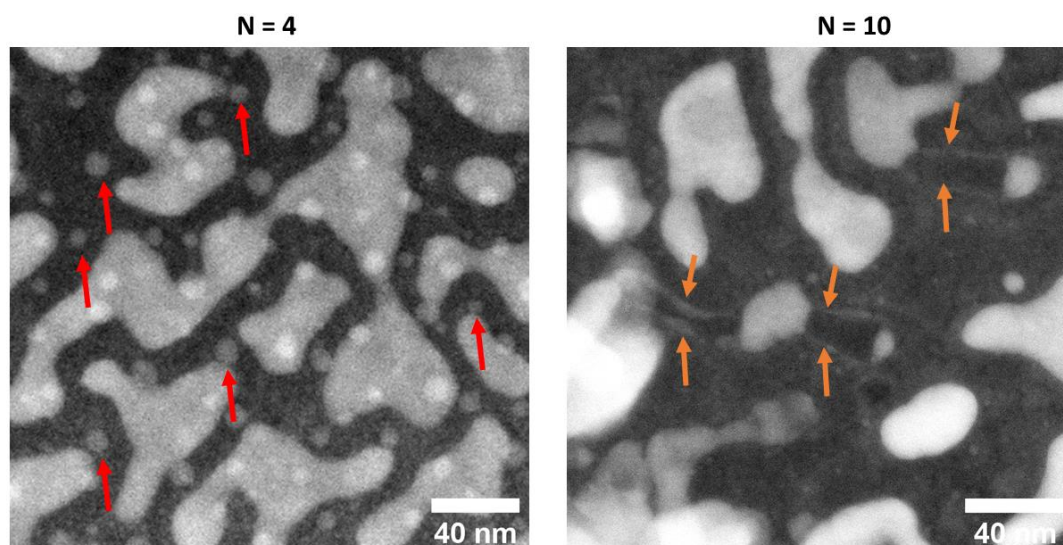


Figure 4.19 – HAADF-STEM images of the sample after laser marking. Left: The sample after $N = 4$ highlighting the presence of fragmented, small NPs indicated by the red arrows. Right: HAADF-STEM image of the sample after $N = 10$, where the orange arrows show some traces of fragmented NPs marked in the TiO_2 matrix during the separation.

These NPs can be found preferentially near the bigger nanoislands, where the local curvature of the contour of the nanoislands are very small. These are the spatial regions, where the electric near-field enhancement is expected to be high, reaching values higher than the incident electric field intensity by several orders of magnitude [194], promoting NP fragmentation process. The

cross-section images in Figure 4.20 evidence the migration of Ag NPs towards the free surface after laser exposure. Initially, all Ag NPs are embedded between the two TiO₂ layers. It implies that some amount of the small, fragmented NPs that we see on the plan-view STEM images might be on the top surface. Even so, based on their positions observed from the top, we can be certain that the fragmentation and the subsequent migration process is promoted locally where the near-field enhancement is high. In the cross-section image at N = 4, Ag content is observable in the TiO₂ layers, which results from the STEM lamella preparation.

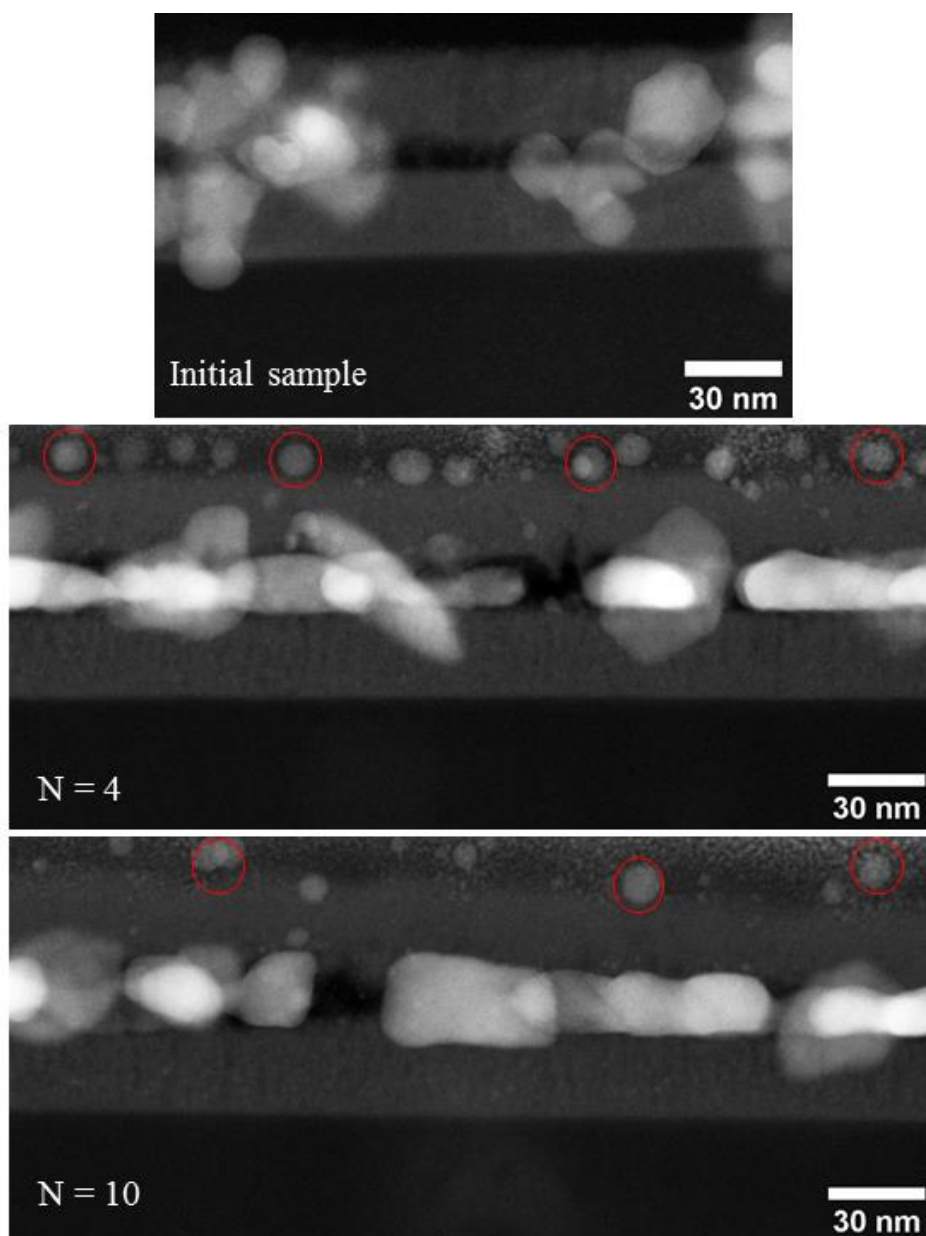


Figure 4.20 – Cross-section STEM images of the initial and the laser-processed samples. The red circles in the images of the laser-processed samples indicate some migrated Ag NPs on the top surface.

Other interesting finding is highlighted in Figure 4.19 in the right image by the orange arrows. Several indications of the traces of fragmented NPs marked in the TiO₂ during the fragmentation and separation process. Beside the traces, one can also observe the segments on the bigger NPs from where the fragmented NPs are detached. These are clear indication of NP fragmentation process. As described in the previous chapter, the photoexcited electrons having enough energy to overcome the Schottky barrier at the Ag/TiO₂ interface are injected in the conduction band of TiO₂, leaving behind positively charged ions at the surface of the nanoisland. The strong repulsive force between neighboring Ag⁺ ions leads to ion ejection. Subsequently, similarly to the case of fragmentation process of aqueous Au NPs illustrated in Figure 4.1, surface melting can be involved, reducing the surface tension (surface energy) of the NPs. Eventually, the charged, unstable NPs can emit smaller fragments. These fragments can propagate a few nm in the TiO₂ matrix owing to the initial kinetic energy, as revealed by the STEM images. Subsequently, the ionic Ag⁺ can diffuse toward the film surface, where they can grow and form rather spherical NPs (Figure 4.20). The time resolved experiments have to be interpreted in the scope of these observations, *i.e.*, the reshaping of the NPs being dominated by fragmentation (size reduction).

4.3.7.2 Mechanisms driving the NP reshaping

Knowing the generally accepted models of the NP reshaping described in the introduction, several aspects can be adapted to our system as well. At first, the results obtained in the multi-pulse regime shown in Figure 4.12 - Figure 4.14 are discussed. Each fs pulse reduces the size of the initial nanoislands resulting in a blue-shift of the LSPR spectrum. There are two indications for the transforming LSPR band. Firstly, the persistent transmittance decrease after each pulse, secondly, the change in sign of the transient signal during the ultrafast e-e interaction. As demonstrated in section 2.1 on several example transient absorption measurements (Figure 2.2 - Figure 2.4), the transient absorption spectrum around a plasmon band exhibits altering transient transparency (decrease in absorption) and induced absorption features. As the first two laser pulses blue-shift the LSPR, the 630 nm approaches the short wavelength wing of the LSPR, which is reflected in the optical signal during the e-e dynamics after the third pulse. The ultrafast increase of the transmittance during the e-e interaction (Figure 4.12, when $N > 2$) is a clear indication that 630 nm approached a spectral region of plasmon bleaching (for comparison, note the ultrafast decrease in transmittance when $N < 3$).

When $N \geq 6$, instead of pulse-by-pulse persistent transmittance decrease, we detect persistent transmittance increase after each pulse (Figure 4.12 and Figure 4.13, right images). The activation of a slower NP reshaping process is detected optically as the sudden, pronounced transmittance increase starting at 200 ps (Figure 4.13 vertical, red line). The process seems not to finish even until 1000 ps. On this timescale, a group of mechanisms is expected to occur simultaneously, such as Ag^+ atomic diffusion within the TiO_2 matrix, NP reformation on the surface and in the matrix and NP fragmentation (Figure 4.1). The activation of this slower process is clearly promoted by the temperature rise in the TiO_2 matrix, since the activation point at 200 ps lies in the time scale of the ph-ph interaction. At earlier timescale, charge-assisted atomic desorption (Ag^+ release resulting in NP size shrinkage) and NP melting occur, possibly after each pulse. The released Ag^+ content in the matrix serves for the seeds for the NP reformation on the surface and in the matrix.

Finally, it is important to note that the 450 nm probe wavelength does not seem to reflect this slower reshaping process (Figure 4.15) even when $N > 5$. The long time-scale dynamics does not evidence any obvious increase in transmittance independently from the pulse number. Additionally, the transmittance decreases after each fs pulse until $N = 11$, no persistent increase is observed as in the case of the 630 nm beginning at $N = 6$. The complex wavelength-dependent spectral transformations were demonstrated in the previous chapter in the multi-pulse regime. The evolution of the transmission coefficient in the visible spectral range is shown in Figure 4.21 demonstrating the tendency of the evolution of the polarized transmission until $N = 58$ pulses.

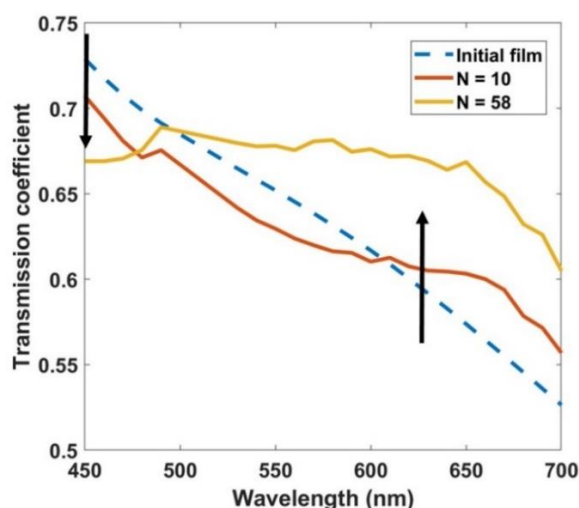


Figure 4.21 – The evolution of the transmission spectrum with increasing pulse number N . The figure is reused from Figure 3.9 in the previous chapter. The pump and the probe polarizations are perpendicular, as in the present experiment. The two black arrows indicate the spectral tendencies at the probe wavelengths of 450 nm and 630 nm.

The black arrows indicate the opposite evolution at the probe wavelengths of 450 nm and 630 nm. In that experiment, the same size reduction is evidenced as in the present case. As described in the previous chapter, the nanoisland shrinkage tends to decrease their initial absorption in the infrared, and the formation of small particles on the top surface contribute to increase the absorption at low wavelength ($\lambda < 470$ nm).

4.3.8 Dynamics above single-pulse ablation threshold

In these experiments, the laser peak fluence in the beam center is increased to 52 mJ/cm^2 to slightly exceed the film ablation threshold after the first fs pulse (measured to $\sim 50 \text{ mJ/cm}^2$). The temporal dynamics of the relative transmittance (630 nm probe wavelength) and the OPD are shown in Figure 4.22. The transmittance's ultrafast dynamics shows the same tendency as the results below the ablation region in the ultrashort timescale (left image in Figure 4.10). The sudden signal decrease until 400 fs due to e-e coupling establishing a hot Fermi distribution. The signal starts to increase at 400 fs that is faster compared to the 600 fs measured in the lower fluence experiment. This indicates that the higher temperature electron plasma starts heating the lattice earlier. The subsequent rapid increase indicates NP heating via e-ph coupling. The heated NPs start to equilibrate with the surrounding matrix via ph-ph interaction. The sudden transmittance increase starting at 50 ps indicates the onset of the ablation process, and its interpretation is discussed later.

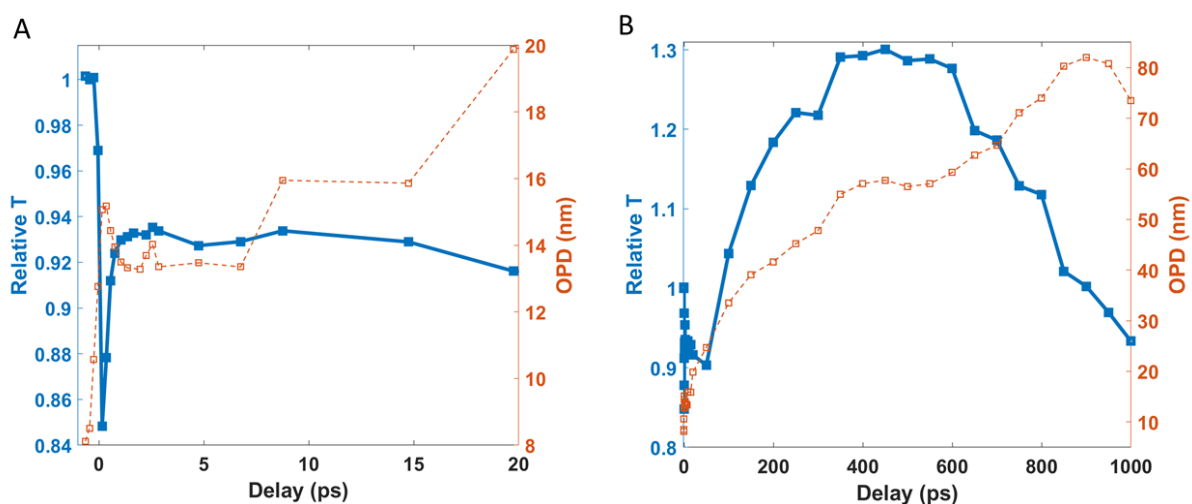


Figure 4.22 – Ultrafast dynamics of relative transmittance (blue curve) and OPD (red curve) recorded at 630 nm in the ultrashort time (image A) and longer timescales (image B). The probe wavelength is 630 nm.

The OPD information reveals the increase of the optical path length (OPL) containing information on the refractive index and the thickness the sample, *i.e.*, $OPL = \int n(s) ds$. The OPD provides the change of the OPL at a delay time compared to the initial sample: $OPD(\tau) = OPL(\tau) - OPL(0)$. Either the refractive index or the sample thickness changes, the measurement reflects it. The OPD exhibits immediate increase of ~ 14 nm during the internal electronic thermalization at ultrashort delays. After a short plateau lasting until ~ 6 ps, clear increasing tendency indicates the heating of the NPs, and subsequently the surrounding, which is not finished even after 1 ns. The OPD increase exceeds 80 nm (at 630 nm probe wavelength), indicating strong variation of the refractive index and thickness of the irradiated area. However, it is not possible to decompose the contributions of the refractive index variation and the sample thickness change, one can interpret 80 nm OPD increase by attributing dominant contribution to the sample thickness elevation. Here, one has to consider strong structural deformation of the material that eventually results in the removal of the film evidenced by the sequence of images recorded at different time delays shown in Figure 4.23 (probe wavelength is 630 nm) and Figure 4.24 (probe wavelength is 450 nm). The images recorded at 16.6 μ s are the second frames of the video files where the delay is set to -0.25 ps. In both intensity and OPD images, a small portion of the film is shown to be detached from the laser-heated area. The underlying mechanisms are detailed in the discussion section.

Furthermore, two kinds of ring pattern are observable in these images. Inside the laser spot, the intensity image at 1000 ps delay recorded at 630 nm clearly shows a dark center, a bright ring and a dark outer ring (Figure 4.23, intensity image at 1000 ps). This ring pattern confined the ablated region is called Newton ring, it is a direct evidence of film expansion, and will be discussed later. Furthermore, this probe wavelength evidence a second ring pattern appearing outside the ablated spot, which is still observable even after the removal of a film disk. This ring pattern confined outside the laser spot has fundamentally different origin from the transient Newton ring. The scattered probe light from the ablating crater towards the non-excited region interferes with the direct light leading to constructive/destructive interference regions, therefore these rings outside the laser spot are diffraction-induced rings [195]–[197]. Their appearance is a further indicator for the onset of mechanical deformation. Such diffraction rings are evidenced by the 450 nm probe wavelength also (Figure 4.24), however Newton rings are not detected using this wavelength. The latter can be attributed to the strong probe light scattering, and is further evaluated in the discussion section.

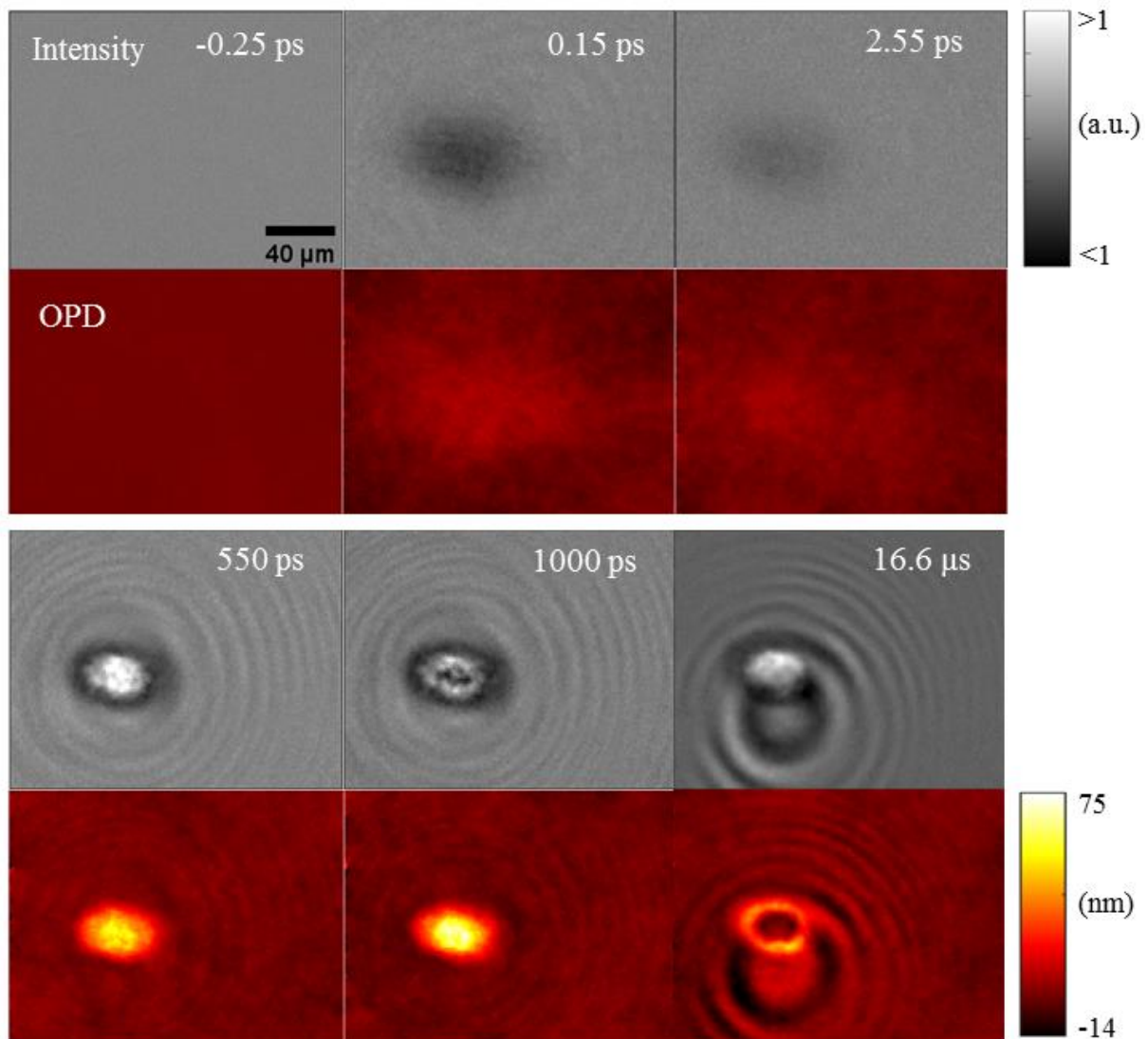


Figure 4.23 – Sequence of intensity and OPD images at characteristic time delays. The intensity images are normalized by the intensity image of the initial sample. In both cases, the images recorded at 16.6 μs are the second frame of the video file where the delay is set to -0.25 ps. The probe wavelength is 630 nm.

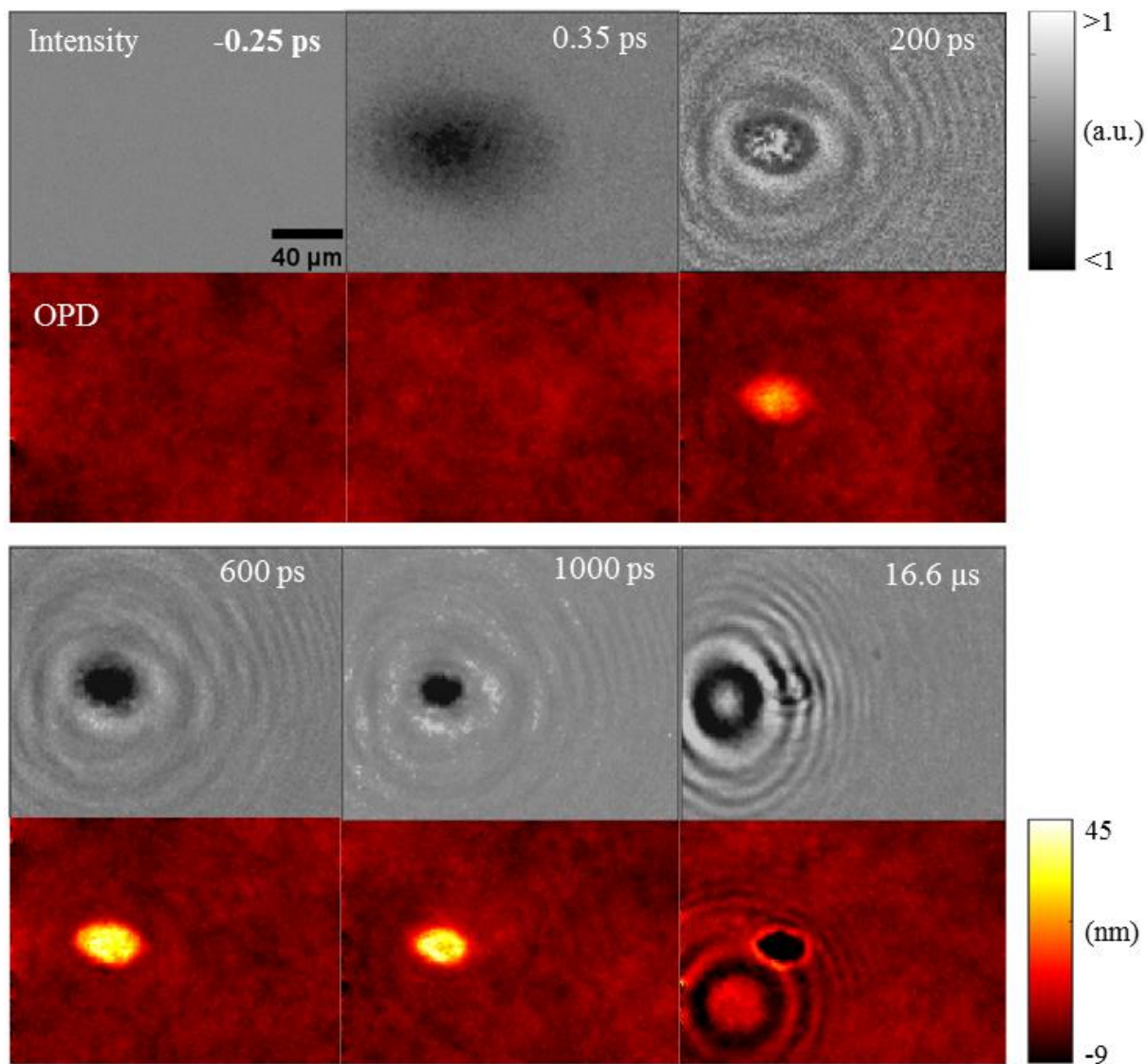


Figure 4.24 – Sequence of intensity and OPD images at characteristic time delays. The intensity images are normalized by the intensity image of the initial sample. In both cases, the images recorded at 16.6 μs are the second frames of the video files where the delay is set to -0.25 ps. The probe wavelength is 450 nm.

4.3.9 Local fluence-dependent dynamics above the ablation threshold

Spatially-resolved relative transmittance and OPD traces recorded at 630 nm probe wavelength are shown in Figure 4.25.

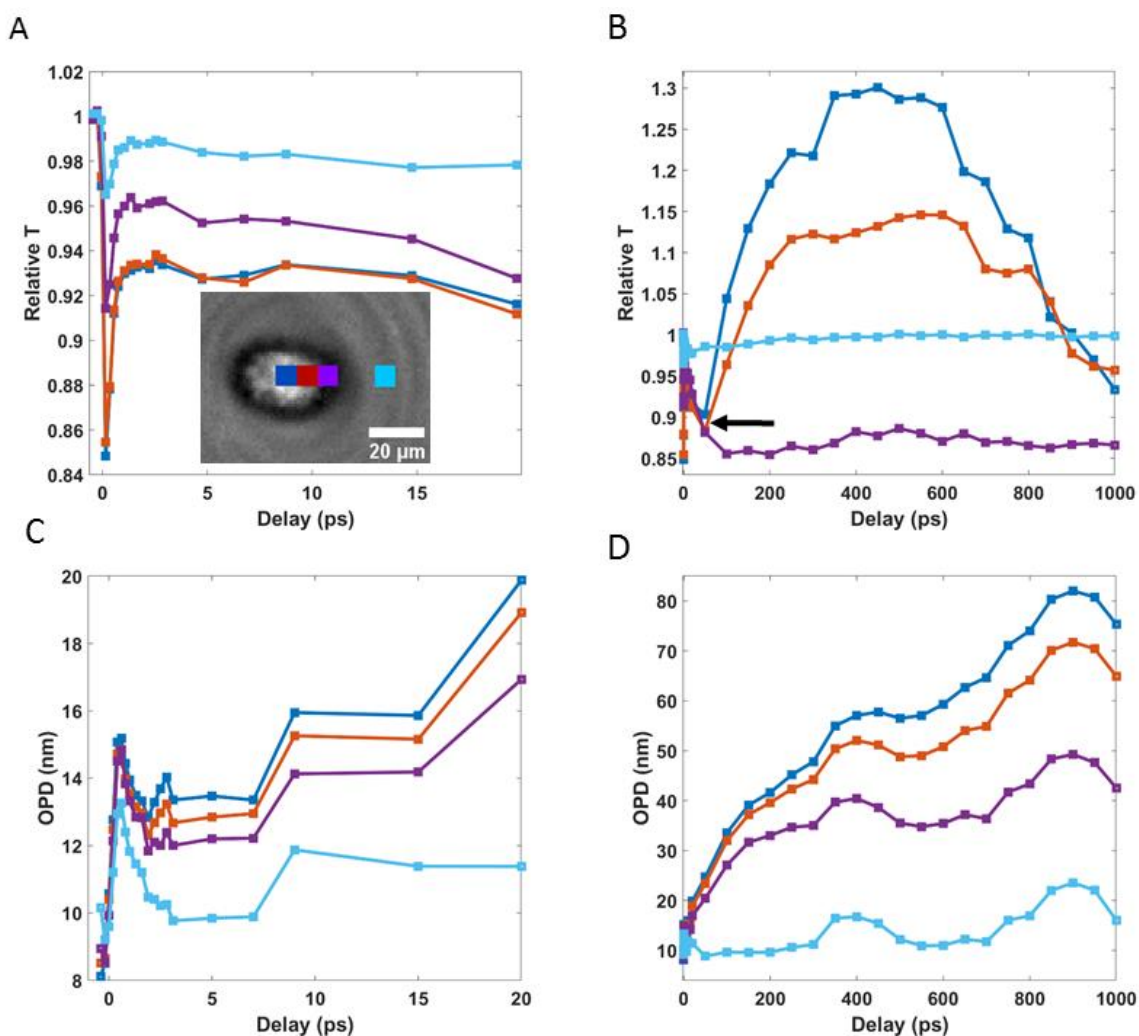


Figure 4.25 – Spatially-resolved relative transmittance and OPD traces. A: Ultrafast dynamics of relative transmittance at different spatial locations. The inset shows the transmission image of the sample at 200 ps. The colors of the curves in each image correspond to the colors of the rectangles in the inset image. B: Same as image A on longer time delays. The black arrow indicates the onset of the ablation mechanism, where the different curves start to deviate. C: Ultrafast dynamics of the OPD on short time delays. C: Same as image C on longer time delays. The probe wavelength is 630 nm.

The ultrashort dynamics of the transmittance reflects the electron plasma thermalization via e-e coupling. The signal amplitudes at the minimum reflects the variation of the temperature rise of the electron plasma with the local laser fluence, similarly to the results in the lower excitation

regime reported in Figure 4.11. Laser fluence-dependent dynamics is observed in longer time-scales during the heating of the surrounding. The deviation of the different curves starts at 50 ps indicated by the black arrow. Within the ablation region, the higher fluence results in stronger change in the transmittance (blue and red curves). Outside the ablated region, no specific dynamics is observed on this timescale (purple and cyan curves), *i.e.*, the strong spectral changes are finished before the cooling of the NP. The local laser fluence-dependent OPD increase reflects the heating and expansion of the laser affected area at different positions. The curves at different locations alter exclusively in amplitudes at any fixed delays. This can be easily interpreted as the lower local fluence results in lower local temperature rise. The general tendency of increasing optical thickness reproduces at any local fluences.

The temporal evolution of the spatially resolved transmittance and OPD probed at 450 nm are shown in Figure 4.26.

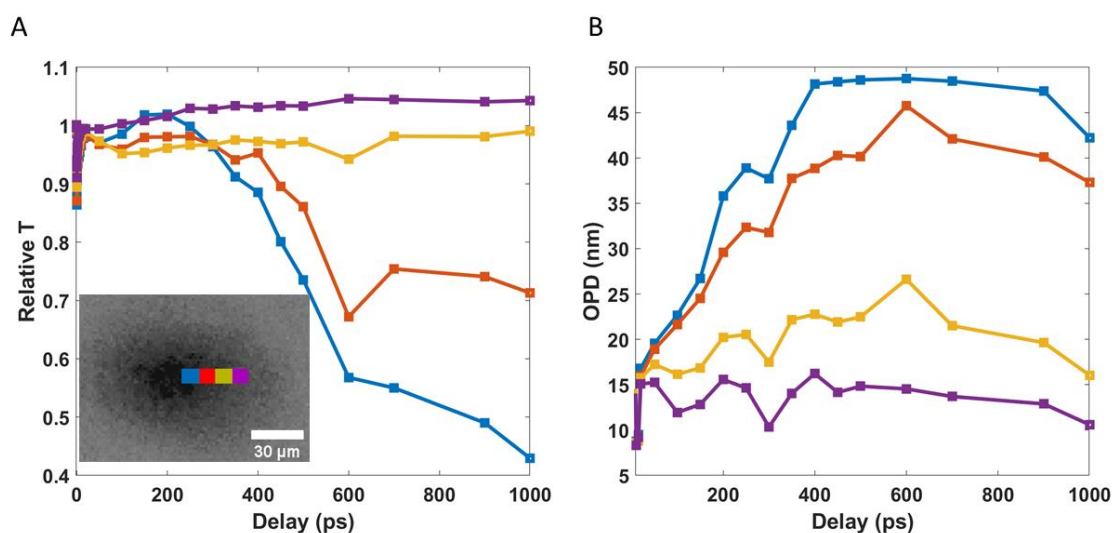


Figure 4.26 – Ultrafast dynamics recorded at 450 nm. A: Ultrafast dynamics of relative transmittance at different spatial locations. The inset shows the transmission image of the sample at 0.35 ps. The colors of the curves in each image correspond to the colors of the rectangles in the inset image. B: Ultrafast dynamics of the OPD at different sample locations which are the same as in image A.

In general, the blue probe wavelength also reflects the particular temporal dynamics of the ablation process, *i.e.*, the transmission increase starting at 50 ps, and the onset of the transmission decrease at 200 ps. Regarding the dynamics of the OPD at different local fluences, it exhibits similar tendency as the red wavelength (Figure 4.25). One important difference is that the OPD reaches a saturation value around 50 nm, which is not the case for the red wavelength.

The comparison between the wavelength-dependent transmission dynamics above 50 ps is shown in Figure 4.27, and it can be attributed to the formation of Newton rings as a result of

film bulge, and it is further evaluated in the following discussion section. The onset of the ablation process at both wavelength is at 50 ps indicated by the arrows in this figure.

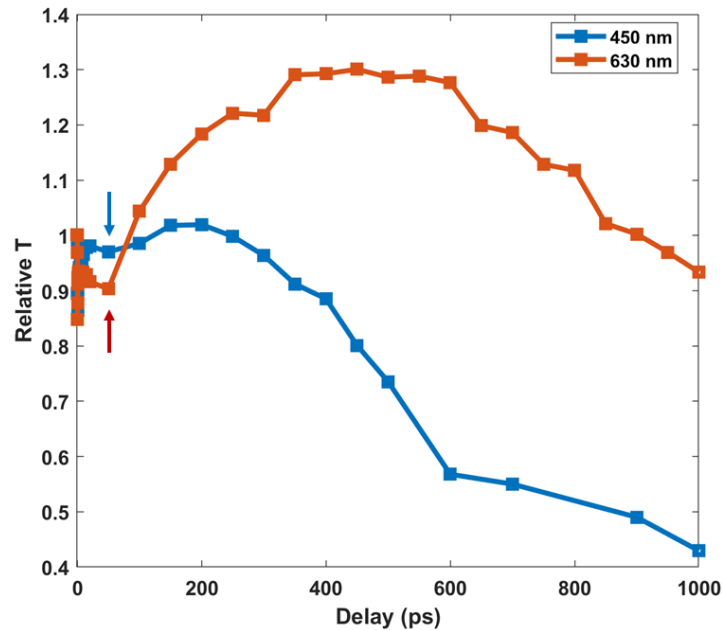


Figure 4.27 – Comparison of time traces at the two different probe wavelengths on long time delays. The arrows at 50 ps indicate the onset of the ablation process.

4.3.10 Discussion on ablation phenomena

The comparison between the results above and below ablation threshold reveals that relevant differences in the dynamics emerge on the scale of hundreds of ps delay. In the earliest time delays, the same mechanisms are expected to occur as discussed previously, *i.e.*, development of hot Fermi electron plasma, which relaxes via e-ph and ph-ph interactions. Indeed, the ultra-short time-resolved investigations of laser-induced ablation of metallic thin films reported the same mechanisms with additional processes due to the extreme high initial electron energies. The series of mechanisms described by other studies on laser ablation can be summarized as follows.

In the first ps, photon absorption, electron heating and ultrafast melting were described [198]. The ablation onset was estimated approximately around 10 ps, driven by phase explosion, when the laser fluence strongly exceeded the ablation threshold. In such conditions, the matter was ejected in a diffuse and cluster-like liquid–gas state [199], [200]. Using fluence just above the

ablation threshold was reported to cause stress confinement in the excited layer, forming a cavity between two interfaces followed by an ejection of the upper liquid shell, which was referred to as film spallation [198]. In the latter case, the detailed evolution of the pressure and stress is described in [201], and summarized for metals in the followings.

During the first few picoseconds, the temperature of the lattice rises without a significant increase in volume, resulting in a buildup of pressure in the heated layer. A strong pressure gradient is created. The high pressure in the heated layer relaxes via expansion along direction of the pressure gradient, toward the free surface. The pressure gradient below the heated layer launches a compressive wave into the bulk. Behind the compressive wave, a rarefaction wave follows that results in a buildup of a tensile stress in the material. At sufficiently high fluences, the mechanical stress is strong enough to overcome the cohesive strength of the metal leading to film damage, known as spallation, which is the dominant mechanism for material removal in metals. In this process, the metal melting temperature is reached, and the compressive and tensile stress evolves in the thin molten layer at the surface. As the tensile stress intensifies, free volumes (voids) in the hot liquid coalesce, further increasing the stress within the heated area. Eventually, it can exceed the cohesive strength of the liquid, the layer breaks releasing an upper liquid layer. In case of fs laser ablation of very thin films (thickness around 50 nm), rapid surface expansion was reported due to the generation of high compressive stress on the film surface and the buildup of small upward tensile stress on the film/substrate interface [202]. This tensile stress triggered the initial delamination of the film. When the high compressive stress propagating from the film surface inside the film reached the film/substrate interface, it enhanced the delamination, and the relaxation of high compressive stress caused surface deformation.

In studies above the ablation threshold, concentric ring pattern were observed in the ablated area in many studies [196], [203]. Such rings in the ablated spot originate from interference phenomenon. Light is reflected by the upper liquid layer and the stationary surface of the sample, and the two rays interfere. As the displacement of the moving layer increases (increasing dome height, film bulge), the phase difference between the reflected rays varies. It was demonstrated in previous studies that the speed of material ejected after fs laser irradiation is proportional to the local fluence [106]. In most experiments, the laser pulse has a Gaussian spatial distribution, therefore the ejected layer forms a dome with a spatial displacement proportional to the local fluence. With increasing phase difference between light rays reflected from the expanding layer and the stationary sample, the interference pattern will contain successive maxima and minima, whose numbers vary as the film expands. Such interference pattern is called Newton rings. In case of bulk materials, shock-wave injection into the solid was reported, while expansion of the ablation front started with a subsequent rarefaction wave after a few 10s ps

[204]. As a result, bulge of the heated area and formation of Newton rings were observed [205], [206].

In our sample, the sudden transmittance increase observed at 50 ps for both probe wavelength (Figure 4.25, black arrow and Figure 4.27, arrows) indicates the onset of the ablation processes. At earlier delays, development of hot Fermi electron plasma, and subsequent relaxation via e-ph and ph-ph interactions are expected to occur. The ablation starting at 50 ps is triggered upon sample heating generating high compressive stress, and the buildup of upward tensile stress relaxing via film expansion, as described previously in the case of very thin films and metals [201], [202]. Optically, in the present case, the peculiar increase and subsequent decrease observed at both probe wavelength (Figure 4.27) can be attributed to the dynamical evolution of the Newton ring pattern due to the film bulge. The intensity image at 1000 ps delay recorded at 630 nm clearly shows inside the laser-ablated area a dark center, a bright ring and a dark outer ring (Figure 4.23). Unfortunately, the 450 nm probe wavelength experiences stronger probe light scattering than the red wavelength due to the mixture of ablated material, shielding the sample surface, and it does not show any clear Newton rings pattern. Otherwise, wavelength-dependent ring spacing would be observable for the same delay. Similar shielding effect was reported in other studies, involving phase explosion that caused scattering of the probe pulse on the gas-liquid mixture [198], [203], [205]. One could expect that more rings would appear at 630 nm above 1000 ps. It is worth noting that the formation of the Newton rings in transmission configuration involves the interference between the transmitted direct light and the back-reflected light from the upper layer of the expanding layer. The strong heating and film expansion is further supported by the increasing OPD at both probe wavelength (Figure 4.25 and Figure 4.26). OPD variations of several tens of nm are clearly detected at both probe wavelengths, in relation with the overall heat-induced refractive index change ($\Delta n(t)$), and the bulge of the multilayer sample ($\Delta d(t)$).

At higher delays, a portion of the film lifts off, and eventually the separated film floats away on the microsecond timescale owing to its initial kinetic energy.

4.4 Conclusion

In this chapter, the ultrafast dynamics of the energy relaxation in fs-laser-excited Ag/TiO₂ nanocomposites was investigated both above and below the shape transformation threshold. In the latter case, the transient absorption spectra could be understood by the combination of photo-induced absorption and plasmon bleaching contributions of the LSPR bands in the steady-state absorbance spectrum. The characteristics of these resonances were transiently affected when

illuminating the sample with ultrashort laser pulses. Narrow resonance bands hidden in broader resonance bands could be clearly revealed by investigating the transient spectra.

In the high energetic region, below the ablation threshold, the shape transformation was shown to be governed by size reduction due to charge-assisted atomic desorption and local NP fragmentation processes, undoubtedly revealed by the *ex situ* electron microscopy investigations. Two-color pump-probe microscopy revealed the ultrafast dynamics of the pulse-to-pulse LSPR transformation. Additionally, slower reshaping process was evidenced after a few pulses ($N > 5$) with a definite onset at 200 ps, and lasting on a scale of hundreds of ps. Ag^+ diffusion within the TiO_2 matrix, nucleation and growth leading to the formation of spherical NPs on the surface, fragmentation and further NP reformation within the matrix were ascribed for this slower reshaping process. Beside the size reduction, the electron microscopy characterizations evidenced self-organized reshaping resulting from localized melting of NPs.

Slightly above the ablation threshold, the dynamical evolution of Newton ring pattern was probed at two wavelengths. The dynamics of the sample transmittance could be fairly described by considering the existing model of ultrafast laser ablation of thin metal films taking into account buildup of tensile stress, film expansion and subsequent Newton rings formation. The ablation onset is measured to 50 ps in our experiments. Due to the strong heating and structural transformation of the multilayer sample, the ultrafast evolution of the OPD was also possible to detect. OPD variation of several tens of nm was clearly detected at both probe wavelengths, in relation with the overall heat-induced refractive index change ($\Delta n(t)$), and the bulge of the multilayer sample ($\Delta d(t)$).

The combination of the multipulse shape transformation study presented in chapter 3 with the ultrashort dynamics of the NP reshaping detailed in this chapter enabled to conclude about several general aspects of the laser-matter interactions in such multilayer nanocomposites on a variety of timescales. The presented groups of results will be useful for further researches aiming to employ such materials in promising applications such as printed image multiplexing,

5 Investigation of coherent acoustic pulse emission by plasmonic NP ensembles

In the previous chapter, transient absorption spectroscopy revealed the relaxation of photoexcited plasmonic nanoisland ensembles, when pump laser fluence below the irreversible reshaping threshold was applied. Various heat energy relaxation pathways were discussed on different timescales following the instantaneous photon absorption. Beside the heat energy transfer to the surrounding, the metallic layer affects the matrix and the substrate via its mechanical transformation as well. The ultrashort nanoisland thermalization leads to a buildup of compressive stress within the layer, which further evolves into an acoustic wave travelling at the local speed of sound in the medium. Hereby, the pump photon energy is partially converted into mechanical energy that relaxes in the surrounding at the same time with the thermal relaxation of the heated NPs. In this chapter, the excitation and propagation of acoustic waves emitted by random plasmonic NPs are investigated. The dynamics of the energy dissipation of the acoustic pulse during its propagation in glass medium is characterized. This work was carried out in collaboration with the FemtoNanoOptics group of Institut Lumière Matière in Villeurbanne, France.

5.1 Introduction

Efficient coupling between light pulses and the acoustic phonons of a material can be realized using different types of opto-acoustic transducer, enabling the generation of coherent wavepacket of phonons with picoseconds pulse duration and spatial extent in the range of tens of nm. Such acoustic pulses find applications in nanoscale imaging of mechanical properties [18], or in fundamental studies on frequency-dependent sound attenuation, *e.g.* in disordered media [207]–[209]. Thin metallic films are frequent choices for opto-acoustic transducers [210], [211]. Several investigations were also conducted with size-reduced transducers, which are crucial for improving the lateral resolution in imaging applications (lateral resolution being limited by diffraction to a few hundreds of nm in the film case). Quantum wells were for instance used as acoustic sources [212].

Additionally, attempts were made for using single metallic NPs as transducers, whose vibrational eigenmodes have been widely investigated [13], [38], [39], [213]–[217]. Guillet *et al.* detected ultrasonic waves emitted by a single submicronic Au particle in the surrounding silica matrix using picosecond ultrasonics technique [218]. Single cylindrical shaped Au NPs on a

silicon wafer were demonstrated to exhibit excellent potential for transduction of bulk transverse waves [219]. Yu *et al.* demonstrated that laser excitation of a single Au micrometer-sized nanoplate efficiently generates longitudinal acoustic waves in glass substrate, which were detected by their associated Brillouin oscillations [220]. Hypersounds emitted by a single copper nanowire in the surrounding silicon membrane were also detected [221]. Another study evidenced that a single Au nanorod can act like an opto-acoustic nanosource of propagating longitudinal acoustic wave in silica substrate [222]. Beside the acoustic pulse emission into the bulk matrix, hypersonic surface waves can be excited, as well as detected, using single plasmonic nanoantennas [223].

Ensembles of metal NPs represent an intermediate case between those discussed above (continuous film and single NP). In earlier studies, near-coalescence metallic nanoislands were demonstrated as excellent candidates for fabricating nanoscale electronic components [224]–[226], surface enhanced Raman scattering [227] and pioneering sensing approaches [228]. Additionally, there have been numerous investigations on excitation of acoustic vibration modes on NP ensembles. These studies, mostly performed on NPs embedded in a solid matrix or in solution, have in particular addressed in detail the size, shape and environment dependence of vibrational frequencies [15], [229]–[235].

In this chapter, the excitation and propagation of coherent acoustic pulses emitted by a layer of Ag NPs with broad size dispersion are investigated. Following the description of the theoretical grounds of acoustic pulse excitation and detection, samples with different morphological properties (various interparticle distances and NP shapes) are characterized. The features of the acoustic waves emitted by the samples with various NP morphologies are investigated using a simplified theoretical model, allowing to better understand at which condition they are similar to those of the waves emitted by the traditional continuous thin films.

5.2 Principles of coherent acoustic pulse excitation and detection

5.2.1 Opto-acoustic conversion

When intense ultrashort laser pulse is absorbed by a thin metallic layer, the photon energy is converted into high-energy electron distribution, whose energy relaxes back to equilibrium with the surrounding resulting in a rapid increase in the temperature of the metallic layer, and thereby a compressive stress is generated.

The laser-induced temperature depth-profile $\Delta T(z)$ in the metal film can be approximated as [236]

$$\Delta T(z) = (1 - R) \frac{Q}{\rho A \zeta c_V} e^{-z/\zeta}, \quad (5.1)$$

where R is the reflection of the pump beam on the air/metal interface, A is the irradiated area, ζ is the skin depth, Q is the pulse energy, ρ is the material density and c_V is the specific heat at constant volume. The small absorption length in the metal being much smaller than the typical focal spot sizes of focused Gaussian laser beams ($\sim \mu\text{m}$ range) justifies the consideration of generation of solely longitudinal acoustic phonons by the pump laser. Additionally, the film is assumed to be elastically isotropic. The temperature distribution according to Eq. (5.1) results in an isotropic thermal stress $\sigma(z)$ given as

$$\sigma(z) = -3K\alpha\Delta T, \quad (5.2)$$

where K is the bulk modulus and α is the linear expansion coefficient. The developed strain can be represented by the strain tensor, whose elements equal zero except η_{33} due to the sole presence of longitudinal strain. The solution of the equations of elasticity provides the analytical expression for $\eta_{33}(z, t)$ [236]. Strain wave is launched in both the positive and negative z directions in the film [237], bounce back and forth, and get partially transmitted into the substrate each time it hits the metal/substrate interface. Each back-reflection from the metal/substrate interface reduces the amplitude of the strain wave by a reflection factor

$$r_{ac} = \frac{Z_S - Z_f}{Z_S + Z_f}, \quad (5.3)$$

where Z_S and Z_f are the acoustic impedances of the substrate and the metallic film, respectively [238]. The acoustic impedances can be calculated as the product of the density and the sound velocity in the media. The strain wave is totally back-reflected with change of sign when reaching the air/metal interface to become a tensile (positive) stress wave, resulting in a strictly antisymmetric spatio-temporal profile [237]. The strain wave in the substrate has a spatial extent of

$$d' = d_f \cdot \left(\frac{v_s}{v_f} \right), \quad (5.4)$$

after crossing the metal/substrate interface, where d_f is the thickness of the metallic film, v_s and v_f are the sound velocities in the substrate and the film, respectively.

The typical shape of the strain pulse penetrating the substrate as a function of the distance from the metal layer/substrate interface is illustrated in Figure 5.1.

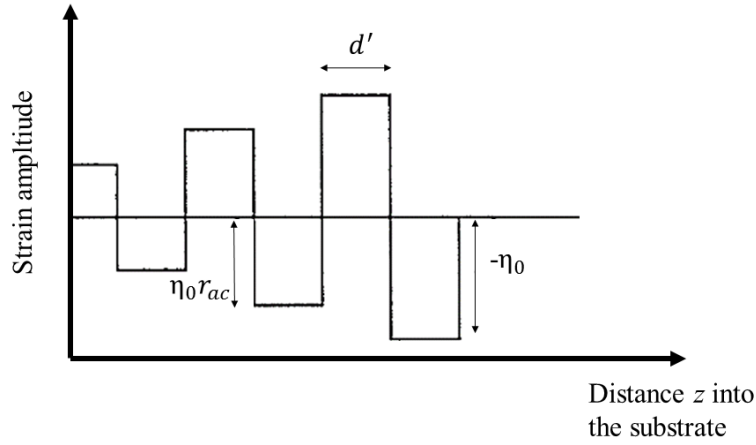


Figure 5.1 – Shape of acoustic strain pulse generated in a metallic thin film and transmitted into the substrate. The notation is described in the text.

The initial amplitude η_0 of the zig-zag function can be expressed as [238]

$$\eta_0 = \frac{1 + \nu}{1 - \nu} \beta \Delta T \frac{2Z_f}{Z_s + Z_f} \frac{\nu_f}{\nu_s}, \quad (5.5)$$

where ν is the Poisson's ratio of the film, β is the linear thermal coefficient. The sign of the initial amplitude indicates the fact that the strain wave begins with a compression in the substrate, the strain component has a negative value. The strain pulse has a typical pulse duration of a few ps, consequently its Fourier frequency spectrum is broad spanning in the range of a few tens of GHz up to hundreds of GHz [239]. The spectral content is strongly dependent on the thickness of the metallic thin film and on the properties of the interfaces within the material [237].

5.2.2 Principles of detecting the acoustic pulse propagation

Picosecond acoustic technique is a common approach to access the spectral properties of the generated strain pulse. The principle of the experimental arrangement is shown in Figure 5.2. The general idea is that time-delayed optical pulse probes the temporal evolution of the strain wave-packet. The signal measured in the typical picosecond acoustic experiments arises from an interference phenomenon.

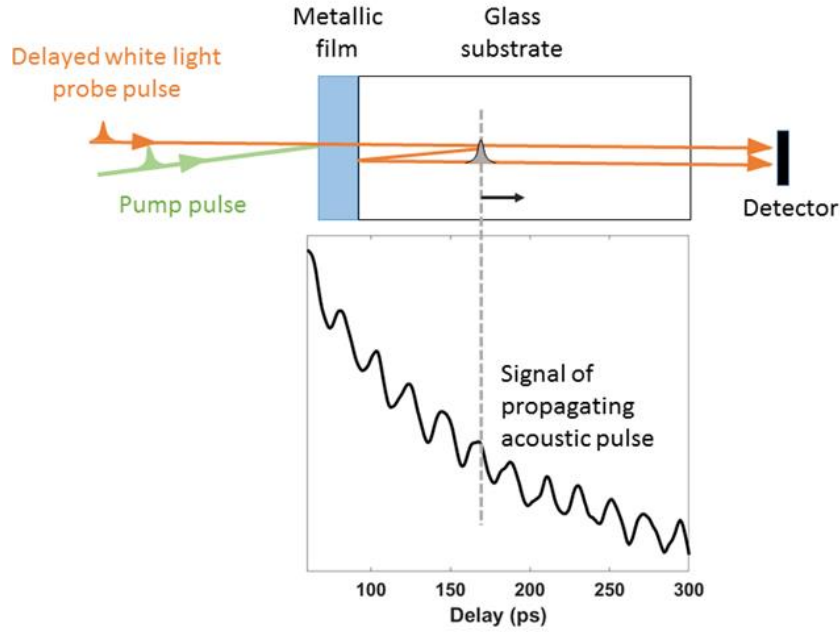


Figure 5.2 – The experimental arrangement for detecting the acoustic pulse propagation in the substrate emitted by a metallic film using pump-probe technique. A typical time-resolved signal is shown for illustration.

The probe laser light is partially back-reflected from local modification of the refractive index of the medium produced by the presence of the strain pulse through the photoelastic effect, *i.e.*, $\Delta n = \frac{\partial n}{\partial \eta} \eta$, where Δn is the local refractive index variation due to the strain η . The back-reflected portion of the beam escapes the sample after reflection on the transducer layer, and interferes with the transmitted light in the detector.

The phase relation between the interfering light paths constantly varies due to the propagation of the strain pulse at the local speed of sound in the medium giving rise to an oscillating signal in time domain corresponding to constructive and destructive interferences. The period of the oscillating signal can be determined based on simple optical phase calculations. If the light phase shift δ equals 2π between reflected light paths from the strain pulse at the spatial positions of Z and $Z + \Delta Z$, then one can write

$$\delta = \frac{2\pi n}{\lambda} 2vT = 2\pi, \quad (5.6)$$

where n is the refractive index of the medium, λ is the probe wavelength in vacuum, v is the phase velocity of strain wave, and T is the time of wave propagation between Z and $Z + \Delta Z$. From Eq. (5.6), one can express T as

$$T = \frac{\lambda}{2nv}. \quad (5.7)$$

T corresponds to the period of the oscillating signal in the time-resolved experiments (Figure 5.2). In the case of an angle of incidence θ different from 0° , the denominator contains a multiplicative factor $\cos \theta$. If one measures the period of the sinusoidal oscillation at a given probe wavelength, knowing the refractive index of the medium, one can determine the sound velocity. If the sound velocity has a gradient in the function of the propagation distance in the medium, it results in a sinusoidal signal with varying frequency.

The interaction between the probe photon and the acoustic wave composed of acoustic phonons, known as Brillouin scattering, is governed by the law of the momentum conservation [240]. One monitors the time evolution of the spatial Fourier component with wave number $\vec{q} = \pm\Delta\vec{k}$ in an optically excited acoustic wave-packet, where $\pm\Delta\vec{k}$ is the modification of the photon wave vector after scattering from the strain. There are two kinds of the scattering interaction referred to as Stokes and Anti-Stokes component. In the configuration shown in Figure 5.2, *i.e.*, strain pulse moving away from the light beam, Stokes component has to be considered. One can express the phase-matching condition in the case of the Stokes component as

$$\vec{k}_{bs} = \vec{k}_0 - \vec{q}, \quad (5.8)$$

where \vec{k}_{bs} is the wave vector of the back-scattered photon, \vec{k}_0 is the wave vector of the initial photon, and \vec{q} is the phase-matched acoustic wave vector [241]. The corresponding angular frequency relationship in the interaction is expressed as

$$\omega_{bs} = \omega_0 - \omega_{phonon}, \quad (5.9)$$

where ω_{bs} is the angular frequency of the back-scattered photon, ω_0 the initial photon angular frequency, ω_{phonon} is the angular frequency of the acoustic phonon involved in the scattering process. The frequency of the back-scattered photon is downshifted by the frequency of the phase-matched Fourier component, which is referred to as Brillouin-shift in the literature. This frequency shift is typically negligible considering the spectral width of the probe pulse [237]. The same relationships in the case of the Anti-Stokes scattering components are expressed as

$$\vec{k}_{bs} = \vec{k}_0 + \vec{q}, \quad (5.10)$$

and

$$\omega_{bs} = \omega_0 + \omega_{phonon}. \quad (5.11)$$

Assuming normal angle of photon incidence, the probe photon with k wave number is back-scattered from the phase-matched phonon of the strain wave-packet, which has a wave number $q = 2k$ and angular frequency $\omega_{phonon} = 2kv$, where v is the sound velocity. From the expression of the phonon angular frequency

$$\omega_{phonon} = 2kv = 2 \frac{2\pi n v}{\lambda}, \quad (5.12)$$

one obtains immediately the relationship between the frequency of the phase-matched phonon and the period of the sinusoidal vibration in the time-resolved signal in Eq. (5.7) as

$$f_{phonon} = T^{-1}. \quad (5.13)$$

The amplitude of the oscillating signal that one measures using a single probe wavelength is proportional to the amplitude of the phase-matched phonon of the acoustic wave-packet. In consequence, the damping of this component becomes possible to monitor by investigating the attenuation of the signal oscillation amplitude. In our data analysis in the result section, we investigate the sound attenuation of different acoustic frequencies in glass medium.

5.3 Multilayer samples with different Ag thicknesses

The steady-state transmittance spectra of each sample investigated in this study is reported in Figure 5.3. Multilayer Ag/TiO₂ samples with different nominal Ag thicknesses are prepared on N-BK7 glass substrate using the same preparation method and conditions described in the Experimental methods section of chapter 3. The chemical composition of the substrate is provided as 69.13 SiO₂, 10.75 B₂O₃, 10.40 Na₂O, 6.29 K₂O, 3.07 BaO and 0.36 Sb₂O₃ in wt %. Three samples with initial Ag thicknesses of 1.5 nm, 5 nm and 10 nm are prepared. Additionally, the sample containing 5 nm thick Ag layer was submitted to laser processing by 515 nm wavelength using 31 mJ/cm² laser fluence in order to persistently reshape the initial NP size and shape distribution. The experimental conditions are described in the next section. The thicknesses of both TiO₂ layers are fixed at 30 nm in all samples.

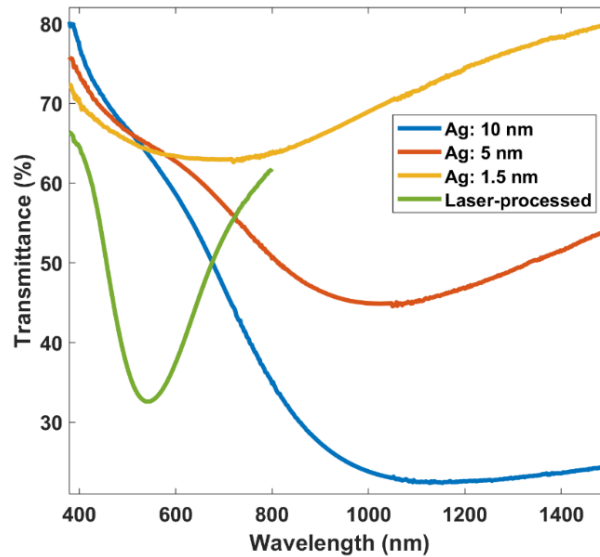


Figure 5.3 – Steady-state transmittance spectra of the samples. The nominal thicknesses of the initial samples are indicated in the labels. In the followings, the same nomenclature is used to identify the different samples.

5.4 Results and discussion

5.4.1 Detection of acoustic pulse propagation

In Figure 5.4 panel A, the first three columns contain HAADF-STEM images of the samples with different initial nominal thicknesses (10 nm, 5 nm and 1.5 nm), the corresponding cross-section images and the 2D maps of transient absorption spectra after thermal background removal. The fourth column contains an additional measurement performed on the *Ag: 5 nm* sample after submission to laser processing by 515 nm wavelength using 31 mJ/cm² laser fluence in order to persistently reshape the initial NP size and shape distribution. Laser inscriptions are performed on a laser-processed area of 5-by-5 mm². Strongly overlapping parallel laser lines (line separation of 2 μm) are inscribed by constant scanning speed corresponding to $N_{eff} = 6000$. The setup is the same as described in chapter 3, without the use of the supercontinuum source (Figure 3.2). As a result of the laser inscription, rather spherical NPs distribution with considerably smaller filling factor is achieved. As revealed by the cross-section HAADF-STEM image of this sample, the multilayer system collapses into a single layer of TiO₂ with NPs embedded due to the high laser-induced temperature rise in the material. The mechanisms are described

in details in the discussion section of chapter 3. In each cross-section image, Ag content is observable in the TiO₂ layers, which results from the STEM lamella preparation. Pump wavelengths are chosen to directly excite the LSPR of the different samples, *i.e.*, 1100 nm, 1000 nm and 700 nm respectively for the three initial samples with decreasing Ag thicknesses, and 540 nm for an additional laser-processed sample.

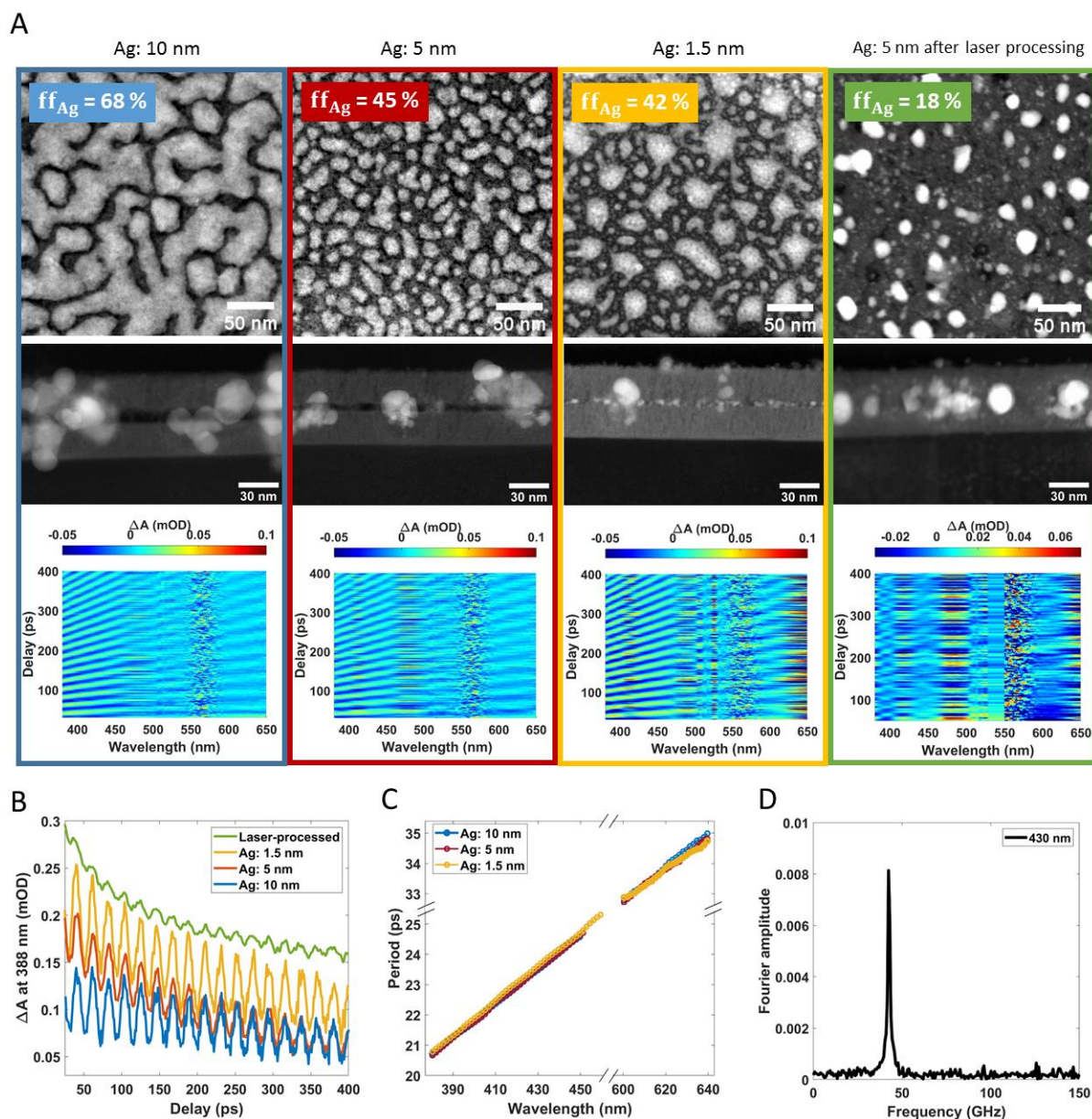


Figure 5.4 – Investigations of acoustic pulse emission. A: Plan-view and cross-section HAADF-STEM images of the different samples, and the 2D maps of the corresponding transient absorption spectra after thermal background subtraction highlighting the Brillouin signals. ff_{Ag} stands for Ag filling factor. Note that even the laser-processed sample, the 2D carpet evidences small amplitude Brillouin signal between 380 and 400 nm. B: Example time traces probed at 388 nm for each sample before background removal (raw experimental data). The trace of the laser-processed sample (green) is shifted vertically for clear observation of the residual Brillouin oscillation. C: Plot of vibration period vs probe wavelength for the

different samples. The data from the laser-processed sample is not plotted due to the small vibration amplitude and wavelength range. D: Fourier amplitude spectrum of the representative probe wavelength of 430 nm (from Ag: 10 nm sample) indicating the presence of a single frequency component of 42.7 GHz.

The comparison of the STEM images at different nominal thicknesses reveals two main structural characteristics. Firstly, the correlation between the Ag thickness and the average neighboring distance between the adjacent NPs, *i.e.*, smaller Ag thickness results in higher NP separation. This results in smaller LSPR coupling, reflected as a blue-shifting resonance in the steady-state spectra (Figure 5.3). Secondly, the morphology and connectivity of the film NPs, *i.e.*, the thickest sample contains highly connected complex structures, which transform into more simple distributions of clearly separated rod-like (Ag: 5 nm) and rather spherical particles (Ag: 1.5 nm and laser-processed sample). In the latter two cases, NP diameters vary on a scale from a few nm until few tens of nm (typically 30 nm – 40 nm), and the average interparticle distance is estimated in the range of 10 nm and less in all samples (*ImageJ* software was used for evaluation). The Ag: 10 nm sample is the one with the morphology closest to the one used in traditional time-domain Brillouin scattering experiments, where continuous metallic layers with typical thicknesses around 10 nm are used as transducers.

The 2D carpets of the transient absorption spectra reveal the presence of an oscillatory signal for all samples (Figure 5.4A), which is ascribed to Brillouin oscillations induced by the propagation of an acoustic pulse in the underlying glass substrate. The amplitudes of these oscillations exhibit strong probe wavelength-dependence. Beside the observed large amplitudes, Brillouin oscillations are not detected in the spectral region 540 nm – 590 nm due to low probe intensity, and the amplitude is strongly disturbed by noise in the region 450 nm – 490 nm. It is important to notice that the 2D carpet of the laser-processed sample also contains an oscillatory signal component in the reduced wavelength range of 380 nm – 400 nm. However, its amplitude is considerably smaller than that of the three intact samples. Figure 5.4B shows the example time trace of 388 nm for the four samples (the green curve is shifted vertically for clarity). The limited efficiency for the coherent pulse excitation in the case of the laser-processed sample is attributed to the low NP filling factor, and it will be investigated in the numerical investigation section of this chapter.

Figure 5.4C shows that the period of the vibrations linearly increases with probe wavelength from 20.8 ps to 35.3 ps for the three intact samples, in agreement with Eq. (5.7) and the low dispersion of the glass refractive index on this probe wavelength range. The period at each probe wavelength is determined based on averaging 10 oscillations. Figure 5.4D shows the

Fourier amplitude spectrum of a representative time trace at 430 nm (*Ag: 10 nm* sample) with a single spectral peak at 42.7 GHz, which is the phase-matched acoustic phonon frequency at this particular wavelength.

The sound velocity of 5993 ± 14 m/s in N-BK7 is determined based on the expression of the oscillation period in Eq. (5.7) using the average of the oscillation periods at each probe wavelength and the refractive index spectrum of N-BK7 provided by Schott. We can assume that each frequency component propagates with the same phase velocity. For comparison, the sound velocity in vitreous silica thin films measured by the same experimental technique reported by Ayrinhac *et al.*, 5995 ± 10 m/s is very close to our value [237]. The similarity of these determined sound velocities is consistent with the fact that silica is the main component of N-BK7 glass.

The amplitude of the oscillations exhibits a non-monotonic decrease tendency towards longer probe wavelength, as shown in Figure 5.5 for the three intact samples.

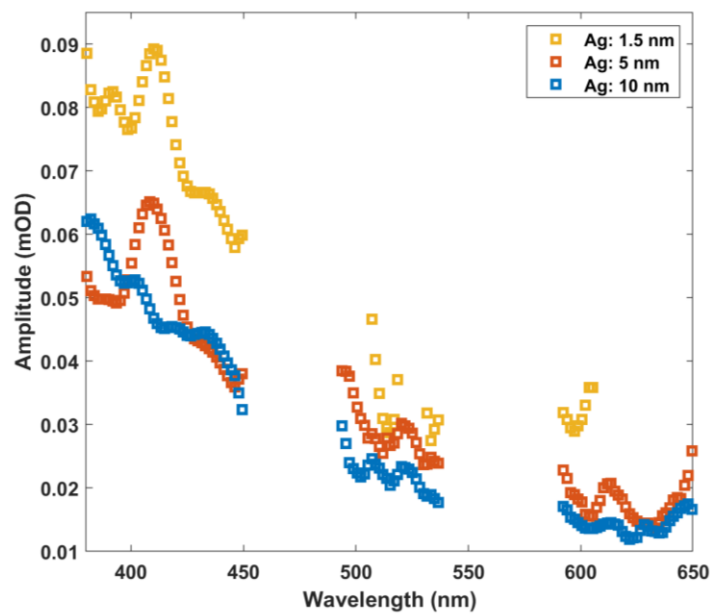


Figure 5.5 – The probe wavelength dependence of the Brillouin signal’s amplitude for the different samples.

The amplitude values contain the average of the first three cycles in the vibration for each wavelength. The decreasing tendency in the oscillation amplitude is not related to the excitation of the acoustic pulse since the power of the pump laser is identical for all the probe wavelengths, nor to the spectral intensity profile of the probe laser. One should note that the probe photon energy for a shorter wavelength is higher and closer to the energy band gap of the N-BK7 glass substrate. For Schott BK7 borosilicate glass, the energy band gap was calculated from the transmission spectrum of the glass to be 4.28 eV [242]. The 380 nm probe should be more sensitive

to the band gap energy modulation induced by the traveling acoustic pulse, but less for higher probe wavelengths with lower energies. In other words, the photoelastic coupling for the N-BK7 glass is stronger for a blue probe wavelength than for a longer wavelength [243].

Ishioka *et al.* studied the probe wavelength-dependence of Brillouin oscillations in GaP and Si [244]. They measured that the differential reflectivity amplitude of the oscillations increased significantly for GaP towards shorter probe wavelength, but moderately for Si. Baydin *et al.* measured drastic increase of the amplitude of Brillouin oscillations toward higher probe energies, maximized near the direct optical transitions of GaP [245]. Above the direct band gap, a nontrivial wavelength-dependence was measured. The authors developed a theoretical model to quantitatively explain the oscillation amplitude-photon energy dependence. Assuming weak strain amplitudes, *i.e.*, strains $< 10^{-4}$, a simple expression was derived stating that the differential reflectivity amplitude of the Brillouin oscillation is proportional to the photon energy derivative of the complex dielectric function $\epsilon(E)$ of the medium, where the pulse propagates [245]:

$$A_{osc} \propto \left| \frac{\partial \epsilon}{\partial E} \right| = \sqrt{\left(\frac{\partial \epsilon_r}{\partial E} \right)^2 + \left(\frac{\partial \epsilon_i}{\partial E} \right)^2}, \quad (5.14)$$

where ϵ_r and ϵ_i are the real and imaginary parts, respectively. Thereby, the dielectric function of the medium in which the acoustic pulse propagates determines the probe wavelength-dependence of the Brillouin oscillation's amplitude. Qualitatively, the non-monotonic decreasing tendency of the measured oscillation amplitude in the present case (Figure 5.5) could be also related to the $|\partial \epsilon / \partial E|$ spectrum of the glass substrate. In glass, one can neglect the second term in Eq. (5.14) in the visible wavelength range as $\epsilon_i \ll \epsilon_r$, therefore the oscillation amplitudes is determined by the energy derivative of the real dielectric function. The spectra of ϵ_i and ϵ_r , and the calculated $|\partial \epsilon / \partial E|$ for N-BK7 are reported in Figure 5.6. Due to the rapidly decreasing vibration amplitude the wavelength-dependent attenuation is investigated exclusively for the spectral region of 380 nm – 450 nm in the followings.

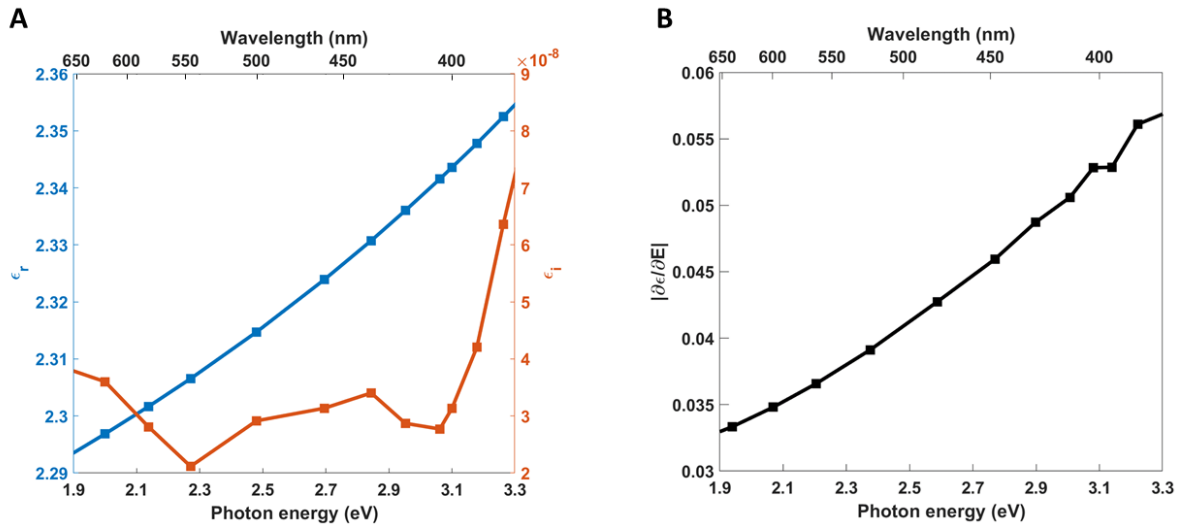


Figure 5.6 – A: Variation of real and imaginary parts of the dielectric function with photon energy (wavelength) for N-BK7 glass. B: The variation of the absolute value of the photon energy derivative.

The logarithm of the oscillation amplitude as a function of the oscillation number is demonstrated in Figure 5.7 using the example time trace of 430 nm, where circles show the determined amplitude of the oscillations, and red solid line shows linear fit to the data points.

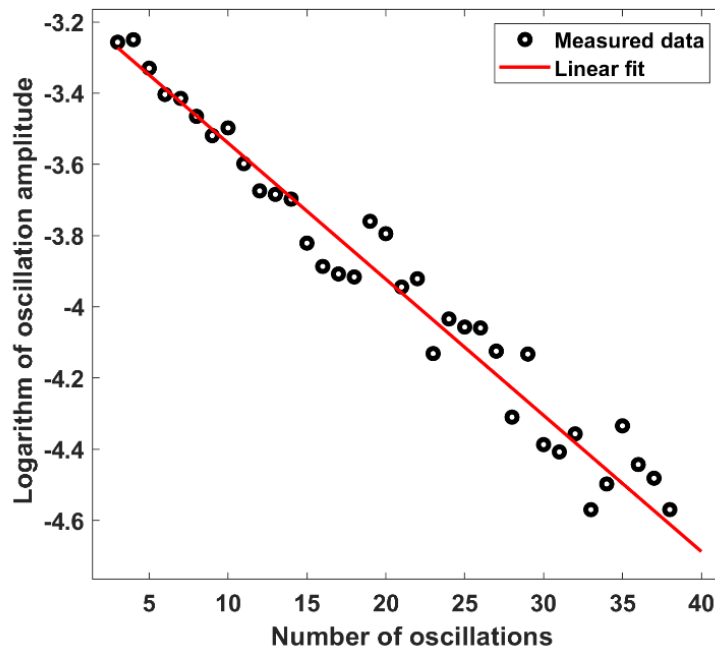


Figure 5.7 – The decay of the logarithm of the oscillation amplitude with increasing oscillation number for the representative example time trace of 430 nm (from Ag: 10 nm sample). The linear fit to the measured data points is indicated by red line.

The data fit on a straight line in presence of exponential decay of the phase-matched phonon during the propagation. Deviation from exponential decay would indicate acoustic pulse diffraction, *i.e.*, spreading of the pulse during propagation, or significant density of inhomogeneities inside the glass [238]. Each oscillation corresponds to an acoustic pulse propagation by a distance of $\lambda_0 / 2n$. Until the coherent signal is lost (~ 1000 ps), the strain pulse propagates a distance of about ~ 6 μm away from the NP layer in the bulk glass.

From the fit of the experimental data to the straight line, one can conclude that the amplitude $A(d)$ decays exponentially with increasing propagation distance d : $A(d) \propto e^{-\alpha d}$, where α is the attenuation coefficient determined from the linear fit. In the followings, the acoustic frequency-dependent attenuation is investigated in details.

5.4.2 Acoustic frequency-dependent attenuation in disordered materials

The α attenuation coefficient is determined for each probe wavelength in the range 375 nm – 460 nm for the three intact samples, covering the acoustic frequency range 39.6 GHz – 48.1 GHz that is obtained as the inverse of the oscillation periods. The acoustic linewidth parameters that would have been measured in a scattering experiment [246]–[249] are calculated as $\Gamma/2\pi = \alpha v/\pi$, where v is the previously obtained sound velocity in N-BK7. The obtained linewidth values are reported in Figure 5.8. For comparison, data measured in pure SiO₂ from visible Brillouin light scattering (vis-BLS) technique at three scattering angles [250], and from UV-BLS technique measured at two angles [251] or at two wavelengths [252] are also plotted.

The acoustic frequency dependence of the sound attenuation in disordered materials originates from an interplay of several physical mechanisms from the ultrasonic to the THz frequency regions at different temperatures. The room temperature sound damping is ruled by two main mechanisms in the acoustic frequency region of few tens of GHz until a few hundreds of GHz; *i.e.*, internal friction due to anharmonic interactions of the acoustic waves with the thermal phonon bath, and the thermally activated relaxation (TAR) of structural inhomogeneities [237], [253]. At 35 GHz and room temperature, the sound damping due to anharmonicity contributes nearly twice compared to thermally activated relaxation [254]. This results in a nontrivial frequency dependent attenuation, however, the tendency could be approached by a quadratic scaling in agreement with the Akhiezer mechanism [239], [255]. This was supported by experimental characterizations using ultrasonics and Brillouin light scattering [250]–[252]. Theoretical models have been developed and proposed to describe the relaxation processes of sound

attenuation in glasses [209], [256]–[258]. Towards higher frequencies, the contribution of TAR exhibits saturation and anharmonicity becomes the dominant source of sound damping approaching the frequency region of ~ 200 GHz. Further increasing acoustic frequencies around \sim THz exhibits damping proportional to the fourth power of the acoustic frequency as measured in densified silica and lithium diborate glasses by inelastic x-ray scattering [247], [248]. The increased rate of damping is expected for elastic scattering in a statistically disordered medium, compatible with the Rayleigh law [255], [259]. In the middle acoustic frequencies in the region of hundreds of GHz until the onset of the Rayleigh regime, a non-trivial frequency dependence was reported by several experimental works [237], [253], [260], [261].

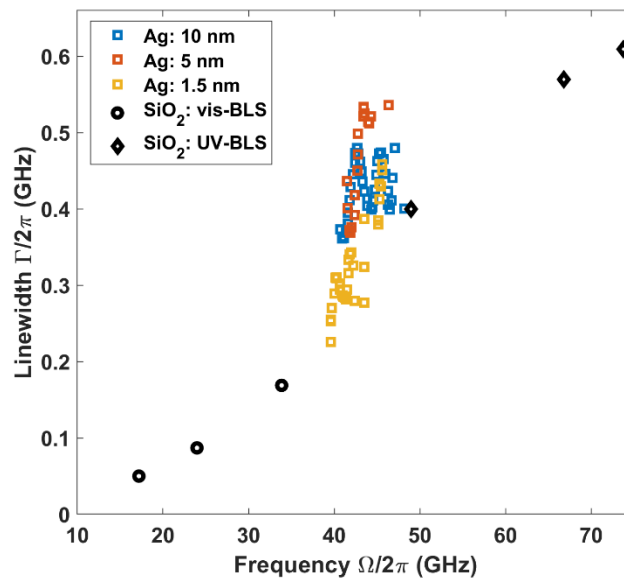


Figure 5.8 – The measured linewidth parameters in the function of the acoustic frequency for the different samples. Data obtained in pure SiO₂ measured by visible BLS [250] and UV-BLS [251], [252] techniques are plotted for comparison.

As shown in the reference [237], the data points from the BLS experiments in Figure 5.8 align precisely to the theoretical prediction of the sum of anharmonicity and TAR mechanisms with nearly two times stronger contribution from anharmonicity. Based on the quantitative fit of our data points among the BLS data, we suggest that these two mechanisms rule the sound attenuation in the present N-BK7 multicomponent glass as well in the acoustic frequency region of tens of GHz.

5.4.3 Numerical investigation of acoustic wavefront distortions

As previously discussed, the work demonstrates that a discontinuous metallic layer made of near-coalescence nanoislands or well-separated NPs can generate optically detectable acoustic waves in its supporting glass substrate. In the following, we describe a simple 2D model built to qualitatively explain this experimental observation and better understand the relation between the morphological properties of a NP layer and the features of the acoustic waves that it produces. The model is developed by Dr. Aurélien Crut from FemtoNanoOptics group of Institut Lumière Matière in Villeurbanne, France.

This model addresses the simplified case of an infinite one-dimensional chain of uncoupled, point-like emitters with non-uniform density, emitting scalar waves in a half-plane, whose attenuation upon propagation is neglected. The density of emitters is described by a function $f(a)$, with a the spatial coordinate along the emitter chain (located at $z = 0$). All emitters are assumed to generate coherent acoustic pulses of same angular frequency $\omega = 2\pi f$ and duration τ , described by the damped oscillating function of time $h(t)$ such as (using complex notation) :

$$h(t) = \begin{cases} 0 & \text{if } t < 0 \\ e^{-\frac{t}{\tau}} e^{i\omega t} & \text{if } t \geq 0. \end{cases} \quad (5.15)$$

The wave created at a (x, z) point located at a distance z from the 1D emitter chain results from the interferences between the circular waves generated in the $z > 0$ half-plane by all the emitters. Its complex amplitude $A(x, z, t)$ thus writes, introducing $a' = a - x$:

$$A(x, z, t) = \int_{-\infty}^{\infty} f(a' + x) \frac{h\left(t - \frac{\sqrt{a'^2 + z^2}}{c_L}\right)}{(a'^2 + z^2)^{\frac{1}{4}}} da', \quad (5.16)$$

where c_L denotes the speed of sound in the $z > 0$ half-plane, and $\sqrt{a'^2 + z^2}$ corresponds to the distance between the emitter located in $(a, 0)$ and the point in (x, z) , where the amplitude is calculated. Since $h(t) = 0$ for $t < 0$ (Eq. (5.15)), $A(x, z, t) = 0$, when $t < \frac{z}{c_L}$, *i.e.*, time is needed for acoustic waves to cover the distance z . At slightly larger times $t = \frac{z}{c_L} + t'$ such that $t' \ll \frac{z}{c_L}$, the emitters with non-zero contribution to the integral of Eq. (5.16) are located in a spatial region such that

$$|a'| \leq \sqrt{(c_L t)^2 - z^2} = a'_{max}(z, t), \quad (5.17)$$

with $a'_{max}(z, t) \approx \sqrt{2zc_L t'} \ll z$. The $(a'^2 + z^2)^{\frac{1}{4}}$ denominator appearing in Eq. (5.16) can then be approximated as \sqrt{z} , while the oscillating function $h\left(t - \frac{\sqrt{a'^2 + z^2}}{c_L}\right)$ can be approximated as $h\left(t - \frac{z}{c_L} - \frac{a'^2}{2c_L z}\right)$. Equation (5.16) then becomes

$$A(x, z, t) \approx \frac{e^{\left(-\frac{1}{\tau} + i\omega\right)t'}}{\sqrt{z}} \int_{-a'_{max}(z, t)}^{a'_{max}(z, t)} f(a' + x) e^{\left(\frac{1}{\tau} - i\omega\right)\frac{a'^2}{2c_L z}} da'. \quad (5.18)$$

The $f(a)$ density can be generally written as $f(a) = \bar{f} + f_{fluct}(a)$, with \bar{f} being its average value. Separating the contributions of \bar{f} and $f_{fluct}(a)$ in the integral of Eq. (5.18), and expressing the former one A_{film} (corresponding to a constant emitter density, as e.g. in the thin film case) as a function of the sole $t' = t - \frac{z}{c_L}$ variable using the *erf* error function, Eq. (5.18) can be rewritten as

$$A(x, z, t) \approx A_{film}(t') + \frac{e^{\left(-\frac{1}{\tau} + i\omega\right)t'}}{\sqrt{z}} \int_{-a'_{max}(z, t)}^{a'_{max}(z, t)} f_{fluct}(a' + x) e^{\left(\frac{1}{\tau} - i\omega\right)\frac{a'^2}{2c_L z}} da', \quad (5.19)$$

with

$$A_{film}(t') = \bar{f} \sqrt{\frac{2\pi c_L}{\frac{1}{\tau} - i\omega}} \operatorname{erf}\left(i \sqrt{\left(\frac{1}{\tau} - i\omega\right)t'}\right) e^{\left(-\frac{1}{\tau} + i\omega\right)t'}. \quad (5.20)$$

The integral appearing in Eq. (5.19) represents the perturbation of the spatio-temporal profile of the emitted wave induced by an inhomogeneous emitter density (non-zero f_{fluct}), as compared to the case of a homogeneous one of same average density \bar{f} . Its integrand is a product of a function of zero average value ($f_{fluct}(a)$) and of an oscillatory function of a' ($e^{\left(\frac{1}{\tau} - i\omega\right)\frac{a'^2}{2c_L z}}$). Its value is thus expected to strongly depend on the characteristic distance d_f over which the f function fluctuates, and to become much smaller than A_{film} , when d_f is much smaller than the characteristic fluctuation distance of $e^{\frac{-i\omega a'^2}{2c_L z}}$. This can be seen by decomposing the integral of Eq. (5.19) as a sum of integrals on intervals small enough for the oscillating function to remain

approximately constant, but large enough for the average value of f_{fluct} to approach its 0 overall average value. This exponential has a local wavelength $\Lambda' = 4\pi \frac{c_L z}{\omega a'}$. Since $|a'| \leq a'_{max} \cong \sqrt{2z c_L t'}$, Λ' obeys $\Lambda' \geq \Lambda \sqrt{\frac{2z}{c_L t'}}$, where $\Lambda = \frac{c_L}{f}$ is the acoustic wavelength. The $d_f \ll \Lambda'$ condition is thus always fulfilled at the front of the emitted pulse, as $\Lambda' \rightarrow \infty$ when $t' \rightarrow 0$. A general criterion for the whole emitted acoustic pulse to resemble that emitted by a homogeneous transducer can be obtained by replacing t' by the duration of the emitted pulse τ , leading to

$$d_f \ll \Lambda \sqrt{\frac{2z}{c_L \tau}}. \quad (5.21)$$

In our experiments, c_L is about 6000 m/s, and the $f = 40$ -50 GHz detected acoustic frequencies correspond to acoustic wavelengths in the 120-150 nm range. As the acoustic quality factors of substrate-supported nano-objects $Q = \pi f \tau$ is typically of the order of 10 [262], τ is estimated to be of the order of 100 ps for an acoustic source emitting at 50 GHz. Thus, after propagation on distance of a few μm , the $\sqrt{\frac{2z}{c_L \tau}}$ factor has a value of a few units (≈ 5 for $z = 6 \mu\text{m}$).

Numerical simulations of the waves produced by emitters with inhomogeneous density, based on Eq. (5.16) are presented in Figure 5.9. An emitter chain extending over 10 μm was considered in these simulations (a finite emitter chain being required for numerically estimating the integral of Eq. (5.16) with random f values). Several random functions with the same average values but differing by the d_f characteristic distance over which they fluctuate were used for f . This was practically done by considering functions with independent and equiprobable random values of 0 and $2\bar{f}$ over successive d_f intervals (d_f values of 1, 10 and 100 nm being considered in Figure 5.9). The results of these simulations confirm and illustrate the conclusions of the analytical analyses presented above. Indeed, they show that the emitted waves resemble more and more those emitted by a homogeneous transducer (shown in Figure 5.9D) as d_f is decreased, and that this similarity is strong, when the criterion of Eq. (5.21) is fulfilled, which is the case when $d_f = 1$ nm or 10 nm (Figure 5.9B-C).

For the actual samples used in this study, d_f can be roughly estimated as the average interparticle distance in the sample, whose value is of the order of less than 10 nm for all samples. The criterion of Eq. (5.21) is thus satisfied, as d_f is more than 10 times smaller than $\Lambda \sqrt{\frac{2z}{c_L \tau}}$ for acoustic propagation over distances of a few microns, which is consistent with the successful experimental detection of Brillouin oscillations for all samples. Eq. (5.20), which shows that

the amplitude of the emitted wave scales as the average emitter density, also partly explains the strongly reduced amplitude of these Brillouin oscillations for the laser-processed sample, whose filling factor is much lower than that of the other samples. Such explanation is however only partial, as the amplitude of the measured optical signals is also expected to depend on the frequency content of the emitted acoustic wave-packets, which may be very different for the laser-processed sample as compared to other ones.

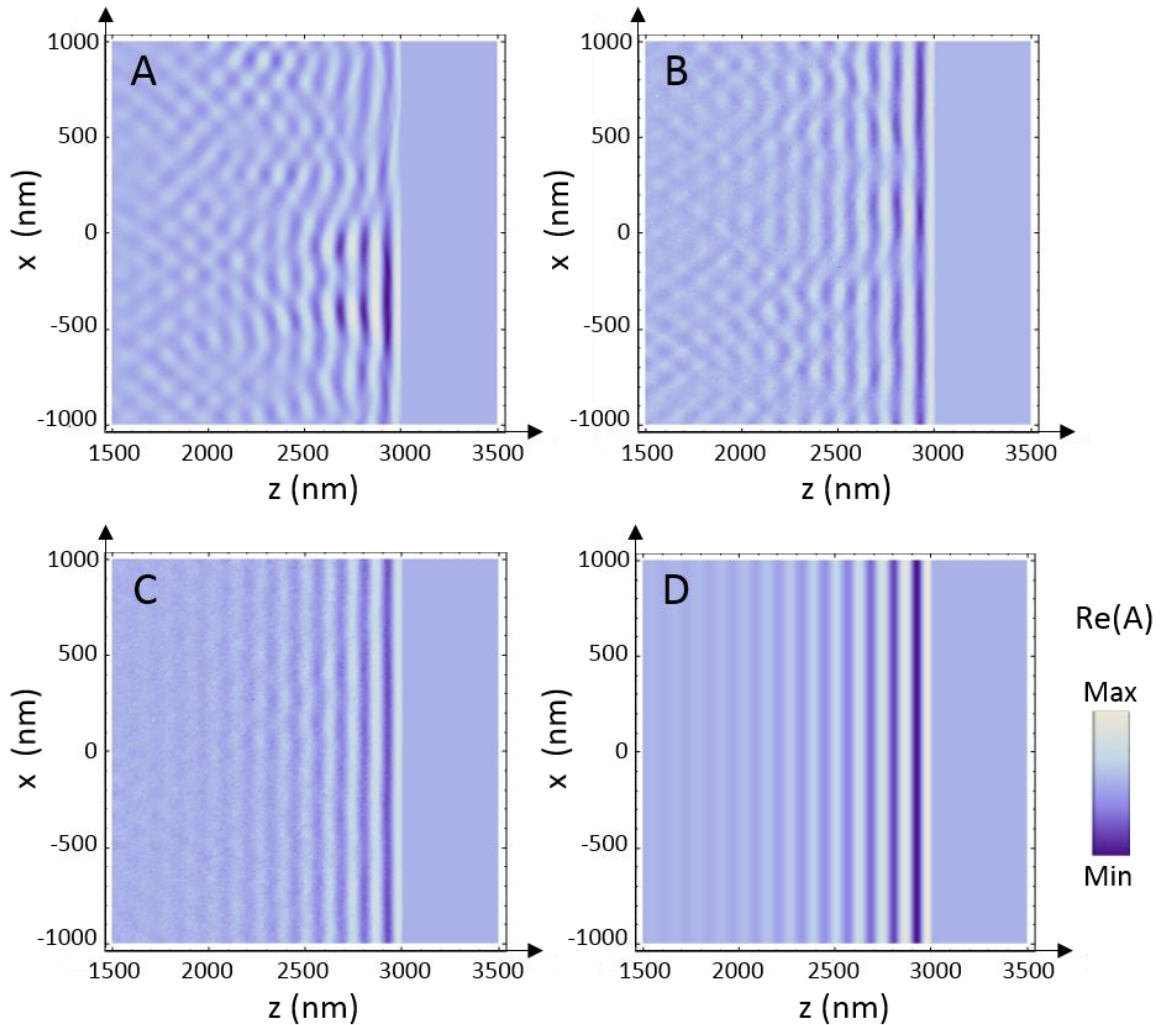


Figure 5.9 – Numerical simulations of the waves generated by an inhomogeneous chain of emitters. Calculations were based on the model described in the main text (Eq. (5.16)), considering a $10\ \mu\text{m}$ long chain of emitters. Emitter densities with randomly chosen, equiprobable 0 or $2\bar{f}$ values every $d_f=100$ nm (A), 10 nm (B) and 1 nm (C) intervals (and thus with same average value \bar{f}) were considered in these calculations. The case of an emitter chain with homogeneous \bar{f} density is also shown for comparison (D). A $c_L=6000$ m/s sound velocity was used, and calculations were done for $t=0.5$ ns time.

5.5 Conclusion

In this chapter, ultrafast laser excitation of plasmonic nanoislands with broad size dispersion (diameter varying from few to few tens of nm) was shown to enable the generation of a coherent acoustic pulse propagating in its supporting N-BK7 glass substrate for all the samples tested. The coherent pulse generation efficiency was demonstrated to dramatically reduce following reshaping of the NPs, the pulse propagation became detectable exclusively in a narrow probe spectral range, where the photoelastic coupling between the photons and the acoustic phonons is the highest. The reduced pulse emission efficiency was attributed to the considerably lower NP filling factor after laser processing. This experimental observation was found to be qualitatively consistent with a simplified model of wave emission by an ensemble of emitters with non-uniform spatial density, showing in particular at which condition the effect of a non-uniform emitter density becomes negligible.

The acoustic pulse propagation in N-BK7 glass was detected as GHz oscillations in transmission time-resolved measurements. The attenuation rates of 40-50 GHz acoustic phonons were determined, revealing their acoustic propagation over several micrometers in the glass, with attenuation rates very close to that previously measured on chemically pure silica, and thus also dominated by anharmonic interactions with the thermal phonon bath. The similarity was attributed to the high proportion of silica in N-BK7 composition.

General conclusions and perspectives

In this thesis, the laser-matter interactions in plasmonic nanocomposites consisting of Ag NP ensembles encapsulated between two TiO₂ thin layers were studied by time-resolved optical techniques as well as *ex situ* characterizations. The relaxation mechanisms following impulsive fs laser excitation were studied on broad timescales, either in conditions of irreversible shape transformations or reversible excitation, depending on the applied laser fluence.

In the third chapter, a high-repetition-rate fs pump - ns spectrally tunable probe arrangement was used to study the pulse-to-pulse evolution of the polarized transmission spectrum of the plasmonic nanocomposite multilayer system. Combined with *ex situ* electron microscopy characterizations, simulations of the temperature rise and simulations of the optical properties of the guided modes supported by the multilayer, the study unveiled the different mechanisms that successively drive the reshaping and self-organization of Ag NPs embedded between TiO₂ layers. The multipulse shape transformations under high-repetition rate, visible fs laser irradiation were studied following the effect of 50000 pulses. The detailed investigation of the evolution of laser-induced nanostructures at different pulse number regimes revealed the decisive laser-induced physico-chemical mechanisms. A chronology of the mechanisms was proposed as following.

The shape transformation is dominated by size reduction at low fs pulse number due to photodissociation of Ag nanoislands. Self-organized nano-pattern forms at this stage with spatial period close to the laser wavelength, which originates from two factors. Firstly, excitation of forward scattered guided mode inside the multilayer film interfering with the incident laser light giving rise to spatial periodic intensity modulation. Secondly, the maximum of the spatial temperature modulation in the Ag layer exceeds the melting temperature of the NP ensemble while the minimum stays below, leading to local reshaping and coalescence within sub-micrometric periodic fringes. With further increasing number of pulses, the shape transformation of nanoislands into prolate spheroids is finished within 6000 pulses, involving the accumulative laser-induced temperature rise exceeding the melting temperature of Ag everywhere in the film, resulting in homogeneous NP melting and solidification. The observed shape anisotropy of the nanoparticles was attributed to directed emission of electrons and Ag⁺ ions, their recombination and diffusion back at the poles. Simultaneously, Ag nanoparticles disperse in a single TiO₂ layer due to collapse of the multilayer system. After tens of thousands of pulses, the increased effective refractive index of the guided mode due to the collapsed multilayer results in a small period interference pattern. The high temperature promotes Ostwald ripening mechanisms that

very slowly form low period gratings, where Ag nanoparticles grow in the low intensity regions, and shrink in the high intensity regions.

The fourth chapter described a work continuing the investigation of multipulse NP shape transformations on the ultrafast timescales. In addition, the dynamics below reshaping threshold and above single pulse ablation threshold were investigated. Starting with the investigations of the dynamics below reshaping fluence threshold, transient absorption spectroscopy revealed complex spectral response containing of a set of combined photo-induced absorption and plasmon bleaching contributions, which could be associated with ground-state plasmon bands in the steady-state absorbance spectrum. The characteristics of these plasmon bands were transiently affected when irradiating the sample with ultrashort laser pulses. Somewhat hidden resonance bands could be clearly revealed by investigating the features of the transient spectra. The decay of all the transients seemed to finish within roughly one ns after the excitation.

The multipulse shape transformation was governed by NP size reduction by charge-assisted atomic desorption and fragmentation processes. Two-color pump-probe microscopy revealed the ultrafast dynamics of the pulse-by-pulse blue-shifting plasmon band due to NP size reduction and increased NP separation. The ultrafast e-e interactions probed relatively close to the LSPR center clearly reflected the pulse-by-pulse band transformation. A slow NP reshaping process was revealed with a definite onset at 200 ps, and lasting on a scale of hundreds of ps. Ag⁺ diffusion within the TiO₂ matrix, nucleation and grow leading to the formation of spherical NPs on the surface, fragmentation and further NP reformation within the matrix were ascribed for this slower reshaping process. *Ex situ* electron microscopy images of laser-marked samples revealed fragmented NPs within the matrix, and NPs formed on the free surface of the multilayer. Beside the size reduction and fragmentation, formation of self-organized nanogratings was evidenced in some sample area by the electron microscopy images.

In experiments characterizing single-pulse nanocomposite ablation, the formation of Newton ring pattern dominated the dynamics on hundreds of ps scale with both selected probe wavelengths. The dynamics of the sample transmittance could be fairly described with existing models of ultrafast laser ablation of very thin films taking into account buildup of tensile stress, film bulge and subsequent Newton rings formation. The film ablation optically indicated by abrupt and definite transmittance increase at both probe wavelengths started at 50 ps. Due to the strong heating and structural transformation of the multilayer sample, quantitative phase measurements using QLSI technique evidenced OPD increase starting after a few ps in relation with the strong heating of the system. OPD variation of several tens of nm was clearly detected at both probe wavelengths, due to overall refractive index modification and the expanding multilayer

sample. At long delays in the range of 10 μs , film removal in the laser-heated area was clearly visible on the microscopy images.

In the last chapter, the excitation, propagation and energy dissipation of acoustic waves emitted by inhomogeneous plasmonic NP ensembles were investigated. By comparing NP ensemble with radically different morphological properties (filling factor, characteristic NP size variation), the coherent pulse generation efficiency was demonstrated to dramatically reduce in samples with low Ag nanoisland filling factor. This experimental observation was supported by a simplified numerical model considering of an infinite, one-dimensional chain of uncoupled, point-like acoustic emitters with non-uniform density, emitting scalar waves. The model demonstrated the relation between the morphological properties of a NP layer and the features of the produced acoustic waves, particularly at which condition the effect of a non-uniform emitter density becomes negligible.

Experimentally, the acoustic pulse energy dissipation during propagation in glass medium was investigated by monitoring the amplitude decay of Brillouin oscillations with increasing propagation distances (several micrometers in glass). The attenuation rates of 40-50 GHz acoustic phonons were measured. The measured attenuation rates were very close to the values measured on chemically pure silica by other groups, implying the same phonon damping mechanisms in the two types of glass. The similarity was attributed to the high proportion of silica in the investigated multicomponent composition (N-BK7).

The broad range of characterizations provided in this thesis about the laser-matter interactions in Ag/TiO₂ multilayer nanocomposites will hopefully serve for improving the applications of such materials in real-world applications. The group, where this work was conducted already provided several impressive demonstrations of printed image multiplexing using Ag/TiO₂ nanocomposites [3], [4]. This technique enables to encode several independent images on the same laser-treated area under different illumination and observation conditions. This feature is particularly useful, *e.g.* in the field of secure documents. The technique strongly relies on laser-generated nanostructures (LIPSS and self-organized NP gratings) and controlling the shape distribution of NP shapes. The presented general description of the mechanisms might contribute to the optimization of this unique optical effect. The investigation of the applicability of such multilayer nanocomposites in that technique has recently started in the group. The following optimization efforts aim at extending the range of macroscopic color gamut on large-extent laser-processed areas using ns laser processing. In parallel, fundamental investigation of the material response to ns laser excitation will be conducted in the multipulse regime, *i.e.*, similar characterizations as in chapter 3 in the present thesis. As the thermal effects in case of ns laser irradiation are much more stronger than those of fs pulses, radically different kinetics for the spectral variation might be expected.

Appendix

In section 2.2.2 in Figure 2.6, fast electron-hole plasma recombination and exciton emission (referred to as electron-hole plasma mechanism), and a slower trap-mediated recombination were described as relaxation pathways in photoexcited ZnO nanorod. Photoexcitation of ZnO by simultaneous two-photon absorption in the near-infrared spectral region promotes electrons from the valence band to the conduction band, resulting in free charge carriers in the conduction band and leaving behind hole states in the conduction band (Figure A1). An electron and a hole can be bound together by Coulomb forces, collectively referred as exciton state, whose energy lies just below the conduction band edge. Alternatively, the electron can become trapped in the crystal lattice at defect sites. Electron-hole recombination from an exciton state results in photon emission centered at 390 nm, and trap-mediated recombination gives rise to a visible emission centered at 550 nm.

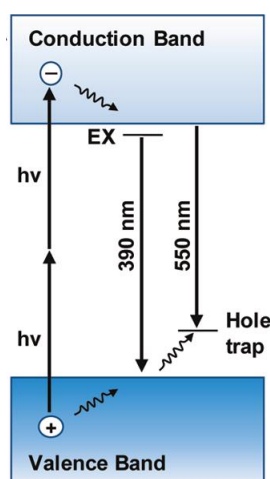


Figure A1 – Illustration of ZnO band structure illustrating two-photon excitation promoting an electron to the conduction band, and leaving behind a hole in the valence band. Electron-hole recombination from an exciton state (bound electron-hole state) is accompanied by photon emission at 390 nm, and trap-mediated recombination is accompanied by a photon emission at 550 nm. Figure is adapted from [105].

Bibliography

- [1] N. Destouches, J. Martínez-García, M. Hébert, N. Crespo-Monteiro, G. Vitrant, Z. Liu, A. Trémeau, F. Vocanson, F. Pigeon, S. Reynaud, and Y. Lefkir, “Dichroic colored luster of laser-induced silver nanoparticle gratings buried in dense inorganic films,” *J. Opt. Soc. Am. B*, vol. 31, no. 11, pp. C1–C7, 2014.
- [2] A. Stalmashonak, G. Seifert, and A. Abdolvand, *Ultra-short pulsed laser engineered metal–glass nanocomposites*. Heidelberg: Springer, 2013.
- [3] N. Destouches, N. Sharma, M. Vangheluwe, N. Dalloz, F. Vocanson, M. Bugnet, M. Hébert, and J. Siegel, “Laser-empowered random metasurfaces for white light printed image multiplexing,” *Adv. Funct. Mater.*, vol. 31, no. 18, p. 2010430, 2021.
- [4] N. Dalloz, V. D. Le, M. Hebert, B. Eles, M. A. . Flores Figueroa, C. Hubert, H. Ma, N. Sharma, F. Vocanson, S. Ayala, and N. Destouches, “Anti-counterfeiting white light printed image multiplexing by fast nanosecond laser processing,” *Adv. Mater.*, vol. 34, no. 2, p. 2104054, 2022.
- [5] N. Crespo-Monteiro, N. Destouches, and T. Fournel, “Updatable random texturing of Ag/TiO₂ films for goods authentication,” *Appl. Phys. Express*, vol. 5, no. 7, p. 75803, 2012.
- [6] S. Kawata, Y. Inouye, and P. Verma, “Plasmonics for near-field nano-imaging and superlensing,” *Nat. Photonics*, vol. 3, no. 7, p. 388, 2009.
- [7] X. Yin, Z. Ye, J. Rho, Y. Wang, and X. Zhang, “Photonic spin Hall effect at metasurfaces,” *Science*, vol. 339, no. 6162, p. 1405, 2013.
- [8] L. Huang, X. Chen, H. Mühlenbernd, H. Zhang, S. Chen, B. Bai, Q. Tan, G. Jin, K. W. Cheah, C. W. Qiu, J. Li, T. Zentgraf, and S. Zhang, “Three-dimensional optical holography using a plasmonic metasurface,” *Nat. Commun.*, vol. 4, p. 2808, 2013.
- [9] H. A. Atwater and A. Polman, “Plasmonics for improved photovoltaic devices,” *Nat. Mater.*, vol. 9, no. 3, p. 205, 2010.
- [10] G. V Hartland, “Optical studies of dynamics in noble metal nanostructures,” *Chem. Rev.*, vol. 111, no. 6, pp. 3858–3887, 2011.
- [11] A. Crut, P. Maioli, N. Del Fatti, and F. Vallée, “Time-domain investigation of the acoustic vibrations of metal nanoparticles: size and encapsulation effects,” *Ultrasonics*, vol. 56, pp. 98–108, 2015.
- [12] A. Warth, J. Lange, H. Graener, and G. Seifert, “Ultrafast dynamics of femtosecond laser-induced shape transformation of silver nanoparticles embedded in glass,” *J. Phys. Chem. C*, vol. 115, no. 47, pp. 23329–23337, 2011.
- [13] A. Crut, P. Maioli, N. Del Fatti, and F. Vallée, “Optical absorption and scattering spectroscopies of single nano-objects,” *Chem. Soc. Rev.*, vol. 43, no. 11, pp. 3921–3956, 2014.
- [14] H. E. Saucedo, D. Mongin, P. Maioli, A. Crut, M. Pellarin, N. Del Fatti, F. Vallée, and I. L. Garzón, “Vibrational properties of metal nanoparticles: atomistic simulation and

- comparison with time-resolved investigation,” *J. Phys. Chem. C*, vol. 116, no. 47, pp. 25147–25156, 2012.
- [15] H. Petrova, C. H. Lin, S. De Liejer, M. Hu, J. M. McLellan, A. R. Siekkinen, B. J. Wiley, M. Marquez, Y. Xia, J. E. Sader, and G. V. Hartland, “Time-resolved spectroscopy of silver nanocubes: observation and assignment of coherently excited vibrational modes,” *J. Chem. Phys.*, vol. 126, no. 9, p. 094709, 2007.
- [16] R. Vacher, S. Ayrinhac, M. Foret, B. Rufflé, and E. Courtens, “Finite size effects in Brillouin scattering from silica glass,” *Phys. Rev. B*, vol. 74, no. 1, p. 012203, 2006.
- [17] R. Côte and A. Devos, “Refractive index, sound velocity and thickness of thin transparent films from multiple angles picosecond ultrasonics,” *Rev. Sci. Instrum.*, vol. 76, no. 5, p. 053906, 2005.
- [18] V. E. Gusev and P. Ruello, “Advances in applications of time-domain Brillouin scattering for nanoscale imaging,” *Appl. Phys. Rev.*, vol. 5, no. 3, p. 031101, 2018.
- [19] E. M. Grumstrup, M. M. Gabriel, E. E. M. Cating, E. M. Van Goethem, and J. M. Papanikolas, “Pump-probe microscopy: visualization and spectroscopy of ultrafast dynamics at the nanoscale,” *Chem. Phys.*, vol. 458, pp. 30–40, 2015.
- [20] T. Stoll, “Ultrafast electronic, acoustic and thermal properties of metal nanoparticles and clusters,” University of Lyon, PhD thesis, 2014.
- [21] F. Medeghini, “Optics and acoustics with a single nano-object: environment effects,” University of Lyon, PhD thesis, 2018.
- [22] N. Del Fatti, C. Voisin, M. Achermann, S. Tzortzakis, D. Christofilos, and F. Vallée, “Nonequilibrium electron dynamics in noble metals,” *Phys. Rev. B*, vol. 61, no. 24, pp. 16956–16966, 2000.
- [23] C. Kittel, *Introduction to solid state physics*, 8th ed. Hoboken: Wiley, 2004.
- [24] N. W. Ashcroft and N. D. Mermin, *Solid state physics*. New York: Holt, Rinehart & Winston, 1976.
- [25] C. Voisin, N. Del Fatti, D. Christofilos, and F. Vallee, “Ultrafast electron dynamics and optical nonlinearities in metal nanoparticles,” *J. Phys. Chem. B*, vol. 105, no. 12, pp. 2264–2280, 2001.
- [26] G. Bassani and F. Pastori-Parravicini, *Electronic states and optical transitions in solids*. New York: Pergamon Press, 1975.
- [27] R. Rosei, “Temperature modulation of the optical transitions involving the Fermi surface in Ag: Theory,” *Phys. Rev. B*, vol. 10, no. 2, pp. 474–483, 1974.
- [28] J. H. Hodak, I. Martini, and G. V. Hartland, “Spectroscopy and dynamics of nanometer-sized noble metal particles,” *J. Phys. Chem. B*, vol. 102, no. 36, pp. 6958–6967, 1998.
- [29] V. A. Markel, “Introduction to the Maxwell Garnett approximation: tutorial,” *J. Opt. Soc. Am. A*, vol. 33, no. 7, p. 1244, 2016.
- [30] M. L. Brongersma, N. J. Halas, and P. Nordlander, “Plasmon-induced hot carrier science and technology,” *Nat. Nanotechnol.*, vol. 10, no. 1, pp. 25–34, 2015.

- [31] C. Voisin, D. Christofilos, N. Del Fatti, F. Vallée, B. Prével, E. Cottancin, J. Lermé, M. Pellarin, and M. Broyer, “Size-dependent electron-electron interactions in metal nanoparticles,” *Phys. Rev. Lett.*, vol. 85, no. 10, pp. 2200–2203, 2000.
- [32] J. Hohlfeld, S. S. Wellershoff, J. Güdde, U. Conrad, V. Jähnke, and E. Matthias, “Electron and lattice dynamics following optical excitation of metals,” *Chem. Phys.*, vol. 251, no. 1–3, pp. 237–258, 2000.
- [33] M. Nisoli, S. Stagira, S. De Silvestri, A. Stella, P. Tognini, P. Cheyssac, and R. Kofman, “Ultrafast electronic dynamics in solid and liquid gallium nanoparticles,” *Phys. Rev. Lett.*, vol. 78, no. 18, pp. 3575–3578, 1997.
- [34] A. Stella, M. Nisoli, S. De Silvestri, and O. Svelto, “Size effects in the ultrafast electronic dynamics of metallic tin nanoparticles,” *Phys. Rev. B*, vol. 53, no. 23, pp. 15497–15500, 1996.
- [35] E. D. Belotskii and P. M. Tomchuk, “Surface electron-phonon energy exchange in small metallic particles,” *Int. J. Electron.*, vol. 73, no. 5, pp. 955–957, 1992.
- [36] S. Link, C. Burda, M. Mohamed, B. Nikoobakht, and M. El-Sayed, “Femtosecond transient-absorption dynamics of colloidal gold nanorods: shape independence of the electron-phonon relaxation time,” *Phys. Rev. B*, vol. 61, no. 9, pp. 6086–6090, 2000.
- [37] N. Del Fatti, C. Voisin, D. Christofilos, F. Vallée, and C. Flytzanis, “Acoustic vibration of metal films and nanoparticles,” *J. Phys. Chem. A*, vol. 104, no. 18, pp. 4321–4326, 2000.
- [38] J. Burgin, P. Langot, N. Del Fatti, F. Vallée, W. Huang, and M. A. El-Sayed, “Time-resolved investigation of the acoustic vibration of a single gold nanoprism pair,” *J. Phys. Chem. C*, vol. 112, no. 30, pp. 11231–11235, 2008.
- [39] H. Staleva and G. V. Hartland, “Transient absorption studies of single silver nanocubes,” *J. Phys. Chem. C*, vol. 112, no. 20, pp. 7535–7539, 2008.
- [40] G. V. Hartland, “Measurements of the material properties of metal nanoparticles by time-resolved spectroscopy,” *Phys. Chem. Chem. Phys.*, vol. 6, no. 23, pp. 5263–5274, 2004.
- [41] M. A. Van Dijk, M. Lippitz, and M. Orrit, “Detection of acoustic oscillations of single gold nanospheres by time-resolved interferometry,” *Phys. Rev. Lett.*, vol. 95, no. 26, p. 267406, 2005.
- [42] V. Juvé, M. Scardamaglia, P. Maioli, A. Crut, S. Merabia, L. Joly, N. Del Fatti, and F. Vallée, “Cooling dynamics and thermal interface resistance of glass-embedded metal nanoparticles,” *Phys. Rev. B*, vol. 80, no. 19, p. 195406, 2009.
- [43] T. Stoll, P. Maioli, A. Crut, S. Rodal-Cedeira, I. Pastoriza-Santos, F. Vallée, and N. Del Fatti, “Time-resolved investigations of the cooling dynamics of metal nanoparticles: Impact of environment,” *J. Phys. Chem. C*, vol. 119, no. 22, pp. 12757–12764, 2015.
- [44] M. Hu and G. V. Hartland, “Heat dissipation for Au particles in aqueous solution: relaxation time versus size,” *J. Phys. Chem. B*, vol. 106, no. 28, pp. 7029–7033, 2002.
- [45] Z. Ge, D. G. Cahill, and P. V. Braun, “AuPd metal nanoparticles as probes of nanoscale thermal transport in aqueous solution,” *J. Phys. Chem. B*, vol. 108, no. 49, pp. 18870–18875, 2004.

- [46] O. M. Wilson, X. Hu, D. G. Cahill, and P. V. Braun, "Colloidal metal particles as probes of nanoscale thermal transport in fluids," *Phys. Rev. B*, vol. 66, no. 22, pp. 2243011–2243016, 2002.
- [47] A. J. Schmidt, J. D. Alper, M. Chiesa, G. Chen, S. K. Das, and K. Hamad-Schifferli, "Probing the gold nanorod-ligand-solvent interface by plasmonic absorption and thermal decay," *J. Phys. Chem. C*, vol. 112, no. 35, pp. 13320–13323, 2008.
- [48] H. Ma, "Numerical study of laser micro- and nano-processing of nanocomposite porous materials," University of Lyon, PhD thesis, 2021.
- [49] Z. Liu, "Self-organization of metallic nanoparticles in waveguides by laser: mechanisms modelling and new approaches," University of Lyon, PhD thesis, 2016.
- [50] Z. Liu, N. Destouches, G. Vitrant, Y. Lefkir, T. Epicier, F. Vocanson, S. Bakhti, Y. Fang, B. Bandyopadhyay, and M. Ahmed, "Understanding the growth mechanisms of Ag nanoparticles controlled by plasmon-induced charge transfers in Ag-TiO₂ films," *J. Phys. Chem. C*, vol. 119, no. 17, pp. 9496–9505, 2015.
- [51] S. Jiang, Y. Zhang, Y. Gan, Z. Chen, and H. Peng, "Molecular dynamics study of neck growth in laser sintering of hollow silver nanoparticles with different heating rates," *J. Phys. D: Appl. Phys.*, vol. 46, no. 33, p. 335302, 2013.
- [52] H. Pan, S. H. Ko, and C. P. Grigoropoulos, "The coalescence of supported gold nanoparticles induced by nanosecond laser irradiation," *Appl. Phys. A*, vol. 90, no. 2, pp. 247–253, 2008.
- [53] H. Pan, S. H. Ko, and C. P. Grigoropoulos, "The solid-state neck growth mechanisms in low energy laser sintering of gold nanoparticles: a molecular dynamics simulation study," *J. Heat Transfer*, vol. 130, no. 9, p. 092404, 2008.
- [54] Y. Wang and C. Dellago, "Structural and morphological transitions in gold nanorods: a computer simulation study," *J. Phys. Chem. B*, vol. 107, no. 35, pp. 9214–9219, 2003.
- [55] Z. Liu, G. Vitrant, Y. Lefkir, S. Bakhti, and N. Destouches, "Laser induced mechanisms controlling the size distribution of metallic nanoparticles," *Phys. Chem. Chem. Phys.*, vol. 18, no. 35, pp. 24600–24609, 2016.
- [56] H. Ma, S. Bakhti, A. Rudenko, F. Vocanson, D. Slaughter, N. Destouches, and T. Itina, "Laser-generated Ag nanoparticles in mesoporous TiO₂ films: formation processes and modeling-based size prediction," *J. Phys. Chem. C*, vol. 123, no. 42, pp. 25898–25907, 2019.
- [57] Z. Liu, J. Siegel, M. Garcia-Lechuga, T. Epicier, Y. Lefkir, S. Reynaud, M. Bugnet, F. Vocanson, J. Solis, G. Vitrant, and N. Destouches, "Three-dimensional self-organization in nanocomposite layered systems by ultrafast laser pulses," *ACS Nano*, vol. 11, no. 5, pp. 5031–5040, 2017.
- [58] A. Furube, L. Du, K. Hara, R. Katoh, and M. Tachiya, "Ultrafast plasmon-induced electron transfer from gold nanodots into TiO₂ nanoparticles," *J. Am. Chem. Soc.*, vol. 129, no. 48, pp. 14852–14853, 2007.
- [59] A. Arbouet, C. Voisin, D. Christofilos, P. Langot, N. Del Fatti, F. Vallée, J. Lermé, G. Celep, E. Cottancin, M. Gaudry, M. Pellarin, M. Broyer, M. Maillard, M. P. Pileni, and

- M. Treguer, “Electron-phonon scattering in metal clusters,” *Phys. Rev. Lett.*, vol. 90, no. 17, p. 177401, 2003.
- [60] C. E. Rodríguez, R. J. Peláez, C. N. Afonso, S. Riedel, P. Leiderer, D. Jimenez-Rey, and A. C. Font, “Plasmonic response and transformation mechanism upon single laser exposure of metal discontinuous films,” *Appl. Surf. Sci.*, vol. 302, pp. 32–36, 2014.
- [61] R. J. Peláez, T. Kuhn, C. E. Rodríguez, and C. N. Afonso, “Dynamics of laser induced metal nanoparticle and pattern formation,” *Appl. Phys. Lett.*, vol. 106, no. 6, p. 061914, 2015.
- [62] J. Doster, G. Baraldi, J. Gonzalo, J. Solis, J. Hernandez-Rueda, and J. Siegel, “Tailoring the surface plasmon resonance of embedded silver nanoparticles by combining nano- and femtosecond laser pulses,” *Appl. Phys. Lett.*, vol. 104, no. 15, p. 153106, 2014.
- [63] G. Baraldi, J. Gonzalo, J. Solis, and J. Siegel, “Reorganizing and shaping of embedded near-coalescence silver nanoparticles with off-resonance femtosecond laser pulses,” *Nanotechnology*, vol. 24, no. 25, p. 255301, 2013.
- [64] A. Stalmashonak, A. Podlipensky, G. Seifert, Graener, and H., “Intensity-driven, laser induced transformation of Ag nanospheres to anisotropic shapes,” *Appl. Phys. B*, vol. 94, no. 3, pp. 459–465, 2009.
- [65] A. A. Unal, A. Stalmashonak, H. Graener, and G. Seifert, “Time-resolved investigation of laser-induced shape transformation of silver nanoparticles,” *Phys. Rev. B*, vol. 80, p. 115415, 2009.
- [66] A. Stalmashonak, G. Seifert, and H. Graener, “Spectral range extension of laser-induced dichroism in composite glass with silver nanoparticles,” *J. Opt. A Pure Appl. Opt.*, vol. 11, no. 6, p. 65001, 2009.
- [67] K. L. Kelly, E. Coronado, L. L. Zhao, and G. C. Schatz, “The optical properties of metal nanoparticles: the influence of size, shape, and dielectric environment,” *J. Phys. Chem. B*, vol. 107, no. 3, pp. 668–677, 2003.
- [68] M. Birnbaum, “Semiconductor surface damage produced by ruby lasers,” *J. Appl. Phys.*, vol. 36, no. 11, p. 3688, 1965.
- [69] J. Bonse and S. Gräf, “Maxwell meets Marangoni — a review of theories on laser-induced periodic surface structures,” *Laser Photonics Rev.*, vol. 14, no. 10, p. 2000215, 2020.
- [70] F. Garrelie, J.-P. Colombier, F. Pigeon, S. Tonchev, N. Faure, M. Bounhalli, S. Reynaud, and O. Parriaux, “Evidence of surface plasmon resonance in ultrafast laser-induced ripples,” *Opt. Express*, vol. 19, no. 10, p. 9035, 2011.
- [71] M. Huang, F. Zhao, Y. Cheng, N. Xu, and Z. Xu, “Origin of laser-induced near-subwavelength ripples: interference between surface plasmons and incident laser,” *ACS Nano*, vol. 3, no. 12, pp. 4062–4070, 2009.
- [72] J. Bonse, A. Rosenfeld, and J. Krüger, “On the role of surface plasmon polaritons in the formation of laser-induced periodic surface structures upon irradiation of silicon by femtosecond-laser pulses,” *J. Appl. Phys.*, vol. 106, no. 10, p. 104910, 2009.
- [73] J. E. Sipe, J. F. Young, J. S. Preston, and H. M. Van Driel, “Laser-induced periodic surface structure. I. Theory,” *Phys. Rev. B*, vol. 27, no. 2, pp. 1141–1154, 1983.

- [74] J. F. Young, J. S. Preston, H. M. Van Driel, and J. E. Sipe, "Laser-induced periodic surface structure. II. Experiments on Ge, Si, Al, and Brass," *Phys. Rev. B*, vol. 27, no. 2, pp. 1155–1172, 1983.
- [75] J. F. Young, J. E. Sipe, and H. M. Van Driel, "Laser-induced periodic surface structure. III. Fluence regimes, the role of feedback, and details of the induced topography in Germanium," *Phys. Rev. B*, vol. 30, no. 4, pp. 2001–2015, 1984.
- [76] H. Zhang, J. P. Colombier, C. Li, N. Faure, G. Cheng, and R. Stoian, "Coherence in ultrafast laser-induced periodic surface structures," *Phys. Rev. B*, vol. 92, no. 17, p. 174109, 2015.
- [77] J. Z. P. Skolski, G. R. B. E. Römer, J. Vincenc Obona, and A. J. Huis In't Veld, "Modeling laser-induced periodic surface structures: finite-difference time-domain feedback simulations," *J. Appl. Phys.*, vol. 115, no. 10, p. 103102, 2014.
- [78] T. R. Anthony and H. R. Cline, "Surface rippling induced by surface-tension gradients during laser surface melting and alloying," *J. Appl. Phys.*, vol. 48, p. 3888, 1977.
- [79] D. Jost, W. Lüthy, H. . Weber, and R. . Salathé, "Laser pulse width dependent surface ripples on silicon," *Appl. Phys. Lett.*, vol. 49, p. 625, 1986.
- [80] G. Gorodetsky, J. Kanicki, T. Kazyaka, and R. L. Melcher, "Far UV pulsed laser melting of silicon," *Appl. Phys. Lett.*, vol. 46, no. 6, p. 547, 1985.
- [81] N. Destouches, N. Crespo-Monteiro, G. Vitrant, Y. Lefkir, S. Reynaud, T. Epicier, Y. Liu, F. Vocanson, and F. Pigeon, "Self-organized growth of metallic nanoparticles in a thin film under homogeneous and continuous-wave light excitation," *J. Mater. Chem. C*, vol. 2, no. 31, pp. 6256–6263, 2014.
- [82] Z. Liu, J. Siegel, M. Garcia-Lechuga, T. Epicier, Y. Lefkir, S. Reynaud, M. Bugnet, F. Vocanson, J. Solis, G. Vitrant, and N. Destouches, "Three-dimensional self-organization in nanocomposite layered systems by ultrafast laser pulses," *ACS Nano*, vol. 11, no. 5, pp. 5031–5040, 2017.
- [83] N. Sharma, N. Destouches, C. Florian, R. Serna, and J. Siegel, "Tailoring metal-dielectric nanocomposite materials with ultrashort laser pulses for dichroic color control," *Nanoscale*, vol. 11, no. 40, pp. 18779–18789, 2019.
- [84] N. Sharma, M. Vangheluwe, F. Vocanson, A. Cazier, M. Bugnet, S. Reynaud, A. Vermeulin, and N. Destouches, "Laser-driven plasmonic gratings for hiding multiple images," *Mater. Horizons*, vol. 6, no. 5, pp. 978–983, 2019.
- [85] K. Loeschner, A. Kiesow, and A. Heilmann, "Periodic structure formation in polymer films with embedded gold nanoparticles," *Adv. Solid State Phys.*, vol. 46, pp. 73–86, 2007.
- [86] K. Loeschner, G. Seifert, and A. Heilmann, "Self-organized, gratinglike nanostructures in polymer films with embedded metal nanoparticles induced by femtosecond laser irradiation," *J. Appl. Phys.*, vol. 108, no. 7, p. 73114, 2010.
- [87] A. Kiesow, S. Strohark, K. Löschner, A. Heilmann, A. Podlipensky, A. Abdolvand, and G. Seifert, "Generation of wavelength-dependent, periodic line pattern in metal nanoparticle-containing polymer films by femtosecond laser irradiation," *Appl. Phys.*

- Lett.*, vol. 86, no. 15, p. 153111, 2005.
- [88] L. Eurenium, C. Hägglund, E. Olsson, B. Kasemo, and D. Chakarov, “Grating formation by metal-nanoparticle-mediated coupling of light into waveguided modes,” *Nat. Photonics*, vol. 2, pp. 360–364, 2008.
- [89] Y. Fuentes-Edfuf, M. Garcia-Lechuga, D. Puerto, C. Florian, A. Garcia-Leis, S. Sanchez-Cortes, J. Solis, and J. Siegel, “Coherent scatter-controlled phase-change grating structures in silicon using femtosecond laser pulses,” *Sci. Rep.*, vol. 7, no. 1, p. 4594, 2017.
- [90] N. Destouches, N. Crespo-Monteiro, G. Vitrant, Y. Lefkir, S. Reynaud, T. Epicier, Y. Liu, F. Vocanson, and F. Pigeon, “Self-organized growth of metallic nanoparticles in a thin film under homogeneous and continuous-wave light excitation,” *J. Mater. Chem. C*, vol. 2, no. 31, pp. 6256–6263, 2014.
- [91] N. Del Fatti and F. Vallée, “Ultrafast optical nonlinear properties of metal nanoparticles,” *Appl. Phys. B Lasers Opt.*, vol. 73, no. 4, pp. 383–390, 2001.
- [92] C. Voisin, N. Del Fatti, D. Christofilos, and F. Vallee, “Ultrafast electron dynamics and optical nonlinearities in metal nanoparticles,” *J. Phys. Chem. B*, vol. 105, no. 12, pp. 2264–2280, 2001.
- [93] J. Y. Bigot, J. Y. Merle, O. Cregut, and A. Daunois, “Electron dynamics in copper metallic nanoparticles probed with femtosecond optical pulses,” *Phys. Rev. Lett.*, vol. 75, no. 25, pp. 4702–4705, 1995.
- [94] X. Wang, Y. Guillet, P. R. Selvakannan, H. Remita, and B. Palpant, “Broadband spectral signature of the ultrafast transient optical response of gold nanorods,” *J. Phys. Chem. C*, vol. 119, no. 13, pp. 7416–7427, 2015.
- [95] K. Yu, L. Polavarapu, and Q. H. Xu, “Excitation wavelength and fluence dependent femtosecond transient absorption studies on electron dynamics of gold nanorods,” *J. Phys. Chem. A*, vol. 115, no. 16, pp. 3820–3826, 2011.
- [96] G. A. Wurtz, R. Pollard, W. Hendren, G. P. Wiederrecht, D. J. Gosztola, V. A. Podolskiy, and A. V. Zayats, “Designed ultrafast optical nonlinearity in a plasmonic nanorod metamaterial enhanced by nonlocality,” *Nat. Nanotechnol.*, vol. 6, no. 2, pp. 107–111, 2011.
- [97] T. O. Otomalo, L. Di Mario, C. Hamon, D. Constantin, K. Van Do, P. O’Keeffe, D. Catone, A. Paladini, and B. Palpant, “Sharp spectral variations of the ultrafast transient light extinction by bimetallic nanoparticles in the near-UV,” *Adv. Opt. Mater.*, vol. 9, no. 8, p. 2001778, 2021.
- [98] S. Yu, J. Zhang, Y. Tang, and M. Ouyang, “Engineering acoustic phonons and electron-phonon coupling by the nanoscale interface,” *Nano Lett.*, vol. 15, no. 9, pp. 6282–6288, 2015.
- [99] J. Wang, P. He, C. Chen, Y. Shao, J. Han, and Y. Gao, “Nonlinear absorption and the ultrafast dynamic process of Au-Ag nanoshuttles,” *OSA Contin.*, vol. 3, no. 9, p. 2485, 2020.
- [100] Q. Cui, F. Ceballos, N. Kumar, and H. Zhao, “Transient absorption microscopy of monolayer and bulk WSe₂,” *ACS Nano*, vol. 8, no. 3, pp. 2970–2976, 2014.

- [101] M. M. Gabriel, J. R. Kirschbrown, J. D. Christesen, C. W. Pinion, D. F. Zigler, E. M. Grumstrup, B. P. Mehl, E. E. M. Cating, J. F. Cahoon, and J. M. Papanikolas, "Direct imaging of free carrier and trap carrier motion in silicon nanowires by spatially-separated femtosecond pump-probe microscopy," *Nano Lett.*, vol. 13, no. 3, pp. 1336–1340, 2013.
- [102] H. Staleva, S. E. Skrabalak, C. R. Carey, T. Kosel, Y. Xia, and G. V. Hartland, "Coupling to light, and transport and dissipation of energy in silver nanowires," *Phys. Chem. Chem. Phys.*, vol. 11, no. 28, pp. 5866–5866, 2009.
- [103] B. Gao, G. V. Hartland, and L. Huang, "Transient absorption spectroscopy of excitons in an individual suspended metallic carbon nanotube," *J. Phys. Chem. Lett.*, vol. 4, no. 18, pp. 3050–3055, 2013.
- [104] E. M. Grumstrup, M. M. Gabriel, E. M. Cating, C. W. Pinion, J. D. Christesen, J. R. Kirschbrown, E. L. Vallorz, J. F. Cahoon, and J. M. Papanikolas, "Ultrafast carrier dynamics in individual silicon nanowires: characterization of diameter-dependent carrier lifetime and surface recombination with pump-probe microscopy," *J. Phys. Chem. C*, vol. 118, no. 16, pp. 8634–8640, 2014.
- [105] B. P. Mehl, J. R. Kirschbrown, R. L. House, and J. M. Papanikolas, "The end is different than the middle: spatially dependent dynamics in ZnO rods observed by femtosecond pump-probe microscopy," *J. Phys. Chem. Lett.*, vol. 2, no. 14, pp. 1777–1781, 2011.
- [106] K. Sokolowski-Tinten, J. Bialkowski, A. Cavalleri, D. Von der Linde, A. Oparin, J. Meyer-Ter-Vehn, and S. I. Anisimov, "Transient states of matter during short pulse laser ablation," *Phys. Rev. Lett.*, vol. 81, no. 1, pp. 224–227, 1998.
- [107] M. Garcia-Lechuga, J. Siegel, J. Hernandez-Rueda, and J. Solis, "Femtosecond laser ablation of dielectric materials in the optical breakdown regime: expansion of a transparent shell," *Appl. Phys. Lett.*, vol. 105, no. 11, p. 112902, 2014.
- [108] M. Garcia-Lechuga, D. Puerto, Y. Fuentes-Edfuf, J. Solis, and J. Siegel, "Ultrafast moving-spot microscopy: birth and growth of laser-induced periodic surface structures," *ACS Photonics*, vol. 3, no. 10, pp. 1961–1967, 2016.
- [109] M. K. Bhuyan, P. K. Velpula, J. P. Colombier, T. Olivier, N. Faure, and R. Stoian, "Single-shot high aspect ratio bulk nanostructuring of fused silica using chirp-controlled ultrafast laser Bessel beams," *Appl. Phys. Lett.*, vol. 104, no. 2, p. 021107, 2014.
- [110] M. Somayaji, M. K. Bhuyan, F. Bourquard, P. K. Velpula, C. D'Amico, J. P. Colombier, and R. Stoian, "Multiscale electronic and thermomechanical dynamics in ultrafast nanoscale laser structuring of bulk fused silica," *Sci. Rep.*, vol. 10, no. 1, p. 15152, 2020.
- [111] P. Bon, G. Maucort, B. Wattellier, and S. Monneret, "Quadriwave lateral shearing interferometry for quantitative phase microscopy of living cells," *Opt. Express*, vol. 17, no. 15, p. 13080, 2009.
- [112] H. Robert, "Optical heating of gold nanoparticles and thermal microscopy. Applications in hydrothermal chemistry and single cell," Aix-Marseille University, PhD thesis, 2018.
- [113] J. Primot and L. Sogno, "Achromatic three-wave (or more) lateral shearing interferometer," *J. Opt. Soc. Am. A*, vol. 12, no. 12, p. 2679, 1995.
- [114] J. Primot, "Three-wave lateral shearing interferometer," *Appl. Opt.*, vol. 32, no. 31, p.

- 6242, 1993.
- [115] B. Wattellier, J. Fuchs, J. P. Zou, K. Abdeli, C. Haefner, and H. Pépin, “High-power short-pulse laser repetition rate improvement by adaptive wave front correction,” *Rev. Sci. Instrum.*, vol. 75, no. 12, pp. 5186–5192, 2004.
- [116] G. Baffou, P. Bon, J. Savatier, J. Polleux, M. Zhu, M. Merlin, H. Rignault, and S. Monneret, “Thermal imaging of nanostructures by quantitative optical phase analysis,” *ACS Nano*, vol. 6, no. 3, pp. 2452–2458, 2012.
- [117] L. Gallais and S. Monneret, “Time-resolved quantitative-phase microscopy of laser-material interactions using a wavefront sensor,” *Opt. Lett.*, vol. 41, no. 14, p. 3245, 2016.
- [118] B. Eles, P. Rouquette, J. Siegel, C. Amra, J. Lumeau, A. Moreau, C. Hubert, M. Zerrad, and N. Destouches, “Mechanisms driving self-organization phenomena in random plasmonic metasurfaces under multipulse femtosecond laser exposure: a multitime scale study,” *Nanophotonics*, vol. 11, no. 10, pp. 2303–2318, 2022.
- [119] K. Naoi, Y. Ohko, and T. Tatsuma, “TiO₂ films loaded with silver nanoparticles: control of multicolor photochromic behavior,” *J. Am. Chem. Soc.*, vol. 126, no. 11, pp. 3664–3668, 2004.
- [120] K. Naoi, Y. Ohko, and T. Tatsuma, “Switchable rewritability of Ag-TiO₂ nanocomposite films with multicolor photochromism,” *Chem. Commun.*, no. 10, pp. 1288–1290, 2005.
- [121] D. K. Diop, L. Simonot, J. Martínez-García, M. Hébert, Y. Lefkir, G. Abadias, P. Guérin, D. Babonneau, and N. Destouches, “Spectral and color changes of Ag/TiO₂ photochromic films deposited on diffusing paper and transparent flexible plastic substrates,” *Appl. Spectrosc.*, vol. 71, no. 6, pp. 1271–1279, 2017.
- [122] N. Crespo-Monteiro, N. Destouches, L. Bois, F. Chassagneux, S. Reynaud, and T. Fournel, “Reversible and irreversible laser microinscription on silver-containing mesoporous titania films,” *Adv. Mater.*, vol. 22, no. 29, pp. 3166–3170, 2010.
- [123] Y. Ohko, T. Tatsuma, T. Fujii, K. Naoi, C. Niwa, Y. Kubota, and A. Fujishima, “Multicolour photochromism of TiO₂ films loaded with silver nanoparticles,” *Nat. Mater.*, vol. 2, no. 1, pp. 29–31, 2003.
- [124] X. Wang, S. Fu, X. Zhang, X. Han, S. Liu, L. Kang, Y. Zhang, and Y. Liu, “Visible laser-assisted reduction of plasmonic Ag nanoparticles with narrow-band optical absorption for colored holographic reconstruction,” *Opt. Express*, vol. 25, no. 25, pp. 31253–31262, 2017.
- [125] Q. Qiao, X. Zhang, Z. Lu, L. Wang, Y. Liu, X. Zhu, and J. Li, “Formation of holographic fringes on photochromic Ag/TiO₂ nanocomposite films,” *Appl. Phys. Lett.*, vol. 94, no. 7, p. 074104, 2009.
- [126] R. Han, X. Zhang, L. Wang, R. Dai, and Y. Liu, “Size-dependent photochromism-based holographic storage of Ag/TiO₂ nanocomposite film,” *Appl. Phys. Lett.*, vol. 98, no. 22, p. 221905, 2011.
- [127] Y. Zhang, L. Shi, D. Hu, S. Chen, S. Xie, Y. Lu, Y. Cao, Z. Zhu, L. Jin, B. O. Guan, S. Rogge, and X. Li, “Full-visible multifunctional aluminium metasurfaces by in situ anisotropic thermoplasmonic laser printing,” *Nanoscale Horiz.*, vol. 4, no. 3, pp. 601–609, 2019.

- [128] A. S. Roberts, S. M. Novikov, Y. Yang, Y. Chen, S. Boroviks, J. Beermann, N. A. Mortensen, and S. I. Bozhevolnyi, “Laser writing of bright colors on near-percolation plasmonic reflector arrays,” *ACS Nano*, vol. 13, no. 1, pp. 71–77, 2019.
- [129] X. Wang, A. Kuchmizhak, D. Storozhenko, S. Makarov, and S. Juodkazis, “Single-step laser plasmonic coloration of metal films,” *ACS Appl. Mater. Interfaces*, vol. 10, no. 1, pp. 1422–1427, 2018.
- [130] Y. Kuroiwa and T. Tatsuma, “Laser printing of translucent plasmonic full-color images with transmission-scattering dichroism of silver nanoparticles,” *ACS Appl. Nano Mater.*, vol. 3, no. 3, pp. 2472–2479, 2020.
- [131] S. N. Chowdhury, P. Nyga, Z. A. Kudyshev, E. Garcia Bravo, A. S. Lagutchev, A. V. Kildishev, V. M. Shalaev, and A. Boltasseva, “Lithography-free plasmonic color printing with femtosecond laser on semicontinuous silver films,” *ACS Photonics*, vol. 8, no. 2, pp. 521–530, 2021.
- [132] M. Wang, B. Gompf, M. Dressel, N. Destouches, and A. Berrier, “Pure circular dichroism by curved rows of plasmonic nanoparticles,” *Opt. Mater. Express*, vol. 8, no. 6, pp. 1515–1527, 2018.
- [133] L. Eurenus, C. Hägglund, E. Olsson, B. Kasemo, and D. Chakarov, “Grating formation by metal-nanoparticle-mediated coupling of light into waveguided modes,” *Nat. Photonics*, vol. 2, pp. 360–364, 2008.
- [134] E. Fort, C. Ricolleau, and J. Sau-Pueyo, “Dichroic thin films of silver nanoparticle chain arrays on faceted alumina templates,” *Nano Lett.*, vol. 3, no. 1, pp. 65–67, 2003.
- [135] N. Sharma, M. Vangheluwe, F. Vocanson, A. Cazier, M. Bugnet, S. Reynaud, A. Vermeulin, and N. Destouches, “Laser-driven plasmonic gratings for hiding multiple images,” *Mater. Horizons*, vol. 6, no. 5, pp. 978–983, 2019.
- [136] S. H. Ko, H. Pan, D. Lee, C. P. Grigoropoulos, and H. K. Park, “Nanoparticle selective laser processing for a flexible display fabrication,” *Jpn. J. Appl. Phys.*, vol. 49, no. 5, p. 05EC03, 2010.
- [137] H. Pan, D. J. Hwang, S. H. Ko, T. A. Clem, J. M. J. Fre, D. Ba, and C. P. Grigoropoulos, “High-throughput near-field optical nanoprocessing of solution-deposited nanoparticles,” *Small*, vol. 6, no. 16, pp. 1812–1821, 2010.
- [138] Y. Son, J. Yeo, H. Moon, T. W. Lim, S. Hong, K. H. Nam, S. Yoo, C. P. Grigoropoulos, D. Yang, and S. H. Ko, “Nanoscale electronics: digital fabrication by direct femtosecond laser processing of metal nanoparticles,” *Adv. Mater.*, vol. 23, no. 28, pp. 3176–3181, 2011.
- [139] Y. Son, J. Yeo, C. Ha, and S. Hong, “Fabrication of submicron-sized metal patterns on a flexible polymer substrate by femtosecond laser sintering of metal nanoparticles,” vol. 9, no. 5–6, pp. 468–476, 2013.
- [140] A. Akin Unal, A. Stalmashonak, G. Seifert, and H. Graener, “Ultrafast dynamics of silver nanoparticle shape transformation studied by femtosecond pulse-pair irradiation pulse-pair irradiation,” *Phys. Rev. B*, vol. 79, no. 11, p. 115411, 2009.
- [141] G. Seifert, M. Kaempfe, K. Berg, and H. Graener, “Femtosecond pump-probe

- investigation of ultrafast silver nanoparticle deformation in a glass matrix,” *Appl. Physics B*, vol. 71, no. 6, pp. 795–800, 2000.
- [142] A. Stalmashonak, A. Podlipensky, G. Seifert, Graener, and H., “Intensity-driven, laser induced transformation of Ag nanospheres to anisotropic shapes,” *Appl. Phys. B*, vol. 94, no. 3, pp. 459–465, 2009.
- [143] J. M. Liu, “Simple technique for measurements of pulsed Gaussian-beam spot sizes,” *Opt. Lett.*, vol. 7, no. 5, pp. 196–198, 1982.
- [144] M. Garcia-Lechuga and D. Grojo, “Simple and robust method for determination of laser fluence thresholds for material modifications: an extension of Liu’s approach to imperfect beams,” *Open Res. Eur.*, vol. 1, p. 7, 2021.
- [145] P. Rouquette, C. Amra, M. Zerrad, and C. Grèzes-Besset, “Photo-induced thermal radiation within multilayers optics,” in *Proc. SPIE*, 2021, vol. 11872, pp. 109–117.
- [146] C. Amra, D. Petiteau, M. Zerrad, S. Guenneau, G. Soriano, B. Gralak, M. Bellieud, D. Veynante, and N. Rolland, “Analogies between optical propagation and heat diffusion: Applications to microcavities, gratings and cloaks,” *Proc. R. Soc. A*, vol. 471, no. 2183, p. 20150143, 2015.
- [147] M. Amra, C., Lequime, M., Zerrad, *Electromagnetic optics of thin-film coatings: light scattering, giant field enhancement, and planar microcavities*. Cambridge University Press: Cambridge, 2021.
- [148] H. A. Macleod, *Thin-film optical filters*, 4th ed. Boca Raton: CRC Press, 2010.
- [149] C. Amra, “First-order vector theory of bulk scattering in optical multilayers,” *J. Opt. Soc. Am. A*, vol. 10, no. 2, pp. 365–374, 1993.
- [150] C. Amra, M. Zerrad, and M. Lequime, “Trapped light scattering within optical coatings: a multilayer roughness-coupling process,” *Opt. Express*, vol. 29, no. 16, pp. 25570–25592, 2021.
- [151] B. Wang, X. Wang, Y. Qin, X. Ni, Z. Shen, and J. Lu, “Temperature field analysis of optical coatings induced by millisecond and nanosecond lasers,” *Opt. Appl.*, vol. 42, no. 4, pp. 783–793, 2012.
- [152] S. A. Shakir and A. F. Turner, “Method of poles for multilayer thin-film waveguides,” *Appl. Phys. A Solids Surfaces*, vol. 29, no. 3, pp. 151–155, 1982.
- [153] E. Anemogiannis, E. N. Glytsis, and T. K. Gaylord, “Determination of guided and leaky modes in lossless and lossy planar multilayer optical waveguides: reflection pole method and wavevector density method,” *J. Light. Technol.*, vol. 17, no. 5, pp. 929–941, 1999.
- [154] M. A. Asoro, J. Damiano, and P. J. Ferreira, “Size effects on the melting temperature of silver nanoparticles: in-situ TEM observations,” *Microsc. Microanal.*, vol. 15, no. SUPPL. 2, pp. 706–707, 2009.
- [155] J. Y. Bigot, V. Halté, J. C. Merle, and A. Daunois, “Electron dynamics in metallic nanoparticles,” *Chem. Phys.*, vol. 251, no. 1–3, pp. 181–203, 2000.
- [156] J. Hohlfeld, J. G. Müller, S.-S. Wellershoff, and E. Matthias, “Time-resolved thermorefectivity of thin gold films and its dependence on film thickness,” *Appl. Phys. B*, vol. 64, no. 3, pp. 387–390, 1997.

- [157] S. Linic, P. Christopher, and D. B. Ingram, "Plasmonic-metal nanostructures for efficient conversion of solar to chemical energy," *Nat. Mater.*, vol. 10, no. 12, pp. 911–921, 2011.
- [158] C. Clavero, "Plasmon-induced hot-electron generation at nanoparticle/metal-oxide interfaces for photovoltaic and photocatalytic devices," *Nat. Photonics*, vol. 8, no. 2, pp. 95–103, 2014.
- [159] Y. Tian and T. Tatsuma, "Mechanisms and applications of plasmon-induced charge separation at TiO₂ films loaded with gold nanoparticles," *J. Am. Chem. Soc.*, vol. 127, no. 20, pp. 7632–7637, 2005.
- [160] N. M. Bulgakova, R. Stoian, A. Rosenfeld, I. V. Hertel, and E. E. B. Campbell, "Electronic transport and consequences for material removal in ultrafast pulsed laser ablation of materials," *Phys. Rev. B*, vol. 69, no. 5, p. 054102, 2004.
- [161] E. Kazuma and T. Tatsuma, "Photoinduced reversible changes in morphology of plasmonic Ag nanorods on TiO₂ and application to versatile photochromism," *Chem. Commun.*, vol. 48, no. 12, pp. 1733–1735, 2012.
- [162] N. Crespo-Monteiro, N. Destouches, L. Nadar, S. Reynaud, F. Vocanson, and J. Y. Michalon, "Irradiance influence on the multicolor photochromism of mesoporous TiO₂ films loaded with silver nanoparticles," *Appl. Phys. Lett.*, vol. 99, no. 17, p. 173106, 2011.
- [163] T. Siefke, S. Kroker, K. Pfeiffer, O. Puffky, K. Dietrich, D. Franta, I. Ohlídal, A. Szeghalmi, E. B. Kley, and A. Tünnermann, "Materials pushing the application limits of wire grid polarizers further into the deep ultraviolet spectral range," *Adv. Opt. Mater.*, vol. 4, no. 11, pp. 1780–1786, 2016.
- [164] J. Franc, N. Morgado, R. Flaminio, R. Nawrodt, I. Martin, L. Cunningham, A. Cumming, S. Rowan, and J. Hough, "Mirror thermal noise in laser interferometer gravitational wave detectors operating at room and cryogenic temperature," *arXiv Prepr. arXiv 0912.0107*, 2009.
- [165] Y. A. Cengel, *Heat and mass transfer: a practical approach*, 3rd ed. New York: McGraw-Hill, 2006.
- [166] P. B. Johnson and R. W. Christy, "Optical constant of the noble metals," *Phys. Rev. B*, vol. 6, no. 12, pp. 4370–4379, 1972.
- [167] A. Salazar, "On thermal diffusivity," *Eur. J. Phys.*, vol. 24, no. 4, pp. 351–358, 2003.
- [168] H. M. Lu, P. Y. Li, Z. H. Cao, and X. K. Meng, "Size-, shape-, and dimensionality-dependent melting temperatures of Nanocrystals," *J. Phys. Chem. C*, vol. 113, no. 18, pp. 7598–7602, 2009.
- [169] W. Luo, W. Hu, and S. Xiao, "Size effect on the thermodynamic properties of silver nanoparticles," *J. Phys. Chem. C*, vol. 112, no. 7, pp. 2359–2369, 2008.
- [170] M. Es-Souni, M. Es-Souni, S. Habouti, N. Pfeiffer, A. Lahmar, M. Dietze, and C. H. Solterbeck, "Brookite formation in TiO₂-Ag nanocomposites and visible-light-induced templated growth of Ag nanostructures in TiO₂," *Adv. Funct. Mater.*, vol. 20, no. 3, pp. 377–385, 2010.

- [171] M. M. Viana, N. D. S. Mohallem, D. R. Miquita, K. Balzuweit, and E. Silva-Pinto, "Preparation of amorphous and crystalline Ag/TiO₂ nanocomposite thin films," *Appl. Surf. Sci.*, vol. 265, pp. 130–136, 2013.
- [172] J. Kulczyk-Malecka, P. J. Kelly, G. West, G. C. B. Clarke, J. A. Ridealgh, K. P. Almqvist, A. L. Greer, and Z. H. Barber, "Investigation of silver diffusion in TiO₂/Ag/TiO₂ coatings," *Acta Mater.*, vol. 66, pp. 396–404, 2014.
- [173] S. Bakhti, N. Destouches, and A. V. Tishchenko, "Singular representation of plasmon resonance modes to optimize the near- and far-field properties of metal nanoparticles," *Plasmonics*, vol. 10, no. 6, pp. 1391–1399, 2015.
- [174] Y. Battie, N. Destouches, F. Chassagneux, D. Jamon, L. Bois, N. Moncoffre, and N. Toulhoat, "Optical properties of silver nanoparticles thermally grown in a mesostructured hybrid silica film," *Opt. Mater. Express*, vol. 1, no. 5, pp. 1019–1033, 2011.
- [175] Z. Liu, G. Vitrant, Y. Lefkir, S. Bakhti, and N. Destouches, "Laser induced mechanisms controlling the size distribution of metallic nanoparticles," *Phys. Chem. Chem. Phys.*, vol. 18, no. 35, pp. 24600–24609, 2016.
- [176] N. T. K. Thanh, N. Maclean, and S. Mahiddine, "Mechanisms of nucleation and growth of nanoparticles in solution," *Chem. Rev.*, vol. 114, no. 15, pp. 7610–7630, 2014.
- [177] A. Stalmashonak, G. Seifert, and H. Graener, "Spectral range extension of laser-induced dichroism in composite glass with silver nanoparticles," *J. Opt. A Pure Appl. Opt.*, vol. 11, no. 6, p. 065001, 2009.
- [178] M. Ferrera, G. Della Valle, M. Sygletou, M. Magnozzi, D. Catone, P. O’Keeffe, A. Paladini, F. Toschi, L. Mattera, M. Canepa, and F. Bisio, "Thermometric calibration of the ultrafast relaxation dynamics in plasmonic Au nanoparticles," *ACS Photonics*, vol. 7, no. 4, pp. 959–966, 2020.
- [179] N. Del Fatti, C. Voisin, M. Achermann, S. Tzortzakis, D. Christofilos, and F. Vallée, "Nonequilibrium electron dynamics in noble metals," *Phys. Rev. B*, vol. 61, no. 24, pp. 16956–16966, 2000.
- [180] D. Werner, A. Furube, T. Okamoto, and S. Hashimoto, "Femtosecond laser-induced size reduction of aqueous gold nanoparticles: in situ and pump–probe spectroscopy investigations revealing Coulomb explosion," *J. Phys. Chem. C*, vol. 115, no. 17, pp. 8503–8512, 2011.
- [181] C. Novo and P. Mulvaney, "Charge-induced Rayleigh instabilities in small gold rods," *Nano Lett.*, vol. 7, no. 2, pp. 520–524, 2007.
- [182] J. M. Voss, P. K. Olshin, R. Charbonnier, M. Drabbels, and U. J. Lorenz, "In situ observation of Coulomb fission of individual plasmonic nanoparticles," *ACS Nano*, vol. 13, no. 11, pp. 12445–12451, 2019.
- [183] A. Plech, V. Kotaidis, M. Lorenc, and J. Boneberg, "Femtosecond laser near-field ablation from gold nanoparticles," *Nat. Phys.*, vol. 2, no. 1, pp. 44–47, 2006.
- [184] M. Lorenc, M. Ziolk, R. Naskrecki, J. Karolczak, J. Kubicki, and A. Maciejewski, "Artifacts in femtosecond transient absorption spectroscopy," *Appl. Phys. B Lasers Opt.*, vol. 74, no. 1, pp. 19–27, 2002.

- [185] X. Zhang, C. Huang, M. Wang, P. Huang, X. He, and Z. Wei, “Transient localized surface plasmon induced by femtosecond interband excitation in gold nanoparticles,” *Sci. Rep.*, vol. 8, no. 1, p. 10499, 2018.
- [186] G. Kedawat, I. Sharma, K. Nagpal, M. Kumar, G. Gupta, and B. K. Gupta, “Studies of ultrafast transient absorption spectroscopy of gold nanorods in an aqueous solution,” *ACS Omega*, vol. 4, no. 7, pp. 12626–12631, 2019.
- [187] X. Wang, Y. Guillet, P. R. Selvakannan, H. Remita, and B. Palpant, “Broadband spectral signature of the ultrafast transient optical response of gold nanorods,” *J. Phys. Chem. C*, vol. 119, no. 13, pp. 7416–7427, 2015.
- [188] G. P. Shevchenko, V. A. Zhuravkov, E. V. Tretyak, S. A. Tikhomirov, O. V. Buganov, A. N. Ponyavina, H. M. Pham, H. T. Do, V. D. Pham, and D. H. Nguyen, “Unusual transient absorption dynamics of silver nanoparticles in solutions of carboxylated amine complexions,” *Adv. Nat. Sci. Nanosci. Nanotechnol.*, vol. 7, no. 3, 2016.
- [189] A. Pinchuk, G. Von Plessen, and U. Kreibig, “Influence of interband electronic transitions on the optical absorption in metallic nanoparticles,” *J. Phys. D. Appl. Phys.*, vol. 37, no. 22, pp. 3133–3139, 2004.
- [190] R. D. Averitt, S. L. Westcott, and N. J. Halas, “Linear optical properties of gold nanoshells,” *J. Opt. Soc. Am. B*, vol. 16, no. 10, p. 1824, 1999.
- [191] S. Link and M. A. El-Sayed, “Spectral properties and relaxation dynamics of surface plasmon electronic oscillations in gold and silver nanodots and nanorods,” *J. Phys. Chem. B*, vol. 103, no. 40, pp. 8410–8426, 1999.
- [192] N. Del Fatti and F. Vallée, “Ultrafast optical nonlinear properties of metal nanoparticles,” *Appl. Phys. B Lasers Opt.*, vol. 73, no. 4, pp. 383–390, 2001.
- [193] M. Hu and G. V. Hartland, “Heat dissipation for Au particles in aqueous solution: relaxation time versus size,” *J. Phys. Chem. B*, vol. 106, no. 28, pp. 7029–7033, 2002.
- [194] H. Zhang and A. O. Govorov, “Optical generation of hot plasmonic carriers in metal nanocrystals: the effects of shape and field enhancement,” *J. Phys. Chem. C*, vol. 118, no. 14, pp. 7606–7614, 2014.
- [195] D. Puerto, J. Siegel, W. Gawelda, M. Galvan-Sosa, L. Ehrentraut, J. Bonse, and J. Solis, “Dynamics of plasma formation, relaxation, and topography modification induced by femtosecond laser pulses in crystalline and amorphous dielectrics,” *J. Opt. Soc. Am. B*, vol. 27, no. 5, p. 1065, 2010.
- [196] G. E. Hallum, D. Kürschner, D. Redka, D. Niethammer, W. Schulz, and H. P. Huber, “Time-resolved ultrafast laser ablation dynamics of thin film indium tin oxide,” *Opt. Express*, vol. 29, no. 19, p. 30062, 2021.
- [197] M. Domke, S. Rapp, M. Schmidt, and H. P. Huber, “Ultrafast pump-probe microscopy with high temporal dynamic range,” *Opt. Express*, vol. 20, no. 9, p. 10330, 2012.
- [198] M. Domke, S. Rapp, M. Schmidt, and H. P. Huber, “Ultra-fast movies of thin-film laser ablation,” *Appl. Phys. A*, vol. 109, no. 2, pp. 409–420, 2012.
- [199] L. V Zhigilei, Z. Lin, and D. S. Ivanov, “Atomistic modeling of short pulse laser ablation

- of metals: connections between melting, spallation, and phase explosion,” *J. Phys. Chem. C*, vol. 113, no. 27, pp. 11892–11906, 2009.
- [200] P. Lorazo, L. J. Lewis, and M. Meunier, “Thermodynamic pathways to melting, ablation, and solidification in absorbing solids under pulsed laser irradiation,” *Phys. Rev. B*, vol. 73, no. 13, p. 134108, 2006.
- [201] K. J. Schrider, “Femtosecond laser interaction with ultrathin metal films: modifying structure, composition, and morphology,” University of Michigan, PhD thesis, 2017.
- [202] P. Das Gupta and G. M. O’Connor, “Comparison of ablation mechanisms at low fluence for ultrashort and short-pulse laser exposure of very thin molybdenum films on glass,” *Appl. Opt.*, vol. 55, no. 9, p. 2117, 2016.
- [203] J. Bonse, G. Bachelier, J. Siegel, J. Solis, and H. Sturm, “Time- and space-resolved dynamics of ablation and optical breakdown induced by femtosecond laser pulses in indium phosphide,” *J. Appl. Phys.*, vol. 103, no. 5, p. 54910, 2008.
- [204] B. Rethfeld, K. Sokolowski-Tinten, D. von der Linde, and S. I. Anisimov, “Timescales in the response of materials to femtosecond laser excitation,” *Appl. Phys. A*, vol. 79, no. 4–6, pp. 767–769, 2004.
- [205] M. Garcia-Lechuga, J. Solis, and J. Siegel, “Key stages of material expansion in dielectrics upon femtosecond laser ablation revealed by double-color illumination time-resolved microscopy,” *Appl. Phys. A*, vol. 124, no. 3, p. 221, 2018.
- [206] D. von der Linde and K. Sokolowski-Tinten, “The physical mechanisms of short-pulse laser ablation,” *Appl. Surf. Sci.*, vol. 154–155, pp. 1–10, 2000.
- [207] C. J. Morath and H. J. Maris, “Phonon attenuation in amorphous solids studied by picosecond ultrasonics,” *Phys. Rev. B*, vol. 54, no. 1, pp. 203–213, 1996.
- [208] R. Vacher, E. Courtens, and M. Foret, “Anharmonic versus relaxational sound damping in glasses. II. Vitreous silica,” *Phys. Rev. B*, vol. 72, no. 21, p. 214205, 2005.
- [209] J. Fabian and P. B. Allen, “Theory of sound attenuation in glasses: the role of thermal vibrations,” *Phys. Rev. Lett.*, vol. 82, no. 7, pp. 1478–1481, 1999.
- [210] T. C. Zhu, H. J. Maris, and J. Tauc, “Attenuation of longitudinal-acoustic phonons in amorphous SiO₂ at frequencies up to 440 GHz,” *Phys. Rev. B*, vol. 44, no. 9, pp. 4281–4289, 1991.
- [211] C. Klieber, E. Peronne, K. Katayama, J. Choi, M. Yamaguchi, T. Pezeril, and K. A. Nelson, “Narrow-band acoustic attenuation measurements in vitreous silica at frequencies between 20 and 400 GHz,” *Appl. Phys. Lett.*, vol. 98, no. 21, p. 211908, 2011.
- [212] K. H. Lin, C. M. Lai, C. C. Pan, J. I. Chyi, J. W. Shi, S. Z. Sun, C. F. Chang, and C. K. Sun, “Spatial manipulation of nanoacoustic waves with nanoscale spot sizes,” *Nat. Nanotechnol.*, vol. 2, no. 11, pp. 704–708, 2007.
- [213] B. Ostovar, M. N. Su, D. Renard, B. D. Clark, P. D. Dongare, C. Dutta, N. Gross, J. E. Sader, C. F. Landes, W. S. Chang, N. J. Halas, and S. Link, “Acoustic vibrations of Al nanocrystals: size, shape, and crystallinity revealed by single-particle transient extinction spectroscopy,” *J. Phys. Chem. A*, vol. 124, no. 19, pp. 3924–3934, 2020.

- [214] R. Marty, A. Arbouet, C. Girard, A. Mlayah, V. Paillard, V. K. Lin, S. L. Teo, and S. Tripathy, “Damping of the acoustic vibrations of individual gold nanoparticles,” *Nano Lett.*, vol. 11, no. 8, pp. 3301–3306, 2011.
- [215] P. V. Ruijgrok, P. Zijlstra, A. L. Tchebotareva, and M. Orrit, “Damping of acoustic vibrations of single gold nanoparticles optically trapped in water,” *Nano Lett.*, vol. 12, no. 2, pp. 1063–1069, 2012.
- [216] P. Zijlstra, A. L. Tchebotareva, J. W. M. Chon, M. Gu, and M. Orrit, “Acoustic oscillations and elastic moduli of single gold nanorods,” *Nano Lett.*, vol. 8, no. 10, pp. 3493–3497, 2008.
- [217] A. Crut, P. Maioli, N. Del Fatti, and F. Vallée, “Acoustic vibrations of metal nano-objects: time-domain investigations,” *Phys. Rep.*, vol. 549, pp. 1–43, 2015.
- [218] Y. Guillet, C. Rossignol, B. Audoin, G. Calbris, and S. Ravaine, “Optoacoustic response of a single submicronic gold particle revealed by the picosecond ultrasonics technique,” *Appl. Phys. Lett.*, vol. 95, no. 6, p. 061909, 2009.
- [219] A. Amziane, L. Belliard, F. Decremps, and B. Perrin, “Ultrafast acoustic resonance spectroscopy of gold nanostructures: towards a generation of tunable transverse waves,” *Phys. Rev. B*, vol. 83, no. 1, p. 014102, 2011.
- [220] K. Yu, T. Devkota, G. Beane, G. P. Wang, and G. V. Hartland, “Brillouin oscillations from single Au nanoplate opto-acoustic transducers,” *ACS Nano*, vol. 11, no. 8, pp. 8064–8071, 2017.
- [221] C. Jean, L. Belliard, T. W. Cornelius, O. Thomas, Y. Pennec, M. Cassinelli, M. E. Toimil-Molares, and B. Perrin, “Spatiotemporal imaging of the acoustic field emitted by a single copper nanowire,” *Nano Lett.*, vol. 16, no. 10, pp. 6592–6598, 2016.
- [222] F. Xu, Y. Guillet, S. Ravaine, and B. Audoin, “All-optical in-depth detection of the acoustic wave emitted by a single gold nanorod,” *Phys. Rev. B*, vol. 97, no. 16, p. 165412, 2018.
- [223] R. Berte, F. Della Picca, M. Poblet, Y. Li, E. Cortés, R. V. Craster, S. A. Maier, and A. V. Bragas, “Acoustic far-field hypersonic surface wave detection with single plasmonic nanoantennas,” *Phys. Rev. Lett.*, vol. 121, no. 25, p. 253902, 2018.
- [224] M. M. A. Yajadda, I. Levchenko, and K. Ostrikov, “Gold nanoresistors with near-constant resistivity in the cryogenic-to-room temperature range,” *J. Appl. Phys.*, vol. 110, no. 2, p. 023303, 2011.
- [225] M. Mirigliano and P. Milani, “Electrical conduction in nanogranular cluster-assembled metallic films,” *Adv. Phys. X*, vol. 6, no. 1, p. 1908847, 2021.
- [226] S. Lee, M. Shin, S. Hwang, and J. Jang, “Unconventional but tunable phase transition above the percolation threshold by two-layer conduction in electroless-deposited Au nanostructures on silicon substrate,” *Nanotechnology*, vol. 26, no. 50, p. 505202, 2015.
- [227] M. Šubr, M. Petr, O. Kylián, J. Kratochvíl, and J. Procházka, “Large-scale Ag nanoislands stabilized by a magnetron-sputtered polytetrafluoroethylene film as substrates for highly sensitive and reproducible surface-enhanced Raman scattering (SERS),” *J. Mater. Chem. C*, vol. 3, no. 43, pp. 11478–11485, 2015.

- [228] T. Chung, Y. Lee, M.-S. Ahn, W. Lee, S.-I. Bae, C. Soon, H. Hwang, and K.-H. Jeong, “Nanoislands as plasmonic materials,” *Nanoscale*, vol. 11, no. 18, pp. 8651–8664, 2019.
- [229] W. Huang, W. Qian, and M. A. El-Sayed, “Coherent vibrational oscillation in gold prismatic monolayer periodic nanoparticle arrays,” *Nano Lett.*, vol. 4, no. 9, pp. 1741–1747, 2004.
- [230] L. Wang, Y. Nishijima, K. Ueno, H. Misawa, and N. Tamai, “Effect of dipole coupling on near-IR LSPR and coherent phonon vibration of periodic gold pair nanocuboids,” *J. Phys. Chem. C*, vol. 116, no. 33, pp. 17838–17846, 2012.
- [231] W. Huang, W. Qian, and M. A. El-Sayed, “The optically detected coherent lattice oscillations in silver and gold monolayer periodic nanoprism arrays: the effect of interparticle coupling,” *J. Phys. Chem. B*, vol. 109, no. 40, pp. 18881–18888, 2005.
- [232] P. M. Jais, D. B. Murray, R. Merlin, and A. V. Bragas, “Metal nanoparticle ensembles: Tunable laser pulses distinguish monomer from dimer vibrations,” *Nano Lett.*, vol. 11, no. 9, pp. 3685–3689, 2011.
- [233] J. Burgin, P. Langot, A. Arbouet, J. Margueritat, J. Gonzalo, C. N. Afonso, F. Vallée, A. Mlayah, M. D. Rossell, and G. Van Tendeloo, “Acoustic vibration modes and electron-lattice coupling in self-assembled silver nanocolumns,” *Nano Lett.*, vol. 8, no. 5, pp. 1296–1302, 2008.
- [234] A. Nelet, A. Crut, A. Arbouet, N. Del Fatti, F. Vallée, H. Portalès, L. Saviot, and E. Duval, “Acoustic vibrations of metal nanoparticles: high order radial mode detection,” *Appl. Surf. Sci.*, vol. 226, no. 1–3, pp. 209–215, 2004.
- [235] W. Qian, L. Lin, Y. J. Deng, Z. J. Xia, Y. H. Zou, and G. K. L. Wong, “Femtosecond studies of coherent acoustic phonons in gold nanoparticles embedded in TiO₂ thin films,” *J. Appl. Phys.*, vol. 87, no. 1, pp. 612–614, 2000.
- [236] C. Klieber, “Ultrafast photo-acoustic spectroscopy of super-cooled liquids,” Massachusetts Institute of Technology, PhD thesis, 2010.
- [237] S. Ayrihac, M. Foret, A. Devos, B. Rufflé, E. Courtens, and R. Vacher, “Subterahertz hypersound attenuation in silica glass studied via picosecond acoustics,” *Phys. Rev. B*, vol. 83, no. 1, p. 014204, 2011.
- [238] H. N. Lin, R. J. Stoner, H. J. Maris, and J. Tauc, “Phonon attenuation and velocity measurements in transparent materials by picosecond acoustic interferometry,” *J. Appl. Phys.*, vol. 69, no. 7, pp. 3816–3822, 1991.
- [239] E. Pontecorvo, M. Ortolani, D. Polli, M. Ferretti, G. Ruocco, G. Cerullo, and T. Scopigno, “Visualizing coherent phonon propagation in the 100 GHz range: a broadband picosecond acoustics approach,” *Appl. Phys. Lett.*, vol. 98, no. 1, p. 011901, 2011.
- [240] V. E. Gusev, “Detection of nonlinear picosecond acoustic pulses by time-resolved Brillouin scattering,” *J. Appl. Phys.*, vol. 116, no. 6, p. 064907, 2014.
- [241] Z. Bai, H. Yuan, Z. Liu, P. Xu, Q. Gao, R. J. Williams, O. Kitzler, R. P. Mildren, Y. Wang, and Z. Lu, “Stimulated Brillouin scattering materials, experimental design and applications: a review,” *Opt. Mater. (Amst.)*, vol. 75, pp. 626–645, 2018.
- [242] N. F. Mott and E. F. Davis, *Electronic processes in non-crystalline materials*. Oxford: Clarendon Press, 1979.

-
- [243] J. Wang and C. Guo, “Long-lived coherent traveling acoustic pulses induced by femtosecond laser pulses,” *Solid State Commun.*, vol. 144, no. 5–6, pp. 198–201, 2007.
- [244] K. Ishioka, A. Rustagi, U. Höfer, H. Petek, and C. J. Stanton, “Intrinsic coherent acoustic phonons in the indirect band gap semiconductors Si and GaP,” *Phys. Rev. B*, vol. 95, no. 3, p. 035205, 2017.
- [245] A. Baydin, R. Gatamov, H. Krzyzanowska, C. J. Stanton, and N. Tolk, “Energy-dependent amplitude of Brillouin oscillations in GaP,” *Phys. Rev. B*, vol. 99, no. 16, p. 165202, 2019.
- [246] G. Baldi, P. Benassi, L. E. Bove, S. Caponi, E. Fabiani, and D. Fioretto, “Dynamic-to-static crossover in the acoustic attenuation of v-GeO₂,” *EPL*, vol. 78, no. 3, p. 36001, 2007.
- [247] B. Rufflé, M. Foret, E. Courtens, R. Vacher, and G. Monaco, “Observation of the onset of strong scattering on high frequency acoustic phonons in densified silica glass,” *Phys. Rev. Lett.*, vol. 90, no. 9, p. 095502, 2003.
- [248] B. Rufflé, G. Guimbretiére, E. Courtens, R. Vacher, and G. Monaco, “Glass-specific behavior in the damping of acousticlike vibrations,” *Phys. Rev. Lett.*, vol. 96, no. 4, p. 045502, 2006.
- [249] C. Masciovecchio, G. Baldi, S. Caponi, L. Comez, S. Di Fonzo, D. Fioretto, A. Fontana, A. Gessini, S. C. Santucci, F. Sette, G. Viliani, P. Vilmercati, and G. Ruocco, “Evidence for a crossover in the frequency dependence of the acoustic attenuation in vitreous silica,” *Phys. Rev. Lett.*, vol. 97, no. 3, p. 035501, 2006.
- [250] R. Vacher, S. Ayrinhac, M. Foret, B. Rufflé, and E. Courtens, “Finite size effects in Brillouin scattering from silica glass,” *Phys. Rev. B*, vol. 74, no. 1, p. 012203, 2006.
- [251] P. Benassi, S. Caponi, R. Eramo, A. Fontana, A. Giugni, M. Nardone, M. Sampoli, and G. Viliani, “Sound attenuation in a unexplored frequency region: Brillouin ultraviolet light scattering measurements in v-SiO₂,” *Phys. Rev. B*, vol. 71, no. 17, p. 172201, 2005.
- [252] C. Masciovecchio, A. Gessini, S. Di Fonzo, L. Comez, S. C. Santucci, and D. Fioretto, “Inelastic ultraviolet scattering from high frequency acoustic modes in glasses,” *Phys. Rev. Lett.*, vol. 92, no. 24, p. 247401, 2004.
- [253] A. Devos, M. Foret, S. Ayrinhac, P. Emery, and B. Rufflé, “Hypersound damping in vitreous silica measured by picosecond acoustics,” *Phys. Rev. B*, vol. 77, no. 10, p. 100201, 2008.
- [254] R. Vacher, E. Courtens, and M. Foret, “Anharmonic versus relaxational sound damping in glasses. II. Vitreous silica,” *Phys. Rev. B*, vol. 72, no. 21, p. 214205, 2005.
- [255] C. Ferrante, E. Pontecorvo, G. Cerullo, A. Chiasera, G. Ruocco, W. Schirmacher, and T. Scopigno, “Acoustic dynamics of network-forming glasses at mesoscopic wavelengths,” *Nat. Commun.*, vol. 4, pp. 1793–1796, 2013.
- [256] J. Jäckle, L. Piché, W. Arnold, and S. Hunklinger, “Elastic effects of structural relaxation in glasses at low temperatures,” *J. Non. Cryst. Solids*, vol. 20, no. 3, pp. 365–391, 1976.
- [257] K. S. Gilkoy and W. A. Phillips, “An asymmetric double-well potential model for

- structural relaxation processes in amorphous materials,” *Philos. Mag. B Phys. Condens. Matter; Stat. Mech. Electron. Opt. Magn. Prop.*, vol. 43, no. 5, pp. 735–746, 1981.
- [258] U. Buchenau, Y. M. Galperin, V. L. Gurevich, D. A. Parshin, M. A. Ramos, and H. R. Schober, “Interaction of soft modes and sound waves in glasses,” *Phys. Rev. B*, vol. 46, no. 5, pp. 2798–2808, 1992.
- [259] G. Baldi, V. M. Giordano, G. Monaco, and B. Ruta, “Sound attenuation at terahertz frequencies and the boson peak of vitreous silica,” *Phys. Rev. Lett.*, vol. 104, no. 19, p. 195501, 2010.
- [260] C. Klieber, E. Peronne, K. Katayama, J. Choi, M. Yamaguchi, T. Pezeril, and K. A. Nelson, “Narrow-band acoustic attenuation measurements in vitreous silica at frequencies between 20 and 400 GHz,” *Appl. Phys. Lett.*, vol. 98, no. 21, p. 211908, 2011.
- [261] Y. C. Wen, S. H. Guol, H. P. Chen, J. K. Sheu, and C. K. Sun, “Femtosecond ultrasonic spectroscopy using a piezoelectric nanolayer: hypersound attenuation in vitreous silica films,” *Appl. Phys. Lett.*, vol. 99, no. 5, p. 051913, 2011.
- [262] A. Crut, P. Maioli, N. Del Fatti, and F. Vallée, “Acoustic vibrations of metal nano-objects : time-domain investigations,” *Phys. Rep.*, vol. 549, pp. 1–43, 2015.